ISSN 2074-272X

науково-практичний журнал 2023/4

Електротехніка і Електромеханіка

Electrical Engineering & Electromechanics

Електричні машини та апарати
Електротехнічні комплекси та системи
Промислова електроніка
Електроізоляційна та кабельна техніка
Електричні станції, мережі і системи

Журнал включено до найвищої категорії «А»
Переліку фахових видань України

З 2019 р. журнал індексується у Scopus

З 2015 р. журнал індексується
у Web of Science Core Collection:
Emerging Sources Citation Index

Electrical Engineering & Electromechanics

Scientific Journal was founded in 2002
Founder – National Technical University «Kharkiv Polytechnic Institute» (Kharkiv, Ukraine)

From no. 1 2019 Journal «Electrical Engineering & Electromechanics» is indexing in **Scopus** and from no. 1 2015 Journal is indexing in **Web of Science Core Collection: Emerging Sources Citation Index (ESCI)**.

Also included in DOAJ (Directory of Open Access Journals), in EBSCO's database, in ProQuest's databases – Advanced Technologies & Aerospace Database and Materials Science & Engineering Database, in Gale/Cengage Learning databases.

Editorial office address:
National Technical University «Kharkiv Polytechnic Institute», Kyrpychova Str., 2, Kharkiv, 61002, Ukraine
phones: +380 57 7076281, +380 67 3594696, **e-mail:** a.m.grechko@gmail.com (**Grechko O.M.)**

ISSN (print) 2074-272X
ISSN (online) 2309-3404

Printed 01 July 2023. Format 60 × 90 ⅛. Paper – offset. Laser printing. Edition 200 copies.
Printed by Printing house «Madrid Ltd» (18, Gudanova Str., Kharkiv, 61024, Ukraine)

Electrical Engineering & Electromechanics
Scientific Journal

no. 4, 2023

Table of Contents

UDC 621.313.33 https://doi.org/10.20998/2074-272X.2023.4.01

V.I. Milykh

Numerical-field analysis of active and reactive winding parameters and mechanical characteristics of a squirrel-cage induction motor

Introduction. *The active and reactive (inductive) winding resistances of three-phase inductions motors (IMs) are investigated. These important parameters are determined during design and are the basis for calculating a number of energy parameters and characteristics.* ***Problem.*** *In the classical design of IM, the winding resistances are determined with insufficient accuracy due to a number of assumptions and conventions. Especially it concerns the operation of IM with increased slip and it affects the accuracy of realization of its design data, starting parameters and characteristics.* ***Goal.*** *The paper aims to further develop the IM design system by numerical-field computational analysis of active and reactive resistances of the IM windings in the whole range of changes in its slip and calculation of the mechanical characteristic of IM to confirm the adequacy of the calculations of these resistances.* ***Methodology.*** *Resistances of the IM windings are determined by numerous calculations of the magnetic fields of dispersion with the FEMM program within stator and rotor teeth steps, and with current displacement in a squirrel-cage rotor core. Everything is done in the slip range when operating from start-up to idle with changing currents in the slots and the corresponding magnetic saturation of the core teeth. A Lua script has been created for the calculations, controlling the FEMM program and providing automation of all calculations.* ***Results.*** *The numerical-field method shows that the classical design method gives very large errors in determining the magnetic conductivities of IM slot dispersion, as well as current displacement in the bars of the squirrel-cage rotor winding. This is especially evident with increased slips in the start-up mode.* ***Originality.*** *Numerical estimates of the differences between the classical and numerical-field methods are given and the origin of errors is analyzed: the strong saturation of the teeth of the stator and rotor cores. This leads to a significant decrease in the magnetic conductivities of slot dispersion and the practical absence of current displacement in the rotor bars, on which the main emphasis was previously made. The obtained results made it possible to calculate the mechanical characteristic of the IM according to a transparent formula without the use of correction coefficients and reference graphical functions.* ***Practical value.*** *The provided technique of numerical-field analysis and the obtained results of the calculation of active and reactive winding resistances and mechanical characteristic are recommended as a basis for the improvement of the IM design system.* References 18, tables 7, figures 13.

Key words **induction motor, stator and rotor windings, active and reactive resistances, magnetic saturation, eddy currents, mechanical characteristics, classical design, numerical-field calculation analysis.**

Досліджуються реактивні (індуктивні) опори розсіяння і активні опори обмоток трифазних асинхронних двигунів (ТАД). Ці їхні важливі параметри визначаються при проєктуванні і є основою для розрахунку низки енергетичних параметрів та характеристик. При класичному проєктуванні ТАД опори обмоток визначаються з недостатньою точністю через низку припущень і умовностей. Особливо це стосується роботи ТАД з підвищеним ковзанням і відбивається на точності реалізації його проєктних даних, пускових параметрів та характеристик. Метою роботи є подальший розвиток системи проєктування ТАД шляхом чисельно-польового розрахункового аналізу активних і реактивних опорів обмоток ТАД у всьому діапазоні зміни його ковзання, і розрахунок механічної характеристики ТАД для підтвердження адекватності розрахунків цих опорів. Опори обмоток ТАД визначаються чисельними розрахунками магнітних полів розсіяння програмою FEMM у межах зубцевих кроків статора і ротора, а в стрижні короткозамкненого ротора – з витісненням струму. Все робиться у діапазоні ковзання при роботі від пуску до неробочого ходу зі зміною струмів в пазах і відповідного магнітного насичення зубців осердь. Для розрахунків створено скріпт Lua, який керує програмою FEMM і забезпечує автоматизацію усіх обчислень. Чисельно-польовим методом показано, що класична методика проєктування дає дуже великі похибки у визначенні магнітних провідностей пазового розсіяння ТАД, а також витіснення струму в стрижнях короткозамкненої обмотки ротора. Особливо це проявляється при підвищених ковзаннях у пусковому режимі. Надано числові оцінки розходжень класичного і чисельно-польового методів і проаналізовано походження похибок – сильне насичення зубців осердь статора і ротора. Це призводить до значного зменшення магнітних провідностей пазового розсіяння і практичної відсутності витіснення струму в стрижнях ротора, на яке раніше робився основний акцент. Отримані результати дозволили розрахувати механічну характеристику ТАД за прозорою формулою без використання коригувальних коефіцієнтів і довідникових графічних функцій. Надана методика чисельно-польового аналізу і отримані результати розрахунку опорів обмоток та механічної характеристики рекомендуються як основа для удосконалення системи проєктування ТАД. Бібл. 18, табл. 7, рис. 13.

Ключові слова: **асинхронний двигун, обмотки статора і ротора, активні і реактивні опори, магнітне насичення, вихрові струми, механічна характеристика, класичне проєктування, чисельно-польовий розрахунковий аналіз.**

Introduction. Three-phase induction motors (TIMs) are among the most common motors in various spheres of human activity. Their creation and improvement is always relevant, especially considering their diversity and mass production. This also applies to the design process with ensuring the accuracy of the implementation of design data, which allows to get rid of lengthy experimental proofs of the created samples.

Active resistances and inductive resistances of dispersion of stator and rotor windings are important parameters of the TIM, which are determined during design. They are the basis for further calculation of a number of its energy parameters and characteristics, such as operational, mechanical and starting.

For the calculation of these resistances in TIM design systems, there are established methods, set out, for example, in books [1, 2], which practically do not change for decades. In these methods, the calculation of the winding resistances at the level of the nominal load of the TIM is usually not related to fundamental problems, however, for slot, frontal and differential scattering, the

formulas of the specific magnetic conductivities are quite approximate. This is especially true for slot scattering, because different shapes of slots require separate formulas that are based on an a priori accepted simplified structure of the magnetic field.

Determination of winding resistances is significantly complicated for the operation of the TIM with increased slip in the range from the starting point to the critical point with the maximum electromagnetic torque. Here, the winding currents increase significantly and the winding resistances are affected by the saturation of the tooth structures of the stator and rotor cores, as well as the displacement of the high-frequency current in the rods of the short-circuited rotor winding.

It was recognized in [1, 2] that these phenomena primarily affect the slot dispersion of the windings and the active resistance of the rotor core, as well as the differential dispersion.

To calculate the components of the active and reactive resistances of the TIM windings that change due to the saturation of the teeth of the stator and rotor cores, the methodology of their design provides certain algorithms [1, 2]. They are built on significant assumptions, which are added to what is accepted in the calculations of the nominal load mode. For example, displacement of current in rotor slots of various shapes is based on the rectangular slots model, change of slot scattering conductivity is based on a partial reduction of its components in the upper part of the slots. And various clarifying coefficients and generalized graphic dependencies, etc. are added to everything.

Thus, the real picture of the physical phenomena taking place becomes opaque for the designer, and the results of the calculations are very approximate.

Numerical field calculations using appropriate software packages, for example, such popular ones as ANSYS Maxwell, COMSOL Multiphysics, FEMM, etc. can overcome conventions in the calculation of active and reactive resistances of TIM windings.

A large number of works, for example, [3-15] are devoted to the application of these complexes and other computational and experimental studies of parameters and characteristics of TIMs. But, fulfilling their specific purpose, they did not delve into the analysis of the active and reactive parameters of the TIM windings in the entire range of accompanying sliding. That is, they used the results of the TIM design and their created samples, without referring to the design analysis of the specified parameters. Therefore, such a task remains insufficiently studied and relevant.

The goal of the work is the further development of the TIM design system by numerical field calculation analysis of the active and reactive resistances of its windings in the range of slip s change from 1 to 0, and the calculation of the mechanical characteristics of the TIM to confirm the adequacy of the calculations of these resistances.

Analysis of the latest research. Research and use of active and inductive TIM parameters are very broad and diverse in theory, design, and experimental work.

To the already mentioned design methods [1, 2], we will add the article [3], where a numerical-field analysis of the adequacy of the design data of the TIM and a method of their refinement are proposed, which also required the use of the specified parameters.

The work [4] is interesting, where it is emphasized that in order to control and achieve an effective TIM drive, a deep understanding and accurate determination of its parametric characteristics is necessary. Accordingly, a critical analysis of modern methods of their determination is carried out, and based on the T-shaped replacement circuit of TIM, an effective method is proposed, which consists of a test without a rotor and with a double load. In-depth experiments on the study of active resistances and inductances of the windings are performed depending on the stator current and frequency. It is noted that the effect of magnetic saturation, losses in the core and skin effect in the rotor rod is fully taken into account, which ensures the accuracy of the measurement of TIM parameters.

In the practice of calculating parameters and characteristics of TIMs, the evolution took place depending on the availability of technical capabilities and software.

The article [5] is devoted to determining the parameters of the TIM replacement circuit according to the passport data of induction motors and constructing their mechanical characteristics with an analysis of the calculation error. Variants of refinement of the well-known Kloss formula and a modified critical slip formula are considered. But it is not talking about changes in TIM parameters due to saturation of the magnetic core and displacement of current in the rotor winding.

Inductances of stator and rotor windings and magnetic scattering in [6] are determined by the Finite Element Method. The studies are carried out when the magnetizing currents and rotor speed change and reflect the change in TIM parameters. But they are determined for windings as a whole without analysis of components of inductances and current displacement in the rotor rods.

In [7], the parameters of the TIM with a complicated stator winding are also determined by numerical field analysis to prove the improvement of the harmonic composition and performance of the machine. The basis of the analysis is a T-shaped TIM replacement circuit, the parameters of which are based on generally accepted assumptions.

In [8], a 3D mathematical model of transient electromagnetic fields was developed to identify the active and inductive resistances of a short-circuit of the TIM, which takes into account the nonlinearity of the electrophysical and magnetic properties of materials.

In [9], the equation obtained for determining the active resistance of the stator phase winding, which consists of the relationship of the average values of the integral functions of the current and voltage in the steady state mode of operation is considered, which is focused on the analysis of the parametric asymmetry of the induction motor.

In [10], an overview of identification methods for obtaining accurate parameters of an induction motor

offline and online, taking into account the increase in winding temperature, skin effect and saturation of the magnetic core, is provided. During identification, the motor is kept at a standstill and a DC voltage or single-phase AC voltage signal is applied.

The article [11] presents an induction motor parameter estimator based on the model reference adaptive system (MRAS). A new concept of the PQ-MRAS estimator is proposed, which allows simultaneous calculation of the stator and rotor resistances, which is considered its main advantage. The estimator uses the active and reactive powers of the machine, which are calculated from the single measured stator voltage and current.

In [12, 13], an algorithm for calculating mechanical characteristics and methods for analyzing starting modes of induction motors with a short-circuited rotor are proposed. The developed calculation methods are based on a mathematical model of TIM, which takes into account the change in own and mutual differential inductive resistance due to the saturation of the magnetic core and the active resistance of the rotor winding due to the displacement of the current in its rods. However, the actual active and inductive resistances as such are not provided and not analyzed.

The article [14] presents a new methodology for measuring the resistance of an induction motor for mass production, and analyzes the dependence of the inductance of its winding on the magnetizing current and higher-order voltage harmonics, and also provides a simulation model of the motor's resistance to their influence.

In [15] adaptive modeling of TIM is discussed for the purpose of its refined design and compliance with protection standards and a specific purpose. An algorithm for the implementation of static and dynamic simulation of an induction machine is provided, which is verified on the basis of several common methods. One of the foundations of modeling is the T-shaped substitution circuit in various variations of its structure and parameters.

Object of study. To demonstrate the ongoing research, a TIM variant with nominal power P_N = 15 kW; phase voltage U_{sN} = 220 V and frequency f_s = 50 Hz; number of phases m_s = 3 and number of pairs of poles p = 2 was adopted. According to the design calculation of this TIM, in [2] the following was determined: the height of the axis of rotation h = 160 mm, the outer diameters of the stator d_{se} = 0.272 m and the rotor d_r = 0.184 m; air gap δ = 0.5 mm; nominal slip s_N = 0.0026; active length l_a = 0.13 m; rated stator phase current I_{sN} = 29 A; the number of its slots Q_s = 48 and consecutive turns on the phase winding N_s = 112, the number of parallel branches a_s = 2, the winding coefficient K_{Ws} = 0.959; rotor phase current I_{rN} = 442 A; the number of slots Q_r = 38.

The stator winding is single-layer, diametrical, which is typical for TIM of certain power. The rotor winding is short-circuited cast of an aluminum alloy, there is no bevel of the slots, therefore the bevel coefficient K_{sqr} = 1.

The general layout of the TIM is given in Fig. 1.

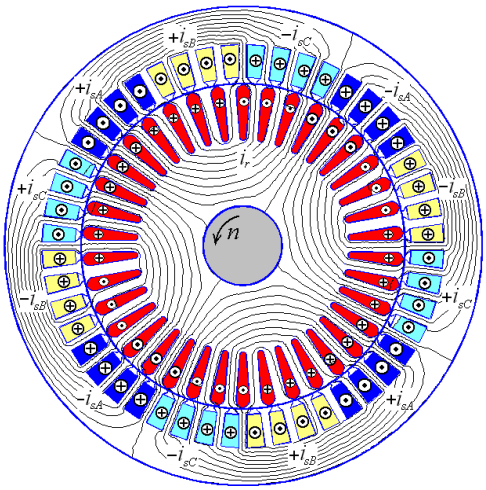

Fig. 1. TIM electromagnetic system with the distribution of currents in its windings and the picture of the lines of force of the magnetic field at nominal load

In this TIM, common shapes of stator and rotor slots of general industrial TIMs [1, 2] are used, which are shown in Fig. 2 together with teeth and size designation (in mm). The rotor core is complicated by a jumper of thickness h_{r0}, which makes the slot closed.

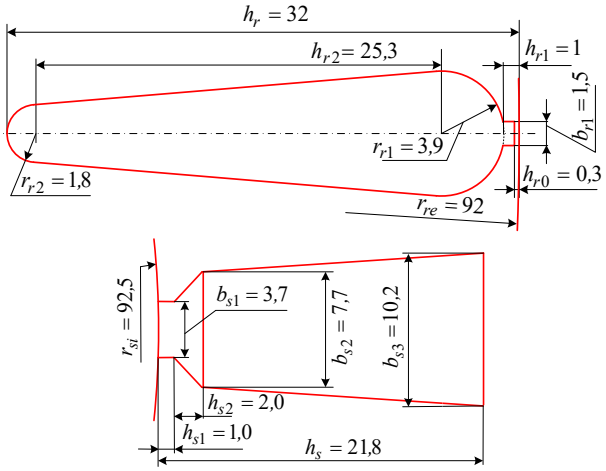

Fig. 2. Slots of the rotor and stator of the considered TIM

Specific formulas of the specific magnetic conductivities of slot scattering correspond to the specific shapes of the slots in the classical method of TIM calculations. But this does not complicate numerical field calculations of magnetic fields, because they are universal and the calculation algorithm does not change when changing from one shape of slot to another. The same applies also to the calculation of the current distribution in the slots of the rotor, taking into account the effect of its displacement.

Fundamentals of numerical-field electromagnetic calculations. Magnetic fields in the TIM are calculated using the well-known Finite Element Method in the popular FEMM software package [16]. Since many calculation options were planned, the process of designing the TIM, building its physical and geometric model in the FEMM software environment, control of magnetic field calculations and determination of the necessary electromagnetic parameters were automated. For this

purpose, following the example in [17] and other author's works, a script was created in the algorithmic language Lua, integrated into the FEMM program.

The stationary magnetic field of the TIM in its central cross-section is described by a well-known 2D differential equation [16]:

$$\mathrm{rot}[\mu_a^{-1}\mathrm{rot}(\vec{k}A_z)] = \vec{k}J_z\,, \qquad (1)$$

where A_z, J_z are the axial components of the magnetic vector potential (MVP) and current density; μ_a is the absolute magnetic permeability; $\vec{k}$ is the ort along the axial axis z.

The propagation of the magnetic field is limited by the outer surface of the stator core, where the Dirichlet boundary condition is set for the MVP: $A_z = 0$. Figure 1 provides an example of a picture of the lines of force of the magnetic field of the TIM at the nominal load.

When calculating the magnetic field together with the eddy currents in the rotor slots, the formulation of the problem changes. In this case, the FEMM program solves the harmonic problem of a plane-parallel electromagnetic field based on the solution of the equation [16]:

$$\mathrm{rot}[\mu_a^{-1}\,\mathrm{rot}(\vec{k}A_z)] = \vec{k}(J_{z\,st} - \gamma_{Al}\frac{\partial A_z}{\partial t})\,, \qquad (2)$$

where A_z, $J_{z\,st}$, $J_{z\,ec} = -\gamma_{Al}\dfrac{\partial A_z}{\partial t}$ are the values of MVP and density of external and eddy currents that change in space and time; γ_{Al} is the specific electrical conductivity of the rotor bar material.

Now, in the complicated case of the mathematical model (2), the axial component of the current density has two components:

$$J_z = J_{z\,st} + J_{z\,ec}\,. \qquad (3)$$

Note that when solving equation (2), the FEMM program operates with complex values that reflect harmonic electromagnetic quantities that change with the frequency of the external current. The calculation results are outputted in the same form, i.e. in their complex values.

To determine a sufficient zone for calculating the distribution of currents in the rotor slots, test calculations were previously performed.

From the considered variants of the electromagnetic field modeling zone, the full geometric model of the TIM, which is shown in Fig. 1, is first selected.

When calculating the current distribution in the rotor winding rods, two rotor winding rods in diametrically located slots are designated as active. The currents in them are directed oppositely to ensure their asymmetry and zero balance of the total current in the calculation zone. There were no currents in the remaining slots of the rotor and stator. The frequency of change of the rotor currents in the start-up mode for the FEMM program is set as $f_r = f_s$.

For the rods in the slots of the rotor, the electrical conductivity of the aluminum casting in the cold state is adopted $\gamma_{Al} = 27$ MS/m [1]. It was found that in both slots the current density distribution was the same with a change of sign.

After preliminary calculations, another calculation model was applied, which is shown in Fig. 3. This is, in fact, a fragment of the complete model in Fig. 1, but within the tooth pitch of the rotor with the capture of the back part of the rotor core and the air gap with the conventional part of the adjacent stator core. Calculations of the magnetic field with eddy currents on this model gave almost the same results as in the previous case. This corresponds to what is done when determining inductive parameters and current displacement in TIM design methods. Moreover, there the calculation zone is limited only to the slot without involving the adjacent parts of the tooth zone, for which the magnetic permeability is considered infinitely large.

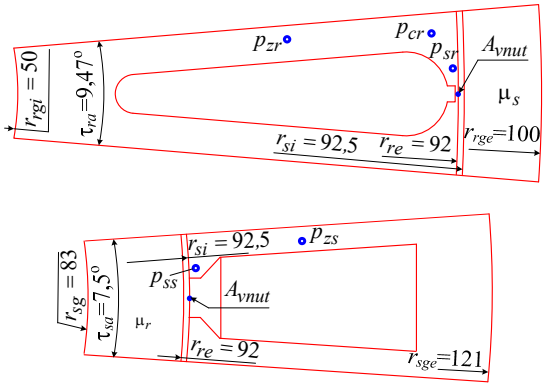

Fig. 3. Calculation models of rotor and stator slots within their tooth pitches

Similarly, the zone of magnetic field calculation is also adopted for the stator slot – it is also shown in Fig. 3 and captures the g slot pitch of the stator core with adjacent parts of its teeth and back, as well as the gap and conventional part of the rotor core.

Thus, when calculating magnetic fields, the calculation models shown in Fig. 3 are used: for the stator slot – according to (1), for the rotor slot – according to (2) taking into account eddy currents.

Since in both cases the magnetic field of slot scattering is calculated, it is considered that beyond the outer limits of the calculation models in Fig. 3 it does not propagate. Therefore, the already mentioned Dirichlet boundary condition is set here for the MVP: $A_z = 0$.

When calculating the magnetic field of the rotor slot, the magnetic properties of the adjacent part of its core were set by the magnetization curve of the corresponding steel, and the constant magnetic permeability μ_s was set for the conventional part of the stator core. When calculating the magnetic field of the stator slot, it was done similarly, and in the conditional part of the rotor core, a constant magnetic permeability μ_r was set. This is indicated in Fig. 3, and below μ_s and μ_r are the relative magnetic permeabilities and their values are given in relative units (p.u.).

Solution of (1), (2) for the FEMM program is a trivial task. Here, external currents are set in the slots, and as a result of the numerical calculation, the program provides the distribution of MVP, and for the rotor slot, the distribution of eddy currents.

After that, it is time to determine the magnetic conductivities of the slot dispersion of the conductors and

the active resistance of the rotor rod. Let's consider the method of this on the example of the rotor slot, for the magnetic conductivities of the stator slot it works similarly.

Examples of pictures of the calculated magnetic fields for the slots of the rotor and stator are given in Fig. 4 (so far without eddy currents in the rotor slot).

For the slot of the rotor or stator, a single (for one conductor) magnetic flux linkage (MFL) is determined together with the «ballast», which is provided by the magnetic field that goes into the gap and the core behind it, Wb:

$$\Psi_{nut} = \frac{1}{S_{nut}} \int_{S_{nut}} A_z dS , \qquad (4)$$

where S_{nut} is the area of the conductor part of the sot, m^2.

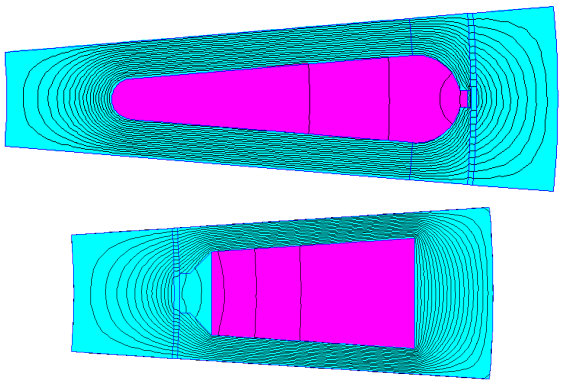

Fig. 4. Pictures of the magnetic field of the rotor bar at μ_s =1000 and stator at μ_r =1000 and nominal currents

MFL of scattering of the inner part of the slot, Wb:

$$\Psi_{rn} = \Psi_{nut} - \Phi_{vnut}, \qquad (5)$$

where Φ_{vnut} is the magnetic flux behind the slot spline (ballast), Wb:

$$\Phi_{vnut} = A_{vnut} \cdot l_a, \qquad (6)$$

where A_{vnut} is the value of MVP, Wb/m, on the surface in the upper part of the slots – at the points given in Fig. 3.

According to MFL (5), the unit inductance of the slot dispersion of conductors in the slot, H, is determined:

$$L_{\sigma rn} = \Psi_{rn} / I_{nut}, \qquad (7)$$

where I_{nut} is the amplitude of the external current, A, in the slot: for the rotor $I_{nut} = \sqrt{2} I_r$ (without eddy currents, which ultimately give a zero contribution); for the stator $I_{nut} = z_{Qs} \sqrt{2} I_s$, where I_r, I_s are the effective values of the currents; z_{Qs} is the number of effective conductors in the stator slot.

The main result is the desired specific magnetic conductivity of the scattering of the inner part of the slot, i.e.:

$$\lambda_{rn} = L_{\sigma rn} / (\mu_0 l_a), \qquad (8)$$

where μ_0 is the magnetic constant ($\mu_0 = 4 \cdot \pi \cdot 10^{-7}$ H/m).

To determine the active resistance of the rotor rod, taking into account the nonuniform distribution of the current density in it, the following steps are carried out.

According to the found distribution of the current density J_z, the active power losses in the rotor core, W, are directly determined by the FEMM program:

$$P_{nr} = \frac{l_a}{\gamma_{Al}} \int_{S_{nut}} J_z^2 dS . \qquad (9)$$

Then the desired active resistance of the rotor winding rod, taking into account the displacement of the current in it, Ω:

$$R_{nr} = 2 \cdot P_{nr} / I_{nut}^2 . \qquad (10)$$

With uniform current distribution, the active resistance of the rotor rod, Ω:

$$R_{nr0} = \frac{l_a}{\gamma_{Al} S_{nut}} . \qquad (11)$$

The degree of change in resistance of the rotor rod is estimated by the coefficient of displacement of its current

$$k_{Rr} = R_{nr} / R_{nr0} . \qquad (12)$$

Analysis of the results of calculations of magnetic fields, eddy currents and parameters of conductors in the slots of the rotor and stator. The main part of the calculations was performed based on the working temperature of the TIM windings, which in the project according to [2] is equal to 115 °C. Here, the specific electrical conductivity of aluminum casting $\gamma_{Al115\ C}$ for the rods of the rotor winding is taken to be equal to 20.5 MS/m.

In order to have basic points of reference, we will give the values of TIM parameters from the project [2]: the magnetic conductivities of the slot dispersion of the rotor λ_{rnb} = 2.64 and the stator λ_{snb} = 1.48, the cross-sectional area of the rotor winding rod S_{rc} = 173.2 mm^2 and its active resistance $R_{nr0} = 34.2 \cdot 10^{-6}$ Ω at temperature of 115 °C.

Considering different calculation modes, the currents in the slots of the rotor and stator (Fig. 3) will be given in relative units (p.u.) as their multiples relative to the nominal values I_{rN} and I_{sN}:

$$k_{Ir} = I_r / I_{rN} ; \quad k_{Is} = I_s / I_{sN}. \qquad (13)$$

To enter the calculations of the magnetic field and parameters at a clear level, let's start with the nominal mode with k_{Ir} = 1, k_{Is} = 1 and the corresponding slip s_N. We will perform the first calculations with unsaturated inactive parts of the calculation models in Fig. 3, for which it is sufficient to take μ_s = 1000 or μ_r = 1000.

The results of the numerical-field calculation of magnetic flux linkages and inductive parameters according to (4)–(8) for the rotor core are given in Table 1, for stator conductors – in Table 2 (in the first rows of the tables), and the pictures of the magnetic fields are already shown in Fig. 4.

Table 1

MFL and inductive parameters of the rotor core at $s = s_N$; k_{Ir} =1; f_r = 1.3 Hz

μ_s, p.u.	Ψ_{nut}, 10^{-4} Wb	A_{vnut}, 10^{-3} Wb/m	Φ_{vnut}, 10^{-4} Wb	Ψ_{rn}, 10^{-4} Wb	$L_{\sigma rn}$, 10^{-7} H	λ_{rn}, p.u.
1000	8,982	4,511	5,864	3,119	4,989	3,054
50	8,400	3,985	5,180	3,220	5,152	3,154
1	4,280	0,6622	0,8609	3,419	5,469	3,348
0,01	3,621	0,1591	0,2068	3,414	5,462	3,343

Table 2

MFL and inductive parameters of stator winding conductors at k_{Is} =1; f_s = 50 Hz

μ_r, p.u..	Ψ_{nut}, 10^{-4} Wb	A_{vnut}, 10^{-3} Wb/m	Φ_{vnut}, 10^{-4} Wb	Ψ_{sn}, 10^{-4} Wb	$L_{\sigma sn}$, 10^{-7} H	λ_{sn}, p.u.
1000	5,41	2,96	3,85	1,562	2,721	1,665
50	4,96	2,62	3,40	1,562	2,720	1,665
1	2,02	0,42	0,556	1,471	2,561	1,568
0,01	1,52	0,070	0,0904	1,431	2,492	1,526

For the main parameter – the magnetic conductivity of slot scattering, the numerical field calculation gave results that exceed the data of classical calculations for rotor and stator slots by 15.7 and 12.5 %. Due to the low frequency of the rotor current f_r = 1.3 Hz, the influence of eddy currents is practically absent.

It can be assumed that the increase in magnetic conductivities was due to a more natural structure of the lines of force of the magnetic field in the upper parts of the slots, where their density and, accordingly, their role is the most significant, while the classical technique is a priori based on an overly simplified structure of the lines of force.

Let us analyze in more detail the structure of the magnetic conductivity of the rotor slot in its upper part – in the jumper zone, which is shown in Fig. 2, 5.

Magnetic conductivity of the slot on the thickness of the jumper according to the conditional formula from the design methodology [2]

$$\lambda_{rnh0} = \frac{1{,}12 \cdot h_{r0}}{I_{rN}} \cdot 10^{-3} = 0{,}760, \qquad (14)$$

and it is also through a numerical field calculation:

$$\lambda_{rnh0\mu} = \frac{A_{nnut} - A_{vnut}}{\mu_0 I_{nut}} = 1{,}243. \qquad (15)$$

where A_{nnut}, A_{vnut} are the values of MVP at the lower and upper points of the jumper, which are indicated in Fig. 5.

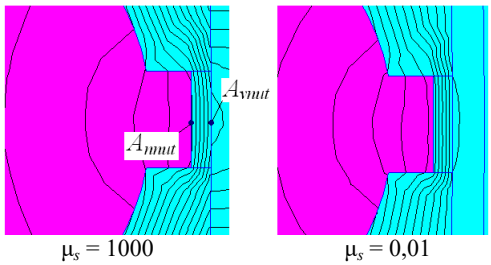

Fig. 5. Fragment of the rotor slot in its upper part

It can be seen that the difference is very large and amounts to 63.5 %, although in the full value of the magnetic conductivity of the dispersion of the rotor slot it looks like 15.9 %. Here, the magnetic flux density in the middle of the jumper is 3.28 T, and the relative magnetic permeability is 12.

It is interesting that if there were no jumper, then this very place, but non-magnetic, would give magnetic conductivity

$$\lambda_{rnh0} = \frac{h_{r0}}{b_{r1}} = 0{,}20, \qquad (16)$$

that is, the steel jumper of the slot significantly increases the value of the inductive parameters of the rotor winding.

In the absence of current displacement in the rotor slot, the active resistance of the rod according to (10) R_{nr} = 36.2·10^{-6} Ω, which is slightly different from the design value R_{nr0} given above. This is due to the fact that the FEMM program by its means determines the cross-sectional area of the rotor winding rod more accurately: S_{nut} = 175.1 mm^2.

On the calculation models in Fig. 3, it was checked how the value of the magnetic conductivity of the inactive part of the calculation zones affects the calculation results. For this, to the already used values μ_s = 1000 and μ_r = 1000 we also added values of 50, 1, and 0.01.

The resulting pictures of the lines of force of the magnetic field are given for the rotor slot in Fig. 6, for the stator slot – in Fig. 7, and the results of the calculations are placed in the next rows of the same Tables 1, 2.

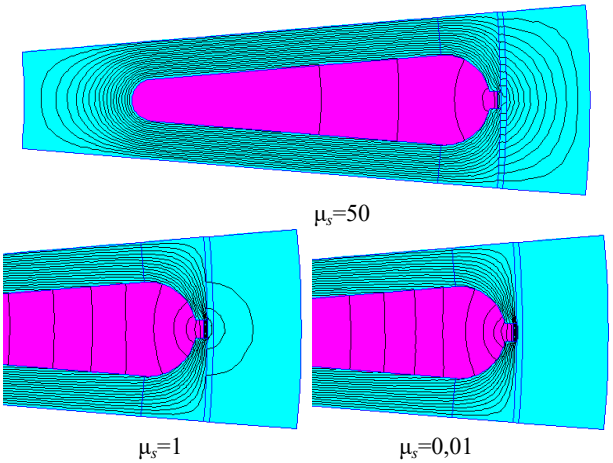

Fig. 6. Pictures of the magnetic field of the rotor rod at different values of the magnetic permeability of the stator core zone

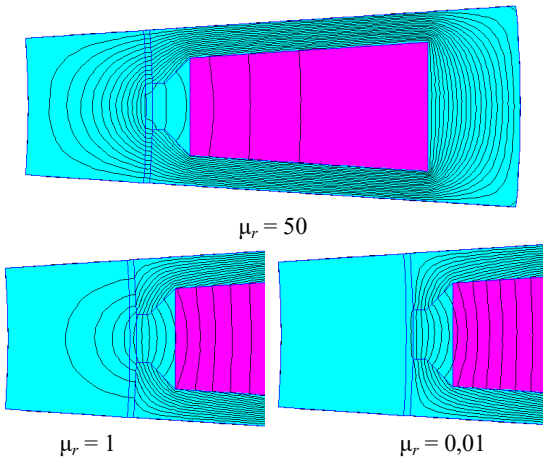

Fig. 7. Pictures of the magnetic field of the stator slot at different values of the magnetic permeability of the rotor core zone

Naturally, as the magnetic permeability of the inactive part decreases, a smaller fraction of the magnetic field passes through the gap, and in the extreme case, at μ_s = 0.01 and μ_r = 0.01, this path is almost completely closed. This just corresponds to the usual assumption when considering slot scattering in [1, 2].

But in other versions, formula (5) singles out exactly the inner slot part of the magnetic field, therefore, in

Tables 1, 2 the conductivity values change relatively weakly. Although there are changes, and this means that there is still some redistribution of the magnetic field. But all the same, the values of λ_{rn} and λ_{rn} turn out to be larger, compared to the basic values from the design calculation.

In classical TIM design, it is considered that the effect of current displacement in the rods of the rotor winding is most pronounced at the initial moment of starting when slip $s = 1$. Moreover, the current distribution is initially determined by analytically solving the equation of the electromagnetic field for a rectangular slot with unsaturated core teeth. Then, for specific shapes of the slot, the result of calculating the active resistance of the winding rod is adjusted on the basis of reference dependencies and correction coefficients formed based on the experience of TIM design. The slot scattering magnetic conductivities obtained for the nominal mode are also corrected in a similar way, and here the saturation of the teeth is indirectly taken into account. It is clear that there is not enough specific physics of the process here, and as a result, a lot of errors in the calculation of the starting parameters accumulate.

Numerical-field calculations are able to bring clarity to this issue and clarify the results, because here conventions and assumptions are made much less, although it is impossible to completely do without them, considering the complexity of the process.

So, let's start as in the classical design, considering the eddy currents in the rotor slot with unsaturated teeth at the multiplicity of the rotor current $k_{Ir} = 1$, but with the slip $s = 1$ and the frequency $f_r = 50$ Hz.

The resulting toned picture of the current density distribution in the rotor slot is given in Fig. 8, where its increase in the upper part of the slot is visible. This is confirmed in Fig. 9, which shows the graphs of the distribution of the current density on the line of symmetry of the Flot by its height. Here there are three options from the complex value of the density of the combined external J_{st} and eddy J_{ec} currents: $|J_{st} + J_{ec}|$ – module; $\mathrm{Re}|J_{st} + J_{ec}|$ – real and $\mathrm{Im}|J_{st} + J_{ec}|$ – imaginary components.

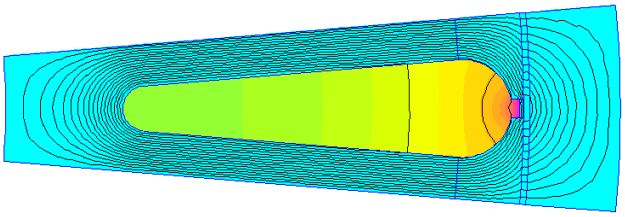

Fig. 8. Picture of the magnetic field of the rotor rod at nonuniform distribution of its current ($f_r = 50$ Hz, $\mu_s = 1000$)

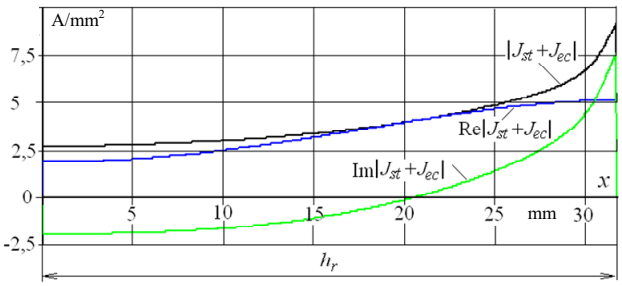

Fig. 9. Distributions of current density components by the height of the rotor slot

A number of calculation results obtained by (8) – (10), (12) are given in Table 3.

Table 3

Data of calculating the parameters of the rotor rod and conductors in the slot of the TIM stator at $f_r = 50$ Hz and $k_{Ir} = 1$, $k_{Ii} = 1$

μ_s, p.u.	P_{nr}, W	R_{nr} μΩ	k_{Rr}	J_{rmax}, A/mm²	J_{rmin}, A/mm²	λ_{rn} p.u.	μ_r, p.u.	λ_{sn} p.u.
1000	9,6	49,0	1,352	5,08	1,85	2,907	1000	1,665
50	9,9	50,6	1,398	5,19	1,73	2,989	50	1,665
1	10,65	54,5	1,506	5,42	1,45	3,133	1	1,568
0,01	10,7	54,8	1,513	5,43	1,43	3,126	0,01	1,526

In numerical form, the nonuniformity of the current density distribution is revealed by the difference in the real component of the current density in the upper J_{rmax} and lower J_{rmin} points of the slot. This is the algebraic sum of the density of external J_{st} and eddy J_{ec} currents. The FEMM program provides output of such data, and they are at $\mu_s = 1000$ in the first line of the Table 3. Naturally, the J_{st} component throughout the slot is constant and equal to 4.83 A/mm², and J_{ec} varies from top to bottom from 0.26 to –2.98 A/mm².

Note that at $\mu_s = 1000$ in this control test version, a noticeable displacement of the current into the upper part of the slot and a corresponding increase in the active resistance of the rod by 1.35 times are manifested, as evidenced by the current displacement coefficient k_{Rr}.

It is also interesting that the specific magnetic conductivity of the rotor slot λ_{rn} compared to the data in Table 1 (without current displacement) decreased by 4.8 %, and the magnetic conductivity of the stator slot λ_{sn} is not related to this.

What was done in the presented calculation at $\mu_s = 1000$ was repeated at other values of the magnetic permeability of the stator core, as it was in Table 1. It can be seen that even when taking into account the displacement of the current with a decrease in μ_s, the coefficient of displacement of the current in the rotor core and the magnetic conductivity λ_{rn} increase. That is, for λ_{rn}, the same happens as in the absence of current displacement, but in the new variant, the values of λ_{rn} turn out to be somewhat smaller.

The performed calculations showed such a level of displacement of the rotor current, which is usually used in the classical design of the TIM. But in these demonstration calculations, the nominal current of the rotor core was artificially accepted, and accordingly the teeth of the rotor core were not saturated (except for the jumper). The value of magnetic flux density and relative magnetic permeability of the rotor tooth at the control points marked in Fig. 3, are given in Table 4 with the specified options for μ_s.

Table 4

Magnetic flux density and magnetic permeability in the rotor teeth at $s = 1$ and $k_{Ir} = 1$

μ_s, p.u.	Rotor tooth							
	Jumper		Crown		Schlitz		Leg	
	B_{rh0}	μ_{rh0}	B_{rc}	μ_{rc}	B_{rs}	μ_{rs}	B_{rz}	μ_{rz}
1000	3,28	12	1,63	1982	1,91	1587	2,19	1068
50	3,30	11	1,50	2137	1,89	1624	2,04	1347
0,01	3,45	8	0,52	2508	1,26	2323	0,87	2435

To increase the level of adequacy, further calculations are performed taking into account realistic values of the currents in the slots of the rotor and stator, which correspond to the start of the TIM. According to the slip s = 1, the frequency of the rotor current is f_r = 50 Hz, and the multiples of the currents are taken according to the TIM project from [2], according to which at the initial moment of start-up k_{Ir} = 6.33 and k_{Is} = 5.84. Here, as in the previous calculations, a number of relative magnetic permeability values μ_s and μ_r are taken for the inactive parts of the models shown in Fig. 3.

The calculation results are given in Table 5 – they are determined by (9), (10), (12) and (8), as well as the current density in the upper and lower points of the rotor slot is given (average value J_{st} = 22.6 A/mm^2).

The saturation level of the rotor and stator teeth is characterized by the data in Tables 6, 7, where the values of magnetic flux density and relative magnetic permeability at the points marked in Fig. 3 are given.

Table 5

Parameters of the rotor rod and conductors of the TIM stator slot at f_r = 50 Hz, k_{Ir} = 6.33 and k_{Is} = 5.84

μ_s, p.u.	P_{nr}, W	R_{nr}, μΩ	k_{Rr}	J_{rmax}, A/mm^2	J_{rmin}, A/mm^2	λ_{rn} p.u.	μ_r, p.u.	λ_{sn} p.u.
1000	284	36,28	1,002	23,0	22,6	0,501	1000	0,435
50	284	36,32	1,003	23,1	22,3	0,555	50	0,476
1	314	40,20	1,110	26,3	18,4	1,260	1	1,092
0,01	342	43,72	1,208	28,0	16,2	1,508	0,01	1,305

Data in Table 4, 6, 7 show that when going from the unsaturated magnetic state at k_{Ir} = 1 and k_{Is} = 1 to the highly saturated state at k_{Ir} = 6.33 and k_{Is} = 5.84, the magnetic flux density increased significantly, and the magnetic permeability decreased accordingly.

Table 6

Magnetic flux density and magnetic permeability in the rotor teeth at s = 1, k_{Ir} = 6.33 and k_{Is} = 5.84

μ_s, p.u.	Rotor tooth							
	Jumper		Crown		Schlitz		Leg	
	B_{rh0}	μ_{rh0}	B_{rc}	μ_{rc}	B_{rs}	μ_{rs}	B_{rz}	μ_{rz}
1	4,32	3	1,83	1701	3,18	17	2,94	99
50	3,5	7	2,45	583	2,79	191	3,06	38

Due to the change in saturation, there were significant changes in the electromagnetic parameters in the slots of the rotor and stator, as evidenced by the comparison of the data in Tables 1, 2, 3, 5.

Table 7

Magnetic flux density and magnetic permeability in the rotor teeth at s = 1 as well as different k_{Ir} and k_{Is}

μ_r, p.u.	k_{Ir} / k_{Ir}, p.u.	Rotor tooth			
		Schlitz		Leg	
		B_{ss}	μ_{ss}	B_{sz}	μ_{sz}
1	6,33 / 5,84	1,62	1998	2,78	196
50	6,33 / 5,84	1,67	1939	3,06	39
50	1 / 1	0,85	2437	1,64	1975
1000	1 / 1	0,92	2433	1,79	1768

The coefficient of current displacement in the rotor rod k_{Rr} significantly decreased, especially in the options μ_s = 50 (the most realistic) and μ_s = 1000. The same happened with the magnetic conductivities of slot scattering λ_{rn} and λ_{sn}, which at μ_s = 50 and μ_r = 50 decreased by 5.49 and 3.5 times respectively. It can be imagined that for the characteristics of the TIM, this will have a more significant impact than changes in the active resistance of the rotor rods, which is usually the focus of attention during their classical design. Moreover, as can be seen from the Table 5, displacement of the current in the rotor bar is practically not manifested.

Mechanical characteristics of TIM. In order to bring all the active and reactive resistances of the TIM windings together and see their realism, their adequacy was checked using the calculation and analysis of the mechanical characteristic $M_{em}(s)$ – the dependence of the electromagnetic torque on slip in the range of its change from 0 to 1.

When calculating the electromagnetic torque, the well-known formula from the TIM theory is used:

$$M_{em} = \frac{pm_s U_s^2 \frac{R_r'}{s}}{\omega_s \left[\left(R_s + C_{\sigma s} \frac{R_r'}{s} \right)^2 + \left(X_{\sigma s} + C_{\sigma s} X_{\sigma r}' \right)^2 \right]}. \quad (17)$$

The following algorithm is used to calculate the parameters of TIM windings by analogy with [1, 2].

Active resistance of the rotor winding

$$R_r = R_{nr} + R_{r\,fr}, \quad (18)$$

where R_{nr} is the resistance of the rod, which is determined by (10); R_{rfr} s the resistance of the short-circuited rings reduced to the rod current.

The inductive resistance of the dispersion of the phase winding of the stator

$$X_{\sigma s} = 1{,}58 \cdot \frac{f_s \cdot l_a \cdot N_s^2 \cdot \lambda_{\sigma s}}{p \cdot q_s \cdot 10^5}, \quad (19)$$

where its total coefficient of scattering conductivity

$$\lambda_{\sigma s} = \lambda_{s n} + \lambda_{s d} + \lambda_{s fh} \quad (20)$$

consists of the coefficients of scattering conductivity of slot $\lambda_{s n}$, differential $\lambda_{s d}$ and frontal $\lambda_{s fh}$.

Inductive resistance of the rotor winding

$$X_{\sigma r} = 7{,}9 \cdot f_s \cdot l_a \cdot \lambda_{\sigma r} \cdot 10^{-6}, \quad (21)$$

where its total coefficient of scattering conductivity

$$\lambda_{\sigma r} = \lambda_{r n} + \lambda_{r d} + \lambda_{r fh} + \lambda_{r sq} \quad (22)$$

consists of the coefficients of scattering conductivity of slot $\lambda_{r n}$, differential $\lambda_{r d}$ and short-circuited rings $\lambda_{r fh}$ ($\lambda_{r sq}$ – the coefficient of dissipation of slot bevel in this case is absent due to the absence of a bevel).

Formula (17) includes the active and inductive resistances of the rotor winding reduced to the stator winding

$$R_r' = K_{sr} R_r; \; X_{\sigma r}' = K_{sr} \cdot X_{\sigma r}, \quad (23)$$

where K_{sr} is the reducing factor.

Among the values that provide (17) according to numerical-field calculations, R_{nr}, $\lambda_{s\ n}$, $\lambda_{r\ n}$ and values dependent on them change.

Differential conductivities, according to [2], also depend on the saturation of the teeth of the cores, but

specific formulas and recommendations are not provided, which requires separate studies. Therefore, in order to reflect the fact of dependence, conventional formulas for the saturated differential conductivities of the stator and rotor are adopted:

$$\lambda_{s\,d} = k_{sd\mu}\lambda_{s\,db}\,;\quad \lambda_{rd} = k_{rd\mu}\lambda_{r\,db}\,, \qquad (24)$$

where are the current-dependent reduction factors

$$k_{sd\mu} = 1 + \frac{(k_{d\mu}-1)(k_{Is}-1)}{(k_{Is1}-1)}\,;\; k_{rd\mu} = 1 + \frac{(k_{d\mu}-1)(k_{Ir}-1)}{(k_{Ir1}-1)}\,,$$

in which $\lambda_{s\,db}$, $\lambda_{r\,db}$ are the base values of conductivities in the unsaturated state (s –> 0); k_{Is1}, k_{Ir1} are the multiples of currents at s = 1; $k_{d\mu}$ is the multiplicity of the differential conductivity at s = 1 relative to the base value at s = 0, which was taken to be equal to 0.7 (in reality it may be less, taking into account the detected changes in slot conductivities). The decrease in differential conductivities is explained by the «smoothing out» of the magnetic inhomogeneity of the tooth-slot structures with strong saturation of their teeth. This issue can be considered separately by analyzing the harmonic composition of the EMF of the windings on the basis of, for example, that presented in [18].

A number of values from (17) – (23) are considered independent of the slip and saturation of the teeth of the cores, and they are accepted according to the project, namely: $R_{r\,fh}$ = 16.2·10^{-6} Ω; R_s = 0.402 Ω; $\lambda_{s\,db}$ = 1.57; $\lambda_{r\,db}$ = 2.08; $\lambda_{s\,fh}$ = 1.45 and $\lambda_{r\,fh}$ = 0.61; K_{sr} = 3636 (the last four are in p.u.).

According to the design calculation of the TIM, the following are also determined: $C_{\sigma s}$ = 1 + $k_{\sigma s}$ is the coefficient of the magnetic circuit for the stator winding, where $k_{\sigma s} = X_{\sigma s} / X_{\mu}$ is its dispersion coefficient; X_{μ} is the main inductive resistance; $\omega_s = 2\pi f_s$ = 314 s^{-1} is the angular frequency of the stator current.

As a result, the dimensionless coefficient $C_{\sigma s}$ varied from 1.018 to 1.027 when the slip changed from 1 to 0.

When calculating the mechanical characteristics according to (17) when the slip s changes, the multiples of the currents of the stator and rotor windings k_{Ir} and k_{Is} were determined according to the design method [2]: their dependence on s in graphic form is given in Fig. 10.

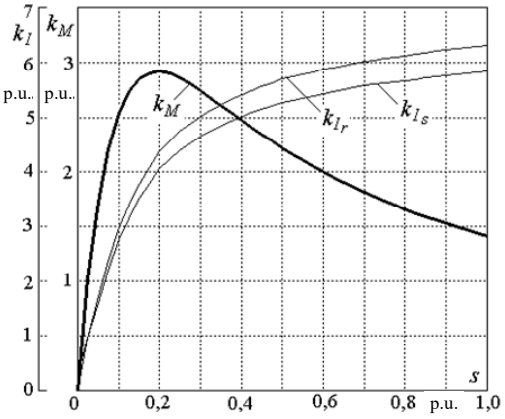

Fig. 10. Dependence of rotor and stator currents on slip and mechanical characteristics of TIM

Calculating each point of this characteristic according to the models in Fig. 3, for inactive parts, that is, parts of the stator and rotor cores, the relative magnetic permeabilities μ_s and μ_r were taken to be equal to 50. Considering the data in the tables, this level corresponds to the saturated state of the teeth, but gives stable results for points with reduced saturation.

A set of parameters for this calculation option for the starting point at s = 1, k_{Ir} = 6.33 and k_{Is} = 5.84 is provided in Tables 5 – 7. The patterns of the magnetic field in the slots of the rotor and stator are shown in Fig. 11, where it can be seen that displacement of the current of the rotor rod actually does not occur: this can be explained in the case of small slips by the low frequency of the current, and in the case of large slips by the strong saturation of the teeth. Note that the detected absence of current displacement in the rotor rods in the start-up mode contradicts the classics, which is news!

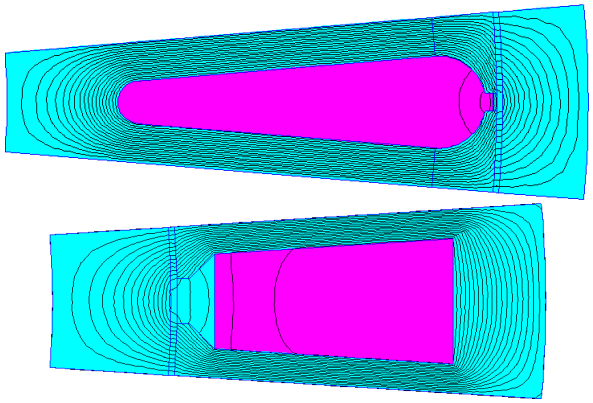

Fig. 11. Pictures of the magnetic field in the slots of the rotor and stator of the calculated version for the starting point

The actual mechanical characteristics in a dimensionless form are shown in Fig. 10, where k_M is the multiple of the torque relative to its nominal value.

According to the calculation of the mechanical characteristics, it was found that the nominal electromagnetic torque 102 N·m; when slip s = 1, the multiplicity of the starting torque k_{M1} = 1.41; overload capacity k_{Mm} = 2.93 at critical slip s_{cr} = 0.20. Note that in the project according to [2], the values of similar quantities were as follows: M_{emN} = 99.4 N·m; k_{M1} = 1.44; k_{Mm} = 2.5 at s_{cr} = 0.15.

But it is also possible to compare the data of the calculated mechanical characteristics of a serial four-pole TIM type AIR160S4 with similar parameters: P_N =15 kW; h = 160 mm; I_{sN} = 29.0 A; k_{I1} = 7; k_{M1} = 1.9; k_{Mm} = 2.9; M_N = 98.1 N·m (nominal torque on the shaft). Then we can verify the adequacy of the given numerical-field method of calculation (we are not talking about experimental confirmation in the general sense, because not all data of serial TIM are known).

In addition to the calculated mechanical characteristics Fig. 12, 13 provide accompanying dependencies of the TIM start-up parameters, where the stability of active and large changes in reactive resistances are visible.

Usually, to increase the starting torque, designers try to make deep slots in the rotor, so that the increase in the active resistance of its rods works. And it turns out that it is not this that works, but a very significant reduction of

slot scattering due to high strongly saturated rotor teeth, as well as stator teeth.

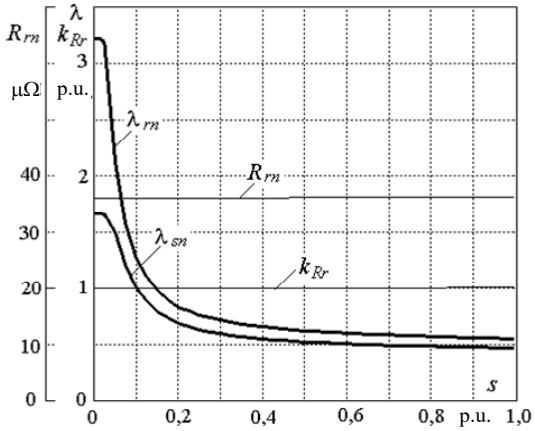

Fig. 12. Active resistance and current displacement coefficient of the rotor rod and magnetic conductivities of the stator and rotor slot scattering as a function of slip

But the influence of the change in the magnetic conductivities of slot scattering on the electromagnetic torque (17) is somewhat smaller, as can be seen from the data in Fig. 12. Because their changes «dissolve» against the background of other more stable active resistances and magnetic conductivities, which are included in (18), (20), (22), (24).

The graphs of the active and reactive resistances of the rotor and stator windings, which are included in (17) as the final values of influence, are given in Fig. 13. And here the undeniable role of reactive resistances and their change in the formation of mechanical characteristics can be seen. But the effect of current displacement, as already mentioned, is practically not manifested, because the active resistance of the phase winding of the rotor R_r' remains practically unchanged.

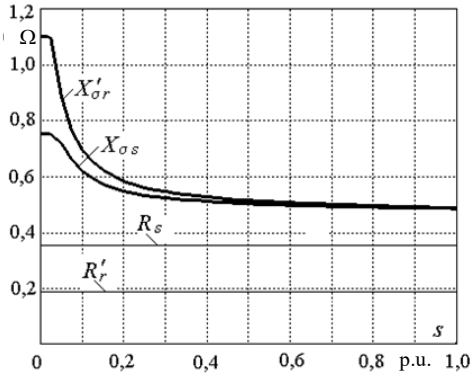

Fig. 13. Active and reactive resistances of TIM windings in the range of changes in slip characteristic of its motor mode of operation

Conclusions.

1. Active and reactive resistances of the windings are important in the TIM design system, but their definition still needs clarification, especially in operating modes with increased slip. Therefore, this problem remains relevant and many theoretical and experimental studies are still devoted to its solution.

2. It was found that for the calculation of the slot scattering fields of the stator and rotor, it is sufficient to use the calculation zone within their tooth pitches with the capture of the slots themselves and adjacent parts of the cores.

3. With unsaturated teeth of the cores, the numerical-field calculation of the magnetic conductivity of slot scattering gave results that exceed the data of classical calculations for rotor slots by 15.7 % and for stator slots by 12.5 %, and for the rotor slot, the main contribution to the error is made by its jumper.

4. Numerical-field calculation of eddy currents in the rotor slot in the same formulation as in classical design, i.e. with unsaturated teeth, nominal current and frequency f_r = 50 Hz gave the current displacement coefficient of 1.35 and an nonuniform distribution of current density with a difference of 2.75 times from the bottom to the top. But when calculating the starting point with real current and strongly saturated teeth, the corresponding values are 1.002 and 1.02, that is, the effect of current displacement is almost absent, contrary to the classics.

5. The method of calculating mechanical characteristics based on the proposed numerical-field approach becomes «transparent» and does not require conditional correction coefficients and reference graphic functions.

6. The calculation of the mechanical characteristics in the slip range from 0 to 1 using the numerical-field method for determining the resistances of the windings, taking into account the corresponding currents in the slots and the saturation of the teeth of the cores, gave results in terms of electromagnetic torque that correspond to the designed and manufactured samples of the TIM, which actually confirms the adequacy of the developed methodology.

7. The analysis showed that when the slip changes, changes in the reactive resistances of the windings have a decisive influence on the shape of the mechanical characteristic and the value of the starting and maximum electromagnetic torques of the TIM, while the active resistances remain practically stable and the effect of current displacement in the rotor slots is almost not manifested, and the main factor is a significant decrease in reactive resistance due to strong saturation of the teeth of the rotor and stator cores.

8. The shown changes in the reactive resistances of the windings are associated with even more pronounced changes in the magnetic conductivities of their slot scattering and, in part, differential scattering. And this is precisely what is affected by the increase in the height of the teeth of the cores, which is associated with an increase in the depth of the slots, but the point is not in the slots and the current squeezed out in them!

9. Thus, the revealed unexpected insignificant effect of current displacement in the squirrel-cage rotor rods on the mechanical characteristics is non-trivial news, and it requires further deeper study and verification on other motors with other shapes and sizes of slots.

Conflict of interest. The author declares no conflict of interest.

REFERENCES

1. Goldberg O.D., Gurin Ya.S., Sviridenko I.S. *Design of electrical machines. 2nd ed., revised and additional*. Moscow, Higher School Publ., 2001. 430 p. (Rus).

2. Kopylov I.P., Goryainov F.A., Klokov B.K. *Electrical machines designing*. Moscow, Yurait Publ., 2011. 767 p. (Rus).
3. Milykh V.I. Numerically-field analysis of the adequacy of the design data of three-phase induction motors and the method of their refinement on this basis. *Technical Electrodynamics*, 2018, no. 1, pp. 47-55. (Rus). doi: https://doi.org/10.15407/techned2018.01.047.
4. Chen H., Bi C. An effective method for determination and characteristic analysis of induction motor parameters. *IET Electric Power Applications*, 2022, vol. 16, no. 5, pp. 605-615. doi: https://doi.org/10.1049/elp2.12180.
5. Ermolaev U., Rudenko T. The definition of asynchronous engines parameters with construction of static characteristics for the milling machine tool СФ-АСТРА-РК8 drives. *Collection of scientific works of KNTU. Machinery in agricultural production, industrial engineering, automation*, 2010, no. 23, pp. 71-77. (Ukr). Available at: http://dspace.kntu.kr.ua/jspui/handle/123456789/1414 (accessed 22 December 2021).
6. Hachicha M.R., Ben Hadj N., Ghariani M., Neji R. Finite element method for induction machine parameters identification. *2012 First International Conference on Renewable Energies and Vehicular Technology*, 2012, pp. 490-496. doi: https://doi.org/10.1109/REVET.2012.6195318.
7. Muteba M., Jimoh A.A. Performance analysis of a three-phase induction motor with double-triple winding layout. *2013 1st International Future Energy Electronics Conference (IFEEC)*, 2013, pp. 131-136. doi: https://doi.org/10.1109/IFEEC.2013.6687492.
8. Yarymbash D.S., Kotsur M.I., Yarymbash S.T., Kotsur I.M. Features of parameter determination of the induction motor substitution circuit for short-circuit mode. *Electrical Engineering and Power Engineering*, 2017, no. 1, pp. 24-30. (Rus). doi: https://doi.org/10.15588/1607-6761-2017-1-4.
9. Tytiuk V., Pozigun O., Chornyi O., Berdai A. Identification of the active resistances of the stator of an induction motor with stator windings dissymmetry. *2017 International Conference on Modern Electrical and Energy Systems (MEES)*, 2017, pp. 48-51. doi: https://doi.org/10.1109/MEES.2017.8248949.
10. Tang J., Yang Y., Blaabjerg F., Chen J., Diao L., Liu Z. Parameter Identification of Inverter-Fed Induction Motors: A Review. *Energies*, 2018, vol. 11, no. 9, art. no. 2194. doi: https://doi.org/10.3390/en11092194.
11. Bednarz S.A., Dybkowski M. Estimation of the Induction Motor Stator and Rotor Resistance Using Active and Reactive Power Based Model Reference Adaptive System Estimator. *Applied Sciences*, 2019, vol. 9, no. 23, art. no. 5145. doi: https://doi.org/10.3390/app9235145.
12. Malyar V.S., Malyar A.V., Andreishyn A.S. A method for calculating mechanical characteristics of induction motors with squirrel-cage rotor. *Electrical Engineering & Electromechanics*, 2019, no. 2, pp. 9-13. doi: https://doi.org/10.20998/2074-272X.2019.2.02.
13. Malyar V.S., Hamola O.Y., Maday V.S., Vasylchyshyn I.I. Mathematical modelling of starting modes of induction motors with squirrel-cage rotor. *Electrical Engineering & Electromechanics*, 2021, no. 2, pp. 9-15. doi: https://doi.org/10.20998/2074-272X.2021.2.02.
14. Dambrauskas K., Vanagas J., Bugenis S., Zimnickas T., Kalvaitis A. Methodology for Asynchronous Motor Impedance Measurement by Using Higher Order Harmonics. *Energies*, 2020, vol. 13, no. 10, art. no. 2541. doi: https://doi.org/10.3390/en13102541.
15. Le Roux P.F., Ngwenyama M.K. Static and Dynamic Simulation of an Induction Motor Using Matlab/Simulink. *Energies*, 2022, vol. 15, no. 10, art. no. 3564. doi: https://doi.org/10.3390/en15103564.
16. *Finite Element Method Magnetics: OldVersions.* FEMM 4.2 11Oct2010 Self-Installing Executable. Available at: http://www.femm.info/wiki/OldVersions (accessed 22 December 2021).
17. Milykh V.I. The system of automated formation of electrical machines computational models for the FEMM software environment. *Technical Electrodynamics*. 2018, no. 4, pp. 74-78. (Ukr). doi: https://doi.org/10.15407/techned2018.04.074.
18. Milykh V.I. Numerical-field analysis of temporal functions and harmonic composition of EMF in windings of a three-phase asynchronous motor. *Technical Electrodynamics*. 2018, no. 3, pp. 56-65. (Rus). doi: https://doi.org/10.15407/techned2018.03.056.

Received 30.08.2022
Accepted 04.11.2022
Published 01.07.2023

V.I. Milykh[1], *Doctor of Technical Science, Professor,*
[1] National Technical University «Kharkiv Polytechnic Institute», 2, Kyrpychova Str., Kharkiv, 61002, Ukraine,
e-mail: mvikemkpi@gmail.com (Corresponding Author)

How to cite this article:
Milykh V.I. Numerical-field analysis of active and reactive winding parameters and mechanical characteristics of a squirrel-cage induction motor. *Electrical Engineering & Electromechanics*, 2023, no. 4, pp. 3-13. doi: https://doi.org/10.20998/2074-272X.2023.4.01

UDC 621.3 https://doi.org/10.20998/2074-272X.2023.4.02

A. Ikhe, Y. Pahariya

Voltage regulation using three phase electric spring by fuzzy logic controller

Introduction. *The renewable energy sources such as solar and wind power have increased significantly in recent years. However, as the generation of renewable energy has become more integrated, its intermission and instability have a major impact on the power system's stability, such as voltage instability and frequency flicker.* ***Purpose****. In order to address the different power quality issues brought on by intermittent and unreliable renewable energy sources, electric spring offers a novel solution. It was proposed as a technique for regulating load and adjusting output power. For the integration of electric springs with noncritical loads, a contemporary control mechanism is described in this paper.* ***Novelty.*** *The suggested work is innovative in that it presents an improved control technique that efficiently maintains voltage stability as voltage changes.* ***Method.*** *The proposed technique is based on an analysis of the initial conditions and input data for developing fuzzy rules for calculating compensating voltages in relation to the difficulties.* ***Results.*** *This suggested fuzzy controller will be able to maintain the regular operation of the electric spring of power output control stability as well as continuing to provide power factor improvement and voltage control for significant loads, including the home's protection system.* ***Practical value.*** *A detailed study of typical voltage regulation is undertaken, supported by simulation results, to demonstrate the effectiveness of the applied control scheme in cancelling the corresponding issues with power quality.* References 25, tables 2, figures 8.

Key words: **voltage stability, fuzzy control, electric spring, power factor, microgrid, renewable energy sources.**

Вступ*. Відновлювані джерела енергії, такі як сонячна та вітрова енергія, значно збільшилися останніми роками. Однак у міру того, як виробництво відновлюваної енергії стало більш інтегрованим, його перебої та нестабільність впливають на стабільність енергосистеми, наприклад, нестабільність напруги та коливання частоти.* ***Мета****. Щоб вирішити різні проблеми з якістю електроенергії, викликані уривчастими та ненадійними відновлюваними джерелами енергії, електрична пружина пропонує нове рішення. Вона була запропонована як метод регулювання навантаження та регулювання вихідної потужності. Для інтеграції електричних пружин із некритичними навантаженнями у цій статті описано сучасний механізм керування.* ***Новизна****. Пропонована робота є новаторською, оскільки представляє вдосконалений метод управління, який ефективно підтримує стабільність напруги за зміни напруги.* ***Метод****. Запропонована методика заснована на аналізі початкових умов і вихідних даних для розробки нечітких правил розрахунку компенсуючих напруг стосовно труднощів.* ***Результати****. Пропонований нечіткий регулятор зможе підтримувати стабільну роботу електричної пружини контролю вихідної потужності, а також продовжувати забезпечувати покращення коефіцієнта потужності та контроль напруги для значних навантажень, включаючи систему захисту будинку.* ***Практична цінність****. Зроблено докладне дослідження типового регулювання напруги, підтверджене результатами моделювання, щоб продемонструвати ефективність схеми управління, що застосовується в усуненні відповідних проблем з якістю електроенергії.* Бібл. 25, табл. 2, рис. 8.

Ключові слова: **стабільність напруги, нечітке управління, електрична пружина, коефіцієнт потужності, мікромережа, відновлювані джерела енергії.**

Introduction. The electricity systems are now incorporating the «Smart Grid» idea, which makes the grid smarter by enabling two-way energy flow between the grid and the consumer. One aspect of the smart grid concept is the integration of renewable energy sources (RES). The system should incorporate major RES's due to the impending energy problem as well as environmental considerations. Solar energy is the most important RES since it is neat, unrestricted, and free. Production of electrical energy in conventional systems is dependent on load demand [1]. In addition, solar energy is infrequent and longwinded. As a result, the emphasis has shifted from source following load to load following source, creating a new paradigm for electric springs (ES). Contrarily, solar photovoltaic (PV) systems produce a low output that is increased by converters and then transformed by inverters for grid synchronization into a pure sinusoidal form. The entire PV system performs at peak efficiency and generates its maximum output power at a certain location on the voltage-current (*V-I*) or voltage-power (*V-P*) curve known as maximum power point (MPP) at varied irradiance and temperatures. The MPP can be monitored using a number of methods. Through the use of maximum power point tracking (MPPT) techniques, the operating point of the PV array is kept at MPP [2, 3].

The power imbalances, voltage instability, voltage swings, and other grid-related problems are all being brought on by solar grid integration. These power quality issues have been addressed using a variety of technologies, including capacitor banks, capacitor reactors, static compensators, and static synchronous series compensators.

Their rapid and dynamic controllers can effectively minimise problems with power quality. The literature claims that ES outperforms existing technologies in dealing with the aforementioned problems [4-6]. This study emphasises the practical integration of a PV system with the grid. The ES is a fast device that controls voltage across significant loads that are prone to voltage variations. A power electronics-based circuit called ES is based on the idea of applying Hook's law to the field of electricity. The ES differs from typical custom power devices in terms of the better voltage profile of the power system. On the load demand side, ES is utilised to stabilise voltage variations brought on by RES.

The ES is a highly dynamic low-cost current control voltage source device [7-10]. The ES is connected in cascade with a noncritical load (NCL) that is less susceptible to voltage fluctuations in order to create a smart load. In order to achieve voltage regulation across the critical load (CL), which is voltage sensitive, the ES creates the compensation voltage or ES voltage V_{ES} perpendicular to the noncritical load current I_{ES}. In the past, simulations were used to research how well ESs worked in the real world. The works [11, 12] discuss the implications of large-scale integration of renewable

energy sources, such as PV, into the grid and its consequences [13-16].

The goal of the paper is to design controller for electric spring to regulate voltage and which allows to increase the reliability of the entire system mechanism operation and significantly simplify the design.

Subject of investigations. This paper carries out a comprehensive study of the ES and understanding of the different parameters to design suitable controller for voltage stability in the system under different environmental condition. This paper gives idea about the behavior of ES as capacitive mode and inductive mode.

Basic calculation relationships and assumptions. By comparing ES to a conventional mechanical spring, the concept was first established [17, 18]. It might be implemented using an inverter and connected in series with noncritical loads like electric heaters, refrigerators, and air conditioners in a RES-powered microgrid, as shown in Fig. 1. This creates a smart load. A building's security system is connected in parallel with this smart load, as are other critical loads. An input-voltage control method was used in earlier iterations of ES to produce reactive power compensation and offer steady-state voltage and power regulation to important loads because RESs only produce power intermittently, the noncritical load voltage and power fluctuate in response to grid fluctuation.

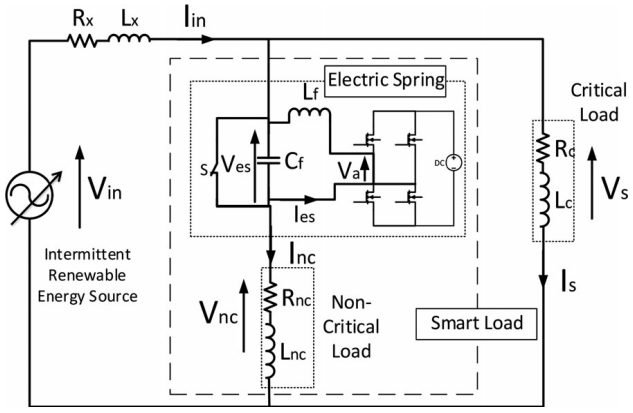

Fig. 1. Structure of ES

The compensation voltage, or ES voltage, V_{es}, should be perpendicular to the noncritical load current, I_{nc}, in order for the ES to exclusively offer reactive power adjustment, where V_s is the line voltage, V_{nc} is the noncritical load voltage, and V_{es} is the ES voltage, governs the ES voltage. A significant reactive power injection can degrade the system's power factor and lower power efficiency in a distribution system with a variety of inductive and capacitive loads.

$$V_{nc} + V_{es} = V_s . \quad (1)$$

Thus, in addition to the current qualities of voltage and power regulation, a power factor correction (PFC) function can be added to the ES. The both active and reactive power correction could be provided from an ES by using a DC source, like a battery, to power the inverter, as shown in Fig. 1. The line current, I_{in}, might be shaped to be in phase with the line voltage, V_s, using this characteristic of an ES. In a system with resistive-inductive loads, or one that has a generally trailing power factor, the phasor diagram in Fig. 2 demonstrates the ES compensation voltage, *Ves*, could help increase the power factor in the distribution system and offer voltage and power support in steady state [19].

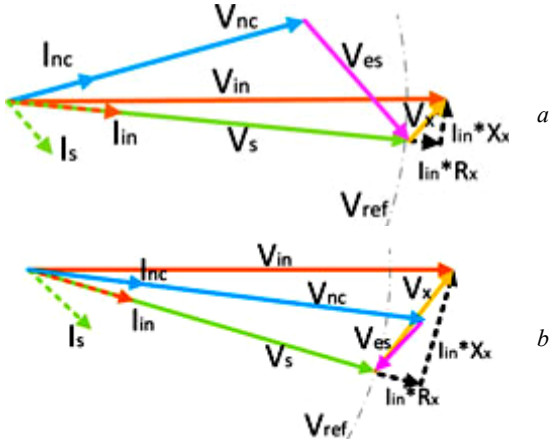

Fig. 2. Phasor diagram of current and voltage for PFC: *a*) undervoltage; *b*) overvoltage

When the line voltage V_s is less than the reference line voltage V_{ref} 230 V is the root mean square (RMS) value this is referred to as the undervoltage case. When the line voltage is higher than the reference line voltage, this is referred to as the overvoltage situation. As seen in Fig. 2,*a*, the ES injects real and capacitive power into the system in the undervoltage situation to raise the line voltage V_s to the reference value of 230 V and maintain the phase of the line voltage V_s and line current I_{in}. According to Fig. 2,*b*, the overvoltage scenario, for similar tasks to line voltage control and PFC, the ES injects a mix of actual and inductive power into the system. The input voltage, voltage across the line impedance, line voltage, noncritical load voltage, and ES voltage are represented in Fig. 2 by V_{in}, V_x, V_s, V_{nc}, and V_{es} respectively. The critical load current, noncritical load current, and line current are represented by I_s, I_{nc}, and I_{in} respectively. Additionally, $R_x + jX_x$ is the power circuit's line impedance, where R_x is resistance, $X_x + L_x$ and L_x is the line inductance.

Basic control action in fuzzy logic control (FLC) is governed by a set of linguistic rules. These rules are set by the system. Since numerical variables in FLC are converted to verbal variables, mathematical modelling of the system is not required. The FLC is divided into three sections: fuzzification, interference engine, and defuzzification [20]. The FLC is specified as 7 fuzzy sets for each input and output. Triangular membership functions are employed for simplicity. Fuzzification by the utilisation of an endless universe of discourse, Mamdani's «min» operator is used to imply implications. Defuzzification uses the height technique.

Fuzzification. The 7 fuzzy subsets used to assign membership function values to the linguistic variables are NB (Negative Big), NM (Negative Medium), NS (Negative Small), Z (Zero), PS (Positive Small), PM (Positive Medium), and PB (Positive Big). The partition of fuzzy subsets and the membership change in error $CE(k)$, error $E(k)$ function's shape adjust the form to the proper system. The value of input error and the change in error are standardised using an input scaling factor. The membership function plot of these variables is shown in Fig. 3.

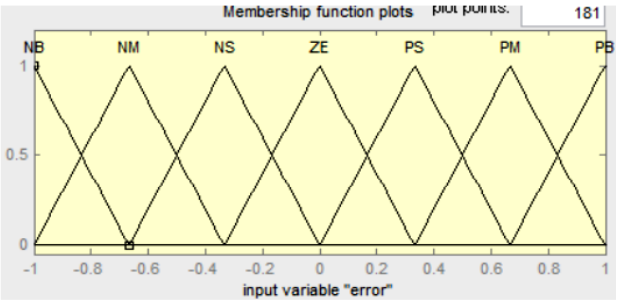

Fig. 3. Fuzzy membership function

This system's input scaling factor was constructed so that input values fall between –1 and +1. This arrangement's membership function has a triangular shape, which suggests that there is only one dominant fuzzy subset for each given $E(k)$ input [21, 22]. The input error for the FLC is as follows.

Inference approach. The max-min and max-dot are two composition approaches that have been put out in the literature. In this study, the min method is used. The output membership function of each rule is determined by the minimum and maximum operators. Table 1 displays the FLC's governing framework.

Table 1

Fuzzy rules

Change in error	Error						
	NB	NM	NS	Z	PS	PM	PB
NB	PB	PB	PB	PM	PM	PS	Z
NM	PB	PB	PM	PM	PS	Z	Z
NS	PB	PM	PS	PS	Z	NM	NB
Z	PB	PM	PS	Z	NS	NM	NB
PS	PM	PS	Z	NS	NM	NB	NB
PM	PS	Z	NS	NM	NM	NB	NB
PB	Z	NS	NM	NM	NB	NB	NB

Defuzzification. Since most plants require a nonfuzzy control value, a defuzzification stage is necessary. The FLC output is calculated using the «height technique» and the FLC output has an impact on the control output. The FLC output also manages the switch on the inverter. It is necessary to maintain the capacitor voltage, line terminal voltage, active power, and reactive power. To regulate these parameters, they are discovered and contrasted with reference values. The following are the membership duties of FLC to achieve this: error, change in error, and output. The following sources served as the basis for the FLC rules. The notation E stands for the system error, C for the change in error, and u for the control variable. A high error E value denotes the absence of a balanced state in the system. The controller should immediately increase the amount of its control variables if the system is out of balance in order to bring it back into balance. A low error E value, on the other hand, indicates that the system is nearly balanced.

Initial conditions and input data. The critical loads of 100 kW and 150 kVAr and noncritical loads of 100 kW and 100 kVAr are both taken into consideration into both cases capacitive and inductive. MATLAB/Simulink is used to model the hybrid power system with the ES as shown in Fig. 4. To lessen harmonics brought on by inverter switching transients, a harmonic filter is connected after the inverter [23]. To control voltage magnitude and frequency as well as to account for reactive power by load, an ES is connected prior to the load in parallel with the critical load and in series with the noncritical load [24, 25].

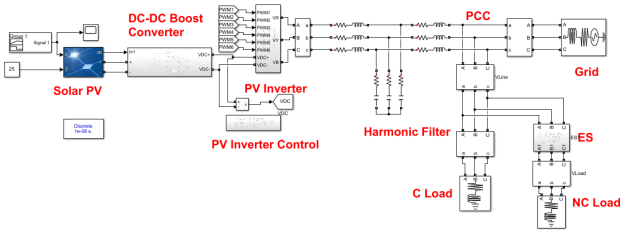

Fig. 4. Hybrid power system in MATLAB/Simulink

Simulation results. Case I: capacitive (voltage boosting) mode of operation of ES. To illustrate the voltage support capability of ES the disturbance source is programmed at $t = 0.2$ s to generate a voltage of 208 V. In order to restore the line voltage back to its nominal reference value the ES is activated at $t = 0.3$ s and voltage of the ES is increased from its near-zero value to about 175 V. As soon as ES is activated, it is observed that voltage across noncritical load decreases to 70 V as indicated in Fig. 5. The voltage is regulated back to its nominal reference value 230 V at $t = 0.3$ s. The corresponding instantaneous value of noncritical load voltage, ES voltage and critical load voltage are clearly indicates that current leads the voltage by 90°. Thus successful implementation of ES in capacitive mode is conducted using MATLAB.

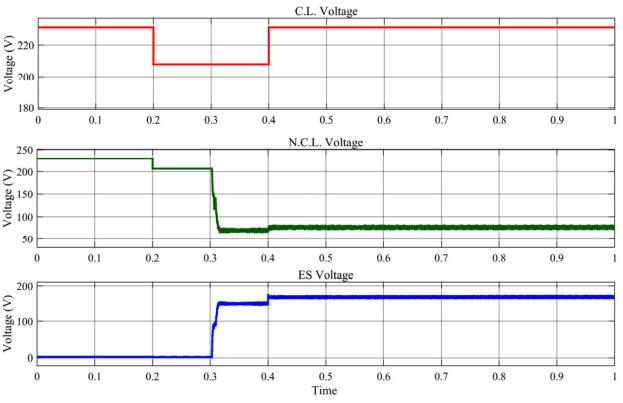

Fig. 5. Observed RMS value of critical voltage, noncritical voltage and ES voltage in capacitive mode

ES voltage in capacitive mode, critical load voltage, and noncritical load voltage are shown in Fig. 6.

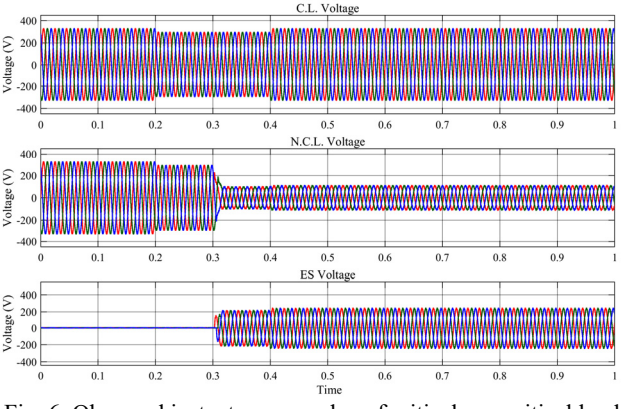

Fig. 6. Observed instantaneous value of critical, noncritical load voltage and ES voltage in capacitive mode

Case II: Inductive (voltage suppression) mode of operation of ES. To test the voltage suppression capability of the ES a disturbance source is programmed at $t = 0.2$ s to generate a voltage of 254 V.

In order to suppress the increased line voltage back to its nominal reference value the ES is activated at $t = 0.3$ s and voltage of ES is changed to stabilize the line voltage as shown in Fig. 7. As soon as ES is activated; it is observed that voltage across noncritical load increases to 250 V. Finally, the voltage is regulated back to its nominal reference value 230 V at $t = 0.3$ s. The corresponding instantaneous value of noncritical load voltage, ES voltage and critical load voltage clearly indicates that current lags the voltage by 90°, representing efficacious working of the ES in inductive mode. Thus successful implementation of ES in inductive mode is conducted using MATLAB.

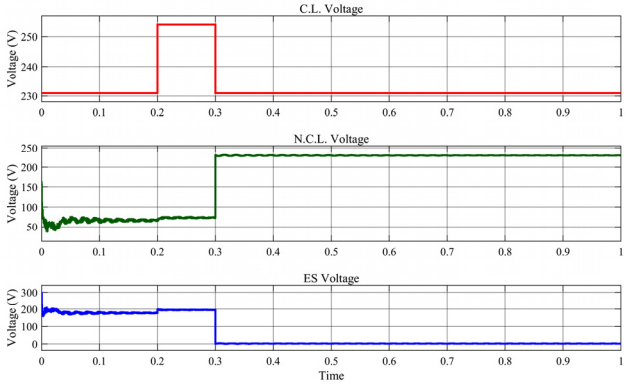

Fig. 7. Observed RMS value of critical voltage, noncritical voltage and ES voltage in inductive mode

The voltage of an ES operating in inductive mode is shown in Fig. 8 together with its critical load and noncritical load.

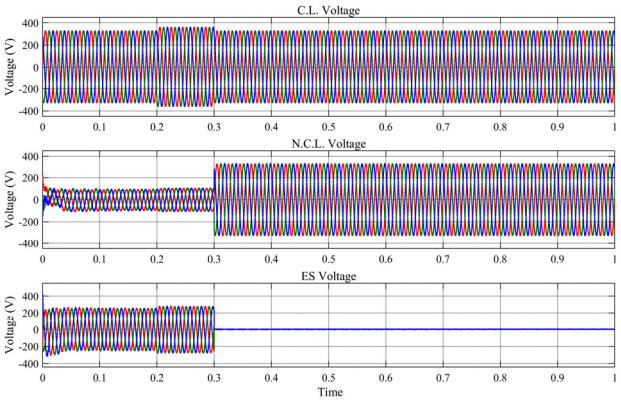

Fig. 8. Observed instantaneous value of critical, noncritical load voltage and ES voltage in inductive mode

Table 2 gives comparative results values in percentage with considering different load conditions and without ES and with ES.

Table 2

With and without ES simulation results

Parameter	Without ES 100 kW, 150 kVAr (CL) and 100 kW, 100 kVAr (NCL)	With ES 10 kW, 15 kVAr (CL) and 10 kW, 10kVAr(NCL)	With ES 100 kW, 150 kVAr (CL) and 100 kW, 100 kVAr (NCL)
Voltage variation, %	50	2	2.1
Frequency variation, %	5	0.1	0.2

Conclusions. It has been shown in this paper and previous research that electric spring is an effective approach for dealing with the issue of power system instability associated to alternate sources driven grids. The employment of a fuzzy control technique by an electric spring to maintain line voltage, power the important load, and increase the device's power factor is shown in this paper. The proposed fuzzy control approach is frequently contrasted with the conventional controller. It has also been demonstrated that voltage regulation and power system enhancement can be handled by a different organization. It is possible to verify the proposed converter by simulating it in the hybrid system using MATLAB/Simulink. The results from the electric spring under various lodes circumstances effectively stabilise the voltage.

Conflict of interest. The authors declare that they have no conflicts of interest.

REFERENCES

1. Survilo J., Boreiko D., Zalitis I., Kozadajevs J. Primary use of renewable energy sources in electric power industry. *2017 5th IEEE Workshop on Advances in Information, Electronic and Electrical Engineering (AIEEE)*, 2017, pp. 1-6. doi: https://doi.org/10.1109/AIEEE.2017.8270531.

2. Chandwani A., Kothari A. Design, simulation and implementation of Maximum Power Point Tracking (MPPT) for solar based renewable systems. *2016 International Conference on Electrical Power and Energy Systems (ICEPES)*, 2016, pp. 539-544. doi: https://doi.org/10.1109/ICEPES.2016.7915987.

3. Shuo Y., Tan S.-C., Lee C.K., Hui S.Y.R. Electric spring for power quality improvement. *2014 IEEE Applied Power Electronics Conference and Exposition - APEC 2014*, pp. 2140-2147. doi: https://doi.org/10.1109/APEC.2014.6803602.

4. Pawar R., Gawande S.P., Kadwane S.G., Waghmare M.A., Nagpure R.N. Five-Level Diode Clamped Multilevel Inverter (DCMLI) Based Electric Spring for Smart Grid Applications. *Energy Procedia*, 2017, vol. 117, pp. 862-869. doi: https://doi.org/10.1016/j.egypro.2017.05.204.

5. Meinhardt M., Mutschler P. Inverters without Transformer in Grid Connected Photovoltaic Applications. *European Electronics Conference 1995*, Sevilla, Spain, September 1995, pp. 86-91.

6. Chen X., Hou Y., Tan S.-C., Lee C.-K., Hui S.Y.R. Mitigating Voltage and Frequency Fluctuation in Microgrids Using Electric Springs. *IEEE Transactions on Smart Grid*, 2015, vol. 6, no. 2, pp. 508-515. doi: https://doi.org/10.1109/TSG.2014.2374231.

7. Tan S.-C., Lee C.K., Hui S.Y. General Steady-State Analysis and Control Principle of Electric Springs With Active and Reactive Power Compensations. *IEEE Transactions on Power Electronics*, 2013, vol. 28, no. 8, pp. 3958-3969. doi: https://doi.org/10.1109/TPEL.2012.2227823.

8. Hui S.Y., Lee C.K., Wu F.F. Electric Springs – A New Smart Grid Technology. *IEEE Transactions on Smart Grid*, 2012, vol. 3, no. 3, pp. 1552-1561. doi: https://doi.org/10.1109/TSG.2012.2200701.

9. Ghosh A., Joshi A. A new approach to load balancing and power factor correction in power distribution system. *IEEE Transactions on Power Delivery*, 2000, vol. 15, no. 1, pp. 417-422. doi: https://doi.org/10.1109/61.847283.

10. Soni J., Panda S.K. Electric Spring for Voltage and Power Stability and Power Factor Correction. *IEEE Transactions on Industry Applications*, 2017, vol. 53, no. 4, pp. 3871-3879. doi: https://doi.org/10.1109/TIA.2017.2681971.

11. Shuo Yan, Tan S.-C., Lee C.-K., Ron Hui S.Y. Reducing three-phase power imbalance with electric springs. *2014 IEEE 5th International Symposium on Power Electronics for Distributed Generation Systems (PEDG)*, 2014, pp. 1-7. doi: https://doi.org/10.1109/PEDG.2014.6878700.

12. Chaudhuri N.R., Lee C.K., Chaudhuri B., Hui S.Y.R. Dynamic Modeling of Electric Springs. *IEEE Transactions on Smart Grid*, 2014, vol. 5, no. 5, pp. 2450-2458. doi: https://doi.org/10.1109/TSG.2014.2319858.
13. Mok K.-T., Ho S.-S., Tan S.-C., Hui S.Y. A Comprehensive Analysis and Control Strategy for Nullifying Negative- and Zero-Sequence Currents in an Unbalanced Three-Phase Power System Using Electric Springs. *IEEE Transactions on Power Electronics*, 2017, vol. 32, no. 10, pp. 7635-7650. doi: https://doi.org/10.1109/TPEL.2016.2636226.
14. Qingsong Wang, Ming Cheng, Chen Z., Zheng Wang. Steady-State Analysis of Electric Springs With a Novel δ Control. *IEEE Transactions on Power Electronics*, 2015, vol. 30, no. 12, pp. 7159-7169. doi: https://doi.org/10.1109/TPEL.2015.2391278.
15. Yan S., Tan S.-C., Lee C.-K., Chaudhuri B., Hui S.Y.R. Electric Springs for Reducing Power Imbalance in Three-Phase Power Systems. *IEEE Transactions on Power Electronics*, 2015, vol. 30, no. 7, pp. 3601-3609. doi: https://doi.org/10.1109/TPEL.2014.2350001.
16. Krishnanand K.R., Hasani S.M.F., Soni J., Panda S.K. Neutral current mitigation using controlled electric springs connected to microgrids within built environment. *2014 IEEE Energy Conversion Congress and Exposition (ECCE)*, 2014, pp. 2947-2951. doi: https://doi.org/10.1109/ECCE.2014.6953799.
17. Wang M.-H., Yang T.-B., Tan S.-C., Hui S.Y. Hybrid Electric Springs for Grid-Tied Power Control and Storage Reduction in AC Microgrids. *IEEE Transactions on Power Electronics*, 2019, vol. 34, no. 4, pp. 3214-3225. doi: https://doi.org/10.1109/TPEL.2018.2854569.
18. Yang T., Liu T., Chen J., Yan S., Hui S.Y.R. Dynamic Modular Modeling of Smart Loads Associated With Electric Springs and Control. *IEEE Transactions on Power Electronics*, 2018, vol. 33, no. 12, pp. 10071-10085. doi: https://doi.org/10.1109/TPEL.2018.2794516.
19. Chen J., Yan S., Yang T., Tan S.-C., Hui S.Y. Practical Evaluation of Droop and Consensus Control of Distributed Electric Springs for Both Voltage and Frequency Regulation in Microgrid. *IEEE Transactions on Power Electronics*, 2019, vol. 34, no. 7, pp. 6947-6959. doi: https://doi.org/10.1109/TPEL.2018.2874495.
20. Ali Moussa M., Derrouazin A., Latroch M., Aillerie M. A hybrid renewable energy production system using a smart controller based on fuzzy logic. *Electrical Engineering & Electromechanics*, 2022, no. 3, pp. 46-50. doi: https://doi.org/10.20998/2074-272X.2022.3.07.
21. Gopal Reddy S., Ganapathy S., Manikandan M. Power quality improvement in distribution system based on dynamic voltage restorer using PI tuned fuzzy logic controller. *Electrical Engineering & Electromechanics*, 2022, no. 1, pp. 44-50. doi: https://doi.org/10.20998/2074-272X.2022.1.06.
22. Sadeghi H., Mohammadi H.R. An Improved Fuzzy Controlled Back-to-Back Electric Spring Using Hybrid Structure of ES-1 and Shunt-APF to Improve Power Quality in Microgrids. *International Journal of Industrial Electronics, Control and Optimization*, 2022, vol. 5, no. 1, pp. 89-98. doi: https://doi.org/10.22111/ieco.2022.40259.1387.
23. Priyanka G., Surya Kumari J., Lenine D., Srinivasa Varma P., Sneha Madhuri S., Chandu V. MATLAB-Simulink environment based power quality improvement in photovoltaic system using multilevel inverter. *Electrical Engineering & Electromechanics*, 2023, no. 2, pp. 43-48. doi: https://doi.org/10.20998/2074-272X.2023.2.07.
24. Liang L., Hou Y., Hill D.J. An Interconnected Microgrids-Based Transactive Energy System With Multiple Electric Springs. *IEEE Transactions on Smart Grid*, 2020, vol. 11, no. 1, pp. 184-193. doi: https://doi.org/10.1109/TSG.2019.2919758.
25. Lee C.-K., Liu H., Tan S.-C., Chaudhuri B., Hui S.-Y.R. Electric Spring and Smart Load: Technology, System-Level Impact, and Opportunities. *IEEE Journal of Emerging and Selected Topics in Power Electronics*, 2021, vol. 9, no. 6, pp. 6524-6544. doi: https://doi.org/10.1109/JESTPE.2020.3004164.

Received 01.09.2022
Accepted 15.12.2022
Published 01.07.2023

Atul Ikhe[1]*, PhD Scholar,*
Yogesh Pahariya [1]*, PhD, Professor,*
[1] Sandip University, Nashik, Maharashtra, 422213, India,
e-mail: atulikhe1@gmail.com (Corresponding Author);
yogesh.pahariya@sandipuniversity.edu.in

How to cite this article:
Ikhe A., Pahariya Y. Voltage regulation using three phase electric spring by fuzzy logic controller. *Electrical Engineering & Electromechanics*, 2023, no. 4, pp. 14-18. doi: https://doi.org/10.20998/2074-272X.2023.4.02

UDC 621.3 https://doi.org/10.20998/2074-272X.2023.4.03

A. Khemis, T. Boutabba, S. Drid

Model reference adaptive system speed estimator based on type-1 and type-2 fuzzy logic sensorless control of electrical vehicle with electrical differential

Introduction. *In this paper, a new approach for estimating the speed of in-wheel electric vehicles with two independent rear drives is presented. Currently, the variable-speed induction motor replaces the DC motor drive in a wide range of applications, including electric vehicles where quick dynamic response is required. This is now possible as a result of significant improvements in the dynamic performance of electrical drives brought about by technological advancements and development in the fields of power commutation devices, digital signal processing, and, more recently, intelligent control systems. The system's reliability and robustness are improved, and the cost, size, and upkeep requirements of the induction motor drive are reduced through control strategies without a speed sensor. Successful uses of the induction motor without a sensor have been made for medium- and high-speed operations. However, low speed instability and instability under various charge perturbation conditions continue to be serious issues in this field of study and have not yet been effectively resolved. Some application such as traction drives and cranes are required to maintain the desired level of torque down to low speed levels with uncertain load torque disturbance conditions. Speed and torque control is more important particularly in motor-in-wheel traction drive train configuration where vehicle wheel rim is directly connected to the motor shaft to control the speed and torque.* ***Novelty*** *of the proposed work is to improve the dynamic performance of conventional controller used of model reference adaptive system speed observer using both type-1 and type-2 fuzzy logic controllers.* ***Purpose.*** *In proposed scheme, the performance of the engine is being controlled, fuzzy logic controller is controlling the estimate rotor speed, and results are then compared using type-1 and type-2.* ***Method****. For a two-wheeled motorized electric vehicle, a high-performance sensorless wheel motor drive based on both type-2 and type-1 fuzzy logic controllers of the model reference adaptive control system is developed.* ***Results.*** *Proved that, using fuzzy logic type-2 controller the sensorless speed control of the electrical differential of electric vehicle EV observer, much better results are achieved.* ***Practical value.*** *The main possibility of realizing reliable and efficient electric propulsion systems based on intelligent observers (type-2 fuzzy logic) is demonstrated. The research methodology has been designed to facilitate the future experimental implementation on a digital signal processor.* References 27, table 3, figures 16.

Key words: **electrical vehicle, induction machines, model reference adaptive system, field oriented control, electric differential, fuzzy logic controller.**

Вступ*. У цій роботі представлений новий підхід до оцінки швидкості колісних електромобілів із двома незалежними задніми приводами. В даний час асинхронний двигун із регульованою швидкістю замінює двигун постійного струму в широкому діапазоні застосувань, включаючи електромобілі, де потрібний швидкий динамічний відгук. Тепер це можливо внаслідок значного покращення динамічних характеристик електроприводів, викликаного технологічними досягненнями та розробками в галузі пристроїв комутації потужності, цифрової обробки сигналів та останнім часом інтелектуальних систем управління. Надійність та стійкість системи підвищуються, а вартість, розмір та вимоги до обслуговування асинхронного двигуна знижуються завдяки стратегіям керування без датчика швидкості. Успішне використання асинхронного двигуна без датчика було виконано для роботи на середніх та високих швидкостях. Проте низькошвидкісна нестабільність і нестабільність за умов збурення заряду продовжують залишатися серйозними проблемами у цій галузі досліджень і досі не вирішені ефективно. У деяких застосуваннях, таких як тягові приводи та крани, потрібно підтримувати бажаний рівень крутного моменту аж до низьких рівнів швидкості з невизначеними умовами збурення крутного моменту навантаження. Контроль швидкості і крутного моменту більш важливий, особливо в конфігурації тягової трансмісії з двигуном в колесі, де обід колеса транспортного засобу безпосередньо з'єднаний з валом двигуна для управління швидкістю і крутним моментом.* ***Новизна*** *запропонованої роботи полягає у поліпшенні динамічних характеристик звичайного регулятора, що використовується в еталонній моделі спостерігача швидкості адаптивної системи з використанням регуляторів нечіткої логіки як першого, так і другого типу.* ***Мета****. У запропонованій схемі контролюються характеристики двигуна, нечіткий логічний контролер управляє оцінною частотою обертання ротора, а потім порівнюються результати з використанням типу 1 і типу 2.* ***Метод****. Для двоколісного моторизованого електромобіля розроблено високопродуктивний бездатчиковий двигун-привід коліс на основі нечітких логічних контролерів як 2-го, так і 1-го типів еталонної системи адаптивного управління.* ***Результати****. Доведено, що з використанням регулятора нечіткої логіки 2-го типу для бездатчикового управління швидкістю EV-спостерігача електричного диференціала електромобіля досягаються значно кращі результати.* ***Практична цінність****. Показано принципову можливість реалізації надійних та ефективних електрореактивних рухових установок на основі інтелектуальних спостерігачів (нечітка логіка 2-го типу). Розроблено методологію дослідження для полегшення майбутньої експериментальної реалізації на цифровому сигнальному процесорі.* Бібл. 27, табл. 3, рис. 16.

Ключові слова: **електромобіль, асинхронні машини, еталонна адаптивна система, полеорієнтоване керування, електричний диференціал, регулятор з нечіткою логікою.**

Introduction. Type-2 fuzzy logic was presented in the mid-70s through the work of Zadeh [1] and later improved by several researchers, with emphasis on the work of Mizumoto and Tanaka [2], and Karnik and Mendel [3]. Type-2 fuzzy logic represents an extension of traditional fuzzy logic (usually called fuzzy logic type-1) or even a second approximation for addressing uncertainties inherent in the real world [4].

Type-2 has been fuzzy logic gaining more and more attention and recognition, especially in systems modeling. While type-1 fuzzy logic presupposes the need for exact knowledge of membership functions, in type-2 fuzzy systems this premise is conceptually questioned, giving rise to so-called type-2 fuzzy sets which, in general terms, offer the possibility of raising the logical and systematic treatment ability for the low accuracy of the information [5]. In this sense, the following very typical situations can be highlighted that suggest the approach or modeling from type-2 fuzzy inference systems:

- identification of fuzzy models for behavior prediction, using noisy data or information;
- rules obtained through information generated by the human expert.

In this sense, type-2 fuzzy logic is effectively applied to the problems of identifying models or inference systems based on human information or that have this as a fundamental element of their construction.

Uncertainties are also present in the daily life of human beings, for example in decision-making, where

uncertain, imprecise, ambiguous or even contradictory terms can be evaluated to originate a decision. Electric vehicles (EVs) are an area where decision-making takes place at all times, in order to promote the movement of the vehicle in a safe, orderly and fast manner. Due to the use of electric motors and inverters in drive systems, electric cars offer many benefits over those powered by internal combustion engines, including quick torque response and independent control of each wheel [6, 7]. Although many control methods with similar benefits have been proposed, their controllers often depend on irrational variables like slip angle and vehicle velocity. Each wheel follows a different trajectory when passing in corners, resulting in a variable distance traveled. This is why differentials are used in automobile technology. The trajectory of the outer wheels also follows a circular arc with a larger radius than that of the inner wheel.

The power transferred to the driving wheels is then divided by the differential, causing the outer wheel to accelerate and the inner wheel to slow down. This suggests that it prevents slippage and improves vehicle handling [8, 9]. There are various benefits when comparing electric differential-based EVs to their conventional counterparts with a central motor. It is undeniable that putting the motors on the wheels substantially simplifies the mechanical design. The electric differential system will minimize the drive line components, improving overall efficiency and dependability [9, 10].

The goal of the paper is the study of Model Reference Adaptive System (MRAS) speed sensorless control is presented where the speed estimation the of in-wheel EVs with 2 independent rear drive was chosen as a case study for the application of a type-2 fuzzy system. Also a comparative study between type-1 and type-2 fuzzy logic controllers (T1FLC, T2FLC) in term of robustness will be simulated and discussed.

Mathematical model of the EV. Dynamics analysis. The vehicle's aerodynamics are taken into account by the control approach suggested in this study, which is not limited to induction motors. This concept is based on the physics and aerodynamics of moving objects. A vehicle's tractive force (F_{te}) is composed of its rolling friction force (F_{rr}), aerodynamic force (F_{ad}), lift force (F_{hc}), acceleration force (F_{la}) and angular acceleration force (F_{wa}):

$$F_{te} = F_{rr} + F_{ad} + F_{hc} + F_{la} + F_{wa}\,. \tag{1}$$

The force that propels the vehicle forward and is transmitted to the ground by the wheels is shown in Fig. 1.

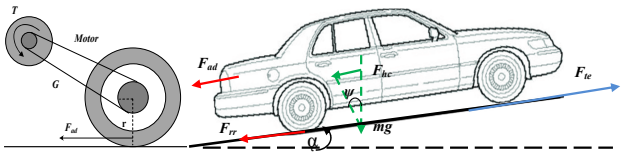

Fig. 1. Elementary forces acting in the EV

The force that will propel the vehicle will depend on the aerodynamic resistance of the vehicles, rolling, auxiliary components and vehicle acceleration if the speed is not constant:

$$F_{rr} = \mu_{rr} \cdot m \cdot g\,, \tag{2}$$

where F_{rr} is the rolling resistive force; μ_{rr} is the rolling resistance coefficient (depends on the tire type and tire pressure, typically on EVs it takes values of 0.005); m is the vehicle mass; g is the gravitational constant.

This resistance depends on the shape of the vehicle, and the way the air surrounds it:

$$F_{ad} = \frac{1}{2} \cdot \rho \cdot A \cdot C_d \cdot \upsilon^2\,, \tag{3}$$

where the aerodynamic force (F_{ad}) characterizes the aerodynamic resistance; ρ is the air density; A is the frontal area of the vehicle; υ is the speed; C_d is the drag coefficient with values typically between 0.3 and 0.19 in a well designed vehicle.

Climb force F_{hc} represents the effort the vehicle makes when climbing a given slope:

$$F_{hc} = m \cdot g \cdot \sin\psi\,, \tag{4}$$

where ψ is the grade angle.

According to Newton's second law, the acceleration force is the force that will apply a linear acceleration to the vehicle:

$$F_{la} = m \cdot a\,, \tag{5}$$

where a is the vehicle acceleration.

For this sizing we need to know what engine torque T is needed to make the wheels rotate:

$$T = \frac{F_{te}}{G} \cdot r\,, \tag{6}$$

where r is the tire radius; F_{te} is the traction force; G is the gear ratio of the engine to the wheel shaft.

The equation in terms of F_{te} is given by:

$$F_{te} = \frac{G}{r} \cdot T\,. \tag{7}$$

The angular speed of the motor will be $\omega = a{\cdot}G/r$, rad·s^{-1}; and the angular acceleration respectively $\dot{\omega} = \upsilon{\cdot}G/r$, rad·s^{-2}; [11, 12].

The torque for this angular acceleration is $T = a{\cdot}J{\cdot}G/r$, where J is the rotor moment of inertia of the motor. The force the wheels need to reach the angular acceleration and determined by:

$$F_{\omega a} = \frac{G}{r} \cdot J \cdot G \cdot \frac{a}{r} = \frac{G^2}{r^2} \cdot J \cdot a\,. \tag{8}$$

Since mechanical systems are not 100 % efficient, we still have to consider the efficiency of the system ρ_g:

$$F_{\omega a} = \frac{G^2}{r^2} \cdot J \cdot a = \frac{G^2}{r^2 \cdot \rho_g} \cdot J \cdot a\,. \tag{9}$$

And finally, the power required to move a vehicle at a speed υ must compensate for the opposing forces:

$$P_{te} = \upsilon F_{te} = \upsilon\left(F_{rr} + F_{ad} + F_{hc} + F_{la} + F_{wa}\right), \tag{10}$$

where υ is the vehicle speed; P_{te} is the vehicle driving power.

Induction motor model and control structure. In this section, the vector technique for induction motor modeling is used, which is important for the study of field oriented control [1, 4]. A system of complex orthogonal axes d and q is defined to represent the three-phase machine. With regard to the flux-current relationship, the dq model can be interpreted as being a two-phase machine with 2 solid and orthogonal magnetic axes d and q [13].

The equations describing the dynamics of the induction motor are:

$$\begin{cases} \bar{u}_s = R_s \bar{i}_s + \sigma L_s \dfrac{\mathrm{d}\bar{i}_s}{\mathrm{d}t} + \dfrac{M}{L_r}\dfrac{\mathrm{d}\bar{\varphi}_s}{\mathrm{d}t} + j\sigma L_s \omega_s \bar{i}_s + j\dfrac{M}{L_r}\omega; \\ 0 = \dfrac{1}{\tau_r}\bar{\varphi}_r - \dfrac{M}{\tau_r}\bar{i}_s + \dfrac{\mathrm{d}\bar{\varphi}_r}{\mathrm{d}t} + j\omega_r \bar{\varphi}_r, \end{cases} \tag{11}$$

where ω_r is the induced rotor current frequency; ω_s is the stator current frequency; j is the inertia; R_s and R_r are the stator and rotor resistances; L_s and L_r are the stator and

rotor inductances; τ_r is the rotor time constant; σ is the leakage flux total coefficient; M is the mutual inductance; ω is mechanical rotor frequency; φ_s and φ_r are the stator and rotor fluxes; i_s and u_s are the rotor current and voltage.

The mechanical equation is written as follows:

$$\Gamma_e - \Gamma_l = j \cdot \frac{\mathrm{d}\Omega}{\mathrm{d}t} + f \cdot \Omega, \quad (12)$$

where Γ_e is the induced electromagnetic torque; Γ_l is the load torque; f is the coefficient of viscous; Ω is the rotor speed.

The electromagnetic torque is:

$$\Gamma_e = \frac{p \cdot M}{L_r}\left(I_{sq} \cdot \varphi_{rd} - I_{sd} \cdot \varphi_{rq}\right), \quad (13)$$

where p is the number of poles pairs.

The observation of stator currents from a fixed reference to a reference flux is what vector modeling in practice aims to achieve. As a result, when a new coordinate system is defined with the direct reference axis, d, or real axis (Re), coincident with the rotor flux vector (φ_r), the component of the rotor flux vector on the quadrature axis, q, or imaginary axis (Im), is eliminated, that is:

$$\varphi_{rq} = 0. \quad (14)$$

The torque determined by (13) can be represented using (14), as follows:

$$T_e = k_c \cdot I_{sq} \cdot \phi_r, \quad (15)$$

where I_{sd} component represents the direct flux; I_{sq} represents the torque control variation, with $k_c = p \cdot M / L_r$.

Speed observer based on MRAS. In the MRAS techniques, rotor speed can be estimated by using 2 estimators (one reference and one adaptive), which estimate the rotor flux components to subsequently use the difference between these estimates to control the speed of the rotor model speed adaptive to the current speed. The MRAS basic setup is shown in (Fig. 2) [14-16].

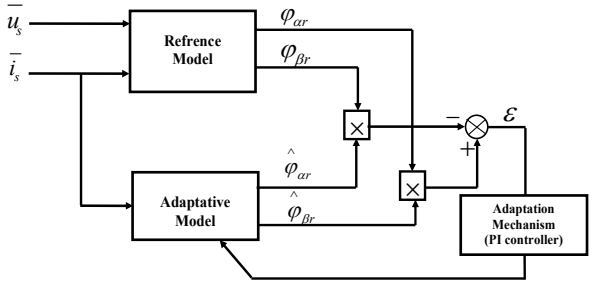

Fig. 2. Induction motor speed estimation using MRAS

The model in the stator reference frame is expressed as:

$$\begin{cases} \bar{u}_s = R_s \cdot \bar{i}_s + \sigma \cdot L_s \cdot \dfrac{\mathrm{d}\bar{i}_s}{\mathrm{d}t} + \dfrac{M}{L_r} \cdot \dfrac{\mathrm{d}\bar{\varphi}_s}{\mathrm{d}t}; \\ 0 = \dfrac{1}{\tau_r} \cdot \bar{\varphi}_r - \dfrac{M}{\tau_r} \cdot \bar{i}_s + \dfrac{\mathrm{d}\bar{\varphi}_r}{\mathrm{d}t} + j \cdot p \cdot \Omega \cdot \bar{\varphi}_r. \end{cases} \quad (16)$$

In the stationary frame (α, β), the time derived from the rotor flux vector is calculated by the MRAS speed observer using 2 independent equations obtained from (4). In [17] are provided these equations which are generally defined as follows:

- the voltage model (reference model):

$$\bar{\varphi}_r = \frac{L_r}{M} \cdot \int \left(\bar{u}_s - R_s \cdot \bar{i}_s\right)\mathrm{d}t - \frac{L_r}{M} \cdot \sigma \cdot L_s \cdot \bar{i}_s; \quad (17)$$

- the current model (adaptive model):

$$\bar{\varphi}_r = \int \left[\left(-\frac{1}{\tau_r} + j \cdot p \cdot \Omega\right)\bar{\varphi}_r + \frac{M}{\tau_r} \cdot \bar{i}_s\right]\mathrm{d}t. \quad (18)$$

Equation (18) can be expressed in an estimated form for the same input:

$$\hat{\bar{\varphi}}_r = \int \left(\frac{M}{\tau_r} \cdot \bar{i}_s - \left(\frac{1}{\tau_r} - j \cdot p \cdot \hat{\Omega}\right)\hat{\bar{\varphi}}_r\right)\mathrm{d}t. \quad (19)$$

The estimation error of the rotor flux is expressed by:

$$\bar{e}_\varphi = \bar{\varphi}_r - \hat{\bar{\varphi}}_r. \quad (20)$$

By subtracting (18) and (19), the dynamic equation of the estimation error is obtained:

$$\dot{\bar{e}}_\varphi = -\left(\frac{1}{\tau_r} - j \cdot p \cdot \Omega\right) \cdot \bar{e}_\varphi + j \cdot p \cdot \left(\Omega - \hat{\Omega}\right) \cdot \hat{\bar{\varphi}}_r. \quad (21)$$

In order to ensure stability of (18); the error ($\bar{\varepsilon}_\phi$) must necessarily this converged to zero [16].

Equation (21) can be rewritten as:

$$\dot{\bar{e}}_k = A \cdot \bar{e}_\varphi - W. \quad (22)$$

To return to ensuring the global stability of the MRAS observer and make the system hyper-stable, we will apply the Lyapunov's stability theorem, where a positive definite function V is chosen such that its derivative is negative semi definite. The proposed function is described in (23). The derivative of this function is shown in (24):

$$V = \bar{e}_\varphi^T \bar{e}_\varphi > 0; \quad (23)$$

$$\dot{V} = \dot{\bar{e}}_\varphi^T \bar{e}_\varphi + \bar{e}_\varphi^T \dot{\bar{e}}_\varphi = \bar{e}_\varphi^T \left(A^T + A\right)\bar{e}_\varphi = -\frac{2}{\tau_r}\bar{e}_\varphi^T \bar{e}_\varphi. \quad (24)$$

The function (24) is negative definite. Inferring the adaptation law from Popov's criterion thus:

$$\int_0^t e_\varphi^T W \mathrm{d}\tau = \int_0^t \left(P \Delta\Omega \begin{bmatrix} e_{\varphi\alpha} & e_{\varphi\beta} \end{bmatrix} J\hat{\bar{\varphi}}_r\right)\mathrm{d}\tau \geq -\delta_o^2. \quad (25)$$

Using the same theorem previously mentioned, assuming that the speed varies slowly, we have:

$$\hat{\Omega} = \delta_0 P \int \begin{bmatrix} e_{\varphi\alpha} & e_{\varphi\beta} \end{bmatrix} J\hat{\bar{\varphi}}_r \mathrm{d}t = \delta_0 P \int \left(e_{\varphi\beta}\hat{\varphi}_{r\alpha} - e_{\phi\alpha}\hat{\varphi}_{r\beta}\right)\mathrm{d}t. \quad (26)$$

There is an incorporated open-loop in the adaption law (offset problem). A low pass filter was recommended in [18] to improve the estimation response.

Equation (26) becomes:

$$\hat{\Omega} = k_p(\bar{\varphi}_r \otimes \hat{\bar{\varphi}}_r) + k_i \int (\bar{\varphi}_r \otimes \hat{\bar{\varphi}}_r)\mathrm{d}t. \quad (27)$$

The classic MRAS observer's poor estimating at low speeds and rotor resistance variation sensitivity is its primary issues. A reviewer provided a number of solutions to this problem. As functional candidates, where an online rotor time constant estimation using the MRAS approach is described in [19-21]. Where the following adaption law gives the estimated value of the inverse rotor time constant ($1/\hat{\tau}_r$):

$$\begin{aligned} 1/\hat{\tau}_r = {} & K_p\left(e_{\phi\alpha}\left(MI_{s\alpha} - \hat{\phi}_{r\alpha}\right) + e_{\phi\beta}\left(MI_{s\beta} - \hat{\phi}_{r\beta}\right)\right) + \\ & + K_i \int \left(e_{\phi\alpha}\left(MI_{s\alpha} - \hat{\phi}_{r\alpha}\right) + e_{\phi\beta}\left(MI_{s\beta} - \hat{\phi}_{r\beta}\right)\right)\mathrm{d}t. \end{aligned} \quad (28)$$

Design of type-2 fuzzy logic controller. The dynamic model of the asynchronous machine is non-linear and strongly coupled, in addition the vehicle dynamics. The use of PI controllers is not suitable for this application; we chose to use fuzzy logic [19-21]. Solutions that are adequate can be found using the T2FLC approach. In this context, we suggest using the T2FLC algorithm to estimate rotor speed in place of the conventional PI of the adaptation mechanism. The rotor flow static and dynamic faults indicated above in (20) serve as the proposed algorithm's inputs and may be expressed as follows [21, 22]:

$$\Delta e_\varphi(k) = e_\varphi(k) - e_\varphi(k-1). \quad (29)$$

The following is how the 3 quantities e_φ, Δe_φ (inputs), $\Delta\hat{\Omega}$ (output) are standardised:

$$e_\varphi = G_{e_\varphi} e_\varphi; \quad \Delta e_\varphi = G_{\Delta e_\varphi} \Delta e_\varphi; \quad \Delta\Omega = G_u \Delta\Omega. \quad (30)$$

The value of the estimated speed is obtained after a discrete integration is performed. Figure 3 shows the structure of the T2FLC created.

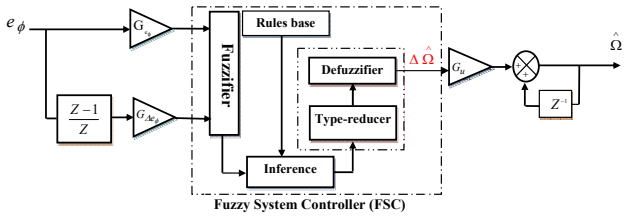

Fig. 3. Proposed type-2 fuzzy logic controllers

The estimated speed constant's expression is as follows:

$$\hat{\Omega}(k) = \hat{\Omega}(k-1) + G_u \Delta\hat{\Omega}(k). \quad (31)$$

The error and variation flux type-2 membership functions are given on the interval [–1, 1] and are similarly determined with Gaussian forms (Fig. 4,*a*). The type-2 fuzzy membership functions of the variation are chosen with intervals form on the interval [–1.5, 1.5] (Fig. 4,*b*).

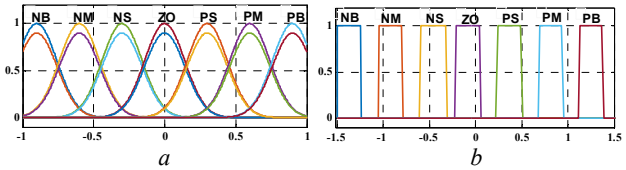

a *b*

Fig. 4. Fuzzy type-2 membership functions to represent: *a* – error and variation flux; *b* – estimated speed

Implementation of the electric differential. Figure 5 shows the implemented system (composed of electrical and mechanical parts) in the MATLAB/Simulink environment.

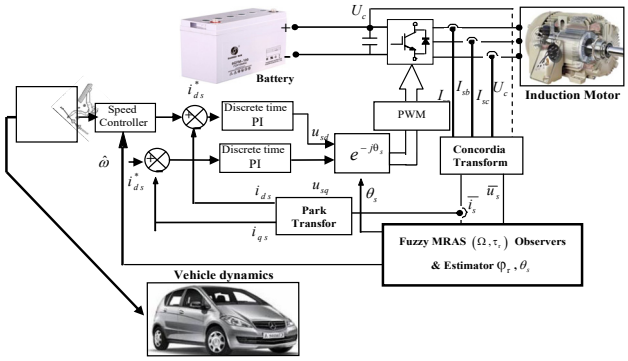

Fig. 5. Basic indirect field oriented control (IFOC) for sensorless IM drives

It should be noted that the 2 inverters share the same DC bus, whose voltage is intended to be steady. In this paper, regenerative braking is not considered. The control system principle could be summarized in 2 principal points:

1) each motor's torque is controlled by a speed network control;

2) speed difference feedback is used to regulate the speed of each rear wheel.

Due to the fact that 2 different motors directly drive the 2 rear wheels, during steering maneuvers, the outer wheel's speed must be higher than the inner wheel's speed (and vice-versa). If the steering wheel's angular speed is sensed by the speed estimator, this condition can be easily met [23-25]. The command for the accelerator pedal then set the common reference speed. The actual reference speeds for the left and right drives are then acquired by modifying the common reference speed using the type-2 fuzzy logic speed estimator's output signal.

The speed of the left wheel of the vehicle rises as it makes a right turn, while the speed of the right wheel stays at the standard reference speed (ω_{ref}). The speed of the right wheel rises when turning to the left, while the speed of the left wheel stays constant at the usual reference speed (ω_{ref}).

The vehicle system model may often be analyzed using a driving trajectory. We used the Ackermann-Jeantaud steering model since it is often used as a driving trajectory. Ackermann steering geometry is a geometric configuration of the steering system's linkages that was created to address the issue of wheels on the inside and outside of bends needing to draw circles with differing radii. Modern vehicles do not employ pure Ackermann-Jeantaud steering, in part because it overlooks significant and compliant effects, although the principle is sound for low-speed maneuvers [26, 27] (Fig. 6).

The following characteristic can be calculated from this model:

$$R = L/\tan\delta, \quad (32)$$

where R is the turn radius; δ is the steering angle; L is the wheel base.

Therefore, the linear speed of each wheel drive is:

$$\begin{cases} V_1 = \omega_v (R - d/2); \\ V_2 = \omega_v (R + d/2), \end{cases} \quad (33)$$

where d is the track width and their angular speed by:

$$\begin{cases} \hat{\omega}_1 = \dfrac{L - (d/2)\tan\delta}{L}\omega_v; \\ \hat{\omega}_2 = \dfrac{L + (d/2)\tan\delta}{L}\omega_v, \end{cases} \quad (34)$$

where ω_v represents the vehicle's angular speed from the turn's center. Therefore, the difference in wheel drive angular speeds is:

$$\Delta\omega = \hat{\omega}_1 - \hat{\omega}_2 = \frac{-d\tan\delta}{L}\omega_v \quad (35)$$

and the direction of the trajectory is indicated by the steering angle:

$$\begin{aligned} &\delta > 0 \Rightarrow \text{turn left;} \\ &\delta = 0 \Rightarrow \text{straight ahead;} \\ &\delta < 0 \Rightarrow \text{turn right.} \end{aligned} \quad (36)$$

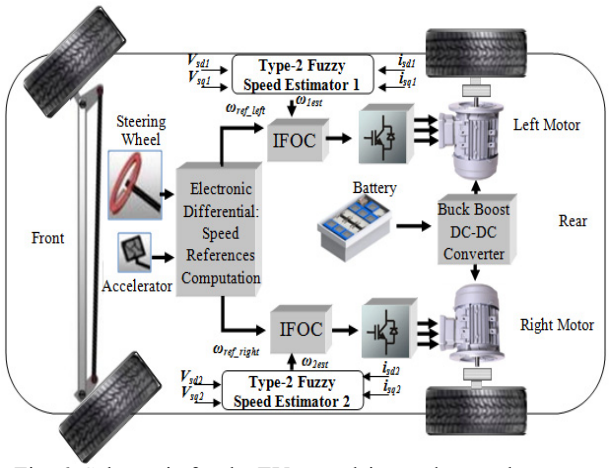

Fig. 6. Schematic for the EV propulsion and control systems

Figure 7 displays the block diagram of the electric differential system employed in simulations that correspond with the equation mentioned above, where $K_1 = 0{,}5$ and $K_2 = -0{,}5$.

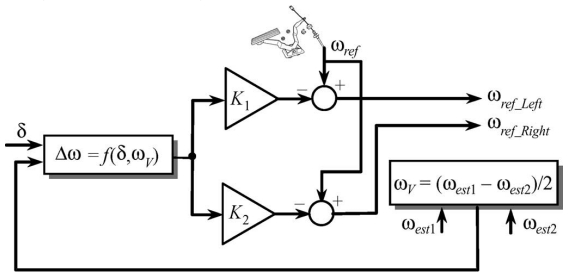

Fig. 7. Block diagram of the electric differential system

The performance of fitness function. The performance of the system is frequently used the IAE (Integral Absolute Error), ITAE (Integral of Time multiplied by Absolute Error), ISE (Integral Squared Error) and ITSE (Integral Time Squared Error) criteria [27]:

$$IAE = \int_0^\infty |e(t)|\mathrm{d}t\,; \tag{37}$$

$$ITAE = \int_0^\infty t|e(t)|\mathrm{d}t\,; \tag{38}$$

$$ISE = \int_0^\infty \{e(t)\}^2\mathrm{d}t\,; \tag{39}$$

$$ITSE = \int_0^\infty t\{e(t)\}^2\mathrm{d}t\,. \tag{40}$$

Simulation and analysis. The test cycle is the urban ECE-15 cycle (Fig. 8). The speed of the vehicle is displayed as a function of time in a driving cycle, which is a collection of data points. It is used to evaluate how well EVs function in urban environments and is distinguished by a modest vehicle speed (50 km/h at most). The first illustration of the electric differential performances is in Fig. 9, which displays the driving speed of each wheel during steering for $0 < t < 1180$ s. The complicated sequence of accelerations, decelerations, and multiple pauses required by the urban ECE-15 cycle clearly demonstrate how well the electric differential functions.

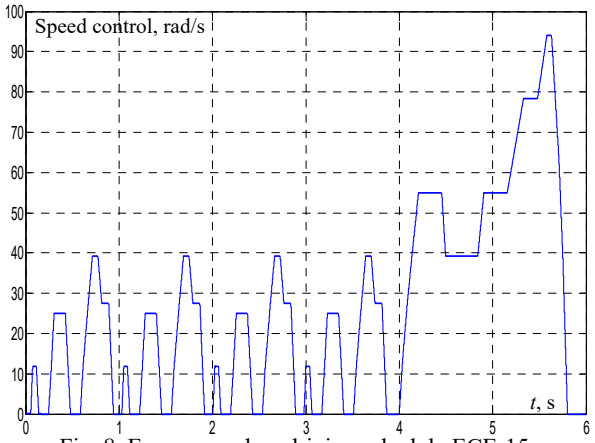

Fig. 8. European urban driving schedule ECE-15

The flux (φ_r) and the developed torque in each wheel drive of the induction motor (left and right) are shown in Fig. 10, 11, respectively, along with variations in the location of the accelerator pedal (Fig. 12) and a variable road profile (rising and descending parts). It should be noted that the variations in flux and torque are as large as variations in the accelerator pedal and the road profile.

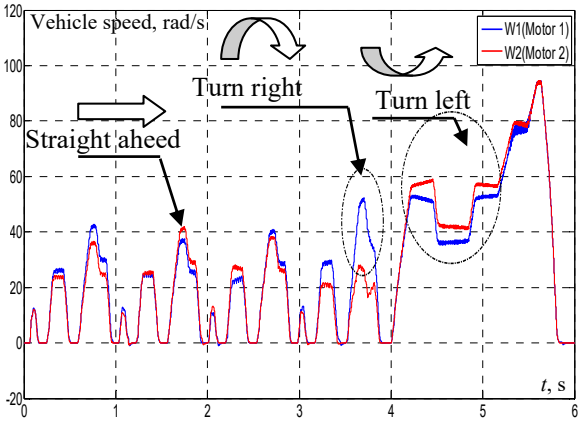

Fig. 9. Vehicle wheels speed

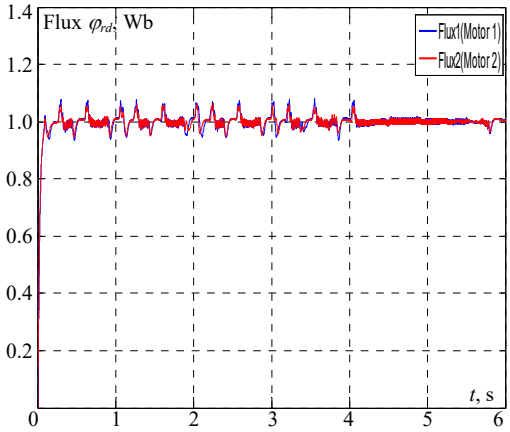

Fig. 10. Flux φ_{rd}

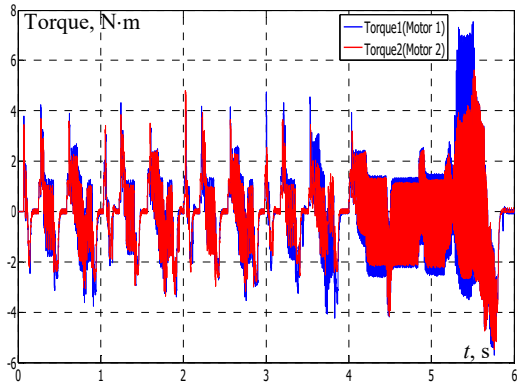

Fig. 11. Torque motors

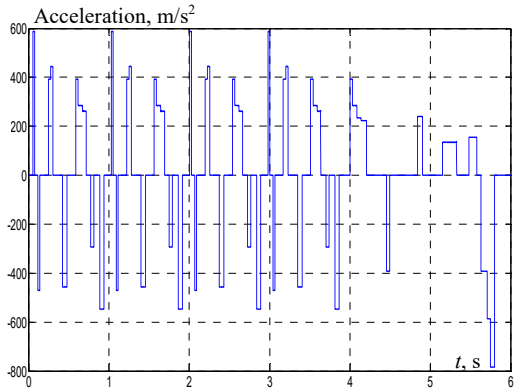

Fig. 12. Acceleration pedal position

Comparative study between T2FLC and T1FLC controllers. A comparison between the simulation results achieved at low-speed zones by T2FLC and T1FLC controllers was done in order to verify the performances of the new control structure employing T2FLC. As illustrated in Fig. 13,*a*, the membership functions of the flux error and its variation are defined on the interval [–1, 1] and are identical in form. In Fig. 13,*b*, the singleton forms over the interval [–2.5, 2.5] are used for the membership functions for the variation in estimated speed.

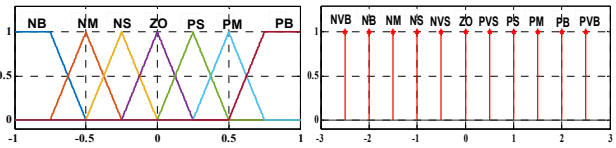

a *b*

Fig. 13. Fuzzy type-1 membership functions to represent: *a* – error and variation flux; *b* – estimated speed

The results provided in Fig. 14 demonstrate the benefit of the suggested observer, the MRAS T2FLC, over the MRAS T1FLC, which shows the measured speed and the estimated value for the different speed as shown in Fig. 15. These figures clearly demonstrate that the estimated speed for this applied profile accurately tracks the measured value even at zero speed. The estimated error between the MRAS T2FLC and MRAS T1FLC is also shown in Fig. 16, and it is immediately apparent that the T2FLC error is significantly smaller than the T1FLC error. It is obvious that the T2FLC controller outperforms its T1FLC predecessor.

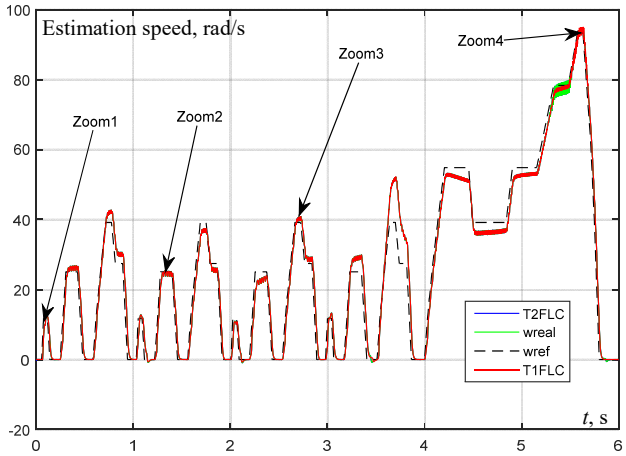

Fig. 14. Estimated and measured vehicle speed

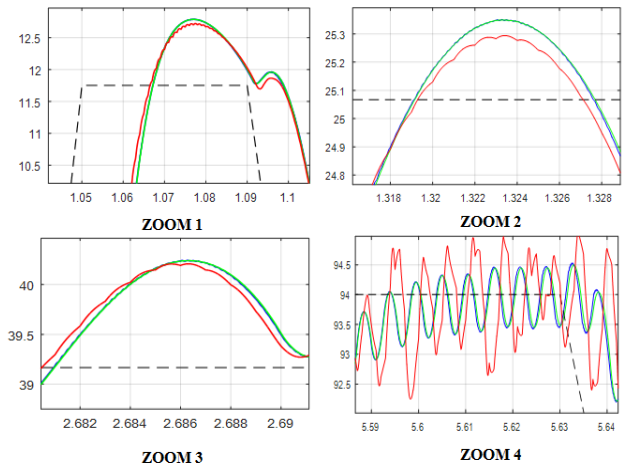

Fig. 15. Zoom of the estimated and measured vehicle speed

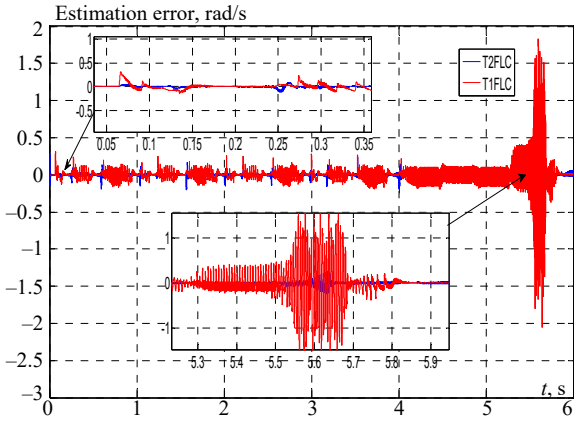

Fig. 16. Speed estimation error

Tables 1, 2 contain comparisons of the results for the various controllers for each of the errors. Our results indicate that the T2FLC technique has better performance than T1FLC controller.

The data of the induction motors are given in Table 3.

Table 1

Performances comparison the first induction motor

Controllers IM1	IAE	ISE	ITAE	ITSE
T1FLC	0.1215	0.0165	0.2995	0.0660
T2FLC	0.0316	0.0014	0.0702	0.0030

Table 2

Performances comparison of the second induction motor

Controllers IM2	IAE	ISE	ITAE	ITSE
T1FLC	0.1160	0.0142	0.2866	0.0552
T2FLC	0.0358	0.0019	0.0846	0.0047

Table 3

Parameters of the induction motor

Rate power P, kW	1.5
Rated stator resistance R_s, Ω	5.72
Rated rotor resistance R_r, Ω	4.2
Rated stator inductance L_s, H	0.462
Rated rotor inductance L_r, H	0.462
Mutual inductance M, H	0.4402
Pole pairs p	2
Inertia J, kg·m^2	0.0049
Friction coefficient f_r, kg·m^2/s	0

Conclusions. In this paper, we introduce a sensorless model reference adaptive system type-2 fuzzy logic controller and observer for electric vehicle electrical differential control. By comparing the results of type-1 and type-2 fuzzy models, it was possible to identify that the type-2 fuzzy model was the best proposal to reproduce the decision making and in the sensorless control of the electrical differential of electric vehicle, especially when driving at high speeds. Also this comparison makes it evident that the model reference adaptive system type-2 fuzzy logic controller approach is effectives. The outstanding performance of the induction motor control is revealed and shown by these data.

Conflict of interest. The authors declare that they have no conflicts of interest.

REFERENCES

1. Zadeh L.A. Fuzzy sets. *Information and Control*, 1965, vol. 8, no. 3, pp. 338-353. doi: https://doi.org/10.1016/S0019-9958(65)90241-X.

2. Mizumoto M., Tanaka K. Some properties of fuzzy sets of type 2. *Information and Control*, 1976, vol. 31, no. 4, pp. 312-340. doi: https://doi.org/10.1016/S0019-9958(76)80011-3.

3. Karnik N.N., Mendel J.M. Applications of type-2 fuzzy logic systems: handling the uncertainty associated with surveys. *FUZZ-IEEE'99. 1999 IEEE International Fuzzy Systems. Conference Proceedings (Cat. No.99CH36315)*, 1999, vol. 3, pp. 1546-1551 doi: https://doi.org/10.1109/FUZZY.1999.790134.
4. Mousavi S.M. A new interval-valued hesitant fuzzy pairwise comparison–compromise solution methodology: an application to cross-docking location planning. *Neural Computing and Applications*, 2019, vol. 31, no. 9, pp. 5159-5173. doi: https://doi.org/10.1007/s00521-018-3355-y.
5. Tsang Y.P., Wong W.C., Huang G.Q., Wu C.H., Kuo Y.H., Choy K.L. A Fuzzy-Based Product Life Cycle Prediction for Sustainable Development in the Electric Vehicle Industry. *Energies*, 2020, vol. 13, no. 15, art. no. 3918. doi: https://doi.org/10.3390/en13153918.
6. Seth A.K., Singh M. Unified adaptive neuro-fuzzy inference system control for OFF board electric vehicle charger. *International Journal of Electrical Power & Energy Systems*, 2021, vol. 130, art. no. 106896. doi: https://doi.org/10.1016/j.ijepes.2021.106896.
7. Williamson S.S., Rathore A.K., Musavi F. Industrial Electronics for Electric Transportation: Current State-of-the-Art and Future Challenges. *IEEE Transactions on Industrial Electronics*, 2015, vol. 62, no. 5, pp. 3021-3032. doi: https://doi.org/10.1109/TIE.2015.2409052.
8. Haddoun A., Benbouzid M.E.H., Diallo D., Abdessemed R., Ghouili J., Srairi K. Modeling, Analysis, and Neural Network Control of an EV Electrical Differential. *IEEE Transactions on Industrial Electronics*, 2008, vol. 55, no. 6, pp. 2286-2294. doi: https://doi.org/10.1109/TIE.2008.918392.
9. Yang J., Zhang T., Zhang H., Hong J., Meng Z. Research on the Starting Acceleration Characteristics of a New Mechanical–Electric–Hydraulic Power Coupling Electric Vehicle. *Energies*, 2020, vol. 13, no. 23, art. no. 6279. doi: https://doi.org/10.3390/en13236279.
10. Tao Guilin, Ma Zhiyun, Zhou Libing, Li Langru. A novel driving and control system for direct-wheel-driven electric vehicle. *2004 12th Symposium on Electromagnetic Launch Technology*, 2004, pp. 514-517. doi: https://doi.org/10.1109/ELT.2004.1398134.
11. Ju-Sang Lee, Young-Jae Ryoo, Young-Cheol Lim, Freere P., Tae-Gon Kim, Seok-Jun Son, Eui-Sun Kim. A neural network model of electric differential system for electric vehicle. *2000 26th Annual Conference of the IEEE Industrial Electronics Society. IECON 2000. 2000 IEEE International Conference on Industrial Electronics, Control and Instrumentation. 21st Century Technologies and Industrial Opportunities (Cat. No.00CH37141)*, vol. 1, pp. 83-88. doi: https://doi.org/10.1109/IECON.2000.973130.
12. Han-Xiong Li, Gatland H.B. A new methodology for designing a fuzzy logic controller. *IEEE Transactions on Systems, Man, and Cybernetics*, 1995, vol. 25, no. 3, pp. 505-512. doi: https://doi.org/10.1109/21.364863.
13. Guezi A., Bendaikha A., Dendouga A. Direct torque control based on second order sliding mode controller for three-level inverter-fed permanent magnet synchronous motor: comparative study. *Electrical Engineering & Electromechanics*, 2022, no. 5, pp. 10-13. doi: https://doi.org/10.20998/2074-272X.2022.5.02.
14. Chekroun S., Abdelhadi B., Benoudjit A. Design optimization of induction motor using hybrid genetic algorithm «a critical analyze». *Advances in Modelling and Analysis C*, 2016, vol. 71, no. 1, pp. 1-23.
15. Naït-Saïd M.-S., Tadjine M., Drid S. Robust backstepping vector control for the doubly fed induction motor. *IET Control Theory & Applications*, 2007, vol. 1, no. 4, pp. 861-868. doi: https://doi.org/10.1049/iet-cta:20060053.
16. Young Ahn Kwon, Dae Won Jin. A novel MRAS based speed sensorless control of induction motor. *IECON'99. Conference Proceedings. 25th Annual Conference of the IEEE Industrial Electronics Society (Cat. No.99CH37029)*, 1999, vol. 2, pp. 933-938. doi: https://doi.org/10.1109/IECON.1999.816537.
17. Khemis A., Benlaloui I., Drid S., Chrifi-Alaoui L., Khamari D., Menacer A. High-efficiency induction motor drives using type-2 fuzzy logic. *The European Physical Journal Plus*, 2018, vol. 133, no. 3, art. no. 86. doi: https://doi.org/10.1140/epjp/i2018-11903-6.
18. Benlaloui I., Drid S., Chrifi-Alaoui L., Ouriagli M. Implementation of a New MRAS Speed Sensorless Vector Control of Induction Machine. *IEEE Transactions on Energy Conversion*, 2015, vol. 30, no. 2, pp. 588-595. https://doi.org/10.1109/TEC.2014.2366473.
19. Zaky M.S., Khater M.M., Shokralla S.S., Yasin H.A. Wide-Speed-Range Estimation With Online Parameter Identification Schemes of Sensorless Induction Motor Drives. *IEEE Transactions on Industrial Electronics*, 2009, vol. 56, no. 5, pp. 1699-1707. doi: https://doi.org/10.1109/TIE.2008.2009519.
20. Vasic V., Vukosavic S. PES News. *IEEE Power Engineering Review*, 2001, vol. 21, no. 11, pp. 16-17. doi: https://doi.org/10.1109/39.961999.
21. Miloud Y., Draou A. Fuzzy logic based rotor resistance estimator of an indirect vector controlled induction motor drive. *IEEE 2002 28th Annual Conference of the Industrial Electronics Society. IECON 02*, vol. 2, pp. 961-966. doi: https://doi.org/10.1109/IECON.2002.1185402.
22. Ali Moussa M., Derrouazin A., Latroch M., Aillerie M. A hybrid renewable energy production system using a smart controller based on fuzzy logic. *Electrical Engineering & Electromechanics*, 2022, no. 3, pp. 46-50. doi: https://doi.org/10.20998/2074-272X.2022.3.07.
23. Bordons C., Ridao M.A., Perez A., Arce A., Marcos D. Model Predictive Control for power management in hybrid fuel cell vehicles. *2010 IEEE Vehicle Power and Propulsion Conference*, 2010, pp. 1-6. doi: https://doi.org/10.1109/VPPC.2010.5729119.
24. Vaez S., John V.I., Rahman M.A. Energy saving vector control strategies for electric vehicle motor drives. *Proceedings of Power Conversion Conference - PCC '97*, vol. 1, pp. 13-18. doi: https://doi.org/10.1109/PCCON.1997.645578.
25. Takeda K., Takahashi C., Arita H., Kusumi N., Amano M., Emori A. Design of hybrid energy storage system using dual batteries for renewable applications. *2014 IEEE PES General Meeting | Conference & Exposition*, 2014, pp. 1-5. doi: https://doi.org/10.1109/PESGM.2014.6938860.
26. Colyer R.E., Economou J.T. Comparison of steering geometries for multi-wheeled vehicles by modelling and simulation. *Proceedings of the 37th IEEE Conference on Decision and Control (Cat. No.98CH36171)*, 1998, vol. 3, pp. 3131-3133. doi: https://doi.org/10.1109/CDC.1998.757992.
27. Xia X., Xing Y., Wei B., Zhang Y., Li X., Deng X., Gui L. A fitness-based multi-role particle swarm optimization. *Swarm and Evolutionary Computation*, 2019, vol. 44, pp. 349-364. doi: https://doi.org/10.1016/j.swevo.2018.04.006.

Received 11.09.2022
Accepted 25.12.2022
Published 01.07.2023

Abderrahmane Khemis[1,2], *Doctor of Technical Science, Associate Professor,*
Tarek Boutabba[1,2], *Doctor of Technical Science, Associate Professor,*
Said Drid [2,3], *PhD, Professor,*
[1] University of Khenchela,
El-Hamma, BP 1252 Road of Batna, Khenchela, 40004, Algeria,
e-mail: khemis05@yahoo.fr; boutabba_tarek@yahoo.fr;
[2] LSPIE Laboratory, University of Batna 2,
53, Constantine road, Fésdis, Batna, 05078, Algeria.
[3] Higher National School of Renewable Energy, Environment and Sustainable Development,
Batna, Constantine road, Fesdis, Batna, 05078, Algeria,
e-mail: s.drid@hns-re2sd.dz (Corresponding Author)

How to cite this article:
Khemis A., Boutabba T., Drid S. Model reference adaptive system speed estimator based on type-1 and type-2 fuzzy logic sensorless control of electrical vehicle with electrical differential. *Electrical Engineering & Electromechanics*, 2023, no. 4, pp. 19-25. doi: https://doi.org/10.20998/2074-272X.2023.4.03

UDC 621.3.013 https://doi.org/10.20998/2074-272X.2023.4.04

B.I. Kuznetsov, T.B. Nikitina, I.V. Bovdui, O.V. Voloshko, V.V. Kolomiets, B.B. Kobylianskyi

Optimization of spatial arrangement of magnetic field sensors of closed loop system of overhead power lines magnetic field active silencing

Aim. *Development of a method for optimization of spatial arrangement and angular position of magnetic field sensors of a closed system to ensure maximum efficiency of active silencing canceling of the magnetic field generated by overhead power lines.* ***Methodology****. Spatial arrangement and angular position of magnetic field sensors of closed loop system of overhead power lines magnetic field active silencing determined based on binary preference relations of local objective for multi-objective minimax optimization problem, in whith the vector objective function calculated based on Biot–Savart law. The solution of this vector minimax optimization problem calculated based on nonlinear Archimedes algorithm of multi-swarm multi-agent optimization.* ***Results.*** *Results of simulation and experimental research of optimal spatial arrangement and angular position of magnetic field sensors of a closed system to ensure maximum efficiency of active silencing of the magnetic field generated by overhead power lines with a barrel-type arrangement of wires.* ***Originality.*** *The method for optimization of spatial arrangement and angular position of magnetic field sensors of a closed system to ensure maximum efficiency of active shielding of the magnetic field generated by overhead power lines is developed.* ***Practical value****. An important practical problem optimization of spatial arrangement and angular position of magnetic field sensors of a closed system to ensure maximum efficiency of active silencing of the magnetic field generated by overhead power lines has been solved.* References 53, figures 10.

Key words: **overhead power transmission line, magnetic field, system of active silencing, spatial arrangement and angular position of magnetic field sensors, multi-objective parametric optimization, computer simulation, experimental research**.

Мета. *Розробка методу оптимізації просторового розташування та кутового положення датчиків магнітного поля замкнутої системи для забезпечення максимальної ефективності активного екранування магнітного поля, яке створюється повітряними лініями електропередачі.* ***Методологія.*** *Просторове розташування та кутове положення датчиків магнітного поля для замкнутої системи активного подавлення магнітного поля, яке створюваєтьс повітряними лініями електропередачі, визначене на основі бінарних відношень переваги локальної цілі для багатокритерійної задачі мінімаксної оптимізації, в якій векторна цільова функція розрахована на основі закону Біо-Савара. Рішення цієї задачі векторної мінімаксимальної оптимізації обчислюється на основі нелінійного алгоритму Архімеда мульти-ройної багатоагентної оптимізації.* ***Результати.*** *Результати моделювання та експериментальних досліджень оптимального просторового розташування та кутового положення датчиків магнітного поля замкнутої системи для забезпечення максимальної ефективності активного екранування магнітного поля, яке створюється повітряними лініями електропередачі з бочкоподібним розташуванням проводів.* ***Оригінальність****. Розроблено метод оптимізації просторового розташування та кутового положення датчиків магнітного поля замкнутої системи для забезпечення максимальної ефективності активного екранування магнітного поля, яке створюється повітряними лініями електропередачі.* ***Практична цінність****. Вирішено важливу практичну задачу проектування оптимального просторового розташування та кутового положення датчиків магнітного поля замкнутої системи для забезпечення максимальної ефективності активного екранування магнітного поля, яке створюється повітряними лініями електропередачі.* Бібл. 53, рис. 10.

Ключові слова: **повітряна лінія електропередачі, магнітне поле, система активного екранування, просторове розташування та кутове положення датчиків магнітного поля, багатокритерійна параметрична оптимізація, комп'ютерне моделювання, експериментальні дослідження.**

Introduction. Electricity has given humanity many benefits. However, as is often the case, the same electricity has created certain problems for humanity. One of such problem is the power frequency magnetic field generated by overhead power lines (MF). Many of overhead power lines often pass in the residential areas and generated a magnetic field, the level of which often exceeds the safe level for the population with an induction of 0.5 μT adopted in Europe, that poses a threat to public health [1-3]. World Health Organization carries out the ongoing global programs connected with climate change, ionizing radiation, chemical safety, etc. The small number of these programs emphasizes the importance of the issues involved. The effect of the electromagnetic field on the population is one of such issues, and it is studied within the framework «The International EMF Project». Research results confirm the high risk of power frequency (50-60 Hz) MF for human health. This leads to modern world trends on stricter sanitary standards on reference levels of power frequency magnetic field.

Currently, strict sanitary standards for the magnetic field induction 0.5 μT have been introduced into the regulatory documents of the Ministry of Energy of Ukraine. However, in Ukraine these norms are universally exceeded, which poses a threat to the health of millions of people living closer than 100 ms from overhead power lines.

Anatolii Pidhornyi Institute of Mechanical Engineering Problems of the National Academy of Sciences of Ukraine carried out experimental research of magnetic field generate by high-voltage transmission lines 10-330 kV [4-7]. It is shown, that their magnetic field are 3-5 times higher than the standard level at the border of sanitary zones previously formed in the electric field. This situation requires urgent measures to reduce by 3-5 times the magnetic field of the existing power lines within the cities of Ukraine.

A similar situation is typical for most industrialized countries of the world [8-11]; however, in these countries, normalization technologies of magnetic field of existing power transmission lines have already been created and are widely used [12-16]. The most effective technology is the reconstruction of power transmission lines by removing it to a safe distance from residential buildings, or replacing an overhead transmission line with a cable line. However, such a reconstruction requires huge material resources. Therefore, less expensive methods of canceling the magnetic field of existing power transmission lines are more acceptable for Ukraine, of which the methods of active contour silencing of the magnetic field provide the necessary efficiency.

The technology of active contour silencing of magnetic field of existing power transmission lines has been developed and used in developed countries of the

world for more than 10 years, for example, in the USA and Israel [17-23]. In Ukraine, at present, both such technology and the scientific foundations of its creation are absent.

The method is implemented using a system of active silencing. System of active silencing consists of silencing coils, with the help of which a silencing magnetic field is formed. The currents in canceling windings automatically generated by a certain algorithm as a function of the signal from the magnetic field sensors installed in the protection zone. For the power supply, the system of active silencing contains a current source that receives energy from an external source.

In the system of active silencing, a different number of canceling windings used, determined by the spatio-temporal characteristic of the initial magnetic field, the geometric dimensions of the silencing space and the required level of the resulting magnetic field in the silencing space. The most common transmission lines in Ukraine, passing near residential and public areas, are double-circuit power lines with a suspension of wires of the «barrel» type. Such transmission lines generate magnetic field, the spatiotemporal characteristic of which is a highly elongated ellipse.

For active silencing of such magnetic field, a single-circuit system of active silencing with one silencing winding is often sufficient. With the help of such system of active silencing, the major axis of the spatiotemporal characteristic ellipse compensated, which makes it possible to obtain a sufficient silencing efficiency of the initial magnetic field. In the area of old residential buildings, single-circuit power lines with a triangular suspension of wires often pass. Such transmission lines generate magnetic field, the spatiotemporal characteristic of which is a circle.

For active silencing of such a magnetic field, it is necessary to use at least a double-circuit system of active silencing with two canceling windings. If it is necessary to shield the magnetic field generated by such a power line in a multi-storey building, three or more silencing windings may be required, depending on the required level of the resulting magnetic field in the silencing space.

For the formation of currents in the silencing windings, open, closed and combined control algorithms can be used [24-29]. With an open-loop control algorithm for silencing windings, one canceling sensor is sufficient, with the help of which the induction of the initial magnetic field is measured [30-35]. This sensor installed outside the silencing space so that the silencing windings do not affect its operation [36-40].

The disadvantage of the open-loop control algorithm for the silencing windings is its relatively low efficiency of silencing the initial magnetic field [41-47]. In particular, with an open-loop control algorithm, it is impossible silencing for changes in the magnetic field induction inside the silencing spase, due to the presence of internal sources of magnetic field, as well as in the process of inevitable changes in the parameters of the system of active silencing control object during its operation [39, 40].

For the correct implementation of a closed algorithm for controlling by all silencing windings, the number of magnetic field sensors is usually equal to the number of silencing windings [30, 31]. Moreover, all these sensors installed inside the shielding space for the correct measurement of the resulting magnetic field generated both by power lines and by all silencing windings.

As an example, Fig. 1 shows a photo of the spatial arrangement of the sensor inside the silencing space, given in [16].

Fig. 1. Spatial arrangement of the magnetic field sensor inside the silencing space

Naturally, the efficiency of active silencing of the initial magnetic field with the help of each silencing windings and all simultaneously operating silencing windings depends on the spatial arrangement and orientation in the silencing space of all magnetic field sensors.

The aim of the work is to develop a method for optimization of spatial arrangement and angular position of magnetic field sensors of a closed system to ensure maximum efficiency of silencing of the magnetic field generated by overhead power lines.

Statement of the problem. Let us consider the formulation of the problem of correctly determining the coordinates of the spatial location and their angular orientation in the silencing space of all magnetic field sensors, which are necessary for the implementation of a closed control algorithm for all silencing windings. Let us introduce the vector Y of the desired parameters of the coordinates of the spatial arrangement and the vector φ of the desired parameters of the angular position of all magnetic field sensors at points Q_i in the silencing space. The components of the angular orientation vector of all magnetic field sensors are vectors of unit length, directed parallel to the desired angular positions of the axes of the magnetic field sensors.

Let us consider the mathematical model of the magnetic field generated in the silencing space by all the wires of the power transmission line and by all the magnetic field windings at the installation points Q_i of the canceling sensors in the magnetic field space. We set the vector $I_p(t)$ of instantaneous values of currents in all wires of the power transmission line of the three-phase current in the form of sinusoidal dependencies

$$I_i(t) = A\sin(\omega(t) + \varphi_i) \tag{1}$$

of the given frequency ω and the given phase φ_i, where i = 1, 2, 3 – the number of the conductor of the three-phase current line.

Then, the instantaneous value of the elementary induction vector $\mathrm{d}B(Q_i, t)$ of the initial magnetic field at the considered point of the space point Q_i at the time t calculated based on Biot–Savart law [4, 5]

$$\mathrm{d}B(Q_i,t) = \frac{\mu_0 I(t)}{4\pi}\frac{\mathrm{d}L_i \times R_i}{|R_i|^3}, \tag{2}$$

where R_i is the vector from the differential current element generic field in point Q_i, $\mathrm{d}L_i$ is the elementary

length vector of the current element, μ_0 is the vacuum magnetic permeability. The sign × denotes the vector product of the vectors dL_i and R_i.

Based on (2) for vector $I_p(t)$ of instantaneous values of currents in all wires of the power transmission line (1) by integrating over the entire length of all current wires of power transmission lines calculated instantaneous value of the initial magnetic field induction vector $B_p(Q_i, t)$ at time t at points Q_i generated by all wires of all transmission lines.

Let us first assume that the number and geometric dimensions of canceling windings are given. Let us set the column vector $I_W(t)$ of the instantaneous values of the currents in the canceling windings. Then, for the given values of the geometric dimensions of the canceling windings and the vector $I_W(t)$ of the instantaneous values of the currents of the instantaneous values of the currents in the silencing windings, based on the Biot–Savart law, similarly (1) calculated the instantaneous value of the magnetic field induction vector $B_W(Q_i, t)$ generated by all wires of all silencing windings at time t at points Q_i.

Then the vector $B_R(Q_i, t)$ of the instantaneous values of the induction of the resulting magnetic field generated by all wires of the power transmission line and all silencing windings at time t at points Q_i in silencing space

$$B_R(Q_i,t) = B_P(Q_i,t) + B_W(Q_i,t) \qquad (3)$$

Based on this vector $B_R(Q_i, t)$ of the instantaneous values of the induction of the resulting magnetic field vectors at the installation points Q_i of the magnetic field sensors, taking into account the vector φ of the spatial position angles of the magnetic field sensors, the vector $B_M(Q_i, t)$ of the projections of the vector $B_R(Q_i, t)$ of the instantaneous values of the induction of the resulting magnetic field onto the vector φ of the angular positions of these magnetic field sensors calculated

$$B_M(Q_i,t) = B_R(Q_i) \otimes \varphi, \qquad (4)$$

here the sign ⊗ denotes the tensor (Kronecker) product of the column vectors. In this case, the elements of the vector $B_M(Q_i, t)$ are the result of the element-by-element scalar multiplication of the components of the column vector $B_R(Q_i, t)$ and the column vector φ. The components of the projection vector $B_M(Q_i, t)$ are scalar values obtained as a result of component-by-component scalar multiplication of the resulting magnetic field induction vectors $B_R(Q_i, t)$ at the magnetic field sensor installation point by unit vectors φ of the angular position of the magnetic field sensors.

The components of this vector $B_M(Q_i, t)$ of projections of the $B_R(Q_i, t)$ vector of instantaneous values of the induction of the resulting magnetic field are the instantaneous values of the voltages $I_W(t)$ at the outputs of the magnetic field sensors

$$y_M(t) = B_R(Q_i,t) \otimes \varphi \otimes K_M + w(t), \qquad (5)$$

where $w(t)$ is the magnetometer noise vector.

This takes into account the vector column K_M of the gain coefficients of the magnetic field sensor taking into account the number of turns of their measuring coils and the gains of the preamplifiers.

Let's take the structure of the system of active shielding of the magnetic field in the following form: we will apply the output voltage $y(t)$ of the corresponding magnetometer to the input $u(t)$ of the PID controller of each channel. Let's write the differential state equation of discrete PID regulators, the input of which is the vector $y(t)$ of measured magnetic field induction components, and the output is the vector $u(t)$ of plant control

$$x_c(t+1) = A_c x_c(t) + B_c y(t), \qquad (6)$$

$$u(t) = C_c x_c(t) + D_c y(t), \qquad (7)$$

in which the elements of the matrices A_c, B_c, C_c, D_c are determined by the PID parameters of the regulators.

Let's write down the models of the control objects of each channel, the input of which is the vector $u(t)$ of output voltages of the PID controller, and the output of which is the vector $I_W(t)$ of instantaneous values of currents silencing windings

$$x_p(t+1) = A_p x_p(t) + B_p u(t), \qquad (8)$$

$$I_w(t) = C_p x_p(t) + D_p u(t), \qquad (9)$$

in which the elements of the matrices A_p, B_p, C_p, D_p are determined by the parameters of the model of the control object, which includes a silencing windings, a power amplifier and current regulator.

Thus, with the help of (4) – (9), the instantaneous value of the current vector $I_W(t)$ in the silencing windings formed in the form of feedback on the vector $B_R(Q_i, t)$ of the induction of resulting magnetic field (3).

Let us introduce the vector X of desired parameters, the components of which are the vector Y of the desired parameters of the coordinates of the spatial arrangement, the vector φ of the desired parameters of the angular position of all magnetic field sensors at points Q_i in the screening space and the desired column vector K of the gain coefficients of the silencing windings PID controllers. Note that if the parameters of the geometric dimensions of the silencing windings not specified, then they can be included in the vector vector X of desired parameters. Let us introduce olso the vector δ of the parameters of the uncertainty of the control object of the system of active silencing, the components of which are the parameters of the uncertainty of the mathematical model of the initial magnetic field and silencing windings [34-38].

We introduce M points P_i in the screening space. Note that the considered M points P_i of the silencing space are selected for reasons of providing a given level of induction of the resulting magnetic field in the entire given silencing space, and their number and spatial arrangement may not correspond to the installation points of the magnetic field sensors. These points usually chosen over the entire silencing space, since with the help of the system of active canceling it is possible to overcompensate the magnetic field near the power line and undercompensate the initial magnetic field away from the power line.

Then based on (2) for vector $I_p(t)$ of instantaneous values of currents in all wires of the power transmission line (1) by integrating over the entire length of all current wires of power transmission lines calculated instantaneous value of the initial magnetic field induction vector $B_p(Q_i, t)$ at time t at points P_i generated by all wires of all transmission lines.

Then, for the given values of the geometric dimensions of the silencing windings and the vector $I_W(t)$ of the instantaneous values of the currents of the instantaneous values of the currents in the silencing

windings calculated by (5), based on the Biot–Savart law, similarly (1) calculated the instantaneous value of the magnetic field induction vector $B_W(X, \delta, P_i, t)$ generated by all wires of all silencing windings at time t at points P_i.

Then the vector $B_R(X, \delta, P_i, t)$ of the instantaneous values of the induction of the resulting magnetic field generated by all wires of the power transmission line and all silencing windings at time t at points P_i in silencing space

$$B_R(X,\delta,P_i,t) = B_P(P_i,t) + B_W(X,\delta,P_i,t). \qquad (10)$$

Let us introduce an M dimensional vector $B_R(X, \delta, P_i)$ of effective values of the resulting magnetic field at M points in the silencing space, calculated by integrating the square of the modulus of the instantaneous value vector $B_R(X, \delta, P_i, t)$ over the interval of the network voltage change period.

Then the design problem of vector X parameters of the coordinates of the spatial arrangement, the vector φ of the desired parameters of the angular position of all magnetic field sensors at points Q_i in the silencing space and the desired column vector K of the gain coefficients of the silencing windings controllers reduces to solving vector minimax optimization wits vector objective function

$$B_R(X,\delta) = \langle B_R(X,\delta,P_1)\rangle. \qquad (11).$$

The components $B_R(X, \delta, P_i)$ of which are the effective values of the induction of the resulting magnetic field at all considered points Q_i in the silencing space.

In this minimax optimization problem it is necessary to find the minimum of the vector objective function (11) by the vector X, but the maximum of the same vector objective function by the vector δ.

At the same time, naturally, it is necessary to take into account restrictions on the control vector and state variables in the form of vector inequality and, possibly, equality

$$G(X) \le G_{\max}, \quad H(X) = 0. \qquad (12)$$

Note that the components of the vector criterion (11) and constraints (12) are the nonlinear functions of the vector of the required parameters of the regulators and their calculation is performed basis on the Biot–Savart law [5, 6].

The method for problem solving. The solution of the vector minimax optimization problem wits vector objective function (11) is the set of unimprovable solutions – the Pareto set of optimal solutions if only one vector objective function is given [48, 49]. Such a statement of the optimization problem is an ill-posed problem, since the solution in the form of a Pareto optimal set of unimprovable solutions is devoid of engineering sense from the point of view of practical application [50, 51]. In addition to the vector optimization criterion (11) and constraints (12), it is also necessary to have information about the binary relations of preference of local solutions to each other in order to correctly solve the problem of multi-criteria optimization. This approach makes it possible to significantly narrow the range of possible optimal solutions to the original multi-criteria optimization problem.

The problem of finding a local minimum at one point of the considered space is, as a rule, multi-extreme, containing local minima and maxima, therefore, for its solution, it is advisable to use algorithms of stochastic. Currently, the most widely used are multi-agent stochastic optimization methods that use only the speed of particles. To find the solution of minimax vector optimization problem (11) from Pareto-optimal decisions [48, 49] taking into account the preference relations, we used special nonlinear algorithms of stochastic multi-agent optimization [50, 51]. First-order methods have good convergence in the region far from the local optimum, when the first derivative has significant values.

The main disadvantage of first-order search methods, which use only the first derivative – the speed of particles, is their low efficiency of the search and the possibility of getting stuck in the search near the local minimum, where the value of the rate of change of the objective function tends to zero. The advantage of second-order algorithms is the ability to determine not only the direction of movement, but also the size of the movement step to the optimum, so that with a quadratic approximation of the objective function, the optimum found in one iteration.

To search the components $X_{ij}(t)$ optimal values of the vector X of the desired parameters minimizing vector optimization criterion (11) under constraints (12), for calculating velocities $V_{ij}(t)$ and accelerations $A_{ij}(t)$ of i particle of j swarm using the following steps

$$\begin{aligned} V_{ij}(t+1) &= W_{1j}V_{ij}(t) + C_{1j}R_{1j}(t)\times \\ &\times H(P_{1ij}(t) - E_{1ij}(t))\left[Y_{ij}(t) - \right. \\ &\left. - X_{ij}(t)\right] + C_{2j}R_{2j}(t)H(P_{1ij}(t) - \\ &- E_{2ij}(t))\left[Y_j^*(t) - X_{ij}(t)\right], \end{aligned} \qquad (13)$$

$$\begin{aligned} A_{ij}(t+1) &= W_{2j}A_{ij}(t) + C_{3j}R_{3j}(t)\times \\ &\times H(P_{3ij}(t) - E_{3ij}(t))\left[Z_{ij}(t) - \right. \\ &\left. - V_{ij}(t)\right] + C_{4j}R_{4j}(t)H(P_{4ij}(t) - \\ &\ldots - E_{4ij}(t))\left[Z_j^*(t) - V_{ij}(t)\right], \end{aligned} \qquad (14)$$

here $Y_{ij}(t)$ and Y_j^* – the best-local and global positions $X_{ij}(t)$, $Z_{ij}(t)$ and Z_j^* – the best-local and global velocity $V_{ij}(t)$ of the i-th particle, found respectively by only one i-th particle and all the particles of j swarm.

Random numbers $R_{ij}(t)$, $E_{ij}(t)$ and constants C_{ij}, P_{ij}, W_j are tuning parameters, H is the Heaviside function.

To search the components $X_{ij}(t)$ optimal values of the vector δ of the parameters of the uncertainty of the control object (2) of the system of active silencing maximizing the same vector optimization criterion (11) under constraints (12), for calculating velocities $V_{ij}(t)$ and accelerations $A_{ij}(t)$ of i particle of j swarm using the steps similarly (13) – (14). However, unlike (13) and (14), the best local and global position and velocity components are those that lead not to a decrease in the corresponding components of the vector objective function (11), but vice versa to their increase. This is where the «malicious» behavior of the vector δ of uncertainties of the designed system is manifested.

The use of the Archimedes algorithm [53] for calculating minimax vector optimization problem (11) solutions with vector constraints (12) and binary preference relations it possible to significantly reduce the calculating time [51, 52].

Results of design of experimental model. As an example, consider the design of optimal spatial arrangement and angular position of magnetic field

sensors for a closed system to ensure maximum efficiency of active silencing of the magnetic field generated by experimental model of double-circuit power transmission line with a suspension of wires of the «Barrel» type in a five-story residential building. Figure 2 shows the spatial arrangement of the transmission line model and the model of a five-story residential building.

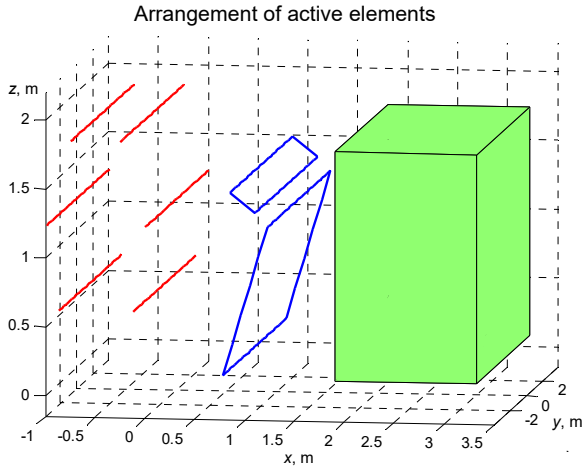

Fig. 2. Spatial arrangement of the transmission line model and the model of a five-story residential building

In the process of designing of optimal spatial arrangement and angular position of magnetic field sensors, the spatial arrangement of the two silencing windings was also designed. The spatial position of these two windings are also shown in Fig. 2.

Figure 3 shows the spatio-temporal characteristics (STC) of the initial magnetic field (1), magnetic field generated by both silencing windings (2) and the resulting magnetic field (3) with the active silencing system turned on. These spatio-temporal characteristics are calculated at the point of optimal spatial arrangement of magnetic field sensors.

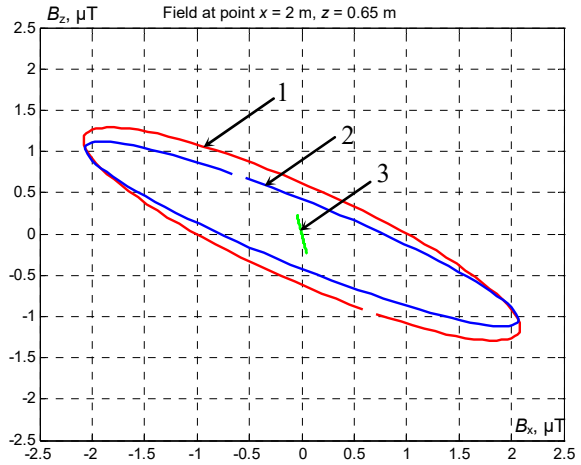

Fig. 3. The spatio-temporal characteristics of the magnetic field

From this figure it follows that with the help of two silencing windings, a sufficiently high value of the silencing factor is realized at the point of the spatial location of the of magnetic field sensors.

Experimental studies. To conduct experimental research, a model of a double-circuit power transmission line with a wire suspension of the «Barrel» type developed, the photo of which shown in Fig. 4.

Fig. 4. Power transmission line model with a wire suspension of the «Barrel» type

A model of a double-circuit system of active silencing with two silencing windings has also been developed, a photo of which is shown in Fig. 5.

To control the currents in the silencing windings and the implementation of the regulators, the system of active silencing model was developed, the photo of which is shown in Fig. 6.

Fig. 5. Two compensating silencing of double-circuit system of active silencing model

Fig. 6. Double-circuit system of active silencing model

Next to the two magnetic field sensors, photo of which shown in Fig. 7. With the help of which a closed-loop control algorithm for two silencing windings implemented, sensors are also installed, with the help of which the STC of the MF is measured.

The sensors mounted on tripods, with the help of which it is possible to set the required positioning angles of the magnetic field sensors.

Fig. 7. Magnetic field sensors

Results of experimental studies. Let us consider the first variant of the angular position of the magnetic field sensors. Both sensors are installed orthogonally to the X and Z coordinate axes. On Fig. 8 shows the experimental silencing factor surface. The silencing factor is greater than 5.

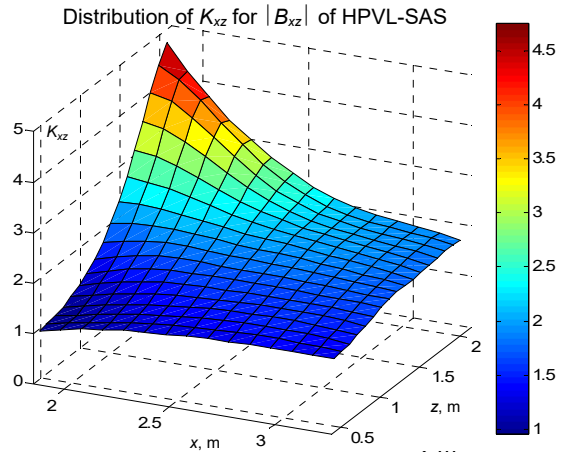

Fig. 8. Experimental silencing factor surface for first variant

Consider now the second variant of the angular position of the magnetic field sensors. The sensors are installed in such a way that their outputs have the maximum voltage when only one silencing winding of the same channel is operating. In this case, the angular positions of the sensors are respectively equal to 113 degrees and 358 degrees. On Fig. 9 shows the experimental silencing factor surface.

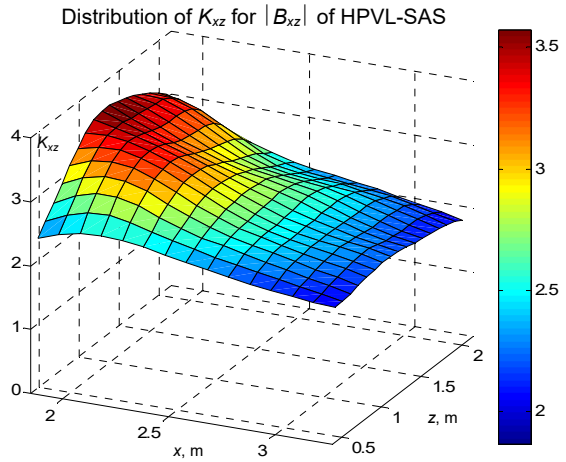

Fig. 9. Experimental silencing factor surface for second variant

The silencing factor is greater than 3.5. With such an installation of the magnetic field sensors, each channel most effectively suppresses the induction of the initial magnetic field in the plane in which this channel generates the magnetic field.

Consider now the third variant of the angular position of the magnetic field sensors. The sensors are installed in such a way that their outputs have a minimum voltage when only one silencing winding of another channel is operating. In this case, the angular positions of the sensors are respectively equal to 222 degrees and 187 degrees. Figure 10 shows the experimental silencing factor surface.

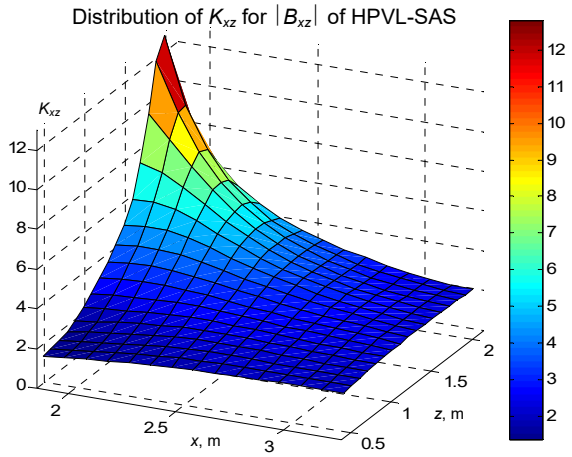

Fig. 10. Experimental silencing factor surface for third variant

The experimental silencing factor is greater than 12. With such an installation of the magnetic field sensors, each channel most effectively suppresses the induction of the initial magnetic field in a plane orthogonal to the plane in which the other channel generates the magnetic field. Therefore, the channels have minimal influence on each other when they work together.

Conclusions.

1. A method for optimizing the spatial arrangement and angular position of magnetic field sensors in a closed system of active silencing of the magnetic field to ensure maximum efficiency of active silencing of the magnetic field created by overhead power lines has been developed.

2. Optimization of the spatial arrangement and angular position of the magnetic field sensors according to the developed method is reduced to the calculation of the solution of the vector minimax optimization problem based on binary preference relations. The objective function vector of the minimax optimization problem and the calculation of constraints are formed on the basis of the Biot–Savart law and this solution is calculated on the basis of stochastic nonlinear algorithms of Archimedes.

3. Based on the developed method, the optimal spatial arrangements and angular positions of two magnetic field sensors, as well as currents in two silencing windings for double-circuit systems of active jamming of the magnetic field in a multi-storey old house, created by double-circuit overhead power lines 110 kV with a «Barrel» type arrangement of wires.

4. The effectiveness of the developed method for optimizing the spatial arrangement and angular position of two magnetic field sensors has been experimentally confirmed on a physical model of a system for active silencing of a magnetic field with a double-circuit power transmission line with a «Barrel» type arrangement of wires, which made it possible to reduce the level of the

magnetic field with an initial induction of 5.7 μT to safe level for the population with an induction of 0.5 μT.

Acknowledgment. The authors express their gratitude to the engineers Sokol A.V. and Shevchenko A.P. of the department of magnetism of technical object of Anatolii Pidhornyi Institute of Mechanical Engineering Problems of the National Academy of Sciences of Ukraine for the creative approach and courage shown during the creation under fire, under martial law, of an experimental installation and successful testing of a laboratory model of the system of active silencing.

Conflict of interest. The authors declare that they have no conflicts of interest.

REFERENCES

1. Sung H., Ferlay J., Siegel R.L., Laversanne M., Soerjomataram I., Jemal A., Bray, F. Global Cancer Statistics 2020: GLOBOCAN Estimates of Incidence and Mortality Worldwide for 36 Cancers in 185 Countries. *CA: A Cancer Journal for Clinicians*, 2021, vol. 71, no. 3, pp. 209-249. doi: https://doi.org/10.3322/caac.21660.

2. *Directive 2013/35/EU of the European Parliament and of the Council of 26 June 2013 on the minimum health and safety requirements regarding the exposure of workers to the risks arising from physical agents (electromagnetic fields)*. Available at: http://data.europa.eu/eli/dir/2013/35/oj (Accessed 25.07.2022).

3. *The International EMF Project. Radiation & Environmental Health Protection of the Human Environment World Health Organization*. Geneva, Switzerland, 1996. 2 p. Available at: https://www.who.int/initiatives/the-international-emf-project (Accessed 25.07.2022).

4. Rozov V.Yu., Grinchenko V.S., Yerisov A.V., Dobrodeyev P.N. Efficient shielding of three-phase cable line magnetic field by passive loop under limited thermal effect on power cables. *Electrical Engineering & Electromechanics*, 2019, no. 6, pp. 50-54. doi: https://doi.org/10.20998/2074-272x.2019.6.07.

5. Rozov V.Y., Pelevin D.Y., Pielievina K.D. External magnetic field of urban transformer substations and methods of its normalization. *Electrical Engineering & Electromechanics*, 2017, no. 5, pp. 60-66. doi: https://doi.org/10.20998/2074-272X.2017.5.10.

6. Rozov V.Yu., Reutskyi S.Yu., Pelevin D.Ye., Kundius K.D. Approximate method for calculating the magnetic field of 330-750 kV high-voltage power line in maintenance area under voltage. *Electrical Engineering & Electromechanics*, 2022, no. 5, pp. 71-77. doi: https://doi.org/10.20998/2074-272X.2022.5.12.

7. Rozov V.Yu., Kundius K.D., Pelevin D.Ye. Active shielding of external magnetic field of built-in transformer substations. *Electrical Engineering & Electromechanics*, 2020, no. 3, pp. 24-30. doi: https://doi.org/10.20998/2074-272x.2020.3.04.

8. Salceanu A., Paulet M., Alistar B.D., Asiminicesei O. Upon the contribution of image currents on the magnetic fields generated by overhead power lines. *2019 International Conference on Electromechanical and Energy Systems (SIELMEN).* 2019. doi: https://doi.org/10.1109/sielmen.2019.8905880.

9. Del Pino Lopez J.C., Romero P.C. Influence of different types of magnetic shields on the thermal behavior and ampacity of underground power cables. *IEEE Transactions on Power Delivery*, Oct. 2011, vol. 26, no. 4, pp. 2659-2667. doi: https://doi.org/10.1109/tpwrd.2011.2158593.

10. Hasan G.T., Mutlaq A.H., Ali K.J. The Influence of the Mixed Electric Line Poles on the Distribution of Magnetic Field. *Indonesian Journal of Electrical Engineering and Informatics (IJEEI)*, 2022, vol. 10, no. 2, pp. 292-301. doi: https://doi.org/10.52549/ijeei.v10i2.3572.

11. Victoria Mary S., Pugazhendhi Sugumaran C. Investigation on magneto-thermal-structural coupled field effect of nano coated 230 kV busbar. *Physica Scripta*, 2020, vol. 95, no. 4, art. no. 045703. doi: https://doi.org/10.1088/1402-4896/ab6524.

12. Ippolito L., Siano P. Using multi-objective optimal power flow for reducing magnetic fields from power lines. *Electric Power Systems Research*, 2004, vol. 68, no. 2, pp. 93-101. doi: https://doi.org/10.1016/S0378-7796(03)00151-2.

13. Barsali S., Giglioli R., Poli D. Active shielding of overhead line magnetic field: Design and applications. *Electric Power Systems Research*, May 2014, vol. 110, pp. 55-63. doi: https://doi.org/10.1016/j.epsr.2014.01.005.

14. Bavastro D., Canova A., Freschi F., Giaccone L., Manca M. Magnetic field mitigation at power frequency: design principles and case studies. *IEEE Transactions on Industry Applications*, May 2015, vol. 51, no. 3, pp. 2009-2016. doi: https://doi.org/10.1109/tia.2014.2369813.

15. Beltran H., Fuster V., García M. Magnetic field reduction screening system for a magnetic field source used in industrial applications. *9 Congreso Hispano Luso de Ingeniería Eléctrica (9 CHLIE)*, Marbella (Málaga, Spain), 2005, pp. 84-99. Available at: https://www.researchgate.net/publication/229020921_Magnetic_field_reduction_screening_system_for_a_magnetic_field_source_used_in_industrial_applications (Accessed 22.06.2021).

16. Bravo-Rodríguez J., Del-Pino-López J., Cruz-Romero P. A Survey on Optimization Techniques Applied to Magnetic Field Mitigation in Power Systems. *Energies*, 2019, vol. 12, no. 7, p. 1332. doi: https://doi.org/10.3390/en12071332.

17. Canova A., del-Pino-López J.C., Giaccone L., Manca M. Active Shielding System for ELF Magnetic Fields. *IEEE Transactions on Magnetics*, March 2015, vol. 51, no. 3, pp. 1-4. doi: https://doi.org/10.1109/tmag.2014.2354515.

18. Canova A., Giaccone L. Real-time optimization of active loops for the magnetic field minimization. *International Journal of Applied Electromagnetics and Mechanics*, Feb. 2018, vol. 56, pp. 97-106. doi: https://doi.org/10.3233/jae-172286.

19. Canova A., Giaccone L., Cirimele V. Active and passive shield for aerial power lines. *Proc. of the 25th International Conference on Electricity Distribution (CIRED 2019)*, 3-6 June 2019, Madrid, Spain. Paper no. 1096. Available at: https://www.cired-repository.org/handle/20.500.12455/290 (Accessed 28 May 2021).

20. Canova A., Giaccone L. High-performance magnetic shielding solution for extremely low frequency (ELF) sources. *CIRED - Open Access Proceedings Journal*, Oct. 2017, vol. 2017, no. 1, pp. 686-690. doi: https://doi.org/10.1049/oap-cired.2017.1029.

21. Celozzi S. Active compensation and partial shields for the power-frequency magnetic field reduction. *2002 IEEE International Symposium on Electromagnetic Compatibility*, Minneapolis, MN, USA, 2002, vol. 1, pp. 222-226. doi: https://doi.org/10.1109/isemc.2002.1032478.

22. Celozzi S., Garzia F. Active shielding for power-frequency magnetic field reduction using genetic algorithms optimization. *IEE Proceedings - Science, Measurement and Technology*, 2004, vol. 151, no. 1, pp. 2-7. doi: https://doi.org/10.1049/ip-smt:20040002.

23. Celozzi S., Garzia F. Magnetic field reduction by means of active shielding techniques. *WIT Transactions on Biomedicine and Health*, 2003, vol. 7, pp. 79-89. doi: https://doi.org/10.2495/ehr030091.

24. Martynenko G. Analytical Method of the Analysis of Electromagnetic Circuits of Active Magnetic Bearings for Searching Energy and Forces Taking into Account Control Law. *2020 IEEE KhPI Week on Advanced Technology (KhPIWeek)*, 2020, pp. 86-91. doi: https://doi.org/10.1109/KhPIWeek51551.2020.9250138.

25. Martynenko G., Martynenko V. Rotor Dynamics Modeling for Compressor and Generator of the Energy Gas Turbine Unit with Active Magnetic Bearings in Operating Modes. *2020 IEEE Problems of Automated Electrodrive. Theory and Practice (PAEP)*, 2020, pp. 1-4. doi: https://doi.org/10.1109/PAEP49887.2020.9240781.

26. Buriakovskyi S.G., Maslii A.S., Pasko O.V., Smirnov V.V. Mathematical modelling of transients in the electric drive of the switch – the main executive element of railway automation. *Electrical Engineering & Electromechanics*, 2020, no. 4, pp. 17-23. doi: https://doi.org/10.20998/2074-272X.2020.4.03.

27. Ostroverkhov M., Chumack V., Monakhov E., Ponomarev A. Hybrid Excited Synchronous Generator for Microhydropower Unit. *2019 IEEE 6th International Conference on Energy Smart Systems (ESS)*, Kyiv, Ukraine, 2019, pp. 219-222. doi: https://doi.org/10.1109/ess.2019.8764202.
28. Ostroverkhov M., Chumack V., Monakhov E. Ouput Voltage Stabilization Process Simulation in Generator with Hybrid Excitation at Variable Drive Speed. *2019 IEEE 2nd Ukraine Conference on Electrical and Computer Engineering (UKRCON)*, Lviv, Ukraine, 2019, pp. 310-313. doi: https://doi.org/10.1109/ukrcon.2019.8879781.
29. Tytiuk V., Chornyi O., Baranovskaya M., Serhiienko S., Zachepa I., Tsvirkun L., Kuznetsov V., Tryputen N. Synthesis of a fractional-order $PI^{\lambda}D^{\mu}$-controller for a closed system of switched reluctance motor control. *Eastern-European Journal of Enterprise Technologies*, 2019, no. 2 (98), pp. 35-42. doi: https://doi.org/10.15587/1729-4061.2019.160946.
30. Zagirnyak M., Serhiienko S., Chornyi O. Innovative technologies in laboratory workshop for students of technical specialties. *2017 IEEE First Ukraine Conference on Electrical and Computer Engineering (UKRCON)*, 2017, pp. 1216-1220. doi: https://doi.org/10.1109/UKRCON.2017.8100446.
31. Chornyi O., Serhiienko S. A virtual complex with the parametric adjustment to electromechanical system parameters. *Technical Electrodynamics*, 2019, pp. 38-41. doi: https://doi.org/10.15407/techned2019.01.038.
32. Shchur I., Kasha L., Bukavyn M. Efficiency Evaluation of Single and Modular Cascade Machines Operation in Electric Vehicle. *2020 IEEE 15th International Conference on Advanced Trends in Radioelectronics, Telecommunications and Computer Engineering (TCSET)*, Lviv-Slavske, Ukraine, 2020, pp. 156-161. doi: https://doi.org/10.1109/tcset49122.2020.235413.
33. Shchur I., Turkovskyi V. Comparative Study of Brushless DC Motor Drives with Different Configurations of Modular Multilevel Cascaded Converters. *2020 IEEE 15th International Conference on Advanced Trends in Radioelectronics, Telecommunications and Computer Engineering (TCSET)*, Lviv-Slavske, Ukraine, 2020, pp. 447-451. doi: https://doi.org/10.1109/tcset49122.2020.235473.
34. Ostroumov I., Kuzmenko N., Sushchenko O., Pavlikov V., Zhyla S., Solomentsev O., Zaliskyi M., Averyanova Y., Tserne E., Popov A., Volosyuk V., Ruzhentsev N., Dergachov K., Havrylenko O., Kuznetsov B., Nikitina T., Shmatko O. Modelling and simulation of DME navigation global service volume. *Advances in Space Research*, 2021, vol. 68, no. 8, pp. 3495-3507. doi: https://doi.org/10.1016/j.asr.2021.06.027.
35. Averyanova Y., Sushchenko O., Ostroumov I., Kuzmenko N., Zaliskyi M., Solomentsev O., Kuznetsov B., Nikitina T., Havrylenko O., Popov A., Volosyuk V., Shmatko O., Ruzhentsev N., Zhyla S., Pavlikov V., Dergachov K., Tserne E. UAS cyber security hazards analysis and approach to qualitative assessment. In: Shukla S., Unal A., Varghese Kureethara J., Mishra D.K., Han D.S. (eds) *Data Science and Security. Lecture Notes in Networks and Systems*, 2021, vol. 290, pp. 258-265. Springer, Singapore. doi: https://doi.org/10.1007/978-981-16-4486-3_28.
36. Zaliskyi M., Solomentsev O., Shcherbyna O., Ostroumov I., Sushchenko O., Averyanova Y., Kuzmenko N., Shmatko O., Ruzhentsev N., Popov A., Zhyla S., Volosyuk V., Havrylenko O., Pavlikov V., Dergachov K., Tserne E., Nikitina T., Kuznetsov B. Heteroskedasticity analysis during operational data processing of radio electronic systems. In: Shukla S., Unal A., Varghese Kureethara J., Mishra D.K., Han D.S. (eds) *Data Science and Security. Lecture Notes in Networks and Systems*, 2021, vol. 290, pp. 168-175. Springer, Singapore. doi: https://doi.org/10.1007/978-981-16-4486-3_18.
37. Shmatko O., Volosyuk V., Zhyla S., Pavlikov V., Ruzhentsev N., Tserne E., Popov A., Ostroumov I., Kuzmenko N., Dergachov K., Sushchenko O., Averyanova Y., Zaliskyi M., Solomentsev O., Havrylenko O., Kuznetsov B., Nikitina T. Synthesis of the optimal algorithm and structure of contactless optical device for estimating the parameters of statistically uneven surfaces. *Radioelectronic and Computer Systems*, 2021, no. 4, pp. 199-213. doi: https://doi.org/10.32620/reks.2021.4.16.
38. Volosyuk V., Zhyla S., Pavlikov V., Ruzhentsev N., Tserne E., Popov A., Shmatko O., Dergachov K., Havrylenko O., Ostroumov I., Kuzmenko N., Sushchenko O., Averyanova Yu., Zaliskyi M., Solomentsev O., Kuznetsov B., Nikitina T. Optimal Method for Polarization Selection of Stationary Objects Against the Background of the Earth's Surface. *International Journal of Electronics and Telecommunications*, 2022, vol. 68, no. 1, pp. 83-89. doi: https://doi.org/10.24425/ijet.2022.139852.
39. Gal'chenko V.Y., Vorob'ev M.A. Structural synthesis of attachable eddy-current probes with a given distribution of the probing field in the test zone. *Russian Journal of Nondestructive Testing*, Jan. 2005, vol. 41, no. 1, pp. 29-33. doi: https://doi.org/10.1007/s11181-005-0124-7.
40. Halchenko V.Y., Ostapushchenko D.L., Vorobyov M.A. Mathematical simulation of magnetization processes of arbitrarily shaped ferromagnetic test objects in fields of given spatial configurations. *Russian Journal of Nondestructive Testing*, Sep. 2008, vol. 44, no. 9, pp. 589-600. doi: https://doi.org/10.1134/S1061830908090015.
41. Ostroumov I., Kuzmenko N., Sushchenko O., Zaliskyi M., Solomentsev O., Averyanova Y., Zhyla S., Pavlikov V., Tserne E., Volosyuk V., Dergachov K., Havrylenko O., Shmatko O., Popov A., Ruzhentsev N., Kuznetsov B., Nikitina T. A probability estimation of aircraft departures and arrivals delays. In: Gervasi O. et al. (eds) *Computational Science and Its Applications – ICCSA 2021. ICCSA 2021. Lecture Notes in Computer Science*, vol. 12950, pp. 363-377. Springer, Cham. doi: https://doi.org/10.1007/978-3-030-86960-1_26.
42. Chystiakov P., Chornyi O., Zhautikov B., Sivyakova G. Remote control of electromechanical systems based on computer simulators. *2017 International Conference on Modern Electrical and Energy Systems (MEES)*, Kremenchuk, Ukraine, 2017, pp. 364-367. doi: https://doi.org/10.1109/mees.2017.8248934.
43. Zagirnyak M., Bisikalo O., Chorna O., Chornyi O. A Model of the Assessment of an Induction Motor Condition and Operation Life, Based on the Measurement of the External Magnetic Field. *2018 IEEE 3rd International Conference on Intelligent Energy and Power Systems (IEPS)*, Kharkiv, 2018, pp. 316-321. doi: https://doi.org/10.1109/ieps.2018.8559564.
44. Maksymenko-Sheiko K.V., Sheiko T.I., Lisin D.O., Petrenko N.D. Mathematical and Computer Modeling of the Forms of Multi-Zone Fuel Elements with Plates. *Journal of Mechanical Engineering*, 2022, vol. 25, no. 4, pp. 32-38. doi: https://doi.org/10.15407/pmach2022.04.032.
45. Hontarovskyi P.P., Smetankina N.V., Ugrimov S.V., Garmash N.H., Melezhyk I.I. Computational Studies of the Thermal Stress State of Multilayer Glazing with Electric Heating. *Journal of Mechanical Engineering*, 2022, vol. 25, no. 1, pp. 14-21. doi: https://doi.org/10.15407/pmach2022.02.014.
46. Kostikov A.O., Zevin L.I., Krol H.H., Vorontsova A.L. The Optimal Correcting the Power Value of a Nuclear Power Plant Power Unit Reactor in the Event of Equipment Failures. *Journal of Mechanical Engineering*, 2022, vol. 25, no. 3, pp. 40-45. doi: https://doi.org/10.15407/pmach2022.03.040.
47. Rusanov A.V., Subotin V.H., Khoryev O.M., Bykov Y.A., Korotaiev P.O., Ahibalov Y.S. Effect of 3D Shape of Pump-Turbine Runner Blade on Flow Characteristics in Turbine Mode. *Journal of Mechanical Engineering*, 2022, vol. 25, no. 4, pp. 6-14. doi: https://doi.org/10.15407/pmach2022.04.006.
48. Ummels M. *Stochastic Multiplayer Games Theory and Algorithms*. Amsterdam University Press, 2010. 174 p.
49. Shoham Y., Leyton-Brown K. *Multiagent Systems: Algorithmic, Game-Theoretic, and Logical Foundations.* Cambridge University Press, 2009. 504 p.

50. Pulido G.T., Coello C.A.C. A constraint-handling mechanism for particle swarm optimization. *Proceedings of the 2004 Congress on Evolutionary Computation* (IEEE Cat. No.04TH8753), Portland, OR, USA, 2004, vol. 2, pp. 1396-1403. doi: https://doi.org/10.1109/cec.2004.1331060.

51. Zhyla S., Volosyuk V., Pavlikov V., Ruzhentsev N., Tserne E., Popov A., Shmatko O., Havrylenko O., Kuzmenko N., Dergachov K., Averyanova Y., Sushchenko O., Zaliskyi M., Solomentsev O., Ostroumov I., Kuznetsov B., Nikitina T. Statistical synthesis of aerospace radars structure with optimal spatio-temporal signal processing, extended observation area and high spatial resolution. *Radioelectronic and Computer Systems*, 2022, no. 1, pp. 178-194. doi: https://doi.org/10.32620/reks.2022.1.14.

52. Xin-She Yang, Zhihua Cui, Renbin Xiao, Amir Hossein Gandomi, Mehmet Karamanoglu. *Swarm Intelligence and Bio-Inspired Computation: Theory and Applications*, Elsevier Inc., 2013. 450 p.

53. Hashim F.A., Hussain K., Houssein E.H., Mabrouk M.S., Al-Atabany W. Archimedes optimization algorithm: a new metaheuristic algorithm for solving optimization problems. *Applied Intelligence*, 2021, vol. 51, no. 3, pp. 1531-1551. doi: https://doi.org/10.1007/s10489-020-01893-z.

Received 30.09.2022
Accepted 05.11.2022
Published 01.07.2023

B.I. Kuznetsov[1], *Doctor of Technical Science, Professor,*
T.B. Nikitina[2], *Doctor of Technical Science, Professor,*
I.V. Bovdui[1], *PhD, Senior Research Scientist,*
O.V. Voloshko[1], *PhD, Junior Research Scientist,*
V.V. Kolomiets[2], *PhD, Assistant Professor,*
B.B. Kobylianskyi[2], *PhD, Associate Professor,*
[1] Anatolii Pidhornyi Institute of Mechanical Engineering Problems of the National Academy of Sciences of Ukraine,
2/10, Pozharskogo Str., Kharkiv, 61046, Ukraine,
e-mail: kuznetsov.boris.i@gmail.com (Corresponding Author)
[2] Educational scientific professional pedagogical Institute of Ukrainian Engineering Pedagogical Academy,
9a, Nosakov Str., Bakhmut, Donetsk Region, 84511, Ukraine,
e-mail: tatjana55555@gmail.com; nnppiuipa@ukr.net

How to cite this article:
Kuznetsov B.I., Nikitina T.B., Bovdui I.V., Voloshko O.V., Kolomiets V.V., Kobylianskyi B.B. Optimization of spatial arrangement of magnetic field sensors of closed loop system of overhead power lines magnetic field active silencing. *Electrical Engineering & Electromechanics*, 2023, no. 4, pp. 26-34. doi: https://doi.org/10.20998/2074-272X.2023.4.04

UDC 621.314 https://doi.org/10.20998/2074-272X.2023.4.05

B. Benazza, A. Bendaoud, H. Slimani, M. Benaissa, M. Flitti, A. Zeghoudi

Experimental study of electromagnetic disturbances in common and differential modes in a circuit based on two DC/DC boost static converter in parallel

Introduction. *An electronic control and closing control at the switch (MOSFET) will allow a parallel connection of two DC/DC boost converters. The reason for paralleling converters is to increase the efficiency of the power conversion process. This means that the overall power loss on the main switches is half the power loss on the main switch of a converter. It has been proven that DC-DC converters operating in parallel have different dynamics than a single converter. In this paper, the study is based on a system of two boost converters operating in parallel under current mode control. Although two converters operating in parallel increase the efficiency of the system, if the control parameters are not chosen correctly, the system becomes unstable and starts to oscillate.* ***Purpose*** *of this work is to present the analysis of high frequency electromagnetic disturbances caused by the switching of power switches in DC/DC boost static converters mounted in parallel in the presence of cables. We will study the improvement of the electromagnetic compatibility performances which can be brought by the choice of a static converters for industrial use.* ***Methods****. For the study of the path of the currents in common mode and in differential mode, it was possible to evaluate experimentally the electromagnetic compatibility impact in common mode and in differential mode of two boost converters connected in parallel in an electric circuit in connection with the source through a printed circuit board of connection between the source and the load, while using the two basic methods, namely the prediction of the conducted electromagnetic interference, the temporal simulation and the frequency simulation.* ***Results****. All the obtained results are validated by experimental measurements carried out at the Djillali Liabes University Sidi-Bel-Abbes in Laboratory of Applications of Plasma, Electrostatics and Electromagnetic Compatibility (APELEC). The experimental results obtained in common mode and in differential mode at low, medium and high frequencies are compared between the parallel boost test with and without electromagnetic compatibility filter.* References 17, figures 10.

Key words: **DC/DC converter; electromagnetic compatibility; conducted emissions; printed circuit board connection; electromagnetic disturbances; common mode; differential mode; high frequency.**

Вступ*. Електронне керування та керування замиканням на перемикачі (MOSFET) дозволяють паралельно підключати два підвищувальні DC/DC перетворювачі. Причина паралельного підключення перетворювачів полягає у підвищенні ефективності процесу перетворення енергії. Це означає, що загальні втрати потужності на головних вимикачах становлять половину втрат потужності на головному вимикачі перетворювача. Було доведено, що DC-DC перетворювачі, що працюють паралельно, мають іншу динаміку, ніж одиночний перетворювач. У цій статті дослідження засноване на системі двох підвищувальних перетворювачів, що працюють паралельно при управлінні по струму. Хоча два перетворювачі, що працюють паралельно, підвищують ККД системи, але при неправильному виборі параметрів управління система стає нестійкою і починає вагатися.* ***Метою*** *даної роботи є представлення аналізу високочастотних електромагнітних перешкод, викликаних перемиканням силових ключів у підвищувальних статичних DC/DC перетворювачах, встановлених паралельно за наявності кабелів. Ми вивчимо покращення показників електромагнітної сумісності, яке може бути викликане вибором статичних перетворювачів для промислового використання.* ***Методи****. Для дослідження шляху струмів у синфазному та диференціальному режимах вдалося експериментально оцінити вплив електромагнітної сумісності у синфазному та диференціальному режимах двох підвищувальних перетворювачів, включених паралельно в електричний ланцюг при з'єднанні з джерелом через друковану плату з'єднання між джерелом та навантаженням, використовуючи два основних методи, а саме прогнозування кондуктивних електромагнітних перешкод, тимчасове моделювання та частотне моделювання.* ***Результати****. Усі отримані результати підтверджені експериментальними вимірюваннями, проведеними у Djillali Liabes University Sidi-Bel-Abbes у Laboratory of Applications of Plasma, Electrostatics and Electromagnetic Compatibility (APELEC). Експериментальні результати, отримані в синфазному та диференціальному режимах на низьких, середніх та високих частотах, порівнюються з паралельним форсованим тестом з фільтром електромагнітної сумісності та без нього.* Бібл. 17, рис. 10.

Ключові слова: **DC/DC перетворювач; електромагнітна сумісність; кондуктивні перешкоди; підключення друкованої плати; електромагнітні перешкоди; загальний режим; диференційний режим; висока частота.**

Introduction. Switching power supplies are widely used in modern electronic systems because they allow a high level of integration, low cost and high efficiency. In the automotive field, the integrated circuits embedded in vehicles for chassis or security applications offer all the power components and control circuits necessary for buck or boost energy conversion (power less than 10 W) [1-4].

Electromagnetic compatibility (EMC) is a scientific and technical discipline which finds its justification today in the problems of cohabitation between industrial systems and their environment. While these problems have always existed, they are now becoming increasingly important due to the concentration in the same environment of devices or systems with very different power and sensitivity levels [1, 5].

Electrical systems based on static converters are designed with an ever increasing level of complexity. Effects on EMC and signal integrity are observed. The presence of a printed circuit board (PCB) connection in a static converter based electrical system is more than necessary nowadays. The EMC design of PCBs plays an important role in the electrical interconnections of any electrical system.

On the other hand, it gives rise to many electromagnetic interferences (EMIs) conducted and radiated. The origin of the latter is related to variations in electrical quantities over short periods of time with high amplitudes and high frequencies [2, 3, 5].

The static DC/DC converter, which is realized with the help of controllable on/off power switches such as MOSFETS, consists of periodically establishing and then interrupting the source-load link by means of the power switch [6-8]. The present work is devoted to the study of low and high frequency conducted electromagnetic disturbances in common mode (CM) and differential

mode (DM) generated by two step-up choppers in parallel in the presence of a connection PCB in the electrical study circuit. Thus to highlight the disturbances caused by these converters, we conducted experimental tests on a test bench consisting of a source + LISN (line impedance stabilization network) + cable + connection PCB + cables + + two converter «Boost» in parallel + cables + load.

Our study presents the comparison of the spectral envelopes of the currents at the LISN in CM and DM of the electrical circuit with and without filter for the case of two boosts in parallel.

Disruptive effect of a step-up chopper on a DC voltage source. With the advent of dispersed generation, more and more static converters are being connected to power grids. They inject the electrical power supplied by the generators, but unlike conventional electric systems, they also introduce low and high frequency disturbances. The objective of this experimental research work is to study the EMC impact of MOSFET-based step-up choppers on a DC voltage source in an electric circuit [9]. In order to highlight the principle of creation of low frequency disturbances by the chopper, we considered the basic model illustrated in Fig. 1. This model allows us to determine the LISN current in CM and DM with and without a filter in a mode where the two boosts are connected in parallel.

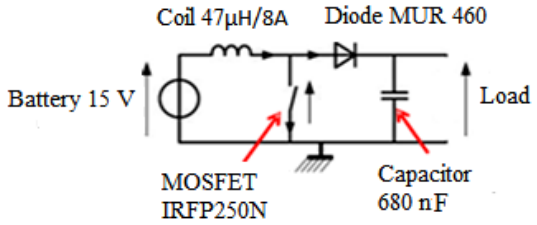

Fig. 1. Boost chopper circuit integrating the elements [7]

Principle of frequency modeling. The boost chopper circuit is shown in Fig. 1. The parasitic inductances and capacitances of the components and tracks are represented and taken into account in the simulation because they will modify the propagation of the HF harmonic currents. These currents are generated by switching the current and voltage. Figure 2 shows the waveform of the switched voltage across the MOSFET.

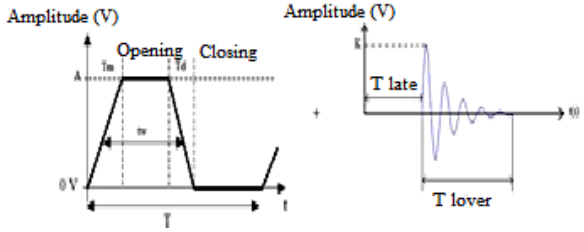

Fig. 2. Temporal model of the disturbance source [8]

This voltage is the sum of a trapezoidal voltage at the switching frequency and damped sinusoidal ripples produced by the parasitic components. The amplitude of this voltage is determined by the V_{DC} bus voltage. The rise and fall times depend on the intrinsic parameters of the power components and the gate resistance of the MOSFET [7, 10]. To realize a boost converter it is necessary to have four electronic components: a coil, a diode, a capacitor and a switch controllable with the ignition and the de-ignition typically a transistor (Fig. 1).

By replacing the diode and MOSFET with voltage sources reproducing trapezoidal and damped oscillatory shapes, we can simulate CM conducted electromagnetic disturbances (Fig. 2). In the literature, it is recommended to replace the switching cell with current sources in the case of DM disturbances [8, 11].

Analysis of high frequency EMC disturbances caused by switching. This work is based on the study of two boost converters in parallel in an electrical circuit connected to the source via a PCB which is loaded by a resistor. One of the two boosts used in the electrical circuit it's essentially composed of:

- MOSFET IRFP250N;
- Diode MUR460;
- Filter capacitor with its parasitic elements.

Disturbing effect of a boost chopper in an electric circuit. The electronic structures of energy conversion are well suited to illustrate the mechanisms of conducted emissions and provide the building blocks for modeling these phenomena. The EMC tends to show that it is necessary to limit the rapid variations of electrical (voltage and current) and electromagnetic fields quantities, whereas switching structures generate brutal variations, at least electrically, to manage the desired energy transfer with lower losses [10]. Indeed, the switching cell, easily identifiable in non-insulated structures, represents the association of two switches, controlled or not. It is the seat of strong voltage and current gradients [12-14].

Average model of the studied system. The model must be close enough to the original system so that the study through the derived model can be performed which is illustrated in Fig. 3. The two boost choppers are connected at the input to a LISN [10] (Fig. 4) via a two-wire shielded connection (cable 1), a connection PCB, cable 2 and cable 3 and at the output, cables 4 and 5 directly connected to the load (Fig. 4).

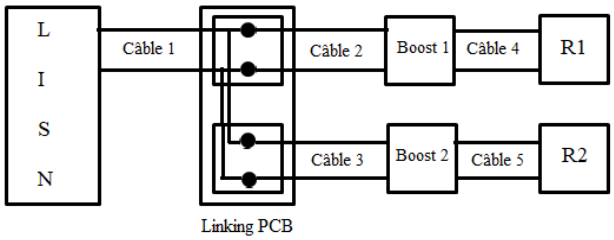

Fig. 3. Block diagram of studied model

For different types of cable lengths upstream and downstream from the PCB, which is intended for the connection of cables to supply two static boost converters in parallel loaded by two resistors there are several structures for an LISN. The one used in this work is shown in Fig. 4. It is compatible with international standards and is the structure available in the laboratory for the experimental tests carried out [15-17].

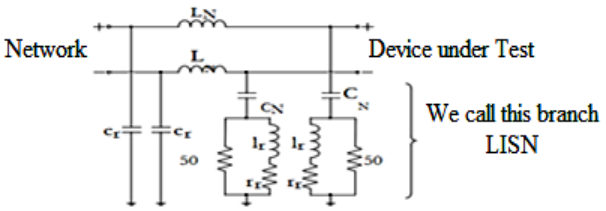

Fig. 4. Line impedance stabilizing network [10]

This paper presents the operation of two DC/DC boost converters in parallel and what problems this can cause without changing the cable lengths. Finally, the possible solutions will be presented, especially the one applied in this study, which worked well.

Experimental results for sum test measurement (both boosts connected in parallel). In this case, we supply both converters boost 1 and boost 2 at the same time, the electrical data of the study system are: $V_s = 16.4$ V; $I_s = 2.12$ A; V_{in} (boost) = 14 V; V_{out} (boost) = 42.1 V; $R_1 = R_2 = 70$ Ω (Fig. 3).

For the test bench, the materials and tools used are:

- DC source (AL936N 60 V 6 A);
- LISN with $L_N = 250$ µH, $C_r = 1$ µF, $C_N = 220$ nF;
- $L_r = 50$ µH, $R_r = 5$ Ω;
- Two identical boost converters (14 V / 42 V);
- Two loads 54 Ω / 5 A;
- Electronic oscilloscope (Tektronix MSO 5204);
- Spectrum analyzer (ROHNDE / SCHWARZ 10 Hz – 3,6 GHz);
- A current probe (Tektronix P6021A);
- Two-wire cables.

Both converters have been sized to switch at a frequency of 100 kHz. For the measurement of the LISN currents, a spectrum analyzer and an electronic oscilloscope were used. It was also necessary to use an interconnection device to allow reproducibility of the measurements for the experimental study, the measurement of LISN current in both DM and CM with and without a filter according to the circuit Fig. 3.

Measurement without filter. Our study system follows the circuit (LISN + cable 1 + connecting PCB + cable 2 + boost 1 + cable 3 + load) in parallel with the circuit (cable 4 +boost 2+ cable 5 + load), without filter.

Differential mode. For the experimental study, the measurement of the LISN current in DM following the circuit (LISN + cable 1 + PCB connection + cable 2 + boost 1 + cable 3 + load R_1) in parallel with the circuit (cable 4 + boost 2 + cable 5 + load R_2) is shown in Fig. 5.

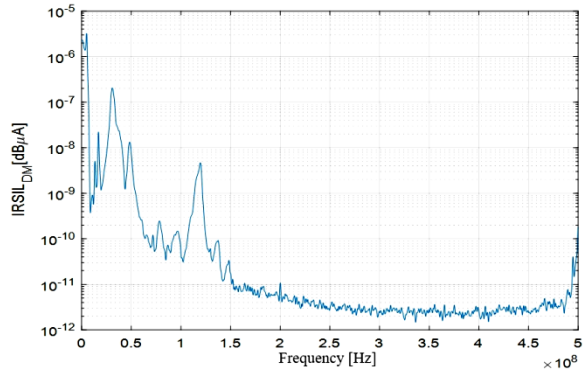

Fig. 5. Frequency response of the LISN current in DM without filter for a circuit with two boosts connected in parallel

In Fig. 5 we notice that the signal presents resonance peaks with amplitudes from 10^{-5} dBµA to 10^{-9} dBµA with frequencies from 1 MHz to 100 MHz due to the disturbances of the switching cell at the level of the two boosts in parallel and to the impact of the cable parasites. Not forgetting the impact of the input impedance of the two converters, as well as the blocked state capacitances of the semiconductors on the signal.

Common mode. We use the same electrical study circuit as in the DM (Fig. 6).

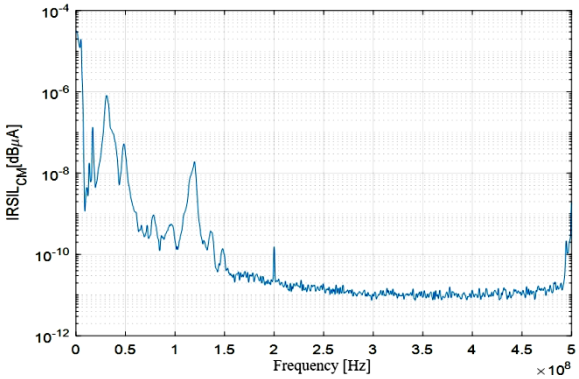

Fig. 6. Frequency response of the LISN current in CM without filter for a circuit of two boosts in parallel

In Fig. 6, the signal clearly shows resonance peaks with amplitudes of 10^{-4} dBµA to 10^{-8} dBµA from 1 MHz to 120 MHz due to the effects of the parasitic CM capacitances of the two boosts, and then from 150 MHz onwards, the signal shows slight EMI due to the inductive effect of the power cables.

Measurement with filter. Our study system follows the circuit (LISN + cable 1 + connecting PCB + cable 2 + boost 1 + cable 3 + load) in parallel with the circuit (cable 4 + boost 2 + cable 5 + load), with filter.

Differential mode. We use the same electrical study circuit as the one without filter (Fig. 7). Figure 7 shows the frequency response of the LISN current in DM with filter for a circuit with two boosts in parallel. The signal shows resonance peaks with amplitudes of 10^{-9} dBµA to 10^{-10} dBµA in the frequency range from 1 MHz to 40 MHz, which are due to switching disturbances at the boosts and cable inductances. At 40 MHz, it can be seen that there is a suppression of the electromagnetic interference due to the presence of the filter.

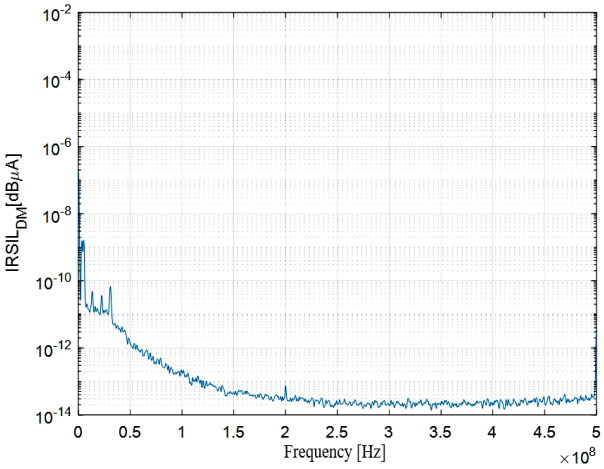

Fig. 7. Frequency response of the LISN current in DM with filter for a circuit of two boosts in parallel

Common mode. The measurement of the LISN current in CM with filter according to the circuit (LISN + cable 1 + connection PCB + cable 2 + boost 1 + cable 3 + load R_1) in parallel with the circuit (cable 4 + boost 2 + cable 5 + load R_2), is shown in Fig. 8. Figure 8 shows the frequency response of the LISN current in CM with filter for a circuit of two boosts in parallel whose signal shows

resonance peaks of amplitude 10^{-7} dBμA to 10^{-10} dBμA from 1 MHz to 30 MHz due to the inductance of the cables and the parasitic capacitances in CM of the two boosts, then from 40 MHz and above, it can be seen that the signal shows slight EMI due to the presence of the filter.

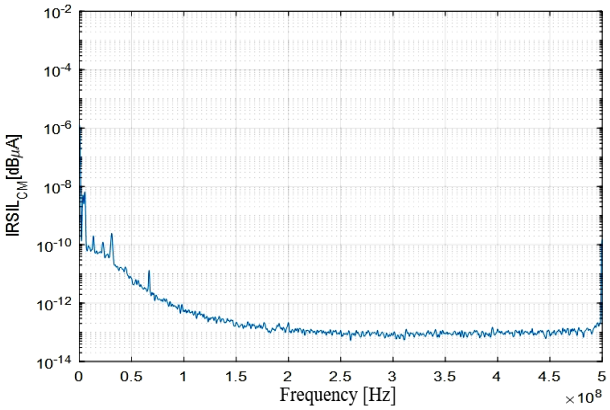

Fig. 8. Frequency response of the LISN current in CM with filter for a circuit of two boosts in parallel

Comparison test in CM with and without filter. Figure 9 shows clearly the CM comparison test for a two boost circuit in parallel between the two cases without and with filter. Figure 9 shows the frequency response of the LISN current in CM with and without filter, as function of the disturbances generated by the two boosts. It can be clearly seen that, over the whole frequency range, the disturbances of CM with filter (blue spectrum) are largely minimal and have low amplitudes of the order of 10^{-8} dBμA compared to that without filter (red spectrum) which are due on the one hand to the effect of the filter, the inductive effect of the power cables and on the other hand to the effect of the CM capacitances of the two boosts.

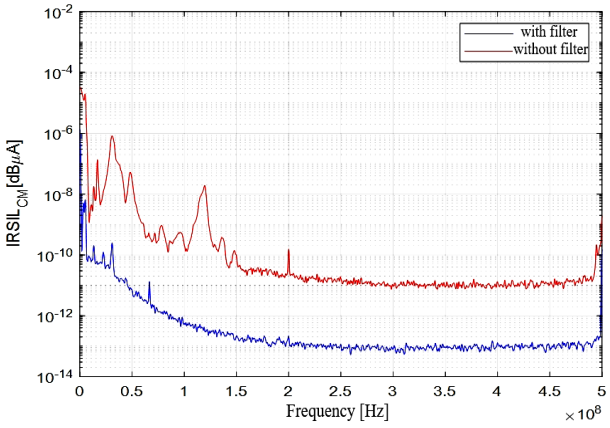

Fig. 9. Frequency response of the CM LISN current with and without filter for the two boost circuit in parallel

Comparison test in DM with and without filter. Figure 10 shows clearly the comparison test in DM between the two cases without and with filter.

We notice that there is no concordance between the two spectra. The spectrum (blue) has less amplitude because of the presence of the filter, but the signal (red) has resonance peaks on the frequency range from 1 MHz to 120 MHz. On the other hand, beyond 150 MHz the two signals present the same EMI appearance because of the inductance of the cables and the parasitic capacities in DM of the two boosts.

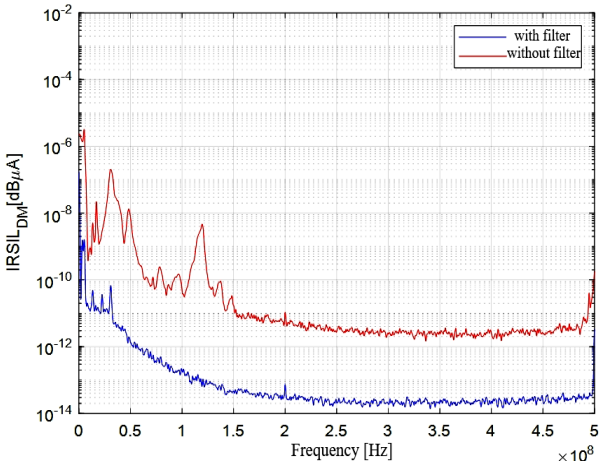

Fig. 10. Frequency response of the LISN current in DM with and without filter for a two boost circuit in parallel

Conclusions.

1. Experimental results showed that parallel connected boost converters start oscillating at 1 MHz up to 110 MHz, but are perfect beyond that. Nevertheless, the overall electromagnetic compatibility disturbance result for the «sum» test case of two boosts with and without a filter in differential and common mode is the main focus, and is illustrated by the line impedance stabilizing network current.

2. It can be seen that the differential or common mode capacitive effect generated by the two boosts is very important. Common mode impedances are usually low parasitic capacitances and therefore high at low frequencies, while differential mode impedances are high parasitic capacitances (negligible compared to the common mode).

3. It can be said that electromagnetic disturbances are transmitted to the outside of any electrical study system via various couplings. The objective of this paper was to present some experimental methods in differential and common mode, which complement other theoretical research previously conducted in order to identify and define the source of electromagnetic interferences that are generated by parallel boosts in a power system.

4. It can be clearly seen that electromagnetic interferences will be increasingly lower in filtered differential mode than in common mode. The experimental results of parallel converters have been presented as a proof of concept. The proposed method can be easily applied to support high power levels. The design of two static DC/DC boost converters in parallel in an electrical circuit is more than desirable in relation to electromagnetic interferences minimization.

Acknowledgement. This research was supported by «La Direction Générale de la Recherche Scientifique et du Développement Technologique (DGRSDT)».

Conflict of interest. The authors declare no conflict of interest.

REFERENCES

1. Benhadda N., Bendaoud A., Miloudi M., Benazza B., Belhenini S. Buck Converter Common-Mode Emission with the Frequency Approach. *International Journal of Electronics and Electrical Engineering Systems*, 2020, vol. 3, no. 4, pp. 9-14.

2. Aulagnier G., Cousineau M., Abouda K., Rolland E., Meynard T. Impact CEM haute fréquence des commutations dans un convertisseur Buck. Etude analytique et application aux

structures parallèles à commandes entrelacées. *Symposium de Génie Électrique 2014*, July 2014, Cachan, France. (Fra).
3. Aulagnier G., Cousineau M., Meynard T., Rolland E., Abouda K. High frequency EMC impact of switching to improve DC-DC converter performances. *2013 15th European Conference on Power Electronics and Applications (EPE)*, 2013, pp. 1-9. doi: https://doi.org/10.1109/EPE.2013.6634463.
4. Costa F., Magnon D. Graphical Analysis of the Spectra of EMI Sources in Power Electronics. *IEEE Transactions on Power Electronics*, 2005, vol. 20, no. 6, pp. 1491-1498. doi: https://doi.org/10.1109/TPEL.2005.857564.
5. Rezini S., Azzouz Z. Impact des émissions EM conduites produites par un hacheur abaisseur *Revue des Energies Renouvelables*, 2017, vol. 20, no. 3, pp. 433-447.
6. Meghnine B. *Mise en parallèle de deux structures de convertisseurs DC/DC Boost*. Polytech Clermont Ferrand, Eaton Corporation 2014-2015. Available at: https://docplayer.fr/41349389-Mise-en-parallele-de-deux-structures-de-convertisseurs-dc-dc-Boost.html (Accessed 22.06.2022). (Fra).
7. Nave M.J. The effect of duty cycle on SMPS common mode emissions: theory and experiment. *National Symposium on Electromagnetic Compatibility*, 1989, pp. 211-216. doi: https://doi.org/10.1109/NSEMC.1989.37182.
8. Huang X. *Frequency Domain Conductive Electromagnetic Interference Modeling and Prediction with Parasitics Extraction for Inverters*. PhD Dissertation Thesis, Faculty of the Virginia Polytechnic Institute and State University, USA, 2004.
9. Labrousse D., Revol B., Costa F. Common-Mode Modeling of the Association of N-Switching Cells: Application to an Electric-Vehicle-Drive System. *IEEE Transactions on Power Electronics*, 2010, vol. 25, no. 11, pp. 2852-2859. doi: https://doi.org/10.1109/TPEL.2010.2051457.
10. Benazza B., Bendaoud A., Schanen J.-L. Impact des longueurs de cable sur les emissions cem conduites d'un convertisseur DC/DC. *Colloque international et exposition sur ma compatibilité électromagnétique CEM*, July 2018, Paris, France. (Fra).
11. Hrigua S., Costa F., Gautier C., Revol B. New modeling method based on transfer functions for EMI analysis in power electronic converters. *International Symposium on Electromagnetic Compatibility - EMC EUROPE*, 2012, pp. 1-6. doi: https://doi.org/10.1109/EMCEurope.2012.6396839.
12. Baghdadi B., Abdelber B., Alain R., Omar D., Helima S. Experimental study of the behaviour of the crosstalk of shielded or untwisted-pair cables in high frequency. *Serbian Journal of Electrical Engineering*, 2019, vol. 16, no. 3, pp. 311-324. doi: https://doi.org/10.2298/SJEE1903311B.
13. Zeghoudi A., Bendaoud A., Slimani H., Benazza B., Miloudi H., Canale L. Power impact and electromagnetic disturbances of different lighting modes from spot LED lamp. *Optik*, 2022, vol. 269, art. no. 169898. doi: https://doi.org/10.1016/j.ijleo.2022.169898.
14. Zeghoudi A., Slimani H., Bendaoud A., Benazza B., Bechekir S., Miloudi H. Measurement and analysis of common and differential modes conducted emissions generated by an AC/DC converter. *Electrical Engineering & Electromechanics*, 2022, no. 4, pp. 63-67. doi: https://doi.org/10.20998/2074-272X.2022.4.09.
15. Zeghoudi A., Bendaoud A., Slimani H., Benazza B., Bennouna D. Determination of electromagnetic disturbances in a buck chopper. *Australian Journal of Electrical and Electronics Engineering*, 2022, vol. 19, no. 2, pp. 149-157. doi: https://doi.org/10.1080/1448837X.2021.2023073.
16. Slimani H., Zeghoudi A., Bendaoud A., Reguig A., Benazza B., Benhadda N. Experimental Measurement of Conducted Emissions Generated by Static Converters in Common and Differential Modes. *European Journal of Electrical Engineering*, 2021, vol. 23, no. 3, pp. 273-279. doi: https://doi.org/10.18280/ejee.230312.
17. Miloudi H., Miloudi M., Gourbi A., Bermaki M.H., Bendaoud A., Zeghoudi A. A high-frequency modeling of AC motor in a frequency range from 40 Hz to 110 MHz. *Electrical Engineering & Electromechanics*, 2022, no. 6, pp. 3-7. doi: https://doi.org/10.20998/2074-272X.2022.6.01.

Received 09.09.2022
Accepted 13.11.2022
Published 01.07.2023

Baghdadi Benazza[1,2], *Lecturer,*
Abdelber Bendaoud[1], *Professor,*
Helima Slimani[1,3], *Lecturer,*
Mohamed Benaissa[4], *Professor,*
Mohamed Flitti[2], *Lecturer,*
Abdelhakim Zeghoudi[1], *PhD,*
[1] Laboratory of Applications of Plasma, Electrostatics and Electromagnetic Compatibility (APELEC),
Djillali Liabes University Sidi-Bel-Abbes, Algeria,
e-mail: baghdadi.benazza@univ-temouchent.edu.dz;
babdelber@gmail.com (Corresponding Author);
hakooumzeghoudi@gmail.com
[2] Electrical Engineering Department;
University of Ain Temouchent, Algeria,
e-mail: mohammed.flitti@univ-temouchent.edu.dz
[3] Department of Mechanical Engineering,
University Ibn Khaldoun of Tiaret, Algeria,
e-mail: Slimani.Halima@yahoo.fr
[4] Faculty of Technology, University Abou bekr Belkaid,
Tlemcen, Information Processing and Telecommunications Laboratory (LTIT), Algeria,
e-mail: moh.benaissa@gmail.com

How to cite this article:
Benazza B., Bendaoud A., Slimani H., Benaissa M., Flitti M., Zeghoudi A. Experimental study of electromagnetic disturbances in common and differential modes in a circuit based on two DC/DC boost static converter in parallel. *Electrical Engineering & Electromechanics*, 2023, no. 4, pp. 35-39. doi: https://doi.org/10.20998/2074-272X.2023.4.05

UDC 621.314 https://doi.org/10.20998/2074-272X.2023.4.06

Y. Lahiouel, S. Latreche, M. Khemliche, L. Boulemzaoud

Photovoltaic fault diagnosis algorithm using fuzzy logic controller based on calculating distortion ratio of values

Introduction. *The efficiency of solar energy systems in producing electricity in a clean way. Reliance on it in industrial and domestic systems has led to the emergence of malfunctions in its facilities. During the operating period, these systems deteriorate, and this requires the development of a diagnostic system aimed at maintaining energy production at a maximum rate by detecting faults as soon as possible and addressing them.* ***Goal****. This work proposes the development of an algorithm to detect faults in the photovoltaic system, which based on fuzzy logic.* ***Novelty****. Calculate the distortion ratio of the voltage and current values resulting from each element in the photovoltaic system and processing it by the fuzzy logic controller, which leads to determining the nature of the fault.* ***Results****. As show in results using fuzzy logic control by calculating the distortion ratio of the voltage and current detect 12 faults in photovoltaic array, converter DC-DC and battery.* References 20, table 5, figures 16.
Key words: **photovoltaic system, fault diagnosis, distortion ratio of voltage and current, fuzzy logic controller.**

Вступ*. Ефективність систем сонячної енергії у виробництві електроенергії у чистий спосіб. Опора на нього в промислових та побутових системах призвела до виникнення несправностей у його об'єктах. У період експлуатації ці системи зношуються, і це вимагає розробки системи діагностики, спрямованої на підтримку вироблення енергії на максимальному рівні за рахунок якнайшвидшого виявлення несправностей та їх усунення.* ***Мета****. У цій роботі пропонується розробка алгоритму виявлення несправностей у фотоелектричній системі, що ґрунтується на нечіткій логіці.* ***Новизна****. Розрахувати коефіцієнт спотворення значень напруги та струму з кожного елемента фотоелектричної системи та обробити його контролером нечіткої логіки, що призводить до визначення характеру несправності.* ***Результати****. Як показують результати, використання нечіткого логічного управління шляхом розрахунку коефіцієнта спотворення напруги та струму дозволяє виявити 12 несправностей у фотоелектричній батареї, DC-DC перетворювачі та акумуляторі.* Бібл. 20, табл. 5, рис. 16.
Ключові слова: **фотоелектрична система, діагностика несправностей, коефіцієнт спотворення напруги та струму, контролер з нечіткою логікою.**

Introduction. The significant increase in global energy consumption along with concerns about the environmental impacts of conventional energies has led the world to gradually move towards renewable energy sources such as solar energy, wind energy and geothermal energy. Photovoltaic (PV) is arguably the most direct way to take advantage of solar energy and is considered the most promising way to harness this energy [1]. It is very popular globally due to its advantages such as abundance, ease of installation, quiet operation, and low cost compared to other renewable energy sources; which led to its enjoyment of a great level of interest in scientific research [2].

PV installation consists of several parts where the PV panels are the main component. The latter is exposed to many environmental and electrical influences that lead to the occurrence of many faults and malfunctions. These faults directly affect the performance of the system and may lead to its failure or even the risk of incidents [3]. Some critical faults need to be quickly detected and treated to ensure healthy performances of the system. Therefore, PV panels require several maintenance operations in order to reach the optimal system performances and expand their lifespan [4]. As any industrial system, the goal is to reach the maximum energy production with minimum maintenance costs.

Several researches have studied the properties of PV modules under unusual conditions and have proposed relatively accurate and intelligent fault diagnosis and detection solutions based on neural networks and fuzzy logic algorithms, etc. [5].

There are research works that talked about this method, we mention the most important:

In [6] the authors present a DC side short circuit fault detection scheme for PV arrays consisting of multiple PV panels connected in a series/parallel configuration. The proposed fault detection scheme is based on a pattern recognition approach that uses a multi-resolution signal decomposition technique to extract the necessary features, based on determined by the fuzzy inference system if a fault occurs.

In [7] authors talk about the development of failure detection routines (FDRs) that operate on acquired data-sets of grid-connected PV systems in order to diagnose the occurrence of failures. The developed FDRs consist of a failure detection and classification phase. More precisely, the failure detection phase was based on a comparative statistic between simulated and measured electrical measurements. In parallel, a fuzzy logic inference was performed in order to analyze the failure model and the exact classification of the error that occurred. The fuzzy rule-based classification system models were constructed for each failure through a supervisory learning process.

In [8] the authors have classified faults for the PV module based on artificial intelligence technology. They applied fuzzy logic to evaluate the critical fault of the PV module, according to its arrangement. The fault probabilities of the PV module are expressed by linguistic variables. The technique of consistency agreement method was used to compile the mysterious number, which was set by experts.

In [9] the authors suggested analyzing 2580 PV modules affected by different types of hotspot, as these PV modules are operated under different environmental

conditions, distributed across the UK. And then it detects the fault. The fault-finding model incorporates a fuzzy inference system using a Mamdani fuzzy controller including 3 input parameters: percentage of power loss, short circuit current (I_{sc}), and open circuit voltage (V_{oc}) in order to test the effectiveness of the proposed algorithm.

In [10] the researchers propose a technique for detecting the partial shading using the measured values for array voltage, array current, and radiation. Fuzzy logical technique (Sugeno) is presented for to detect the diagnosis partial and to classify and identify these defects, and is designed to take appropriate corrective actions.

The **goal** of this paper is the development of an intelligent fault diagnostic algorithm based on Fuzzy Logic Control (FLC) for PV installations. The fault detection initially uses simulated I-V curve estimation along with current and voltage output values form the transformer and battery. A standard test is used to differentiate between the sets of parameters calculated on the basis of various operating conditions. The proposed diagnostic method can detect and classify each specific type of fault and also deals with noise and disturbances. Modelling and diagnostic procedure were developed under MATLAB/Simulink environment.

PV system modeling. PV cells have a complex relationship between their working environment and the energy they produce. In order to adapt the generated power to the load, it is necessary to install a static DC-DC converter as an intermediate stage between the PV generator and the load. This stage is generally controlled by a Maximum Power Point Tracker (MPPT), which makes the system permanently works at its maximum power [11]. The typical architecture of a PV installation is shown in Fig. 1.

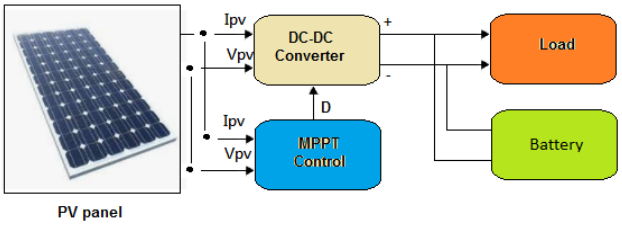

Fig. 1. Typical PV installation

PV cell modeling can be developed from its equivalent electrical circuit. The one-diode model which is also known as five-parameter model is the most commonly used. This model is a combination of a current source I_{ph}, a diode VD, a shunt resistor R_{sh} and a series resistor R_s represents the power losses [12]. The equivalent circuit for this model is illustrated in Fig. 2.

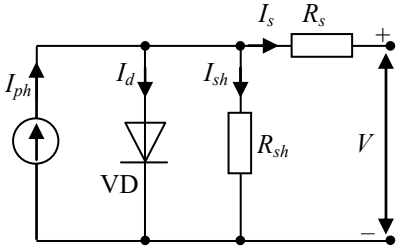

Fig. 2. One-diode PV cell model

The mathematical representation of the one-diode electrical circuit is given by the following equations:

$$I = I_{ph} - I_0 \cdot \left[\exp\left(\frac{q(V + I \cdot R_s)}{n \cdot K \cdot N_s \cdot T} \right) - 1 \right] - I_{sh}; \quad (1)$$

$$I_{ph} = I_{sc} + K_i \cdot (T - 298) \cdot \frac{G}{1000}; \quad (2)$$

$$I_0 = I_{rs} \cdot (T/T_n)^3 \cdot \exp\left[\frac{q \cdot E_{g0} \cdot (1/T_n - 1/T)}{n \cdot K} \right]; \quad (3)$$

$$I_{rs} = \frac{I_{sc}}{\exp\left(\frac{q \cdot V_{oc}}{n \cdot K \cdot N_s \cdot T} \right) - 1}; \quad (4)$$

where I_{ph} and I_{sc} are the photocurrent and the short-circuit current, respectively; K_i = 0.0032 is the short-circuit current of cell at 25 °C; T is the operating temperature; T_n = 298 K is the normal temperature; G is the solar irradiance, W/m^2; q = 1.6·10^{-19} C is the electron charge; V_{oc} is the open-circuit voltage; n = 1.3 is the ideality factor of the diode; K = 1.38·10^{-23} J/K is the Boltzmann constant; E_{g0} = 1.1 eV is the band gap energy of the semiconductor; N_s is the number of cells connected in series; N_p is the number of cells connected in parallel; R_s and R_p are series and parallel resistances, respectively.

PV module characteristics. The dedicated studied system for this work is simulated under a MATLAB/Simulink environment. It is composed of 8 PV modules (2 strings). Each module produces a maximum power of 200 W at 26.4 V. The electrical characteristics of each PV module under standard test conditions are shown in Table 1. The system is also composed of a DC-DC boost converter equipped with a Perturb and Observe MPPT. The simulation is done for a constant irradiance of 1000 W/m^2 and constant temperature of 25 °C. The MATLAB/Simulink model of the simulated PV system is shown in Fig. 3. The simulated *I-V* and *P-V* curves are shown in Fig. 4.

Table 1

Electrical characteristics of simulated PV module

Maximum power P_{mp}, W	200
Voltage at maximum power V_{mp}, V	26.4
Current at maximum power I_{mp}, A	7.58
Open-circuit voltage V_{oc}, V	32.9
Short-circuit voltage I_{sc}, A	8.21
Total number of cells in series N_s	54
Total number of cells in parallel N_p	1

The faults in PV systems can be temporary or permanent. Temporary faults are often caused by environmental effects such as shading and soiling. Permanent faults are usually related to PV module failures such as delamination, bubbles, yellowing, scratches and burnt cells [13]. They can be eliminated by either repairing or replacing defective modules. PV panels are also susceptible to many serious faults that can be caused by short circuits. Also, there are some other factors that can lead to productions losses such as MPPT failures, losses in wiring, defective equipment etc. However, PV system's faults can be classified based on the faulty component, such as module faults, string faults, or power grid faults [14, 15]. The most common PV systems faults are described in Table 2.

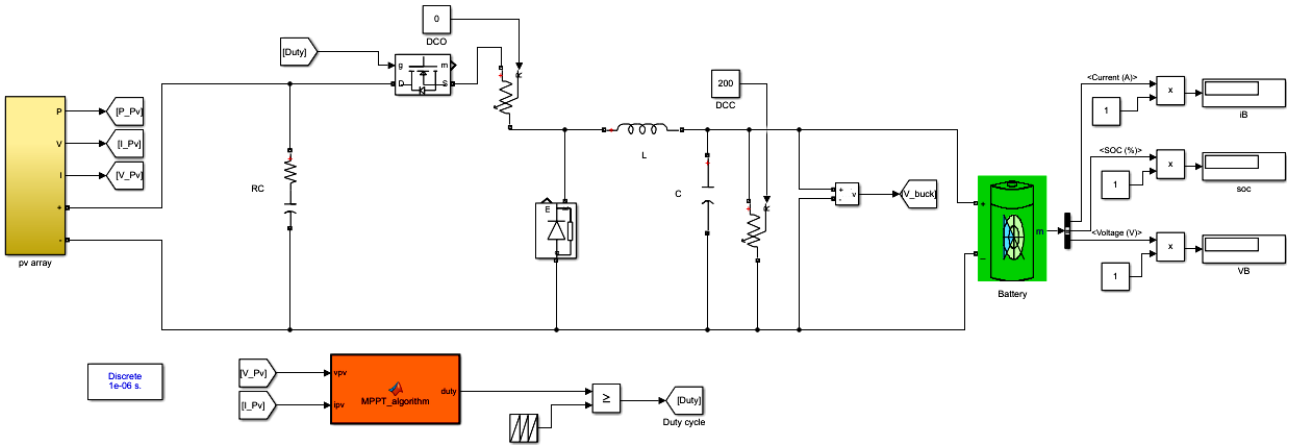

Fig. 3. MATLAB/Simulink model of the simulated PV system

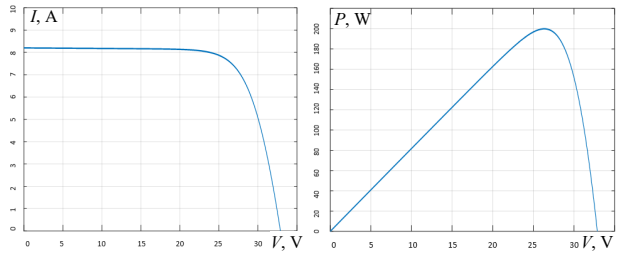

a *b*

Fig. 4. *I-V* (*a*) and *P-V* (*b*) characteristics

Table 2

Faults occurring in the examined PV system

Components	Faults	Fault code
PV array	Less than 50 % total shading	F01
	Less than 50 % partial shading	F02
	More than 50 % total shading	F03
	More than 50 % partial shading	F04
	Temperature increase	F05
	Series resistances	F06
	Shunt resistances	F07
	Interconnection faults	F08
Converter DC-DC	Open circuit	F09
	Short circuit	F10
	MP controller failure	F11
Battery	Charging failure	F12

PV array faults can be divided into several groups depending on their type where there is a failure of the PV panel, cables or failure of external factors [16]. This work focuses only on faults related to the PV panel. In this stage we can talk about shading patterns whether it is total (F01, F03) or partial (F02, F04) or faults related to temperature (F05). In the other hand, PV power degradation can be caused by the increase of the resistance between the units which can be caused by corrosion, water vapor or other related factors (F06, F07). Also, interconnection faults (F08) such as short-circuit are occurred due to faulty cable's insulation or mechanical damage. Different types of PV array faults are shown in Fig. 5. The effect of each type of described faults on the generated power curve compared with ideal working conditions is illustrated in Fig. 6, 7.

DC-DC converter faults. DC-DC converters are used in PV systems in order to charge batteries and also supply DC loads [17].

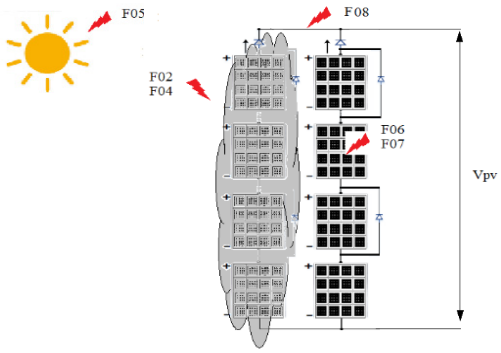

Fig. 5. PV array faults

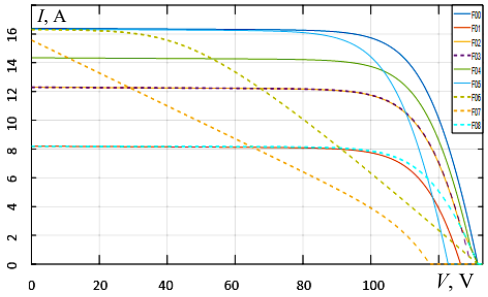

Fig. 6. *I-V* characteristic of PV faults

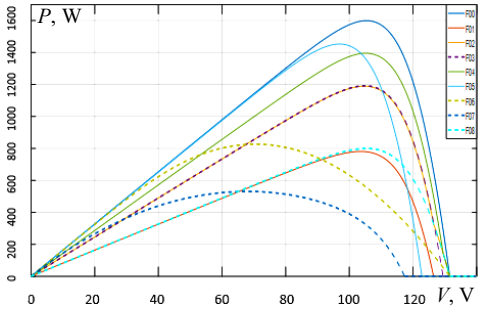

Fig. 7. *P-V* characteristic of PV faults

While linear DC-DC converters maintain DC current flow of their input to the load, switching converters regulate the current flow by chopping the input voltage and controlling the average current flow by varying the ratio cycle. Open circuit faults (F09) refer to disconnection faults in converter circuits. Diagnosis can be done by the inspection of voltage and current indication. In the same way as open-circuit faults, short circuit faults (F10) can also occur in different types of converters. Also, the different types of MPPTs [18] used

to control the converter can also provide system faults such as command fault (F11). The different types of a buck converter related faults and its impact on the output voltage are respectively shown in Fig. 8, Fig. 9.

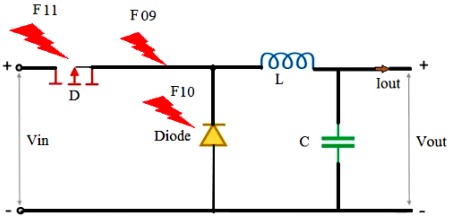

Fig. 8. Buck converter faults

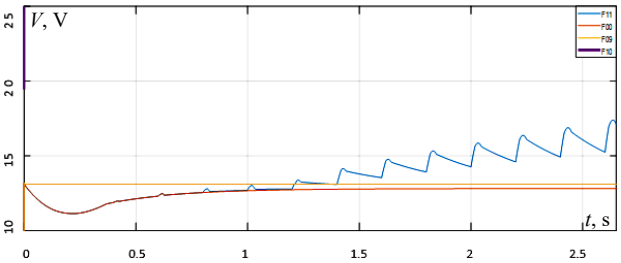

Fig. 9. Impact of faults on buck converter output

Battery faults. When PV production exceeds consumption, the excess of energy is stored in batteries. The stored energy is then used when the consumption rate exceeds production. These batteries are prone to failures such as charging failure (F12) which will be discussed in this article. The effect of batteries charging fault comparing to normal conditions is shown in Fig. 10.

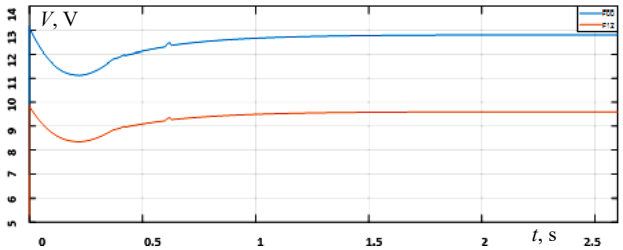

Fig. 10. Battery voltage with charging fault

Fuzzy diagnostic for PV system. The fuzzy logic approach simulates how a person makes decisions to control the problem faster. This logic helps reduce complexity by allowing information to be used in a meaningful way. Its implementation can be software, hardware or a combination of both. In general, the operating procedure of a fuzzy system is accomplished in three steps [19]. The first step is fuzzification, which is the transformation of variables into fuzzy variables which are also called linguistic fuzzy variables. The second step is called fuzzy inference. It is the construction of rules and results based on linguistic variables, using the IF-THEN statement. The last step is the defuzzification phase, which is the transition from a linguistic result to a numerical result.

FLC is one of the modern artificial intelligent techniques used in fault diagnosis in PV systems. The first step is to specify the required input and output values (net data) and their ranges. Next, the net data have to be converted into membership values (fuzzification). After that, the output membership values are synthesized based on extended fuzzy rules (fuzzy inference). Finally, the output membership values are converted into proper output values (defuzzification).

This article proposes a new intelligent technique based on Takagi-Sugeno type fuzzy logic to diagnose and identify faults in the PV generator, buck converter and battery charging failures. This technique is chosen because of its tolerance to imprecise data. It suffices to adjust the inputs/outputs of the system and call the fuzzy rules to improve detection [20]. The diagram block shown in Fig. 11 summarizes the proposed technique.

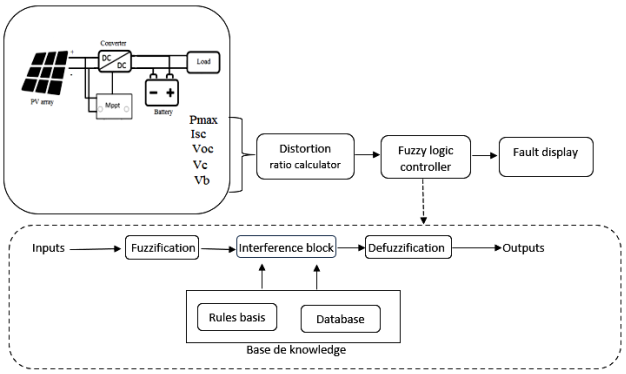

Fig. 11. General structure of a fuzzy system

The fault diagnosis technique used is based on F00 reference values (no fault) and simulated fault values. All cases are discussed and detected. The analysis of the main attributes of the *I-V* and *P-V* characteristics of the PV array plays the main role to accurately locate the faults in which the open-circuit voltage (V_{oc}), short-circuit voltage (I_{sc}) and maximum power ($P_{\max}$) values have been identified to detect different types of faults. In the other hand, converter output voltage (V_c), battery output voltage (V_b) were used to determine the region where the faults occurred in the converter and battery output voltage. Then, the distortion rate I_i of all values is calculated as:

$$I_i = 1 - \frac{val_{cal}}{val_{ref}}; \tag{5}$$

where val_{cal} is the calculated value; val_{ref} is the reference value. The result of distortion rate has to be between 0 and 1 and it is used in FLC.

FLC algorithm is based on the comparison of 5 parameters ($P_{\max}$, V_{oc}, I_{sc}, V_c, V_b) with its reference's values. Reference values of mentioned parameters of each faulty case are illustrated in Table 3.

Table 3

Reference values of FLC for each faulty case

Faults	$P_{\max}$, W	I_{sc}, A	V_{oc}, V	V_c, V	V_b, V
F00	1599	16.4	132	21.65	12.8
F01	780.8	8.199	126.5	26.15	12.8
F02	1189	12.3	132	21.67	12.8
F03	1192	12.3	129	21.66	12.8
F04	1395	14.35	132	21.65	12.8
F05	1453	16.33	123.2	21.9	12.8
F06	826.5	16.32	132	22.63	12.8
F07	530.6	15.58	117	26.15	12.8
F08	799.5	8.199	132	21.65	12.8
F09	1599	16.4	132	12.8	12.8
F10	0.9728	16.4	132	infini	indefined
F11	1599	16.4	132	17.2	12.8
F12	1599	16.4	132	12.8	9.7

Each region of values represents a failure case that could occur in the PV system. In the case of a faulty parameter the algorithm tends to send and alarm. When

increasing the PV installations, it is sufficient to increase the number of sensors so that we can monitor all the signals of the panels. The flowchart of the proposed fuzzy logic algorithm is shown in Fig. 12.

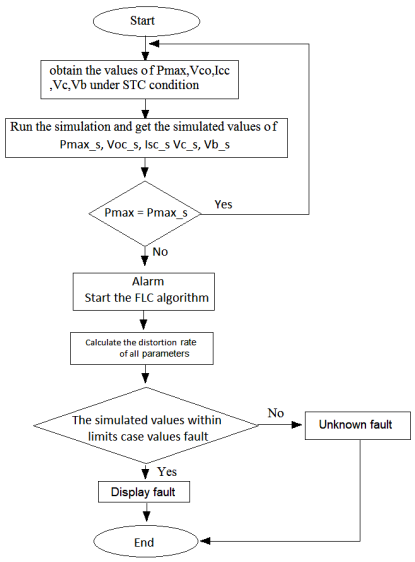

Fig. 12. Flowchart of the proposed FLC fault detection and diagnosis method

Each membership function is calculated on the base of Table 4 values with the calculated I_i values.

Table 4

Distortion rate of all parametric for each faulty case

Fault	Distortion rate of P_{max}	Distortion rate of I_{sc}	Distortion rate of V_{oc}	Distortion rate of V_c	Distortion rate of V_b
F00	0	0	0	0	0
F01	0.511694809	0.500060976	0.041666667	–0.207852194	0
F02	0.256410256	0.25	0	–0.000923788	0
F03	0.254534084	0.25	0.022727273	–0.000461894	0
F04	0.127579737	0.125	0	0	0
F05	0.091307067	0.004268293	0.066666667	–0.011547344	0
F06	0.483114447	0.004878049	0	–0.045265589	0
F07	0.668167605	0.05	0.113636364	–0.207852194	0
F08	0.5	0.500060976	0	0	0
F09	0	0	0	0.408775982	0
F10	0.99939162	0	0	–infini	indefined
F11	0	0	0	0.205542725	0
F12	0	0	0	0.408775982	0.2421875

The membership functions are depended on the mathematical calculation of the examined PV system. The fuzzy logic system is based on If-Then statement. The diagram of the proposed FLC for fault detection is illustrated in Fig. 13.

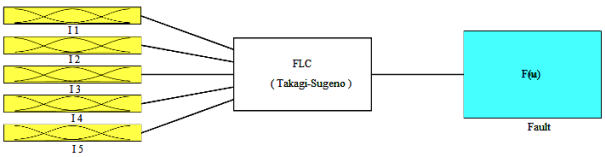

Fig. 13. Five inputs single output Takagi-Sugeno FLC proposed system

If distortion rate of P_{max} is less than 0.3, then we consider it as small.

If distortion rate of P_{max} is greater than 0.6, then we consider it as big.

If distortion rate of P_{max} is between 0.3 and 0.6, then we consider it as middle.

We now translate this human language to fuzzy logic fuzzification (distortion rate of P_{max}, small) = $\mu_{small}(P_{max})$ fuzzification (distortion rate of P_{max}, middle) = $\mu_{middle}(P_{max})$ fuzzification (distortion rate of P_{max}, big) = $\mu_{big}(P_{max})$.

For example:

If distortion rate of P_{max} = 0.127579737; then fuzzification (distortion rate of P_{max}, small) = $\mu_{small}(P_{max}) = 1$ fuzzification (distortion rate of P_{max}, middle) = $\mu_{middle}(P_{max}) = 0$ fuzzification (distortion rate of P_{max}, big) = $\mu_{big}(P_{max}) = 0$.

If distortion rate of P_{max} = 0.668167605; then fuzzification (distortion rate of P_{max}, small) = $\mu_{small}(P_{max}) = 0$ fuzzification (distortion rate of P_{max}, middle) = $\mu_{middle}(P_{max}) = 0.5$ fuzzification (distortion rate of P_{max}, big) = $\mu_{big}(P_{max}) = 0.5$.

If distortion rate of P_{max} = 0.99939162; then fuzzification (distortion rate of P_{max}, small) = $\mu_{small}(P_{max}) = 0$ fuzzification (distortion rate of P_{max}, middle) = $\mu_{middle}(P_{max}) = 0$ fuzzification (distortion rate of P_{max}, big) = $\mu_{big}(P_{max}) = 1$.

The membership functions in this study are shown in Fig. 14.

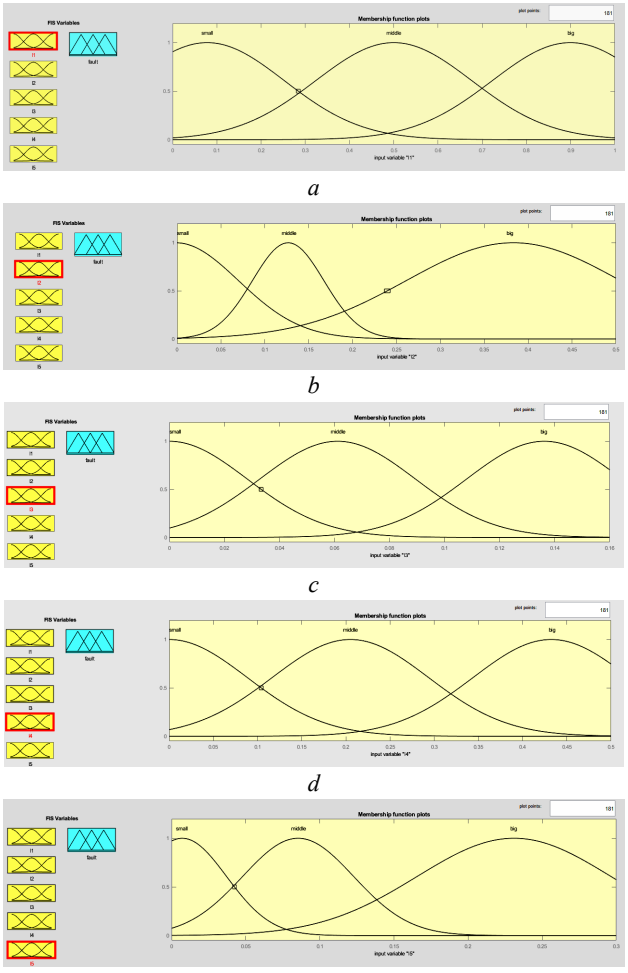

a

b

c

d

e

Fig. 14. Fuzzy logic system inputs:
a) $I_1(P_{max})$; *b*) $I_2(I_{sc})$; *c*) $I_3(V_{oc})$; *d*) $I_4(V_c)$; *e*) $I_5(V_b)$

After the fuzzy variables and membership functions have been defined. The next step is to define If-Then logic inference.

For example, if the distortion rate of P_{max} is middle, the distortion rate of I_{sc} is big, the distortion rate of V_{oc} is middle, the distortion rate of V_c is small and distortion rate of V_b is small, then the fault is F01 (less than 50 % total shading). We translate this logic into fuzzy logic and resume it in Table 5.

Table 5

Fuzzy logic of all parametric for each faulty case

Fault	Distortion rate of				
	P_{max}	I_{sc}	V_{oc}	V_c	V_b
F00	small	small	small	small	small
F01	middle	big	middle	small	small
F02	small	big	small	small	small
F03	small	big	middle	small	small
F04	small	middle	small	small	small
F05	small	small	middle	small	small
F06	middle	small	small	small	small
F07	big	small	big	small	small
F08	middle	big	small	small	small
F09	small	small	small	big	small
F10	big	small	small	small	middle
F11	small	small	small	middle	small
F12	small	small	small	big	big

For a fuzzy system whose end product must be brittle, the step is necessary to turn the ambiguous final aggregate result into a brittle. This step is called defuzzification.

Use the Mean of Maximum (MoM) defuzzification method for pattern recognition applications. This defuzzification method calculates the most logical result. Instead of calculating the average membership scores for the resulting linguistic terms, the MoM defuzzification method determines the typical value for the most correct resulting linguistic term.

Results. The results obtained from the proposed FLC algorithm are respectively illustrated in Fig. 14, 15. Figure 14,*a–e* shows 3 Gaussian membership functions for each input variable, and 12 inferred bases that can be satisfactorily generalize the fault condition product.

Figure 16 shows a set of 12 rules for different faults states. The first 5 columns are the input variables, while the last column represents the output variable from left to right. From the figure we can show that if I_1 = 0.5 W, I_2 = 0.25 A, I_3 = 0.08 V, I_4 = 0.25 V and I_5 = 0.15 V, then the predicted by the fuzzy logic approach PV fault is 0.965, that's to say fault D09 as shown as below:

$$\left.\begin{array}{l} I_1 = 0.5 \text{ W} \rightarrow \mu_{middle}(P_{\max}) = 1; \\ I_2 = 0.25 \text{ A} \rightarrow \mu_{big}(I_{sc}) = 1; \\ I_3 = 0.08 \text{ V} \rightarrow \mu_{middle}(V_{oc}) = 1; \\ I_4 = 0.25 \text{ V} \rightarrow \mu_{middle}(V_c) = 1; \\ I_5 = 0.15 \text{ V} \rightarrow \mu_{big}(V_b) = 1; \end{array}\right\} \text{fault} = 0.965 = \text{D09}.$$

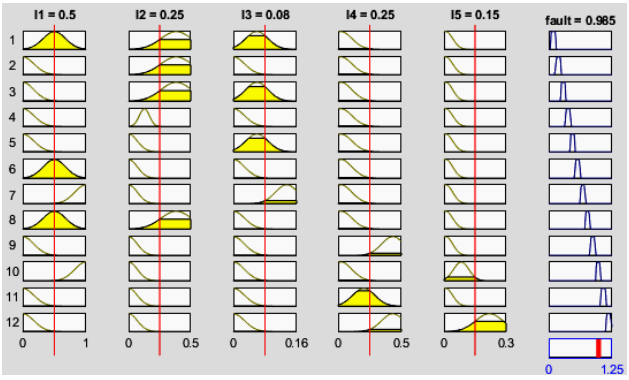

Fig. 15. Rules viewer of fuzzy logic system

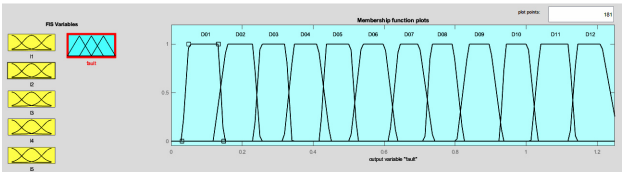

Fig. 16. Fuzzy logic system output

Conclusions. A smart technique based on Takagi-Sugeno type fuzzy logic for the diagnosis and detection of faults in a photovoltaic generator connected with a buck converter and batteries has been proposed. This technique was performed based on 5 parameter values (P_{max}, V_{oc}, I_{sc}, V_c, V_b). These values have been extracted from the analysis of the characteristics of *I-V* and *P-V* curves, the buck converter and the output of the batteries, followed by the extraction of all the output values such as current, voltage and power of the photovoltaic system in cases of healthy and faulty operation. 12 faults have been detected in detail in order to evaluate the performance of the proposed algorithm on the photovoltaic system.

The simulation results obtained have demonstrated the efficiency of the proposed technique. All faults have been accurately identified and classified. This technique is able to identify faults after they are detected in different components of the photovoltaic system. After all, fuzzy logic control was adopted in this study due to its high computational speed and its ability to be applicable in large-scale photovoltaic installations due to its low monitoring cost and economic benefits.

Conflict of interest. The authors declare that they have no conflicts of interest.

REFERENCES

1. Khan S.A., Mahmood T., Awan K.S. A nature based novel maximum power point tracking algorithm for partial shading conditions. *Electrical Engineering & Electromechanics*, 2021, no. 6, pp. 54-63. doi: https://doi.org/10.20998/2074-272X.2021.6.08.

2. Latreche S., Badoud A.E., Khemliche M. Implementation of MPPT Algorithm and Supervision of Shading on Photovoltaic Module. *Engineering, Technology & Applied Science Research*, 2018, vol. 8, no. 6, pp. 3541-3544. doi: https://doi.org/10.48084/etasr.2354.

3. Basnet B., Chun H., Bang J. An Intelligent Fault Detection Model for Fault Detection in Photovoltaic Systems. *Journal of Sensors*, 2020, vol. 2020, art. no. 6960328. doi: https://doi.org/10.1155/2020/6960328.

4. Djalab A.A., Rezaoui M.M., Mazouz L., Teta A., Sabri N. Robust Method for Diagnosis and Detection of Faults in Photovoltaic Systems Using Artificial Neural Networks. *Periodica Polytechnica Electrical Engineering and Computer Science*, 2020, vol. 63, no. 3, pp. 291-302. doi: https://doi.org/10.3311/PPee.14828.

5. Davarifar M., Rabhi A., Hajjaji A.El. Comprehensive Modulation and Classification of Faults and Analysis Their Effect in DC Side of Photovoltaic System. Energy and Power Engineering, 2013, vol. 5, no. 4, pp. 230-236. doi: https://doi.org/10.4236/epe.2013.54B045.

6. Yi Z., Etemadi A.H. Fault Detection for Photovoltaic Systems Based on Multi-Resolution Signal Decomposition and Fuzzy Inference Systems. *IEEE Transactions on Smart Grid*, 2017, vol. 8, no. 3, pp. 1274-1283. doi: https://doi.org/10.1109/TSG.2016.2587244.

7. Livera A., Theristis M., Makrides G., Georghiou G.E. On-line failure diagnosis of grid-connected photovoltaic systems based on fuzzy logic. *2018 IEEE 12th International Conference*

on Compatibility, Power Electronics and Power Engineering (CPE-POWERENG 2018), 2018, pp. 1-6. doi: https://doi.org/10.1109/CPE.2018.8372537.
8. Perveen S., Ashfaq H., Asjad M. Fault Ranking in PV Module based on Artificial Intelligence Technique (AIT). *2019 International Conference on Power Electronics, Control and Automation (ICPECA)*, 2019, pp. 1-6. doi: https://doi.org/10.1109/ICPECA47973.2019.8975619.
9. Dhimish M., Badran G. Photovoltaic Hot-Spots Fault Detection Algorithm Using Fuzzy Systems. *IEEE Transactions on Device and Materials Reliability*, 2019, vol. 19, no. 4, pp. 671-679. doi: https://doi.org/10.1109/TDMR.2019.2944793.
10. Djalab A., Nekbil N., Laouid A.A., Kouzou A., Kadiri K. An Intelligent Technique to Diagnosis and Detection the Partial Shading Based on Fuzyy Logic for PV System. *2020 17th International Multi-Conference on Systems, Signals & Devices (SSD)*, 2020, pp. 235-238. doi: https://doi.org/10.1109/SSD49366.2020.9364109.
11. Boudaraia K., Mahmoudi H., Abbou A. MPPT Design Using Artificial Neural Network and Backstepping Sliding Mode Approach for Photovoltaic System under Various Weather Conditions. *International Journal of Intelligent Engineering and Systems*, 2019, vol. 12, no. 6, pp. 177-186. doi: https://doi.org/10.22266/ijies2019.1231.17.
12. Ali Moussa M., Derrouazin A., Latroch M., Aillerie M. A hybrid renewable energy production system using a smart controller based on fuzzy logic. *Electrical Engineering & Electromechanics*, 2022, no. 3, pp. 46-50. doi: https://doi.org/10.20998/2074-272X.2022.3.07.
13. Madeti S.R., Singh S.N. A comprehensive study on different types of faults and detection techniques for solar photovoltaic system. *Solar Energy*, 2017, vol. 158, pp. 161-185. doi: https://doi.org/10.1016/j.solener.2017.08.069.
14. Nebti K., Lebied R. Fuzzy maximum power point tracking compared to sliding mode technique for photovoltaic systems based on DC-DC boost converter. *Electrical Engineering & Electromechanics*, 2021, no. 1, pp. 67-73. doi: https://doi.org/10.20998/2074-272X.2021.1.10.
15. Mellit A., Tina G.M., Kalogirou S.A. Fault detection and diagnosis methods for photovoltaic systems: A review. *Renewable and Sustainable Energy Reviews*, 2018, vol. 91, pp. 1-17. doi: https://doi.org/10.1016/j.rser.2018.03.062.
16. Latreche S., Khenfer A., Khemliche M. Sensors placement for the faults detection and isolation based on bridge linked configuration of photovoltaic array. *Electrical Engineering & Electromechanics*, 2022, no. 5, pp. 41-46. doi: https://doi.org/10.20998/2074-272X.2022.5.07.
17. Saravanan S., Senthil Kumar R., Prakash A., Chinnadurai T., Tiwari R., Prabaharan N., Chitti Babu B. Photovoltaic array reconfiguration to extract maximum power under partially shaded conditions. *Distributed Energy Resources in Microgrids: Integration, Challenges and Optimization*, 2019, pp. 215-241. doi: https://doi.org/10.1016/B978-0-12-817774-7.00008-9.
18. Abbes H., Abid H., Loukil K., Toumi A., Abid M. Etude comparative de cinq algorithmes de commande MPPT pour un système photovoltaïque. *Revue des Énergies Renouvelables*, 2014, vol. 17, no. 3, pp. 435-445. (Fra).
19. Abdel-Maksoud H., Khater M., Shaaban S. Adaptive Fuzzy Logic PI Control for Switched Reluctance Motor Based on Inductance Model. *International Journal of Intelligent Engineering and Systems*, 2017, vol. 10, no. 4, pp. 41-49. doi: https://doi.org/10.22266/ijies2017.0831.05.
20. Marhraoui S., Abbou A., Cabrane Z., Rhaili S., Hichami N. Fuzzy Logic-Integral Backstepping Control for PV Grid-Connected System with Energy Storage Management. *International Journal of Intelligent Engineering and Systems*, 2020, vol. 13, no. 3, pp. 359-372. doi: https://doi.org/10.22266/ijies2020.0630.33.

Received 18.09.2022
Accepted 19.11.2022
Published 01.07.2023

Younes Lahiouel [1], *PhD Student,*
Samia Latreche[1], *Doctor of Technical Science, Associate Professor,*
Mabrouk Khemliche[1], *Doctor of Technical Science, Professor,*
Lokmane Boulemzaoud [1], *PhD Student,*
[1] Technology Faculty, Electrical Engineering Department, Automation Laboratory of Setif, University of Setif 1, Algeria, e-mail: lahiouelyounes@gmail.com (Corresponding Author); ksamia2002@yahoo.fr; mabroukkhemliche@univ-setif.dz; lokmane@outlook.com

How to cite this article:
Lahiouel Y., Latreche S., Khemliche M., Boulemzaoud L. Photovoltaic fault diagnosis algorithm using fuzzy logic controller based on calculating distortion ratio of values. *Electrical Engineering & Electromechanics*, 2023, no. 4, pp. 40-46. doi: https://doi.org/10.20998/2074-272X.2023.4.06

UDC 621.314 https://doi.org/10.20998/2074-272X.2023.4.07

E. Parimalasundar, R. Jayanthi, K. Suresh, R. Sindhuja

Investigation of efficient multilevel inverter for photovoltaic energy system and electric vehicle applications

Introduction. *This research presents a simple single-phase pulse-width modulated 7-level inverter topology for renewable system which allows home-grid applications with electric vehicle charging. Although multilevel inverters have appealing qualities, their vast range of application is limited by the use of more switches in the traditional arrangement. As a result, a novel symmetrical 7-level inverter is proposed, which has the fewest number of unidirectional switches with gate circuits, providing the lowest switching losses, conduction losses, total harmonic distortion and higher efficiency than conventional topology.* ***The novelty*** *of the proposed work consists of a novel modular inverter structure for photovoltaic energy system and electric vehicle applications with fewer numbers of switches and compact in size.* ***Purpose.*** *The proposed system aims to reduce switch count, overall harmonic distortions, and power loss. There are no passive filters required, and the constituted optimizes power quality by producing distortion-free sinusoidal output voltage as the level count increases while reducing power losses.* ***Methods.*** *The proposed topology is implemented with MATLAB/Simulink, using gating pulses and various pulse-width modulation methodologies. Moreover, the proposed model also has been validated and compared to the hardware system.* ***Results****. Total harmonic distortion, number of power switches, output voltage, current, power losses and number of DC sources are investigated with conventional topology.* ***Practical value.*** *The proposed topology has proven to be extremely beneficial for implementing photovoltaic-based stand-alone multilevel inverter and electric vehicle charging applications.* References 16, table 1, figures 18.

Key words: **conduction loss, multilevel inverter, pulse-width modulation, switching loss, total harmonic distortion.**

Вступ*. У цьому дослідженні представлена топологія простого семирівневого однофазного інвертора з широтно-імпульсною модуляцією для системи з відновлюваними джерелами енергії, яка дозволяє використовувати домашню мережу з зарядкою електромобілів. Хоча багаторівневі інвертори мають привабливі характеристики, широкий спектр їх застосування обмежений використанням більшої кількості перемикачів у традиційній схемі. В результаті запропонований новий симетричний 7-рівневий інвертор, який має найменшу кількість односпрямованих ключів із затворними ланцюгами, забезпечує найменші комутаційні втрати, втрати на провідність, сумарні гармонічні спотворення та вищий ККД, ніж традиційна топологія.* ***Новизна*** *запропонованої роботи полягає у новій модульній структурі інвертора для фотоелектричних енергетичних систем та використання для електромобілів з меншою кількістю перемикачів та компактними розмірами.* ***Мета****. Пропонована система спрямована на зменшення кількості перемикань, загальних гармонічних спотворень та втрат потужності. Пасивні фільтри не потрібні, а складова частина оптимізує якість електроенергії, створюючи синусоїдальну вихідну напругу без спотворень зі збільшенням кількості рівнів при одночасному зниженні втрат потужності.* ***Методи****. Запропонована топологія реалізована за допомогою MATLAB/Simulink з використанням стробуючих імпульсів та різних методологій широтно-імпульсної модуляції. Крім того, запропонована модель також була перевірена та порівняна з апаратною системою.* ***Результати****. Загальні гармонічні спотворення, кількість силових ключів, вихідна напруга, струм, втрати потужності та кількість джерел постійного струму досліджуються за допомогою традиційної топології.* ***Практична цінність****. Запропонована топологія виявилася надзвичайно корисною для реалізації автономних багаторівневих інверторів на основі фотоелектричних систем та застосування для заряджання електромобілів.* Бібл. 16, табл. 1, рис. 18.

Ключові слова: **втрати провідності, багаторівневий інвертор, широтно-імпульсна модуляція, комутаційні втрати, сумарні гармонічні спотворення.**

Introduction. The power grid has experienced energy requirements since the last century due to the growing number of users along with large power companies. Due to the obvious advancements in semiconductor device development, power converter technology is rapidly transforming the way traditional large transformers. So, order to offer clean electricity to users, power converters are frequently employed in renewable energy conversion systems. Switching devices are economical to produce and maintain a competitive advantage because of their minimal costs. Because adding additional switches to an inverter circuit does not considerably increase prices, 2-level traditional converters having large power losses and harmonics content are increasingly becoming substituted by multilevel converters with lower operating frequencies.

Many studies have concentrated on the creation of multilevel inverters (MLIs), including both terms of topologies and control technique. The number of elements used in these sorts of converters is given special consideration. The fewer the elements, the lesser the power dissipation and expenses. Cascaded H-bridge, neutral point, and cascaded H-bridge are some of its most prevalent structures. MLIs with clamped and diode clamped diodes have discovered significant practical demand for high variable speed drives. Additional ripple losses are attributed to presence of clamped diodes and capacitors. Consequently, as compared to cascaded modified MLI, which uses diodes and capacitors, it is a much more complex topology [1-4].

Single-phase MLIs can play an important role in this area, converting the photovoltaic (PV) system's DC voltage into a continuous AC signal accessible by loads as well as the gird significantly fewer harmonic filters and increased performance. The 7-level power conditioning unit inverter has been proposed for this purpose, with appealing features such as low number of switches and the ability to generate multiple voltage ranges at the result [5, 6].

Modified MLI designs based on a decreased number of circuit elements are implemented to tackle the previous shortcomings. In this research, a 7-level pulse-width modulation (PWM) inverter with independent DC input supplies and appropriate circuit combinations for switches and total harmonic distortion (THD) minimization is proposed. Furthermore, it necessitated a greater switching devices and external power supply, resulting in a larger inverter size and expense. In order to reduce the amount of power devices and converter losses, a staircase MLI is proposed [7-9].

This configuration, on the other hand, takes into account something even increasing switching devices. The quantity of external DC sources is decreased due to the absence of voltage multiplication across input split-capacitors. This configuration, on the other hand, can be employed for up to 5 levels of composition without the need for flexible modification. MLI with decreased switches is offered for some further switching minimization, but output voltage generation takes a massive number of discrete DC sources [10, 11].

For low voltage PV panels, a new single-phase MLI inverter featuring wattage capabilities was proposed. It is, therefore, appropriate for low rated power applications and has 2 adapt an appropriate, resulting in increased power losses. For cascade multilevel output-voltage, a small MLI is given employing 2 capacitors within every component and a decrease in number of external power supply. However, for high-power applications, this boosts inverter energy capacity and compact. For energy storage systems, novel MLI topologies for single/3-phase applications with fewer components and a single DC-source are required [12-16].

Inspired by an analysis of relevant literature, this research introduces single-phase 7-level PWM inverter with decreased power number of switches, THD, switching losses, and conduction losses for stand-alone grid-integrated PV systems and electric charging applications. The suggested inverter minimises the needed amount of parts to a competitive level in order to increase efficiency, footprint, and cost. The primary and secondary networks of the intended MLI are separated. The primary circuit is a simple H-bridge inverter that controls output voltage orientation, while the supplementary circuit is a series of switching that generate every output voltage level. The PV fed proposed MLI application in domestic and electric vehicle (EV) charging is shown in Fig. 1.

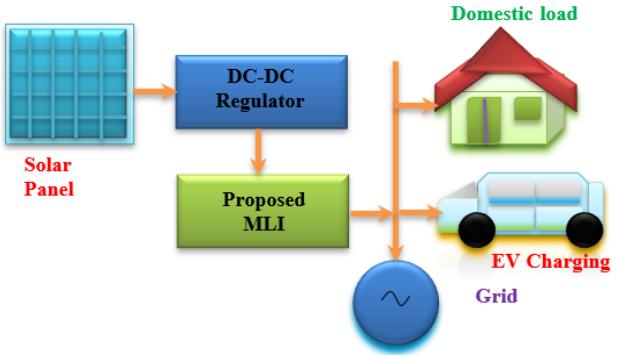

Fig. 1. PV fed proposed MLI application in domestic and EV charging

Proposed topology and modes of operation. In a traditional topology, a cascaded H-bridged MLI has 3 DC sources and 3 H-bridge units, typically having switching devices, for a total of 12 switches: $L = (S+2)/2$, where S is the number of switches and L is the level of output voltage in steps in the configuration. Each bridge produces 3 levels: $+V_{dc}$, $0V_{dc}$, and $0V_{dc}$. Generating stepped 7 level staircase wave patterns by cascading 3 bridges in this manner. In a suggested MLI, 10 number of switching devices and 3 DC sources have been included (Fig. 2).

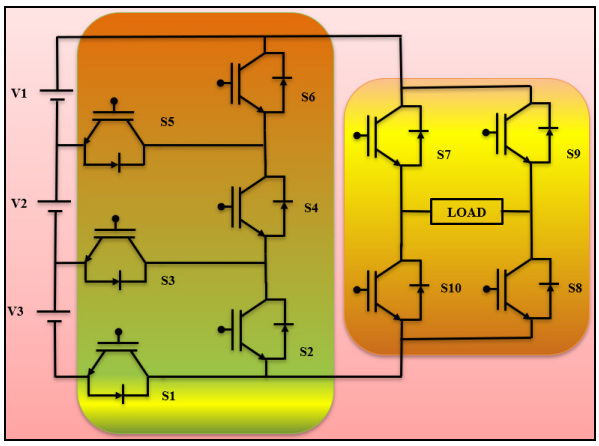

Fig. 2. Proposed topology of MLI

Throughout mode I operation, the output voltage has been determined, which is $+V_{dc}$ (Fig. 3); similarly, during mode II operation, input DC voltages are added by 2 number of DC sources, resulting in an output voltage of $+2V_{dc}$; and finally, a positive third level of voltage has to be estimated, which is $+3V_{dc}$ (Fig. 4, 5). Furthermore, using the equivalent circuits of Fig. 6–8, the negative sequence of output voltage levels of $-V_{dc}$, $-2V_{dc}$ and $-3V_{dc}$ has been determined. Figure 9 shows that the proposed inverter combines a multicarrier PWM technique to verifying 7 levels, 6 different triangular waves, and one reference wave signal to produce switching patterns.

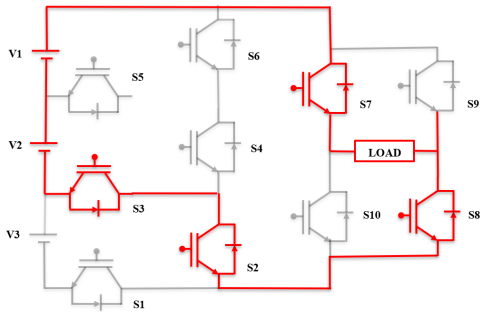

Fig. 3. Mode I operation

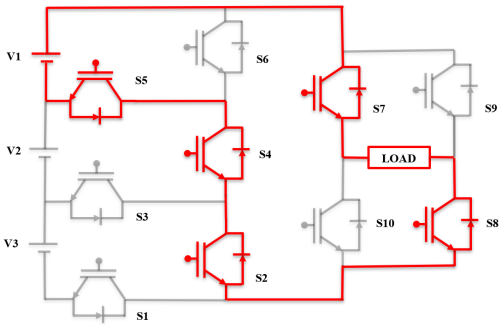

Fig. 4. Mode II operation

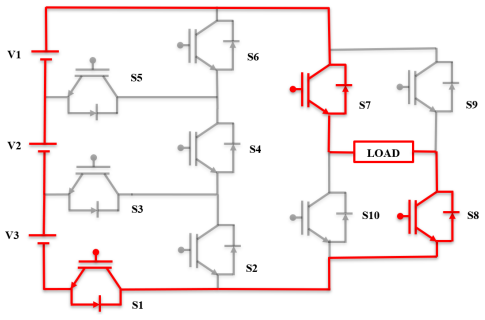

Fig. 5. Mode III operation

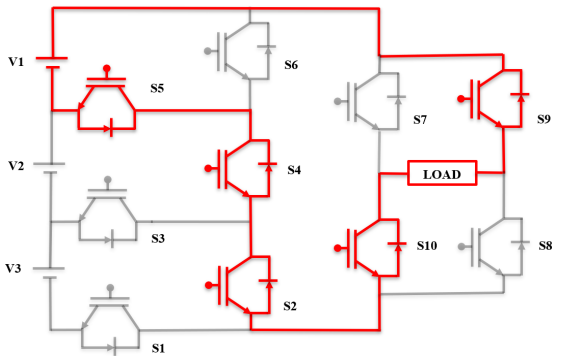

Fig. 6. Mode IV operation

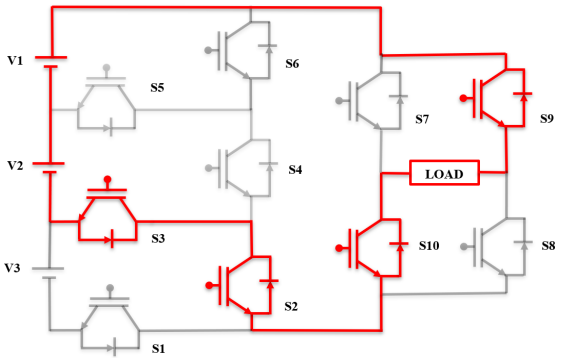

Fig. 7. Mode V operation

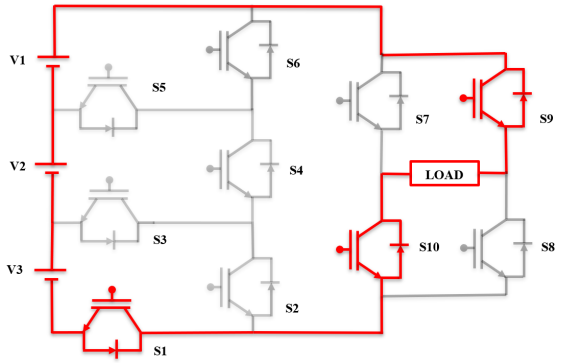

Fig. 8. Mode VI operation

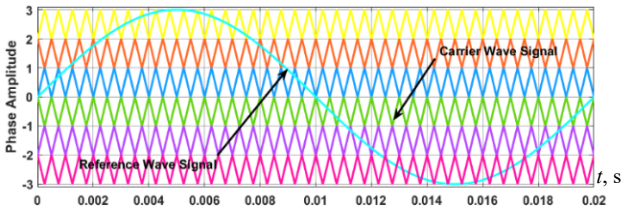

Fig. 9. Sinusoidal PWM for generating switching pulses

Results and discussion. The output voltage and current of the proposed MLI with a resistance of 100 Ω are shown in Fig. 10, 11 respectively. Since output current precedes output voltage, these 2 waveforms are nearly symmetrically maintained. Figure 12 shows the results of a THD investigation of an inverter with resistive load; the THDs collected have a similar pattern due to the unique wave pattern. The output voltage and current of the proposed MLI for resistance values of 100 Ω and 25 mH are shown in Fig. 13, 14. The output current pattern changes due to the inductance feature, hence these 2 waveforms are distinct. Figure 15 shows the results of an inverter's THD assessment under resistance and inductive load.

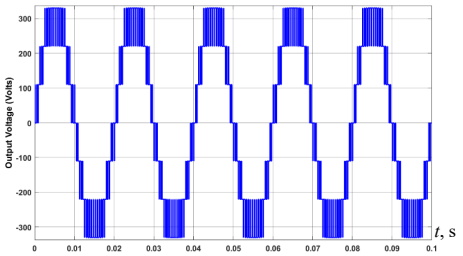

Fig. 10. Output voltage of proposed MLI for resistive load

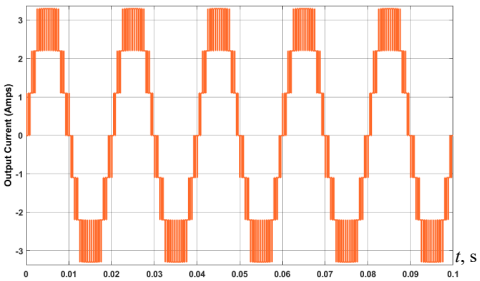

Fig. 11. Output current of proposed MLI for resistive load

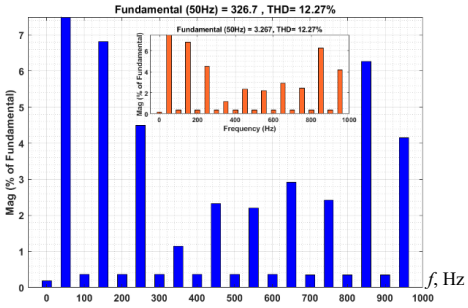

Fig. 12. THD analysis of proposed MLI during resistive load

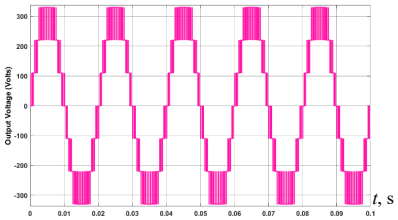

Fig. 13. Output voltage of proposed MLI for *RL* load

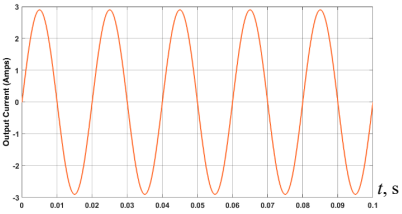

Fig. 14. Output current of proposed MLI for *RL* load

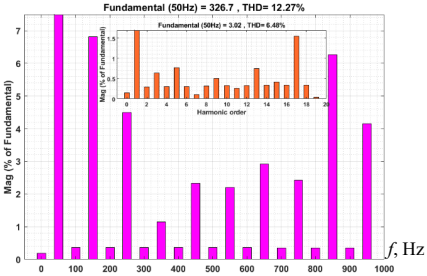

Fig. 15. THD analysis of proposed MLI during *RL* load

Power loss and efficiency. The modulation index of PWM signal is evaluated as:

$$A_m = F_m / F_r \,, \qquad (1)$$

where F_m and F_r are represented as the modulated and reference signals respectively.

Voltage THD of proposed MLI is calculated by (2), in the same manner current harmonics also calculated as:

$$THD = \sqrt{\frac{V_2^2 + V_3^2 + V_4^2 + ... + V_n^2}{V_1}}, \quad (2)$$

where V_1 is the fundamental root mean square (RMS) voltage; V_2, ..., V_n are the RMS voltage of the n^{th} harmonics. In the similar manner current total harmonics also calculated.

The losses in the developed proposed structure are mostly intense on 3 main power losses, specifically losses during switching ($W_{Switching}$) and conduction ($W_{Conduction}$). Then overall power loss (W_{Loss}) of MLI is:

$$W_{Loss} = W_{Switching} + W_{Conduction}. \quad (3)$$

Conduction loss of power semiconductor devices is:

$$W_{Conduction} = \int_0^{T_0/2} \left\{ \begin{array}{l} \left[V_{CE0} + r i_p \sin \omega t\right] \times \\ \times i_p \sin \omega t \left[\frac{1}{2}\left(1 + A_m \sin(\omega t + \varphi)\right)\right] \end{array} \right\} dt,$$

where V_{CE0} is the zero-current collector to emitter voltage; r is the collector to emitter on-state resistance; A_m is the modulation index; i_p is the peak current of IGBT device.

After simplification we have:

$$W_{Conduction} = \frac{1}{2} \left\{ \begin{array}{l} \left(V_{CE0} \frac{i_p}{\pi} + r \frac{i_p^2}{4} \right) + \\ + \left(A_m \cos\varphi \cdot V_{CE0} \cdot \frac{i_p}{8} \right) + \left(\frac{1}{3\pi} r i_p^2 \right) \end{array} \right\}. \quad (4)$$

Switching loss is expressed as the integration of all the turn-on and turn-off switching energies at the switching instants. In the equation, variable switching time is considered and integrated as:

$$W_{Switching} = f_{sw} \frac{1}{T_0} \int_0^{T_0/2} \left(E_{on} + E_{off}\right) \cdot \left(t, i_p\right) dt, \quad (5)$$

where T_0 is the switching time period; f_{sw} is the switching frequency; E_{on} is the on-state voltage drop; E_{off} is the off-state voltage drop.

The efficiency of MLI is calculation as:

$$Efficiency = \frac{P_{Output}}{P_{Output} + W_{Loss}} \cdot 100\%. \quad (6)$$

Experimental setup and validation. A prototype of a symmetric 7-level inverter was examined under various loading conditions as well as dynamic variations in load values by setting the modulation index to value of 1. The MLI configuration consists of 2 DC sources (V_{dc} = 75 V) and 10 IGBT switches which produces 7-level output with the maximum value of 326 V. The other parameters are considered as follows: FGA25N120 IGBT switch, TLP350 driver circuit, R load value is 100 Ω and RL load value of R = 100 Ω, L = 25 mH and the triggering signal for the IGBT switches is produced by the real-time controller dSpace1104 in real time. The carrier switching frequency is applied for the value of 2 kHz. Figure 16 depicts an experimental arrangement of proposed 7-level inverter. The output voltage THD is 16 % and fundamental peak voltage of 326 V for the RL load (R = 100 Ω and L = 240 mH). Figure 17, 18 show the 7-level voltage pattern and current THD is 8 %.

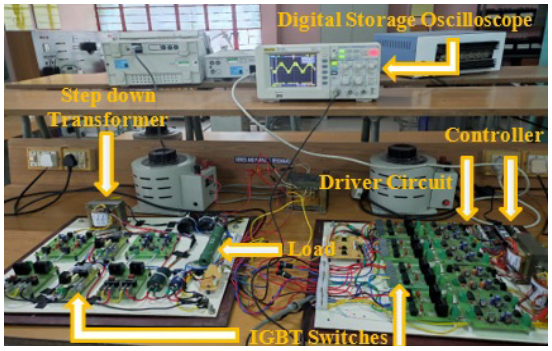

Fig. 16. Experimental setup of proposed MLI

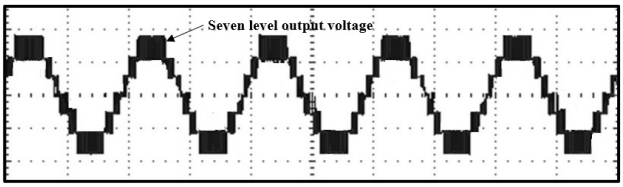

Fig. 17. Output voltage of proposed MLI

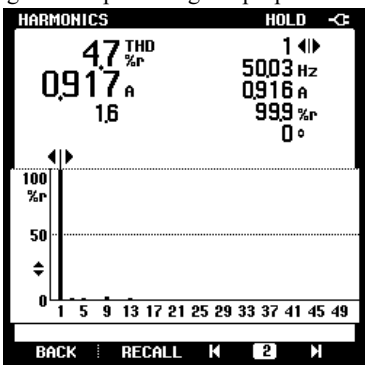

Fig. 18. THD analysis of proposed MLI (current)

While considering AC voltages from same DC source, voltage gain produced from both topologies are same. Proposed converter having the features of more DC link voltage utilization, lower voltage stress and total standing voltage is less. If output power from existing topology THD of voltage and current value obtained as 12.27 % and 8 % during different loads. The designed prototype converter with specification of 325 V is achieved THD value of 8.3 %. Comparison between traditional and proposed converter is given in Table 1.

Table 1

Comparison between traditional and proposed 7-level MLI

Parameters	Conventional topology	Proposed topology
Number of power switches	12	10
Load type	R = 100 Ω	R = 100 Ω
	R = 100 Ω; L = 25 mH	R = 100 Ω; L = 25 mH
Symmetric supply voltage, V	75	75
Number of DC sources	3	3
Modulating frequency f_m, Hz	50	50
Carrier frequency f_c, Hz	2000	2000
Output voltage, (peak value, V)	326.7	326.7
Output current, A	3.26 (R load) 3.04 (RL load)	3.26 (R load) 3.02 (RL load)
Switching losses	0.325	0.121
Conduction losses	48.42	46.75
Power losses	48.86	46.87
Efficiency	94.29	96.25
% THD (voltage)	12.27	12.27
% THD (current)	8.3	6.48

Efficiency and THD values show proposed converter with prototype model is better than traditional converter so efficiency of proposed converter is 96.25 %. Due to less THD 8.3 % than traditional, so proposed converter have more efficiency than traditional converter.

5. Conclusions. Proposed single-phase 7-level inverter is developed with lesser number of switches and it fulfill the needs of the MLI. Proper control signal is applied to the switches in the correct sequence; proposed single-phase 7-level inverter produced 7-level of AC output. Based on the operation of reference and carrier wave signal, power semiconductor switches are controlled in efficient manner. Proposed single-phase 7-level inverter operation is initially developed and investigated in MATLAB/Simulink tool and same to be validated in real-time proto-type hardware. THD values obtained between the ranges 8 % with 3 different loads in hardware level. Efficiency of proposed converter is obtained as 96.25 %. From the comparisons proposed single-phase 7-level inverter is much better than traditional converter in both symmetric and asymmetric topology.

Conflict of interest. The authors declare that they have no conflicts of interest.

REFERENCES

1. Benkahla M., Taleb R., Boudjema Z. A new robust control using adaptive fuzzy sliding mode control for a DFIG supplied by a 19-level inverter with less number of switches. *Electrical Engineering & Electromechanics*, 2018, no. 4, pp. 11-19. doi: https://doi.org/10.20998/2074-272X.2018.4.02.

2. Parimalasundar E., Kumar N.M.G., Geetha P., Suresh K. Performance investigation of modular multilevel inverter topologies for photovoltaic applications with minimal switches. *Electrical Engineering & Electromechanics*, 2022, no. 6, pp. 28-34. doi: https://doi.org/10.20998/2074-272X.2022.6.05.

3. Lingom P.M., Song-Manguelle J., Mon-Nzongo D.L., Flesch R.C.C., Jin T. Analysis and Control of PV Cascaded H-Bridge Multilevel Inverter With Failed Cells and Changing Meteorological Conditions. *IEEE Transactions on Power Electronics*, 2021, vol. 36, no. 2, pp. 1777-1789. doi: https://doi.org/10.1109/TPEL.2020.3009107.

4. Ezhilvannan P., Krishnan S. An Efficient Asymmetric Direct Current (DC) Source Configured Switched Capacitor Multi-level Inverter. *Journal Européen Des Systèmes Automatisés*, 2020, vol. 53, no. 6, pp. 853-859. doi: https://doi.org/10.18280/jesa.530611.

5. Siddique M.D., Mekhilef S., Rawa M., Wahyudie A., Chokaev B., Salamov I. Extended Multilevel Inverter Topology With Reduced Switch Count and Voltage Stress. *IEEE Access*, 2020, vol. 8, pp. 201835-201846. doi: https://doi.org/10.1109/ACCESS.2020.3026616.

6. Saeedian M., Adabi M.E., Hosseini S.M., Adabi J., Pouresmaeil E. A Novel Step-Up Single Source Multilevel Inverter: Topology, Operating Principle, and Modulation. *IEEE Transactions on Power Electronics*, 2019, vol. 34, no. 4, pp. 3269-3282. doi: https://doi.org/10.1109/TPEL.2018.2848359.

7. Sandeep N., Yaragatti U.R. Design and Implementation of a Sensorless Multilevel Inverter With Reduced Part Count. *IEEE Transactions on Power Electronics*, 2017, vol. 32, no. 9, pp. 6677-6683. doi: https://doi.org/10.1109/TPEL.2017.2681739.

8. Suresh K., Parimalasundar E. A Modified Multi Level Inverter With Inverted SPWM Control. *IEEE Canadian Journal of Electrical and Computer Engineering*, 2022, vol. 45, no. 2, pp. 99-104. doi: https://doi.org/10.1109/ICJECE.2022.3150367.

9. Parimalasundar E., Senthil Kumar R., Chandrika V.S., Suresh K. Fault diagnosis in a five-level multilevel inverter using an artificial neural network approach. *Electrical Engineering & Electromechanics*, 2023, no. 1, pp. 31-39. doi: https://doi.org/10.20998/2074-272X.2023.1.05

10. Haji-Esmaeili M.M., Naseri M., Khoun-Jahan H., Abapour M. Fault-Tolerant and Reliable Structure for a Cascaded Quasi-Z-Source DC–DC Converter. *IEEE Transactions on Power Electronics*, 2017, vol. 32, no. 8, pp. 6455-6467. doi: https://doi.org/10.1109/TPEL.2016.2621411.

11. Kiran Kumar G., Parimalasundar E., Elangovan D., Sanjeevikumar P., Lannuzzo F., Holm-Nielsen J.B. Fault Investigation in Cascaded H-Bridge Multilevel Inverter through Fast Fourier Transform and Artificial Neural Network Approach. *Energies*, 2020, vol. 13, no. 6, art. no. 1299. doi: https://doi.org/10.3390/en13061299.

12. Belbachir N., Zellagui M., Settoul S., El-Bayeh C.Z., Bekkouche B. Simultaneous optimal integration of photovoltaic distributed generation and battery energy storage system in active distribution network using chaotic grey wolf optimization. *Electrical Engineering & Electromechanics*, 2021, no. 3, pp. 52-61. doi: https://doi.org/10.20998/2074-272X.2021.3.09.

13. Akkouchi K., Rahmani L., Lebied R. New application of artificial neural network-based direct power control for permanent magnet synchronous generator. *Electrical Engineering & Electromechanics*, 2021, no. 6, pp. 18-24. doi: https://doi.org/10.20998/2074-272X.2021.6.03.

14. Gopal Reddy S., Ganapathy S., Manikandan M. Power quality improvement in distribution system based on dynamic voltage restorer using PI tuned fuzzy logic controller. *Electrical Engineering & Electromechanics*, 2022, no. 1, pp. 44-50. doi: https://doi.org/10.20998/2074-272X.2022.1.06.

15. Praveen Kumar T., Ganapathy S., Manikandan M. Improvement of voltage stability for grid connected solar photovoltaic systems using static synchronous compensator with recurrent neural network. *Electrical Engineering & Electromechanics*, 2022, no. 2, pp. 69-77. doi: https://doi.org/10.20998/2074-272X.2022.2.10.

16. Suresh K., Parimalasundar E. Design and Implementation of Universal Converter Conception et implémentation d'un convertisseur universel. *IEEE Canadian Journal of Electrical and Computer Engineering*, 2022, vol. 45, no. 3, pp. 272-278. doi: https://doi.org/10.1109/ICJECE.2022.3166240.

Received 07.06.2022
Accepted 10.11.2022
Published 01.07.2023

Ezhilvannan Parimalasundar[1], *Associate Professor,*
Ramalingam Jayanthi[2], *Professor,*
Krishnan Suresh[3], *Associate Professor,*
Ramachandran Sindhuja[1], *Assistant Professor,*
[1] Department of Electrical & Electronics Engineering,
Sree Vidyanikethan Engineering College,
Tirupati, AP – 517102, India,
e-mail: parimalasundar.e@vidyanikethan.edu (Corresponding Author);
sindhuja.gct@gmail.com
[2] Department of Electrical and Electronics Engineering,
Karpagam College of Engineering, Coimbatore – 641021, India,
e-mail: jnthramalingam@gmail.com
[3] Department of Electrical and Electronics Engineering,
Christ (Deemed to be University), Bangalore, India,
e-mail: sureshk340@gmail.com

How to cite this article:
Parimalasundar E., Jayanthi R., Suresh K., Sindhuja R. Investigation of efficient multilevel inverter for photovoltaic energy system and electric vehicle applications. *Electrical Engineering & Electromechanics*, 2023, no. 4, pp. 47-51. doi: https://doi.org/10.20998/2074-272X.2023.4.07

UDC 621.314 https://doi.org/10.20998/2074-272X.2023.4.08

M.S. Sujatha, S. Sreelakshmi, E. Parimalasundar, K. Suresh

Mitigation of harmonics for five level multilevel inverter with fuzzy logic controller

Introduction. *The advantages of a high-power quality waveform and a high voltage capability of multilevel inverters have made them increasingly popular in recent years. These inverters reduce harmonic distortion and improve the voltage output. Realistically speaking, as the number of voltage levels increases, so does the quality of the multilevel output-voltage waveform. When it comes to industrial power converters, these inverters are by far the most critical.* ***Novelty.*** *Multilevel cascade inverters can be used to convert multiple direct current sources into one direct current. These inverters have been getting a lot of attention recently for high-power applications. A cascade H-bridge multilevel inverter controller is proposed in this paper. A change in the pulse width of selective pulse width modulation modulates the output of the multilevel cascade inverter.* ***Purpose.*** *The total harmonic distortion can be reduced by using filters on controllers like PI and fuzzy logic controllers.* ***Methods.*** *The proposed topology is implemented with MATLAB/Simulink, using gating pulses and pulse width modulation methodology and fuzzy logic controllers. Moreover, the proposed model also has been validated and compared to the hardware system.* ***Results****. Total harmonic distortion, number of power switches, output voltage and number of DC sources are analyzed with conventional topologies.* ***Practical value.*** *The proposed topology has been very supportive for implementing photovoltaic based multilevel inverter, which is connected to large demand in grid and industry.* References 17, table 4, figures 9.

Key words: **cascade H-bridge multilevel inverters, fuzzy logic controller, selective pulse width modulation technique, total harmonic distortion.**

Вступ*. Переваги форми хвилі високої якості та високої напруги багаторівневих інверторів зробили їх дедалі популярнішими в останні роки. Ці інвертори зменшують гармонійні спотворення та покращують вихідну напругу. Насправді, зі збільшенням кількості рівнів напруги якість багаторівневого сигналу вихідної напруги зростає. Коли доходить до промислових перетворювачів енергії, ці інвертори, безумовно, є найважливішими.* ***Новизна****. Багаторівневі каскадні інвертори можуть використовуватися для перетворення кількох джерел постійного струму на один постійний струм. Останнім часом цим інверторам приділяється велика увага при використанні на великій потужності. У статті пропонується каскадний Н-мостовий багаторівневий інверторний регулятор. Зміна ширини імпульсу селективної широтно-імпульсної модуляції модулює вихідний сигнал каскадного багаторівневого інвертора.* ***Мета****. Загальне гармонічне спотворення можна зменшити, використовуючи фільтри на таких контролерах, як ПІ-контролери та контролери з нечіткою логікою.* ***Методи****. Запропонована топологія реалізована за допомогою MATLAB/Simulink з використанням стробуючих імпульсів та методології широтно-імпульсної модуляції, а також контролерів з нечіткою логікою. Крім того, запропонована модель також була перевірена та порівняна з апаратною системою.* ***Результати****. Загальне гармонічне спотворення, кількість силових ключів, вихідна напруга та кількість джерел постійного струму аналізуються за допомогою звичайних топологій.* ***Практична цінність****. Запропонована топологія дуже допомогла реалізувати багаторівневий інвертор на основі фотоелектричних систем, що пов'язано з великим попитом у мережах та промисловості.* Бібл. 17, табл. 4, рис. 9.

Ключові слова: **каскадні Н-мостові багаторівневі інвертори, нечіткий логічний регулятор, селективна широтно-імпульсна модуляція, повне гармонічне спотворення.**

1. Introduction. Modern power generation, transmission, distribution, and use systems all rely on the conversion of DC to AC power. Variable-frequency drives, static var compensators, uninterruptible power supply, induction heating, high-voltage DC power transmission, electric cars, air conditioning, and flexible AC transmission systems are just a few examples of their numerous applications. The demand for equipment with a megawatt rating has increased recently. The mega-watt class AC drives require a medium voltage network connecter. The above-stated reasons provide scope for multilevel inverters (MLIs) as a solution to work with higher voltage levels. A power semiconductor switch cannot be directly connected to a high voltage network due to the increase in demand for high-voltage, high-power inverters. As a result, MLIs have been developed and are now available for purchase. If the voltage sources are increased, a sinusoidal-like waveform appears at the output. The quality of the output waveform is improved while the total harmonic distortion (THD) is reduced by MLIs. Another advantage of MLIs is that they have lower switching losses [1-3]. In industrial drive systems, power electronic inverters are frequently employed. The limitations on voltage and current it is necessary to use series and parallel connections for power semiconductor devices. With the propensity to synthesize waveforms with a better harmonic spectrum and higher voltages, MLIs have gained more importance in literature in recent times [4]. Industrial applications include AC-power supplies, static var compensators, and drives. Diode-clamped (neutral-clamped), capacitor-clamped (flying capacitors), and cascaded inverters with separate DC sources have been suggested for MLIs [5-8]. Space vector modulation and selective pulse width modulation are other modulation and control strategies for MLIs. Using a MLI has the following advantages: These devices are excellent when it comes to distortion and voltage drop. Very little distortion occurs in the input current. The motor bearings aren't put under as much strain when the common voltage is reduced. The elimination of common voltages and a reduction in switching frequency are both possible with advanced modulation techniques. Two types of DC voltage source inverters exist for inverters that have DC voltage sources of the same or different amplitudes. Asymmetric cascaded MLIs provide more output levels than symmetric cascaded MLIs with a comparable number of power electronic devices because their DC voltage sources have different amplitudes. It is thus smaller and less expensive to use asymmetric MLIs [9-12].

Because the DC voltage sources are of equal magnitude, symmetric inverters require a large number of switches, insulated gate bipolar transistors (IGBTs), power diodes, and driver circuits. This problem can only be solved using an asymmetric MLI [13-16]. The disadvantages of

bidirectional power switches will be magnified from a voltage perspective. Two IGBTs with dual anti-parallel diodes and a single driver circuit must be used to make a bidirectional switch. An anti-parallel diode is required for a unidirectional switch. It makes no difference which way a power switch is plugged in, whether it is a one-way or a two-way switch. Many asymmetric cascaded MLI has been proposed to increase the number of output levels. As a primary drawback, these inverters require high-voltage DC power sources. Using a new basic unit, a greater number of output levels can be generated with fewer electronic devices. A cascaded MLI is put forward by connecting several of the basic units that have been proposed. An H-bridge will be added to the inverter's output because only positive and negative voltages can be generated. One of the proposed cascaded MLIs has been developed. H-bridge and diode-clamped MLIs, as well as flying capacitances and fly inductors, are examples of topologies that can reduce harmonic distortion. Clamping diode inverter voltage control becomes more difficult as the number of levels increases. Voltage regulation of a flying capacitor MLI becomes increasingly challenging with more levels. The cascade multilevel [17] is the most efficient of the three topologies. Cascade MLIs have better performance, but they still fall short of IEEE standards as the data presented above shows. Using cascading MLIs and controllers, as well as the selective pulse width modulation technique, reduces THD. Different carrier waveforms are designed for the third and fifth levels of the project to reduce THD. Proportional and integral (PI) and fuzzy logic controllers (FLC) with filters is being used to further reduce harmonic distortion below IEEE standards of 5 %. Using these controllers, it is possible to reduce THD more effectively.

2. System configuration for existing PI, PI with filter controller. Figure 1 illustrates about schematic diagram for MLI with closed loop control scheme. Figure 2 depicts the simulation diagram of five level MLI with single phase system. An example of a five-level MLI's output can be seen in Figure 3. In order to get five level, six carrier signals and one reference signal has been used. Three levels are positive and the other three levels are negative and the left-over level is zero level and these voltages are obtained using different switching paths.

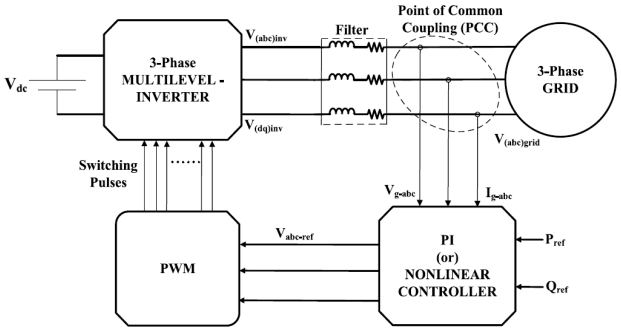

Fig. 1. Schematic diagram for MLI with closed loop control scheme

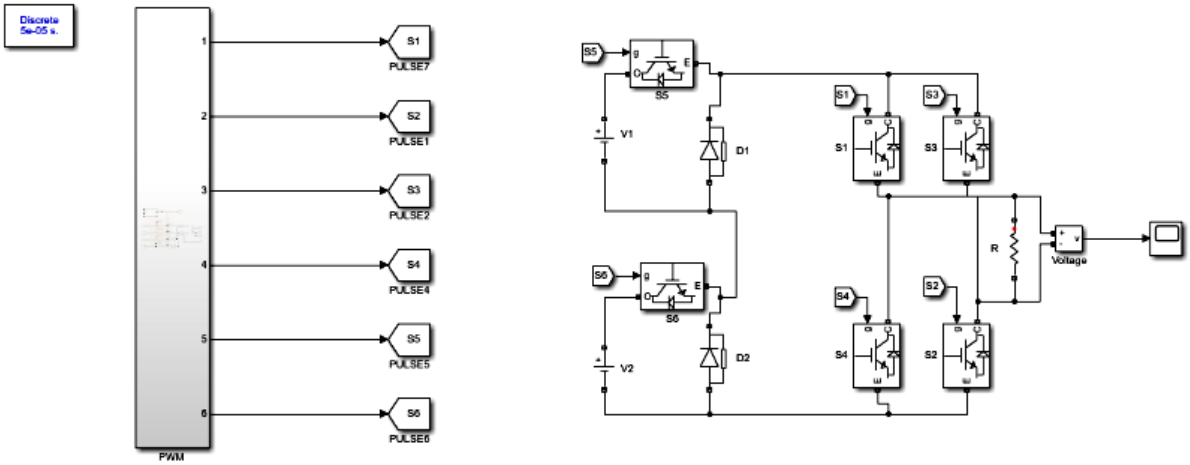

Fig. 2. Simulation diagram of five level MLI with single phase system

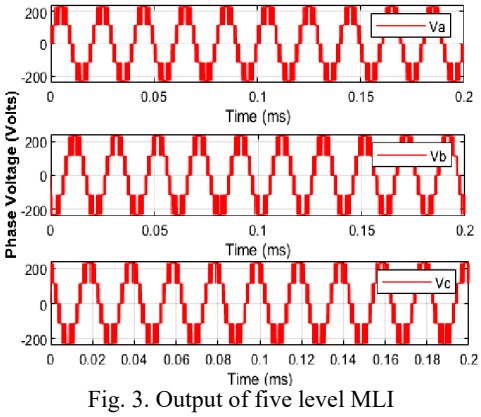

Fig. 3. Output of five level MLI

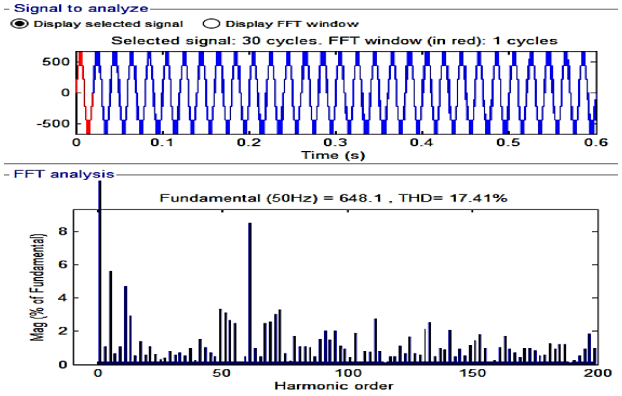

Fig. 4. Distortion level of five level MLI with PI controller

3. Results and discussion. Figure 4 shows MLI fast Fourier transform (FFT) analysis of five-level. Here the THD level obtained is 17.41 % for MLI with PI controller for a fundamental frequency of 50 Hz.

Figure 5 shows MLI FFT analysis of five-level. Here the THD level obtained is 6.56 % for MLI with PI controller and filter for a fundamental frequency of 50Hz.

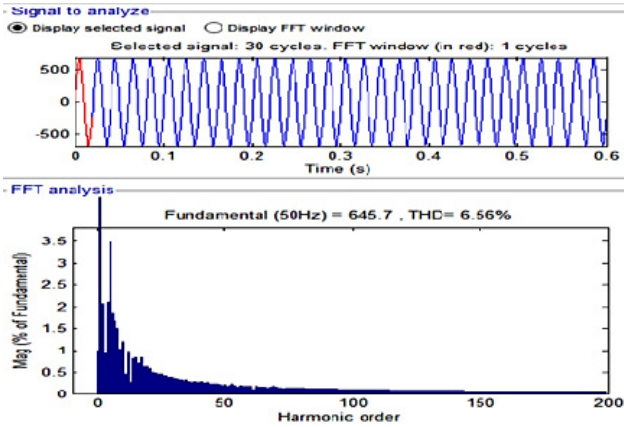

Fig. 5. Distortion level of PI controller with filter

Fuzzy logic is the application of conditional or rule-based logic to the transformation of an input space into an output space. It is a «fuzzy set» if the boundaries are ambiguous. The inclusion of elements with just a sliver of membership is permitted. It deals with difficult-to-define ideas (e.g., fast runner, hot weather). Being only a part of it is fine. Fudged set membership values range from 0 to 1, indicating the extent to which an object is a member of the collection. Input values in a fuzzy set range can be used to determine the appropriate membership value for a given membership functions. This type of multivalve logic is also known as a rule or condition because of the terminology used to describe the inputs and outputs of the multivalve devices. The schematic diagram of FLC is illustrated in Fig. 6.

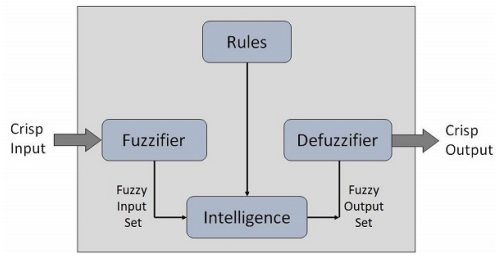

Fig. 6. Schematic diagram of FLC

Weightings, which can be added to each rule in the rule base, can be used to control how much a rule affects the output values. A rule's importance, reliability, or consistency can be assigned a numerical weighting. Depending on the results of other rules, these rule weightings can be either static or dynamic [14].

FLC in the fuzzy logic system is in charge of choosing the fuzzy rules that control it. Error (E) and error change (dE), which are inputs to the FLC system, are shown in the following diagram. Distortion level of FLC and filter for three membership functions is shown in Fig. 7.

Figure 7 shows FFT analysis of five level MLI with FLC and filter for three membership functions. Here the THD level obtained is 5.2 %

MATLAB/Simulink model of FLC is shown in Fig. 8. FLC'S output is determined solely by the rules set by the designer, and the controller does the rest. By doing this we can obtain desired output fuzzy logic system rules as follows in Table 1, where Ne – Negative, Ze – Zero, Pe – Positive, Me – Medium, Sm – Small, B – Big, as a result of implementing these fuzzy rules in a FLC, errors are smaller if the change in error is also smaller, so the output is smaller. If the value of error is negative (Ne) and the error change is zero, a medium result would be achieved which is illustrated in Table 2.

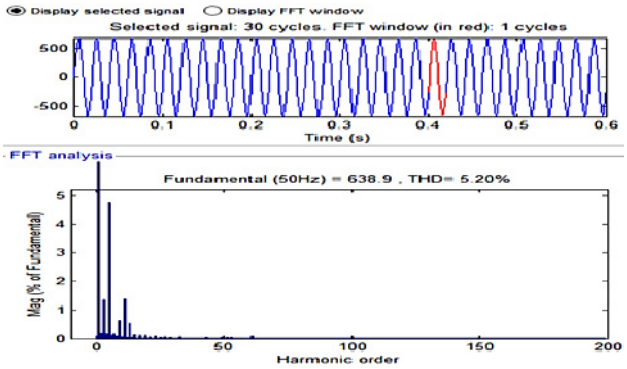

Fig. 7. Distortion level of FLC and filter for three membership functions

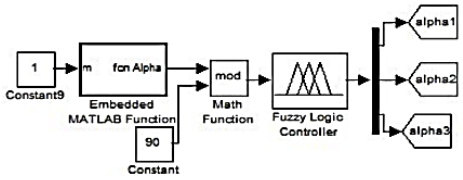

Fig. 8. MATLAB/Simulink of FLC

Table 1

Rules for three membership functions

		Change in error (dE=$\Delta E(t)$)		
		Ne	Ze	Pe
Error $E(t)$	Ne	Sm	Me	Sm
	Ze	Me	B	Me
	Pe	Sm	Me	Sm

Table 2

Rules for five membership functions

	Change in error				
Error	NeB	NeS	ZO	PeS	PeB
NeB	PeB	PeB	PeB	PeS	ZO
NeS	PeB	PeS	ZO	ZO	NeS
ZO	PeS	ZO	ZO	ZO	NeS
PeS	PeS	ZO	ZO	NeS	NeB
PeB	ZO	NeS	NeB	NeB	NeB

If the value of error is negative and the error change is positive, the output will be small. System could get a medium output with no errors or errors changing in a negative direction. A large output would be possible with no errors or errors changing in a negative direction. If the error value is zero and the change in error value is positive, the output would be medium. If the error value is positive and the error change value is negative, the output will be small. It is considered medium-sized when the error rate is more than 10 %.

Figure 9 shows FFT analysis of five level MLI with FLC and filter for five membership functions. Here the THD level obtained is 3.43 %.

Table 3 shows the comparison of THD levels for different controllers. The results show that FLC gives the better response when compared with conventional PI controller. Although the distortion is reduced to some extent when PI controller is used, but it is greatly reduced when Fuzzy controller is used. Table 4 gives the specifications of various parameters used in the simulation.

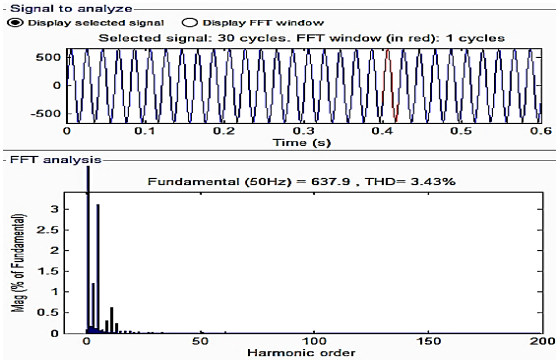

Fig. 9. Distortion level of FLC and filter for five membership functions

Table 3

Comparison of THD for different controllers

Controllers	THD, %
PI controller	17.74
PI controller with filter	6.56
Fuzzy controller with filter for three membership functions	5.20
Fuzzy controller with filter for five membership functions	3.43

Table 4

Specifications of parameters used in the Simulink models

Parameters	Specifications
Resistive load R, Ω	1
Inductive load L, mH	1
Frequency of carrier signal, Hz	1000
Frequency of reference signal, Hz	50
Proportional constant k_p	1.6
Integral constant k_i	36

4. Conclusions. The quality of multilayer output voltage waveform improves as the quantity of levels in a multilevel inverter grows. Different carrier waveforms are used for three and five levels of the project to reduce harmonic distortion. We used a multilevel inverter with a selective pulse width modulation technique to reduce harmonic distortion in five levels. PI and fuzzy logic controllers with filters have been added to the five-level multilevel inverter to further reduce the IEEE standards.

We can achieve from simulation results that total harmonic distortion levels can be reduced to less than 5 % by using the proposed PI and FLC controllers with filters on multilevel inverters. Due to these advantages in both technical and economic terms, it can be concluded that the proposed methodology will be beneficial in a wide range of industrial settings.

In the future, a sinusoidal pulse width modulation will be generated using other techniques for high-frequency applications by means of modified carriers using a fuzzy controller in order to reduce distortion as well as to improve the voltage. Then this proposed selective pulse width modulation will be applied to all types of inverters like voltage source and current source inverters. Previously only five level operations were done using the pulse width modulation technique. So, in the future, more than five-level will be achieved with other controllers. The verification of this inverter for lesser total harmonic distortion and higher frequencies can be done as a part of future work.

Conflict of interest. The authors declare that they have no conflicts of interest.

REFERENCES

1. Khoun-Jahan H. Switched Capacitor Based Cascaded Half-Bridge Multilevel Inverter With Voltage Boosting Feature. *CPSS Transactions on Power Electronics and Applications*, 2021, vol. 6, no. 1, pp. 63-73. doi: https://doi.org/10.24295/CPSSTPEA.2021.00006.

2. Grandi G., Loncarski J., Dordevic O. Analysis and Comparison of Peak-to-Peak Current Ripple in Two-Level and Multilevel PWM Inverters. *IEEE Transactions on Industrial Electronics*, 2015, vol. 62, no. 5, pp. 2721-2730. doi: https://doi.org/10.1109/TIE.2014.2363624.

3. Lingom P.M., Song-Manguelle J., Mon-Nzongo D.L., Flesch R.C.C., Jin T. Analysis and Control of PV Cascaded H-Bridge Multilevel Inverter With Failed Cells and Changing Meteorological Conditions. *IEEE Transactions on Power Electronics*, 2021, vol. 36, no. 2, pp. 1777-1789. doi: https://doi.org/10.1109/TPEL.2020.3009107.

4. Ezhilvannan P., Krishnan S. An Efficient Asymmetric Direct Current (DC) Source Configured Switched Capacitor Multi-level Inverter. *Journal Européen Des Systèmes Automatisés*, 2020, vol. 53, no. 6, pp. 853-859. doi: https://doi.org/10.18280/jesa.530611.

5. Siddique M.D., Mekhilef S., Rawa M., Wahyudie A., Chokaev B., Salamov I. Extended Multilevel Inverter Topology With Reduced Switch Count and Voltage Stress. *IEEE Access*, 2020, vol. 8, pp. 201835-201846. doi: https://doi.org/10.1109/ACCESS.2020.3026616.

6. Saeedian M., Adabi M.E., Hosseini S.M., Adabi J., Pouresmaeil E. A Novel Step-Up Single Source Multilevel Inverter: Topology, Operating Principle, and Modulation. *IEEE Transactions on Power Electronics*, 2019, vol. 34, no. 4, pp. 3269-3282. doi: https://doi.org/10.1109/TPEL.2018.2848359.

7. Sandeep N., Yaragatti U.R. Design and Implementation of a Sensorless Multilevel Inverter With Reduced Part Count. *IEEE Transactions on Power Electronics*, 2017, vol. 32, no. 9, pp. 6677-6683. doi: https://doi.org/10.1109/TPEL.2017.2681739.

8. Suresh K., Parimalasundar E. A Modified Multi Level Inverter With Inverted SPWM Control. *IEEE Canadian Journal of Electrical and Computer Engineering*, 2022, vol. 45, no. 2, pp. 99-104. doi: https://doi.org/10.1109/ICJECE.2022.3150367.

9. Jahan H.K., Panahandeh F., Abapour M., Tohidi S. Reconfigurable Multilevel Inverter With Fault-Tolerant Ability. *IEEE Transactions on Power Electronics*, 2018, vol. 33, no. 9, pp. 7880-7893. doi: https://doi.org/10.1109/TPEL.2017.2773611.

10. Haji-Esmaeili M.M., Naseri M., Khoun-Jahan H., Abapour M. Fault-Tolerant and Reliable Structure for a Cascaded Quasi-Z-Source DC–DC Converter. *IEEE Transactions on Power Electronics*, 2017, vol. 32, no. 8, pp. 6455-6467. doi: https://doi.org/10.1109/TPEL.2016.2621411.

11. Kiran Kumar G., Parimalasundar E., Elangovan D., Sanjeevikumar P., Lannuzzo F., Holm-Nielsen J.B. Fault Investigation in Cascaded H-Bridge Multilevel Inverter through Fast Fourier Transform and Artificial Neural Network Approach. *Energies*, 2020, vol. 13, no. 6, art. no. 1299. doi: https://doi.org/10.3390/en13061299.

12. Belbachir N., Zellagui M., Settoul S., El-Bayeh C.Z., Bekkouche B. Simultaneous optimal integration of photovoltaic distributed generation and battery energy storage system in active distribution network using chaotic grey wolf optimization. *Electrical Engineering & Electromechanics*, 2021, no. 3, pp. 52-61. doi: https://doi.org/10.20998/2074-272X.2021.3.09.

13. Yang S., Sun X., Ma M., Zhang X., Chang L. Fault Detection and Identification Scheme for Dual-Inverter Fed OEWIM Drive. *IEEE Transactions on Industrial Electronics*, 2020, vol. 67, no. 7, pp. 6112-6123. doi: https://doi.org/10.1109/TIE.2019.2922924.

14. Anand A., Akhil Vinayak B., Raj N., Jagadanand G., George S. A Generalized Switch Fault Diagnosis for Cascaded H-Bridge Multilevel Inverters Using Mean Voltage Prediction. *IEEE Transactions on Industry Applications*, 2020, vol. 56, no. 2, pp. 1563-1574. doi: https://doi.org/10.1109/TIA.2019.2959540.

15. Ouni S., Narimani M., Zargari N.R., Cheng Z. A New Fault-Tolerant Control Method for Cascaded H-Bridge Multilevel

Inverter to Increase Maximum Output Voltage. *2019 IEEE Energy Conversion Congress and Exposition (ECCE)*, 2019, pp. 2922-2927. doi: https://doi.org/10.1109/ECCE.2019.8912282.
16. Parimalasundar E., Kumar N.M.G., Geetha P., Suresh K. Performance investigation of modular multilevel inverter topologies for photovoltaic applications with minimal switches. *Electrical Engineering & Electromechanics*, 2022, no. 6, 28-34. doi: https://doi.org/10.20998/2074-272X.2022.6.05.
17. Parimalasundar E., Senthil Kumar R., Chandrika V.S., Suresh K. Fault diagnosis in a five-level multilevel inverter using an artificial neural network approach. *Electrical Engineering & Electromechanics*, 2023, no. 1, pp. 31-39. doi: https://doi.org/10.20998/2074-272X.2023.1.05.

Received 09.09.2022
Accepted 13.11.2022
Published 01.07.2023

M.S. Sujatha [1], *PhD, Professor,*
S. Sreelakshmi [2], *M. Tech., Research Scholar,*
E. Parimalasundar[1], *Associate Professor,*
K. Suresh[3], *Associate Professor,*
[1] Department of Electrical & Electronics Engineering,
Sree Vidyanikethan Engineering College,
Tirupati, AP – 517102, India,
e-mail: sujatha.machineni@gmail.com (Corresponding Author);
parimalpsg@gmail.com
[2] Department of Electrical and Electronics Engineering,
Jawaharlal Nehru Technological University Anantapur,
Anantapuramu, AP – 517102, India,
e-mail: shreelakshmi.yadav@gmail.com
[3] Department of Electrical and Electronics Engineering,
Christ (Deemed to be University), Bangalore, India,
e-mail: sureshk340@gmail.com

How to cite this article:
Sujatha M.S., Sreelakshmi S., Parimalasundar E., Suresh K. Mitigation of harmonics for five level multilevel inverter with fuzzy logic controller. *Electrical Engineering & Electromechanics*, 2023, no. 4, pp. 52-56. doi: https://doi.org/10.20998/2074-272X.2023.4.08

UDC 621.319 https://doi.org/10.20998/2074-272X.2023.4.09

G.V. Bezprozvannych, O.A. Pushkar

Ensuring standardized parameters for the transmission of digital signals by twisted pairs at the technological stage of manufacturing cables for industrial operating technologies

Introduction. *In production control and control systems, buildings use many simple devices - sensors to detect light, heat, movement, smoke, humidity and pressure, mechanisms for activation and control of switches, closing devices, alarm, etc. - «operating technologies» (OT). Different communication protocols and field tire technologies, such as Modbus for conditioning systems, Bacnet for access control and Lonworks for lighting, have been traditionally used and used for their connection. Network fragmentation leads to the need to use gateways to transform protocols when creating a single automation system, which complicates the implementation of complex control systems for any object. At the same time, information networks are unified, but the Ethernet protocol used in them for operating technologies for various reasons (technological, cost) has not been widespread. Due to its high bandwidth compared to existing field tire networks, industrial Ethernet is significantly capable of increasing flexibility in the implementation of additional functions in OT. Modern industrial Ethernet networks are based on non-shielded and shielded twisted pair category 5e cables. The presence of additional metal screens in the structure of twisted pair causes the increase in electrical resistance of conductors due to the effect of closeness, the electrical capacity, and the ratio of attenuation in the range of transmission of broadband signals.* ***Purpose.*** *Substantiation of the range of settings of technological equipment to ensure standardized values of the extinction coefficient and immunity based on the analysis of the results of measurements in a wide frequency range of electrical parameters of shielded and unshielded cables for industrial operating technologies.* ***Methodology.*** *Experimental studies have been performed for statistically averaged electrical parameters of the transmission of pairs for 10 and 85 samples of 305 m long and shielded cables of category 5e, respectively. It is determined that in the frequency range from 1 to 10 MHz, unshielded cables have less values of the attenuation coefficient. In the range of more than 30 MHz, the shielded cables have smaller values of the attenuation due to the influence of the alumopolymer tape screen. It is established that the coefficient of paired correlation between asymmetries of resistance and capacity of twisted pairs is 0,9735 - for unshielded and 0,9257 - for shielded cables. The impact has been proven to a greater extent asymmetry of resistance the pairs on the increasing noise immunity of cables. The influence noise interference on the deviation of the diameter and electrical capacity of the isolated conductor from the nominal values in the stochastic technological process is analyzed. The strategy of technological process settings to ensure the attenuation and the noise immunity in the high-frequency range is substantiated.* ***Practical value.*** *Multiplicative interference, caused by random changes in the stochastic technological process, can lead to a deviation of diameter 2 times from the nominal value at level of probability at 50 %. The equipment settings of the technological equipment must guarantee the coefficient of variation capacity of the insulated conductor at 0.3 % for high level of noise immunity.* References 36, figures 10.

Key words: **industrial Ethernet, twisted pair, ratio of attenuation, noise immunity, ohmic and capacitive asymmetry, stochastic technological process, additive and multiplicative interference, coefficient of variation**.

Сучасні мережі промислового Ethernet засновані на витих парах неекранованих та екранованих кабелів категорії 5е. Впровадження однопарного Ethernet стикається з проблемою забезпечення передачі цифрових сигналів на відстань до 1000 м зі швидкістю до 1 ГБіт/с. Виконано експериментальні дослідження статистично усереднених електричних параметрів передачі витих пар для 10 і 85 вибірок бухт довжиною 305 м неекранованих та екранованих кабелів категорії 5е відповідно. Визначено, що у діапазоні частоти від 1 до 10 МГц неекрановані кабелі мають менші значення коефіцієнту згасання. У діапазоні більше 30 МГц екрановані кабелі мають менші значення коефіцієнту згасання, що обумовлено впливом алюмополімерного екрану. Встановлено, що коефіцієнт парної кореляції між омічною та ємнісною асиметріями витих пар дорівнює 0,9735 – для неекранованого та 0,9257 – для екранованого кабелів. Доведено вплив у більшій мірі омічної асиметрії витих пар на завадостійкість кабелів. Проаналізовано вплив адитивної та мультиплікативної завад на відхилення діаметру та ємності ізольованого провідника від номінальних значень у стохастичному технологічному процесі. Обґрунтовано діапазони налаштувань технологічного процесу для забезпечення нормованих значень коефіцієнту згасання та завадостійкості витих пар у високочастотному діапазоні. Бібл. 36, рис. 10.

Ключові слова: **промисловий Ethernet, вита пара, коефіцієнт згасання, завадостійкість, омічна та ємнісна асиметрії, стохастичний технологічний процес, адитивна та мультиплікативна завади, коефіцієнт варіації.**

Introduction. Many simple devices are used in control and management systems in production and buildings – sensors for detecting light, heat, movement, smoke, humidity and pressure, mechanisms for activating and controlling switches, locking devices, alarms, etc. The used controls, sensors, systems and devices are called Operational Technology (OT). Different communication protocols and fieldbus technologies have traditionally been used to connect them, such as Modbus for air conditioning [1-3], BACnet for access control [1-3] and LonWorks for lighting [1-3]. Network fragmentation leads to the need to use gateways to convert protocols when creating a single automation system, which makes it difficult to implement complex control systems for any objects. At the same time, information networks are unified, but the Ethernet protocol used in them, for operational technologies has not been widely used for various reasons (technological, cost) [4]. Due to its high bandwidth compared to existing fieldbus networks, Ethernet is able to significantly increase flexibility in the implementation of additional functions in OT.

Single-pair Ethernet (SPE) standards [5-10] became the solution to the implementation of the information protocol in OT.

Single-pair Ethernet is the latest technology to meet these new requirements, as it allows data to be transmitted over Ethernet using only one twisted pair, with signal transfer rates from 10 Mbit/s to 1 Gbit/s [10, 11]. For example, for comparison: Fast Ethernet with a signal

transmission speed of 100 Mbit/s requires two, and Gigabit Ethernet requires four twisted pairs [12]. The advantage of single-pair Ethernet is also the ability to simultaneously supply power to end devices using Power over Data Line (PoDL) technology. With a transmission distance of up to 1000 m, single-pair Ethernet becomes a particularly interesting solution for use in the field of automation of any processes, including in the power industry [5, 6].

For example, single-pair Ethernet is already being implemented in new generations of cars instead of CAN and other buses [7-9]. In the future, control, communication and security functions will work in a unified way using Ethernet. This is a basic requirement for managing full network connectivity or autonomous transport in the future.

Single-pair Ethernet is also suitable for use in industrial automation. Single-pair cable connections are quick to install, save space, are inexpensive and easy to operate. Equipping simple sensors, cameras and similar devices with Ethernet interfaces makes SPE the driving force of integrated industry and the Industrial Internet of Things (IIoT) (Fig. 1) [5, 6]. In general, by 2025, the global market for Internet of Things technologies will be estimated at 6.2 trillion USD, of which 4.8 trillion USD will fall on the spheres of health care (2.5 trillion USD) and production (2.3 trillion USD), as the largest market segments [6]. To a greater extent, the growth will come from the connection between machines in production, processing industry, and the field of health care. The field level becomes intelligent, which simplifies and accelerates configuration, initialization and programming thanks to the use of cables based on a single twisted pair [6].

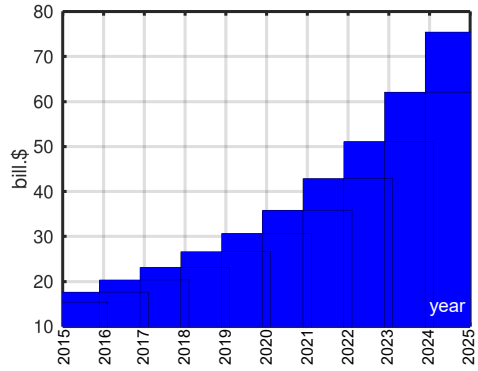

Fig. 1. Growth dynamics of the global Internet of Things market [5]

The cable, as an infrastructural foundation, is a direct transmission line. Depending on the required transmission rate and line length, two standard types of twisted pair are currently available for SPE.

For networks with signal transmission rate 10 Mbit/s for a distance of up to 1000 m, the cable design is regulated by the following Standards: IEC 61156-13 – SPE data transmission cable with bandwidth of up to 20 MHz for stationary installation [10] (a 10Base-T1L cable with a transmission distance of 1000 m in some cases is capable replace more expensive optical cables [12-15]); IEC 61156-14 – SPE data transmission cable with bandwidth up to 20 MHz for flexible installation [10].

Thanks to SPE technology, in which new data coding and scrambling technologies are applied, industrial and technological networks get better characteristics in terms of synchronization of devices connected to the communication line, the level of electromagnetic interference emitted to neighboring pairs is reduced, and higher data protection which are transmitted is ensured (Fig. 2).

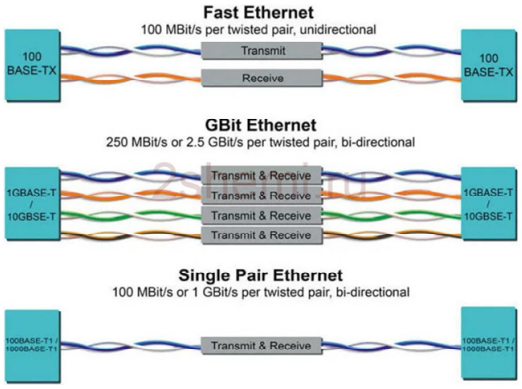

Fig. 2. Implementation of industrial Ethernet technology based on a cable of 4 twisted pairs of category 5e (upper two figures) and SPE (lower figure): when transmitting signals at rate 100 Mbit/s two pairs are used for reception and transmission, two ones – reserve; when transmitting signals at rate of 1 Gbit/s and more – four pairs for simultaneous reception and transmission with a complicated interface [6]

For a network with a signal transfer rate 1 Gbit/s for a distance of up to 40 m, the cable design is determined by the following Standards: IEC 61156-11 – SPE data transmission cable with bandwidth of up to 600 MHz for stationary installation [10]; IEC 61156-12 – SPE data transmission cable with bandwidth up to 600 MHz for flexible installation [10].

In comparison with traditional industrial cables of category 5e with four pairs for transmitting signals over a distance of 100 m at rate of up to 1 Gbit/s (Fig. 2), when implementing the technology of a single-pair cable based on a twisted pair, a reduction in the diameter and weight of the cable is observed, provided that standardized electrical transmission parameters in the frequency range up to 600 MHz: attenuation coefficient, impedance, reflection loss, and resistance to external electromagnetic interference, which determines the shielded design of the twisted pair [6, 13].

The goal of the paper is to substantiate the range of technological equipment settings to ensure standardized values of the attenuation coefficient and noise immunity based on the analysis of the results of measurements in a wide frequency range of electrical parameters of shielded and non-shielded cables for industrial operating technologies.

Review of publications and problem definition. The presence of additional metal shields in the design of a twisted pair leads to an increase in the electrical resistance of the conductors due to the effect of proximity and, to a greater extent, the electrical working capacity, and, in general, the attenuation coefficient, that is, the range of transmission of broadband signals with an increased level of cable immunity [6, 16-24].

Numerical calculation of the 2D model, under the condition that the partial capacity of each of the insulated conductors and the capacity of the shield to the ground of the twisted pair remain constant over the length, shows that the maximum surface energy density in the shielded cable is 1.62 times greater than in the non-shielded cable, and is mainly concentrated in insulation [25]. The simulation results are consistent with the experimental data on the efficiency of the foil-shielded and/or braided twisted pair compared to the non-shielded one in the frequency range up to 170 MHz [25, 26].

Based on the comparison of the capacity of non-shielded and shielded twisted pairs of category 5e, it was proved that the working capacity of shielded cables has increased values [27, 28]. The authors established that variations in the thickness of the insulation, i.e., the working capacity, have a greater influence on the attenuation coefficient compared to the active resistance, provided that the diameters of the conductors of the twisted shielded pair are the same [27]. Recommendations are given for increasing the insulation thickness of cable conductors to ensure the working capacity of twisted shielded pairs in the range of standardized values [25, 26].

It was shown in [29] that an increase in the insulation thickness by 50 % relative to the radius of the conductor leads to a decrease in the capacity of the insulated conductor by 20 %. Such a constructive solution leads to an increase in the mass and dimensional indicators of the twisted pair as a whole. The authors substantiated the methodology of the synthesis of design and technological solutions, including the effectiveness of the use of foam insulation, for regulating the capacity of the twisted pair of cables of industrial networks at the technological stage of the production of an insulated conductor.

Thus, the implementation of modern industrial Ethernet faces the problem of reaching a compromise between shielding and the effect of the shield on the working capacity to reduce the attenuation coefficient while ensuring the transmission of signals in a wide frequency band by shielded twisted pairs [30].

Experimental studies of the effect of the shield on the attenuation coefficient and interference resistance of twisted pairs. The attenuation coefficient α (dB/m) is the frequency-dependent parameter and depends on the active resistance R (the sum of the resistances of the forward and reverse conductors) and the inductance L, the working capacity C, the active conductivity of the insulation G (the electrophysical properties of the insulation – the tangent of the dielectric loss angle tgδ) of a twisted pair twisted with the appropriate step h to increase immunity [31]:

$$\alpha = 8{,}69 \cdot \left(\frac{R}{2} \cdot \sqrt{\frac{C}{L}} + \frac{G}{2} \cdot \sqrt{\frac{L}{C}} \right) = \\ = 8{,}69 \cdot \sqrt{C} \cdot \left(\frac{R}{2} \cdot \sqrt{\frac{1}{L}} + \frac{\omega \cdot \mathrm{tg}\delta}{2} \cdot \sqrt{L} \right). \quad (1)$$

Industrial Ethernet cables are usually made of copper wire with diameter of 24 AWG (0.511 mm) [32] and insulation based on a cable composition with high dielectric properties [33], including polyethylene [31].

The results of the presented electrical parameters of the transmission of twisted pairs are averaged for 10 and 85 samples of 305 m long hanks of each non-shielded and shielded (in general, aluminum polyethylene foil shield) category 5e cables, respectively.

Figure 3 shows the correlation dependence between the working capacity C of twisted pairs of non-shielded $C_1$and shielded C_2 samples of 4-pair cables of category 5e: shielded cables have higher values of working capacity under the condition of the same insulation thickness. Here, the DC resistances of direct R_a and reverse R_b conductors of shielded cables *2* (Fig. 4) also have larger values compared to non-shielded ones *1* (Fig. 4). And, as a result, larger values of the attenuation coefficient α are observed in shielded structures (Fig. 5).

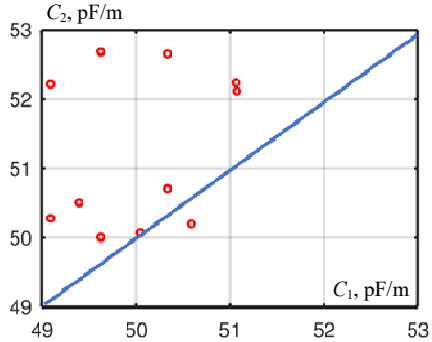

Fig. 3. The effect of the shield on the working capacity of non-shielded and shielded category 5e cables

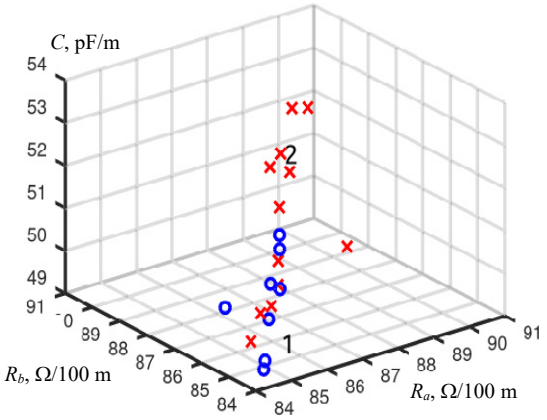

Fig. 4. Correlation dependence between the resistance of conductors and the working capacity of twisted pairs of samples of non-shielded (1) and shielded (2) cables

It turns out (Fig. 5) that the attenuation coefficient of non-shielded cables has smaller values only in the frequency range from 1 MHz to 10 MHz (compare Fig. 5,*a*,*b* and Fig. 6,*a*,*b*).

Shielded cable conductors have higher resistance values for the same diameters and diameter tolerances. This is due to the proximity effect of the shield, which leads to an increase in resistance even to DC.

Increased values of resistance and capacity of shielded network cable pairs lead to higher values of attenuation coefficient. However, this is true only for the frequency range for which the depth of the skin layer (Δ) is less than the thickness (h) of the shield. In the frequency range for which the skin layer and the shield thickness are of the same order, the attenuation coefficient

of shielded cable pairs is equal to α of non-shielded cables (Fig. 4). For the given data, the effect of the shield on the attenuation coefficient begins to appear for frequency of more than 30 MHz: the shielded cable has lower values of the attenuation coefficient (Fig. 5,*b*). For the frequency from 10 MHz to 30 MHz, the values of attenuation coefficients of non-shielded and shielded cables practically do not differ.

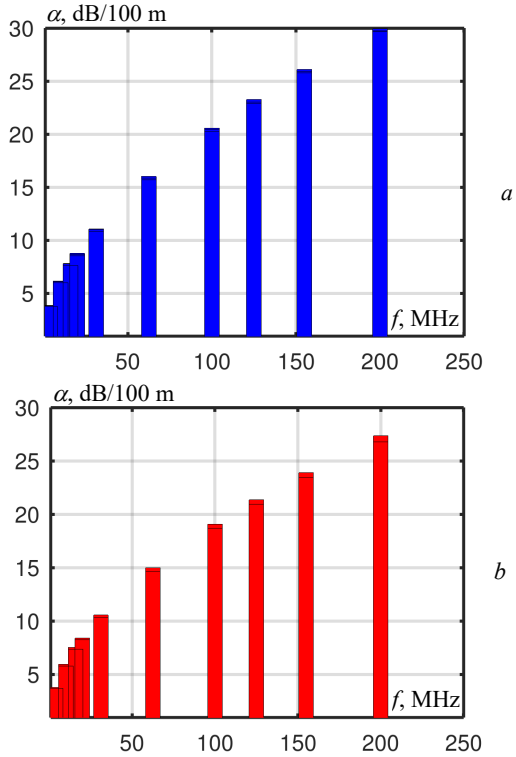

Fig. 5. Histograms of the frequency distribution of the attenuation coefficient of non-shielded (*a*) and shielded (*b*) cables with twisted pairs of category 5e

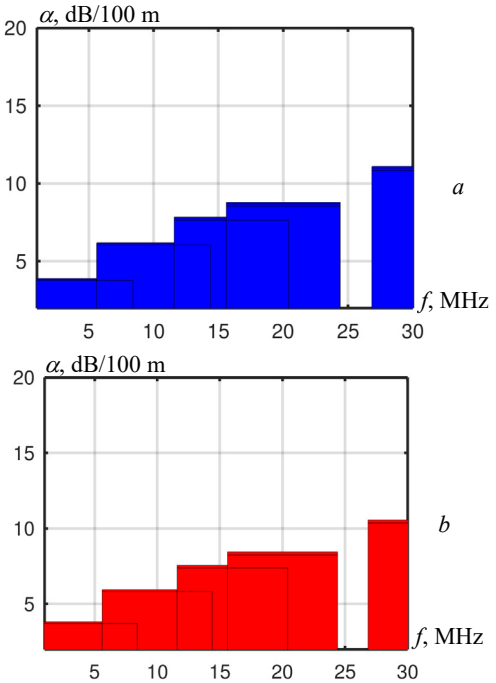

Fig. 6. Attenuation coefficient of non-shielded (*a*) and shielded (*b*) cables in the frequency spectrum from 1 to 30 MHz

External shields, which are placed on the cores from 4 pairs lengthwise, are made of a thin polymer film metallized with aluminum (aluminum polyethylene). A copper drainage conductor with silly with diameter of 0.5 mm is included in the film shield. It ensures the electrical continuity of the shield in case of accidental rupture of the metal foil shield during cable laying, installation and operation. Such a shield provides reliable shielding from the magnetic component of electromagnetic interference. This interference manifests itself in the high frequency range. It is possible to use an additional shield in the form of braiding. It provides protection of cable pairs from electrical interference that occurs in the low frequency range. The use of double-layer shields ensures reliable shielding in the entire operating frequency range of the network cable.

The frequency dependencies of transient attenuation at the near end (*NEXT*) of non-shielded and shielded cables are consistent with the results of the frequency dependence of the attenuation coefficient (Fig. 7):

$$NEXT = 20\lg\left|\pi\left(h_i/h_j+1\right)/\gamma_i h_i\left[1+k\left(h_i/h_j+1\right)/\left(h_i/h_j-1\right)\right]\right|, \quad (2)$$

where h_i, h_j are the twisting steps; γ_i is the propagation coefficient of electromagnetic waves in twisted pair i with a smaller twisting step h_i, which is determined ($\gamma = \alpha + j\beta$) by electrical parameters at the corresponding circular frequency ω $|\gamma| = \sqrt[4]{\left(R^2+\omega^2\cdot L^2\right)\cdot\left(G^2+\omega^2\cdot C^2\right)}$ – module, 1/m; b is the phase coefficient, rad/m); $k = 0.2 – 0.8$ is the coefficient that depends on the cable design and the location of the interacting circuits.

Electromagnetic coupling and influence parameters are determined by the mutual arrangement of pair conductors in the cable, the twisting step, the degree of structural homogeneity, and the quality of the insulation materials [34-36]. Here, the electrical component of the electromagnetic influence is related to the change along the length of the thickness and dielectric permeability of the insulation, the mutual location of the pairs in the cable. Magnetic one – to the change in the diameter of the conductors of the pair along the length of the cable, deviations in the diameters of the forward and reverse conductors (ohmic asymmetry), fluctuations in the twisting step of pairs of conductors along the length, unequal distance between the pairs.

The ratio between the electric and magnetic components of electromagnetic coupling is determined by the operating frequency range of the cable. In the low frequency range (up to 10 kHz), the electrical component of electromagnetic influence prevails. This effect is significant only between closely spaced pairs. For frequency of more than 100 kHz, the influence is caused by both electric and magnetic components, to reduce which different twisting steps of twisted pairs in the cable are used. In a twisted cable, the transient attenuation of pairs will be different due to ohmic and capacitive asymmetries. Twisting pairs with different coordinated steps leads to the fact that the working capacities and resistances of the loops of twisted pairs differ from each other. Capacitive asymmetry arises – the difference in the working capacity of twisted pairs and ohmic one arises –

the difference in the resistances of loops R_s of twisted pairs with different twisting steps and different diameters:

$$\Delta C = \left(C_i - C_j\right) / \left(C_i + C_j\right); \quad (3)$$

$$\Delta R = \left(R_{si} - R_{sj}\right) \cdot \left(R_{si} + R_{sj}\right), \quad (4)$$

where $R_s = R_a + R_b$ is the resistance of the pair loop, which is equal to the sum of the resistances of the direct R_a and the reverse R_b conductors.

The resistances R_a and R_b are also different from each other. The difference between them is that the ohmic asymmetry within the pair is caused only by the different diameters of the conductors.

It was established (Fig. 4) that a positive correlation is characteristic for the direct and reverse conductors of twisted pairs of non-shielded and shielded network cables. Only in this case, the normalized value of the ohmic asymmetry of no more than 1 % of the loop resistance is ensured, which guarantees the protection of the cable from external and internal (between pairs) interferences.

Figure 7 shows the lines of the transient attenuation level for frequency of 10 MHz as a function of ohmic and capacitive asymmetry of twisted pairs of non-shielded (Fig. 7,*a*) and shielded (Fig. 7,*b*) cables, respectively. Figure 8 – for the frequency of 20 (*a*), 62.5 (*b*) and 100 (*c*) MHz of non-shielded (*1*) and shielded (*2*) samples, respectively.

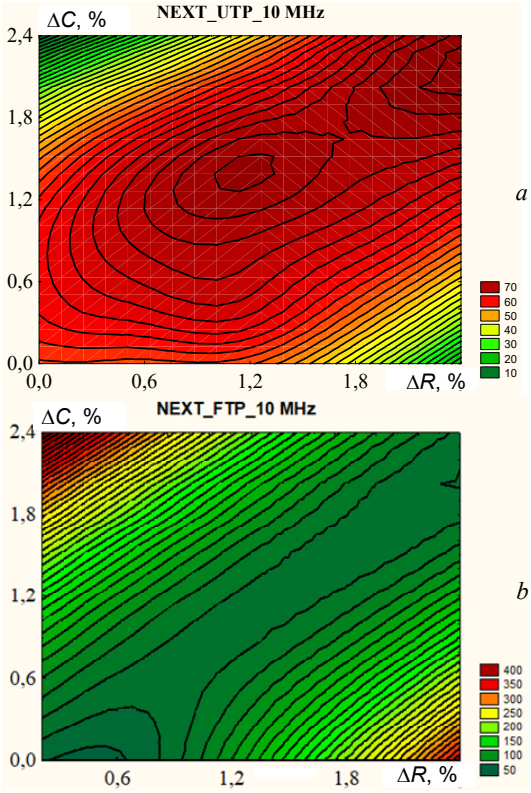

Fig. 7. Transient attenuation at the near end for frequency of 10 MHz depending on ohmic and capacitive asymmetries of twisted pairs of non-shielded (*a*) and shielded (*b*) cables

The use of a shield leads to a smaller spread and an increase in transient attenuation in shielded cable designs (compare curves *1* and *2* in Fig. 8).

The results of experimental studies prove that there is a significant positive correlation between ohmic and capacitive asymmetries. So, the pair correlation coefficient is: **0.9735** – for a non-shielded cable; **0.9257** – for shielded cable. The value of the pairwise correlation coefficient between asymmetry and near-end transient attenuation varies for different hanks (cable length in each hank is 305 m) (as an example, selectively, see below).

For non-shielded cable:

- between ohmic asymmetry and NEXT: **0.6683** – for the first; **0.9058** – for the second; **0.7871** – for the third; **0.4990** – for the fourth;
- between capacitive asymmetry and NEXT: **0.6683** – for the first; **0.7256** – for the second; **0.5567** – for the third; **0.2689** – for the fourth.

For shielded cable:

- between ohmic asymmetry and NEXT: **0.9257**;
- between capacitive asymmetry and NEXT: **0.5868**.

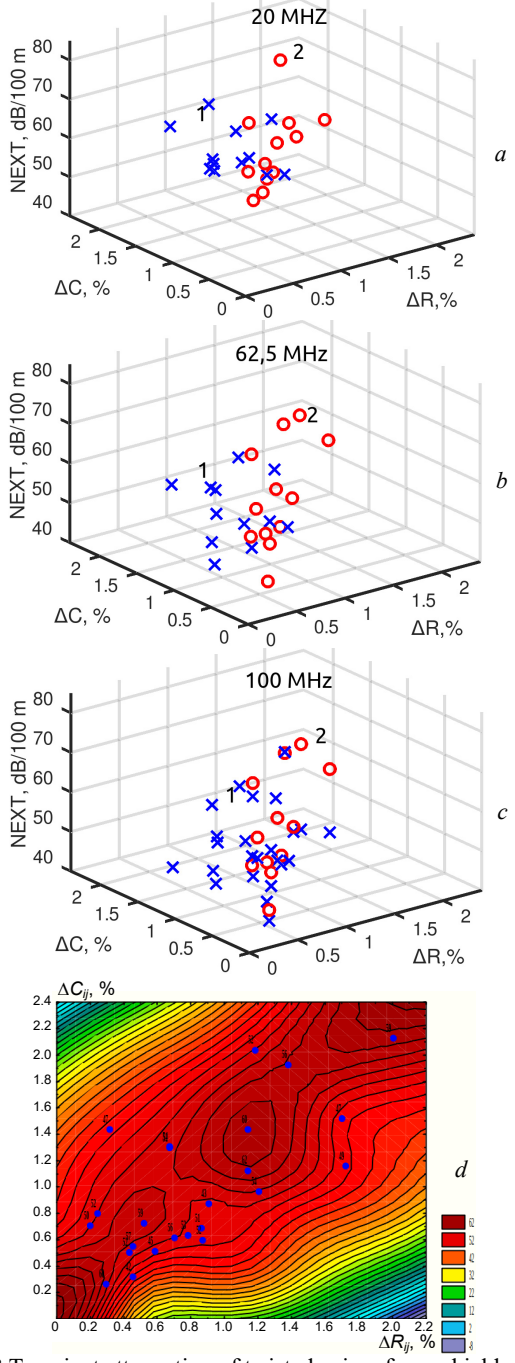

Fig. 8 Transient attenuation of twisted pairs of non-shielded and shielded cables (*a-c*) and non-shielded cable for frequency 100 MHz (*d*)

Thus, the guarantee of the transmission parameters (attenuation coefficient and interference immunity) is determined by the technological process settings to ensure the geometric parameters and homogeneity, first of all, of the twisted pair conductors.

Ranges of technological equipment settings in the manufacture of twisted pairs with standardized transmission parameters. Cables are manufactured on technological equipment that can be affected by random disturbing influences. The cable is a long-dimension product that is made «per pass», in connection with which its geometric parameters have non-constant length values, that is, they are irregular.

This leads to a change in the electrical parameters of the transmission, which requires the introduction of a system of automatic control of the manufacturing process, first of all, the diameter of the conductor to reduce the dispersion of this parameter.

The stochastic model of the technological process takes into account the additive (4) (Fig. 9,*a*,*b*, curves *1* and *2*) and multiplicative (5) (Fig. 9,*a*,*b*, curve *3*) characteristics of the change in the diameter d of the conductor from the nominal d_n (radius r_n)) values in the process of applying insulation

$$d = d_n \cdot \tilde{e}\ ; \qquad (4)$$

$$d = d_n \cdot (1 + \tilde{e}), \qquad (5)$$

where $\tilde{e}$ is the random number with a normal distribution law.

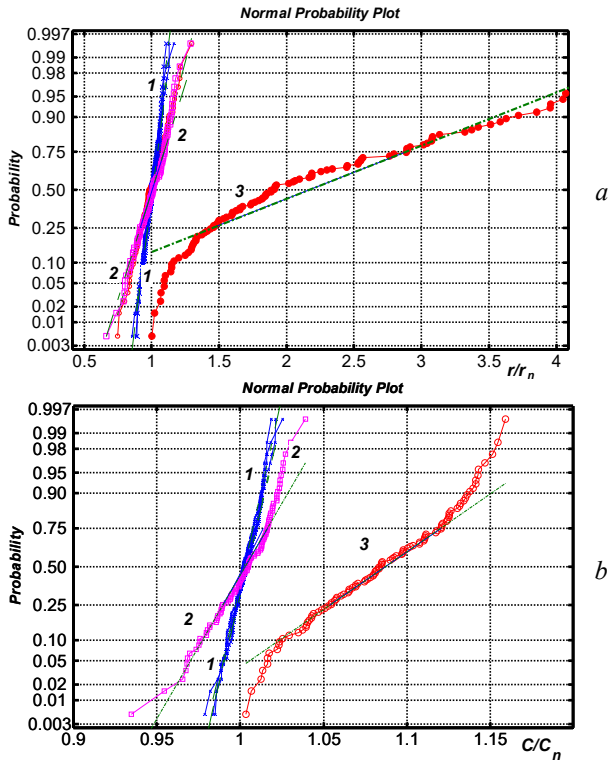

Fig. 9. Integral functions of the distribution of deviations from the nominal values of the diameter (radius) and electric capacity of the insulated conductor in the case of multiplicative and additive nature of variations in the geometric dimensions of the twisted pair of category 5e

Fluctuations in the diameter d also lead to a change in the capacity C from the nominal values C_n of the insulated conductor (Fig. 9,*b*).

Additive interference (Fig. 9,*a*,*b*, curves *1* and *2*, Fig. 10, curves *2* and *4*) is due to external factors affecting the technological process, in particular, a transient process in the power supply network. Multiplicative (Fig. 9,*a*,*b*, curve *3*, Fig. 10, curves *1* and *3*) – due to random changes in the technological process itself.

Figure 10 shows the effect of variations in the capacity of an insulated conductor on transient attenuation at the near end between adjacent pairs. The curves correspond to: *1*, *2* – σ/C = 0.1 % for multiplicative and additive nature; *3*, multiplicative – σ/C = 1 %; *4*, additive – σ/C =1 % (σ is the root mean square deviation).

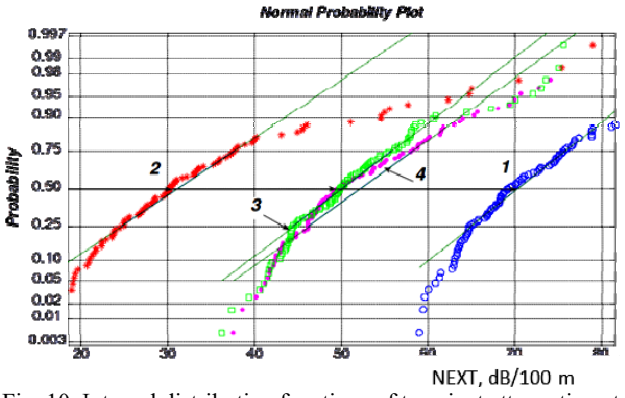

Fig. 10. Integral distribution functions of transient attenuation at the near end between adjacent twisted pairs in the case of additive (curves *2*, *4*) and multiplicative (curves *1*, *3*) character of variations in the capacity of an insulated conductor

With the same coefficients of variation σ/C = 0.1 %, the capacity spread is 0.101 % and 10.1 % in the case of multiplicative (curve *1*) and additive (curve *2*) nature of its change (Fig. 10), respectively. As a result, transient attenuation at the level of 50 % of probability is 2.33 times less, that is, the level of mutual influence between neighboring pairs is greater (Fig. 10, curves *1* and *2*), with the additive nature of the interference.

For the same capacity variations (curves *3* and *4*, Fig. 10) the nature of their change practically does not affect the transient attenuation.

Transient attenuation value for frequency 20 MHz – at the level of 70 dB (Fig. 8,*a*), in the frequency range from 62.5 MHz to 100 MHz – at the level of 60 dB (Fig. 8,*b*,*c*).

Conclusions.

The correlation between the resistance of the conductors and the working capacity of the twisted pairs proves the greater values of the electrical parameters of the shielded compared to the non-shielded ones, provided that the insulation thickness of the conductors of the 4-pair category 5e cables is the same.

It was found that the attenuation coefficient of non-shielded cables has lower values in the frequency range from 1 MHz to 10 MHz. At higher frequency values, the opposite is true: shielded cables have lower attenuation values. For frequency of 200 MHz – by 12 %, which can ensure the transmission of signals over a longer distance.

On the basis of the determined strong positive correlation between ohmic and capacitive asymmetries, it is proved that the transient attenuation at the near end is most affected by the homogeneity of the geometric

dimensions of the twisted pair conductors. Larger values of the pair correlation coefficient between ohmic asymmetry and interference immunity for a shielded cable determine the appropriate settings of the technological process when applying the shield.

It is shown that the multiplicative interference caused by random changes in the stochastic technological process, at the level of 50 % probability, can lead to a deviation of the diameter by 2 times from the nominal value.

To ensure normalized values of interference immunity of twisted pairs in the high-frequency range, the technological equipment settings must guarantee the coefficient of variation of the capacity of the insulated conductor at the level of 0.3 %.

Conflict of interest. The authors declare about absence of conflict of interest.

REFERENCES

1. *Siemens Simatic NET. PROFIBUS Network Manual. System Manual. Edition 04/2009, C79000-G8976-C124-03*. 350 p.

2. Kang S., Han S., Cho S., Jang D., Choi H., Choi J.-W. High speed CAN transmission scheme supporting data rate of over 100 Mb/s. *IEEE Communications Magazine*, 2016, vol. 54, no. 6, pp. 128-135. doi: https://doi.org/10.1109/MCOM.2016.7498099.

3. Lawrenz W. (Ed.). *CAN System Engineering*. Springer London, 2013. 378 p. doi: https://doi.org/10.1007/978-1-4471-5613-0.

4. Thomas D.S. *The costs and benefits of advanced maintenance in manufacturing*. U.S. Department of Commerce. National Institute of Standards and Technology, 2018. 37 p. doi: https://doi.org/10.6028/NIST.AMS.100-18.

5. Reynders D., Wright E. *Practical TCP/IP and Ethernet Networking for Industry*. Elsevier, 2003.320 p. doi: https://doi.org/10.1016/b978-0-7506-5806-5.x5000-5.

6. Fritsche M., Schmidt R., Engels Y. *Single pair Ethernet. The infrastructure for IIoT*. Harting Electronics GmbH, 2020, 10 p.

7. Manoj V., Niresh J. Automotive Networks : A Review. *International Journal of Advanced Engineering, Management and Science*, 2017, vol. 3, no. 5, pp. 504-509. doi: https://doi.org/10.24001/ijaems.3.5.15.

8. Matheus K., Königseder T. *Automotive Ethernet*. Cambridge University Press, 2014. 205 p. doi: https://doi.org/10.1017/CBO9781107414884.

9. Matheus K., Königseder T. *The physical transmission. In Automotive Ethernet*, Cambridge University Press, 2014, pp. 92-133. doi: https://doi.org/10.1017/CBO9781107414884.006.

10. IEEE Standard for Ethernet Amendment 4: Physical Layer Specifications and Management Parameters for 1 Gb/s Operation over a Single Twisted-Pair Copper Cable. *IEEE Std 802.3bp-2016*, 2016, 211 p. doi: https://doi.org/10.1109/IEEESTD.2016.7564011.

11. Mortazavi S., Schleicher D., Schade F., Gremzow C., Gcrfers F. Toward Investigation of the Multi-Gig Data Transmission up to 5 Gbps in Vehicle and Corresponding EMC Interferences. *2018 International Symposium on Electromagnetic Compatibility (EMC EUROPE)*, 2018, pp. 60-65. doi: https://doi.org/10.1109/EMCEurope.2018.8485142.

12. Buntz S., Körber B., Bollati D. *IEEE 100BASE-T1 System Implementation Specification. Open Alliance. Version 1*. 2017, 28 p.

13. Oksman V., Strobel R., Starr T., Maes J., Coomans W., Kuipers M., Tovim E. Ben, Wei D. MGFAST: A New Generation of Copper Broadband Access. *IEEE Communications Magazine*, 2019, vol. 57, no. 8, pp. 14-21. doi: https://doi.org/10.1109/MCOM.2019.1800844.

14. Maes J., Nuzman C.J. The Past, Present, and Future of Copper Access. *Bell Labs Technical Journal*, 2015, vol. 20, pp. 1-10. doi: https://doi.org/10.15325/BLTJ.2015.2397851.

15. Lamparter O., Fang L., Bischoff J.-C., Reitmann M., Schwendener R., Zasowski T., Zhang X. Multi-Gigabit over Copper Access Networks: Architectural Evolution and Techno-Economic Analysis. *IEEE Communications Magazine*, 2019, vol. 57, no. 8, pp. 22-27. doi: https://doi.org/10.1109/MCOM.2019.1800847.

16. *British Cables Company. Product range catalogue*. 2021, 136 p. Available at: https://britishcablescompany.com/Flip/PDF.pdf (accessed 28 March 2022).

17. Knobloch A., Garbe H., Karst J.P. Shielded or unshielded twisted-pair for high speed data transmission? *1998 IEEE EMC Symposium. International Symposium on Electromagnetic Compatibility*, 1998, vol. 1, pp. 112-117 doi: https://doi.org/10.1109/ISEMC.1998.750069.

18. Hejazi A.M., Stockman G.-J., Lefevre Y., Ginis V., Coomans W. Calculating Millimeter-Wave Modes of Copper Twisted-Pair Cables Using Transformation Optics. *IEEE Access*, 2021, vol. 9, pp. 52079-52088. doi: https://doi.org/10.1109/ACCESS.2021.3070192.

19. Bezprozvannych G.V., Ignatenko A.G. The influence of core twisting on the transmission parameters of network cables. *Bulletin of NTU «KhPI»*, 2004, no. 7, pp. 82-87. (Rus).

20. Schaich T., Subramaniam K., de Lera Acedo E., Al Rawi A. High Frequency Impedance Matching for Twisted Pair Cables. *GLOBECOM 2020 - 2020 IEEE Global Communications Conference*, 2020, pp. 1-6. doi: https://doi.org/10.1109/GLOBECOM42002.2020.9322202.

21. Bezprozvannych G.V., Ignatenko A.G. Indirect estimates of to tolerances on the diameters of conductive conductors of twisted pair conductors of network cables. *Bulletin of NTU «KhPI»*, 2005, no. 42, pp. 47-52. (Rus).

22. Yoho J.J., Riad S.M., Muqaibel A.H. Measurement and causal modelling of twisted pair copper cables. *IET Science, Measurement & Technology*, 2021, vol. 15, no. 8, pp. 645-652. doi: https://doi.org/10.1049/smt2.12065.

23. Data communication technology. UTP vs STP. Shielded data cables make the grade. Unshielded data cables reach the limits of their performance. *LEONI Technical Bulletin*, 2015, 5 p.

24. Baghdadi B., Abdelber B., Alain R., Omar D., Helima S. Experimental study of the behaviour of the crosstalk of shielded or untwisted-pair cables in high frequency. *Serbian Journal of Electrical Engineering*, 2019, vol. 16, no. 3, pp. 311-324. doi: https://doi.org/10.2298/SJEE1903311B.

25. Hassoun F., Tarafi R., Zeddam, A. Calculation of per-unit-length parameters for shielded and unshielded twisted pair cables. *2006 17th International Zurich Symposium on Electromagnetic Compatibility*, 2006, pp. 250-253. doi: https://doi.org/10.1109/EMCZUR.2006.214917.

26. Poltz J. Attenuation of screened twisted pairs. *Proceedings 66th International Cable and Connectivity Symposium (IWCS 2017)*, 2017. pp. 219-226.

27. Boyko A.M, Bezprozvannych G.V. Justification of insulation thickness of twisted shielded pairs of structured cable systems. *Bulletin of NTU «KhPI»*, 2011, no. 3, pp. 21-35. (Ukr).

28. Boyko A.N. Draff in the time of the capacity and tangent of the angle of dielectric losses of unexplored and shielded network cables. *Bulletin of NTU «KhPI»*, 2013, no. 42(948). pp. 65-68. (Ukr).

29. Bezprozvannych G.V., Kostiukov I.A., Pushkar O.A. Synthesis of constructive-technological decisions of regulation of working capacitance of cables of industrial networks. *Electrical Engineering & Electromechanics*, 2021, no. 1, pp. 44-49. doi: https://doi.org/10.20998/2074-272X.2021.1.07.

30. Al-Asadi M., Duffy A.P., Hodge K.J., Willis A.J. Twisted Pair Cable Design Analysis and Simulation. *Proceedings of the 49th International Wire & Cable Symposium*, 2000, pp. 111-119.

31. Bezprozvannych G.V., Ignatenko A.G. Optimization of the design of network cables by the attenuation coefficient in the tolerance zone of the geometric dimensions of the transmission parameters. *Electrical Engineering & Electromechanics*, 2004, no. 2. pp. 8-10. (Rus).
32. *ASTM B258-18. Standard Specification for Standard Nominal Diameters and Cross-Sectional Areas of AWG Sizes of Solid Round Wires Used as Electrical Conductors*. ASTM International, 2018, 5 p.
33. Kennefick D.J. FEP as a dielectric material for multi-gigabit, single pair Ethernet cable for automotive. *Proceedings of the 67th International Wire & Cable Symposium (IWCS)*, 2018.
34. Bezprozvannych G.V., Pushkar O.A. Increasing noise immunity of cables for fire protection systems. *Electrical Engineering & Electromechanics*, 2020, no. 4, pp. 54-58. doi: https://doi.org/10.20998/2074-272X.2020.4.07.
35. Ogundapo O., Duffy A., Nche C. Parameter for near end crosstalk prediction in twisted pair cables. *2016 IEEE International Symposium on Electromagnetic Compatibility (EMC)*, 2016, pp. 485-490. doi: https://doi.org/10.1109/ISEMC.2016.7571696.
36. Cai R., Yang S. Analysis and Calculation of Crosstalk for Twisted Communication Cables in Umbilical Cable. *Energies*, 2022, vol. 15, no. 10, art. no. 3501. doi: https://doi.org/10.3390/en15103501.

Received 30.08.2022
Accepted 09.10.2022
Published 01.07.2023

G.V. Bezprozvannych[1], *Doctor of Technical Science, Professor,*
O.A. Pushkar[2] , *General Director, Postgraduate Student,*
[1] National Technical University «Kharkiv Polytechnic Institute», 2, Kyrpychova Str., Kharkiv, 61002, Ukraine,
e-mail: Hanna.Bezprozvannukh@khpi.edu.ua (Corresponding Author)
[2] LLC SPE ALAY,
19-U, Miru Str., Kyiv, 03182, Ukraine,
e-mail: adm@alay.com.ua

How to cite this article:
Bezprozvannych G.V., Pushkar O.A. Ensuring standardized parameters for the transmission of digital signals by twisted pairs at the technological stage of manufacturing cables for industrial operating technologies. *Electrical Engineering & Electromechanics*, 2023, no. 4, pp. 57-64. doi: https://doi.org/10.20998/2074-272X.2023.4.09

UDC 621.315.6 https://doi.org/10.20998/2074-272X.2023.4.10

V.M. Kyrylenko, K.V. Kyrylenko

Theoretical determination of individual values of insulation four-element equivalent circuits elements parameters at technical diagnostics of insulation by absorption methods

*The **aim** of this article is to present a methodology of determining of the individual values of the parameters of four-element equivalent circuits for insulation with through conductivity. **Methodology**. The proposed method consists in the fact that at a time interval of more than 10 s, when the charge indicator no longer contributes to the leakage current, three points t_1, t_2 and t_3 are selected, such that $t_2 – t_1 = t_3 – t_2$. To be able to determine the absorption coefficient R_{60}/R_{15}, it is recommended to take $t_1 = 15$ s, $t_2 = 37.5$ s and $t_3 = 60$ s. At the same time, by subtracting $I(t_2) – I(t_1)$ and $I(t_3) – I(t_2)$, the constant component of the absorption curve is excluded and it becomes possible to determine the individual values of the parameters of the generalized equivalent circuit of insulation, additionally using its conductivity in operator form. **Results.** As calculations show, the correct determination of the parameters of insulation equivalent circuit according to the proposed method is possible only with a certain ratio of these parameters. The charge time of the geometric capacitance $C_g(R_0+R_d)$, where R_0 and R_d are the resistance that forms the charging exponent, and the resistance of the sensor, should be within 0.2 s $<C_g(R_0+R_d)<1$ s, the time constant C_aR_a, where C_a and R_a are the capacitance and resistance of the absorption chain, should be more than 3 s, the product of C_gR_l, where R_l is the leakage resistance, more 0.5 s, the leakage resistance R_l is less than the absorption resistance R_a. Checking the methodology on a model example gives the values of the parameters of the insulation equivalent circuit that match the specified ones with high accuracy. **Practical value.** The use of individual values of the parameters of insulation equivalent circuits when applying absorption diagnostic methods with considering the time values and dimensional factors, allow to calculate all currently used diagnostic parameters, to determine the conditions of certain insulation types, as well as in more detail, in comparison with the existing approach, to assess the technical condition of the insulation and the reasons of its changes.* References 20, figures 2.

Key words: **non-destructive methods of insulation diagnostics, absorption methods of diagnostics, parameters of elements of insulation equivalent circuits.**

Розглянута теоретична методика визначення індивідуальних значень параметрів елементів узагальненої схеми заміщення ізоляції по залежності абсорбційного струму від часу, а також інших чотирьохелементних схем заміщення ізоляції з наскрізною провідністю та їх взаємного перерахунку, що повністю розкриває інформативний потенціал абсорбційних методів діагностування електричної ізоляції. Знання цих значень теоретично дозволяє, враховуючи значення часу та розмірні фактори, сформувати будь-який абсорбційний діагностичний параметр, що використовується зараз, і прослідкувати його зміни в процесі експлуатації ізоляції. Наголошується, що для фізично обґрунтованої інтерпретації результатів діагностичного контролю абсорбційним методом за однією з схем заміщення ізоляції необхідно мати інформацію про склад і структуру ізоляції. Бібл. 20, рис. 2.

Ключові слова: **неруйнівні методи діагностики ізоляції, абсорбційні методи діагностики, параметри елементів схем заміщення ізоляції.**

Introduction. The electrotechnical and electric power equipment used at Ukrainian enterprises has worked out a significant part or all of the designated service life, taking into account that the most intensive commissioning of it took place until the 90s of the last century. This applies to power plant equipment such as generators, transformers, internal demand motors and high-voltage switchgear equipment, insulation of overhead networks and cable lines, as well as induction electric drive motors.

Currently, most of the power generating equipment of TPPs and CHPs has reached their limit service life (more than 200,000 hours), they are worn out and, according to the existing regulatory documentation, they need to be reconstructed or replaced. The distribution of specific damage of the main units of turbo- and hydrogenerators, which increases with increasing power, shows that the stator insulation is subject to control as the most «weak» unit [1].

If we take into account all the main equipment of power plants, it should be noted that great attention should be paid to monitoring the technical condition of power transformers [2-7], especially with extended service life.

Due to wear, in the vast majority of cases (85-95 %), failures of induction motors with a short-circuited rotor (the most widely used in the country's enterprises) with power of more than 5 kW occur due to damage to the stator and rotor windings and are distributed as follows: stator winding – up to 80 %, rotor winding – up to 10 % [1, 8-11]. This causes increased attention to control the reliability of their insulation.

Moral and physical wear of cable lines with voltage of 6-10 kV in power supply systems ranges from 40 to 90 %. Here, up to 70 % of all power supply violations occur when cable lines with voltage of 6-10 kV fail, and therefore control of their technical condition is also an urgent issue [12-15].

When using worn-out electrical equipment, it should be borne in mind that when we talk about the designated service life, according to the regulatory documentation, this is about the group resource, which is defined as the working time of a group of products, for which n percent of the most defective products are rejected. This time is taken as a group service life with a reliability of 1–*n*/100. This generally accepted approach does not take into account that life dissipation can be several hundreds of percent, and therefore the residual life of some products, especially if the life is distributed according to the log-normal law, may be several times greater than intended. Based on this fact, it can be considered justified to try to extend the life of the equipment by determining an extended life. However, we emphasize that the operation

of electrical equipment, which has worked out and for which an extended life has been established, due to the uncertainty of the real life, requires continuous monitoring of its technical condition. Only under such conditions the unused service life of the equipment can be effectively used.

Control of the level of reliability of electrical insulating materials and structures in operation is carried out by measuring the influence of external and operational factors on the parameters of the insulation characteristics, which lead to a change in the technical condition of the insulation, including those that are not related to functioning. Most often, the technical condition of insulation and electrical insulating materials is determined using integral parameters, such as resistance, capacitance, dielectric loss angle tangent, leakage current, absorption coefficient, recovery voltage, etc. [16].

One of the methods of monitoring the technical condition of electrical equipment is absorption diagnostic methods, which are recommended as normative for diagnosing insulation of transformers, synchronous generators, compensators, collector exciters, and AC electric motors [16]. A brief description of absorption methods is given in [1].

Modern scientific studies of absorption methods and their use relate to diagnosing the state of insulation of power transformers [2, 3, 9-12, 15], rotating electric machines [8-11], low- and high-voltage cables [7, 12-14].

Insulation defects and methods of their diagnosis are generally described in [1, 8, 9]. In [1], the general issues of diagnosis of insulation and, in particular, the use of absorption methods are considered. Diagnostic parameters in the case of using absorption diagnostic methods include, firstly, parameters that use the characteristics of the rate of decline of the absorption current curve (increase in insulation resistance) depending on the time of application of constant voltage to the insulation in different sections of this curve, i.e. absorption coefficient, polarization coefficient, dielectric absorption ratio, polarization index and other similar characteristics and their derivatives. The second direction related to absorption methods is the recovery voltage method, which is implemented in two variants. In the first case, the ratio of the maximum value of the recovery voltage resulting from the charge from the absorption capacitance of the insulation disconnected from the voltage source after the discharge of its geometric capacitance to the charging capacitance (capacitive absorption coefficient) is determined. In the second variant, it is the same ratio determined at different time intervals for the discharge of the geometric capacitance, which leads to partial discharge and absorption capacitance. In addition, the initial rate of rise of the r recovery voltage, the time to reach the maximum value of the recovery voltage, nonlinearity coefficients of the recovery voltage, the self-discharge time constant, and other characteristics can be used as diagnostic parameters.

The generalized equivalent insulation replacement circuit (Fig. 1,*a*) is the basis of all absorption diagnostic methods. Its elements include the geometric capacitance C_g, which reflects the capacitance associated with fast processes of electronic and ionic polarization, the through resistance R_l, i.e. the steady value of insulation resistance to the flow of direct current, the absorption capacitance C_a, which is responsible for the slow processes of migration polarization caused by accumulation of free charges on the boundaries of the regions of the dielectric with different electrophysical properties or in the near-electrode regions, and the absorption resistance R_a, which is introduced to correctly reflect the inertial properties of the migration polarization [1].

The absorption coefficient (and other differential diagnostic parameters for the generalized circuit and other four-element substitution circuit), as a rule, can be written in the form:

$$k_a = \frac{R_1 + R_2 \exp\left(-t_2 \alpha_{1v}\right)}{R_1 + R_2 \exp\left(-t_1 \alpha_{1v}\right)},$$

where t_1 and t_2 are the time of measuring resistances R_1, R_2, in the general case R_i are resistive elements, α_{iv} is the function of resistive and capacitive elements of the substitution circuit. Specific expressions for R_i and α_{iv} used for the absorption coefficient will be given below for all four-element insulation replacement circuits.

In [8, 9], the main causes and defects of insulating structures, the processes that occur in the insulation under the action of an electric field and lead to the formation of its defects are considered. In [9], a generalized analysis of control methods and diagnostic parameters of insulation of DC traction motors is presented. Here, a generalized insulation substitution circuit was used, the parameters of the substitution circuit were determined through the parameters of the model containing parallel absorption circuits of series-connected capacitances and resistances.

In [2] it is noted that two fundamental processes take place in insulation: polarization and electrical conductivity, and that both processes should be sensitive to changes in composition and characteristics that occur in the insulation during operation, and a list of potentially possible diagnostic methods is given. In [10], the procedures of constant voltage tests for measuring the insulation resistance and polarization index of the insulated stator, as well as the rotor windings and methods of interpreting the results obtained during the diagnosis of rotating machines are outlined.

At the same time, it was established [11] that when diagnosing the windings of rotors and stators of generators and motors, the insulation resistance and the polarization index well detect moisture and partially conductive inclusions, but are not sensitive to many other defects: the weakening of the turns in the slot, which leads to abrasion of the insulation, delamination of insulation due to use at high temperatures, separation of copper from insulation due to cyclic loads, destruction of protective coatings and partial discharges between coils. The authors suggest using a comparison of charging and discharging current for each phase of the winding and individual coils with simultaneous measurement of resistance and polarization index.

In the works reviewed by us above, the authors use standard indicators, which are standard integral combinations of the parameters of the elements of the generalized equivalent circuit, as was shown for the absorption coefficient, and do not consider the issue of

simultaneous determination of all individual parameters of the elements of the substitution circuit, as such, as well as their interdependence.

If we talk about the possibility of diagnosing electrical insulation with the help of recovery voltage, then the work [3] demonstrated a good correspondence between the model based on the generalized dielectric substitution circuit and real insulation for the coefficients of polarization, depolarization and recovery voltage.

The recovery voltage method is most widely used for power transformers. The conditions for monitoring the insulation of high-voltage transformers by the recovery voltage method are outlined in [4].

In [5], a new approach is considered to combine the results obtained using two methods, namely: reverse voltage measurement and polarization-depolarization current measurement for several power transformers, to find the relationship between the moisture content of oil and paper, relating to power transformers.

In the recovery voltage method [6], the recovery voltage is determined after charging the insulation with DC voltage. The so-called polarization spectrum can be created by repeatedly charging for different times and then obtaining the value of the recovery voltage. The recovery voltage range gives an indication of the condition in which the insulation of the transformer is. The results of measurements on two high-power transformers in operation, which determine the humidity of solid insulation, were analyzed.

With the help of equivalent circuits, in [7] the characteristics of the recovery voltage for paper-oil insulation were studied: the charge time, the shorting time, which was equal to half the charge time, the recovery voltage and the ratio of its maximum to the charging voltage was determined, and the time corresponding to the maximum was also fixed. The simulation was carried out for 14 cycles with different charge times from 0.1 to 819 s, and the moisture content and oil conductivity were evaluated. Analyzing the results, the authors note that traditional diagnostics used the value of a time constant during which the maximum of the recovery voltage is reached, although it can be masked by interphase polarization, which makes the use of this technique unacceptable in practice.

Taking into account that the aging of paper-oil insulation of power transformers occurs mainly due to moisture and oxygen, new methods of assessing the state of insulation based on dielectric response have been developed, but they use expensive tools. The work [7] shows the effectiveness of measuring recovery voltage using simple measuring devices. The relationship between the initial growth rate of the recovery voltage and the state of the insulation is established.

Conducted studies [12] show that the application of voltage response measurement is a very effective tool for determining the aging state of oil paper insulated cables. The initial slope of the charge voltage is directly proportional to the insulation conductivity and the initial slope of the recovery voltage is proportional to the intensity of the polarization processes. Therefore, the two main wear processes (wetting and thermal aging) of oil-paper insulation can be considered separately.

The work [13] considered the application of the voltage triggering method on laboratory-aged low-voltage polymer (PVC and PE) insulated cables and compared the results with the results of chemical and penetration tests. With the help of the method of voltage triggering, it is possible to detect the state of aging of the insulation, that is, the probable decrease in dielectric strength for cables of operational age in comparison with dielectric losses.

Recovery voltage, as a diagnostic factor, was also studied in [14, 15]. In [17], a method for determining the characteristics of phase and belt paper-oil insulation of medium voltage power cables is presented. The methodology is implemented using a three-core cable replacement circuit in a common metal shell and analysis of the results of aggregate measurements of absorption characteristics. The system of linear algebraic equations for determining the characteristics of phase and belt insulation is well conditioned. The article presents the results of determining the absorption characteristics of phase and belt insulation of a power cable at voltage of 6 kV, which are in good agreement with real values.

It should be noted that in the works where the recovery voltage, which depends on the charging voltage and combinations of the values of the elements of the generalized equivalent insulation replacement circuit, as well as related derivative diagnostic parameters, the analytical expressions for which are given below in the article, this is not about determining all the individual values of the parameters of the elements of the generalized equivalent insulation replacement circuit at the same time.

The third direction of diagnostic research is emerging almost now thanks to the works by G.V. Bezprozvannych [17-19], who was one of the first, if not the first, to understand that a statistical approach should be used to diagnose electrical insulation. But even in this case, the simultaneous determination of the individual values of the parameters of the elements of the generalized equivalent insulation replacement circuit remains outside the attention of the authors.

Authors of works on dielectric spectroscopy [12, 14] and others as a diagnostic parameter, the tangent of the dielectric loss angle in the low-frequency region use, which is quite complexly related to the parameters of the elements of the generalized equivalent insulation replacement circuit, and therefore, taking into account the topic of this work, the results obtained by them may not be considered. So, for this direction as well, the simultaneous determination of all individual parameters of substitution circuits is not relevant.

The first work that analyzed in detail the shortcomings of diagnosing electrical insulation by measuring absorption coefficients, polarization index, dielectric absorption ratio and other interval characteristics is the article [20], where the authors noted the ambiguity of the interpretation of the diagnosis results due to the dependence of the diagnostic criteria on the values of the parameters of several elements of substitution circuits at the same time, which can vary in the process of aging of the insulation, leading to ambiguity of diagnostic parameters, as well as due to the extremity of these diagnostic parameters. There was also

a lack of information about the explicit value of the parameters of the resistive elements of the substitution circuit, or their implicit use for diagnostic parameters based on the method of recovery voltage, but a detailed analysis of these methods was not carried out.

In the opinion of the authors of this article, there is an opportunity to significantly increase the informativeness of absorption diagnostic methods and partially eliminate the ambiguity of their interpretation by determining the individual values of the parameters of the elements of the four-component insulation replacement circuits. It is clear that knowledge of the individual values of these parameters will theoretically allow to form, taking into account time and dimensional factors, any diagnostic parameter based on absorption methods.

The goal of the article is to develop the scientific basis of the methodology for determining individual parameter values of four-element insulation replacement circuits with through-conduction.

The article considers the case when the dielectric has only one absorption exponent, taking into account that the generalization of the technique to several absorption exponents is obvious. For this, it is necessary to exclude first the constant component, and then sequentially the exponents with the largest time constant, subtracting the current corresponding to them from the residual curve and rebuilding the new residual curve on a semi-logarithmic scale. The authors understand that the article is of a purely theoretical nature, the determination of the individual values of the parameters of the insulation replacement circuit is carried out for the curve simulating the absorption current in the insulation, but it is obvious that the application of the proposed technique to the real absorption curve will allow to determine the real values of the parameters of the insulation replacement circuit, which is being investigated. The practical use of the technique for real insulation will be demonstrated in the next article.

Use of dielectric equivalent circuits to diagnose insulation. The insulation of electrotechnical and electric power equipment is characterized by heterogeneity of structure and properties, which is caused by the very structure and composition of the electrical insulating material. In addition, the inhomogeneity of the insulation can arise during the operation of the insulation due to the inhomogeneous distribution of the field associated with the geometry of the dielectric structure itself, as a result of which electrical and thermal aging of the insulation will proceed with different intensity in areas with different field strengths. The influence of the heterogeneity of the material and the geometry of the electrical insulating structure on the configuration of the internal field in the insulation can be estimated by calculation only for some of the simplest cases. If non-homogeneous materials are used in a non-homogeneous field, the superimposition of external and internal inhomogeneities greatly complicates the task. One of the simple approaches to bypassing the emerging complications is to model electrical insulating structures with simple electrical substitution circuits consisting of resistors and capacitors and having frequency characteristics corresponding to the frequency characteristics of the insulation under investigation. It is assumed that with such a replacement, it is possible to make a more or less adequate idea of the degree of heterogeneity of the insulation with a certain interpretation of the obtained results. Note that a similar approach, based on replacing dielectrics with equivalent circuits, is used not only to describe the properties of electrical insulation, but also to study the relationship between the structure and electrophysical properties of heterogeneous composite dielectric materials.

Any four-component substitution circuit with through conduction can correspond to this model absorption current curve. For the correct choice of the replacement circuit and the subsequent interpretation of the diagnostic results, it is necessary to have an idea of the composition, structure and peculiarities of the flow of electrophysical processes in the insulation. This is quite a difficult task, and therefore we will give only some possible options for the interpretation of four-element insulation replacement circuits.

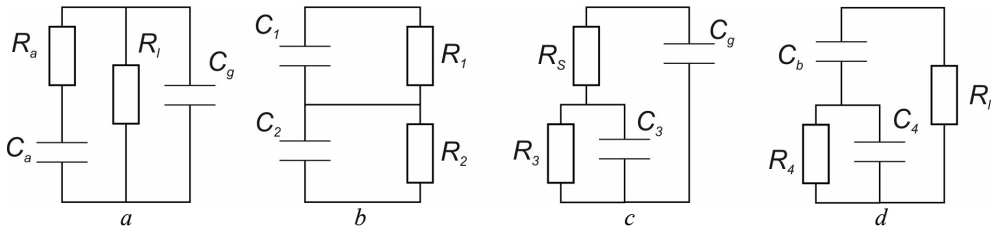

Fig. 1. Four-element insulation replacement circuits with through-conductivity

The interpretation of the generalized insulation replacement circuit (Fig. 1,*a*) was given above.

The layered material, which is a serial connection of two dielectrics with elastic polarization, which is represented by the capacitances C_1 and C_2, and through electrical conductivity, which is represented by the resistances R_1 and R_2, connected in parallel with the corresponding capacances, corresponds to the circuit (Fig. 1,*b*). Provided that $\varepsilon_{r1}\rho_1 \neq \varepsilon_{r2}\rho_2$, the macroscopic inhomogeneity of such two-component insulation leads to the appearance of migration polarization caused by the accumulation of free charges at the interphase boundary, the consequence of which is the exponential decline of current with time at constant voltage and dielectric losses at alternating voltage.

The circuit (Fig. 1,*c*) may correspond to insulation with partially destroyed or broken local inclusions or a composite dielectric material with a subthreshold concentration of a component with much higher electrical conductivity, characterized by the resistance R_b, with which a dielectric (capacitance C_3) with low electrical conductivity is connected in series (resistance R_3), as well as in parallel to this series circuit with capacitance C_g, which reflects fast types of polarization.

And, finally, the circuit (Fig. 1,*d*) can be used for insulation, which is a composition of a high-Q non-polar polymer with very low conductivity (capacitance C_b) and a polar polymer included partly in series with it (circuit C_4, R_4), and partly in parallel (resistance R_l), or for a composite material consisting of an ionic or other low-Q filler in the threshold mode.

Thus, the model curve of the absorption current can be selected for one of the insulation substitution circuits, and it is for this substitution circuit that the individual values of the parameters of its elements can be calculated, but then these values can be recalculated to other substitution circuits as well. First, in the article we will consider how to determine the individual values of the parameters of the elements of the generalized equivalent circuit, and then their recalculation into the individual values of the parameters of the elements of other four-element insulation replacement circuits. Formulas for reverse calculation are also given.

Determination of individual values of the parameters of the elements of the generalized equivalent insulation replacement circuit. Determining the individual values of the parameters of the elements of the generalized equivalent insulation replacement circuit: through resistance, absorption resistance, absorption and geometric capacitances can be implemented in practice by recording and analyzing the transient current in the measuring circuit shown in Fig. 2, with instantaneous supply of constant voltage $U = U_0$.

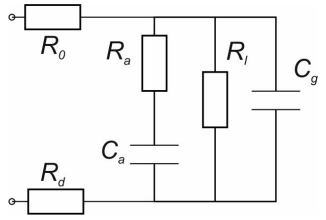

Fig. 2. Equivalent measuring circuit: R_0 – limiting (forming) resistance, R_d – measuring sensor resistance, R_l – through resistance, R_a – absorption resistance, C_a – absorption capacitance, C_g – geometric capacitance

In addition to the insulation, the measuring circuit includes two resistors: the measuring R_d – for measuring the leakage current, and the forming R_0 – for generating an exponent describing the charge of the geometric capacitance of the insulation. The value of the measuring resistance is selected in the range of 10^3 – 10^5 Ω. The forming resistance should be in the range of 10^6 – 10^9 Ω and provide a charge time constant of the geometric capacitance $C_g(R_0+R_d)$ of about a second. Then, in 3-4 s, it will attenuate, and based on later readings of the absorption current, it will be possible to determine the absorption time constant.

The model current through the insulation when the measuring circuit (Fig. 2) is connected to constant voltage U_0 as a function of time will have three components: a constant one and two exponents with the charge for the geometric capacitance $1/a$ and the absorption capacitance $1/b$ time constants:

$$I = C + A \cdot \exp(-at) + B \cdot \exp(-bt). \quad (1)$$

In order to theoretically determine its parameters from the model absorption current curve, we suggest using the three-point method, which makes it possible to determine the constants a and b, and then calculate the coefficients of the absorption curve. Next, using the formula for the leakage current recorded taking into account the expression for the operator conductivity, it is theoretically possible to determine the parameters of the elements of the equivalent substitution circuit, and then the value of the absorption coefficient or other interval diagnostic parameters.

Within the framework of the proposed theoretical method, at a time interval longer than 10 s, where the charging exponent no longer contributes to the leakage current, three points t_1, t_2 and t_3 are selected such that $t_2 - t_1 = t_3 - t_2$. To be able to calculate the absorption coefficient R_{60}/R_{15}, it is recommended to take t_1 = 15 s, t_2 = 37.5 s and t_3 = 60 s.

The proposed choice of three calculation points allows, due to the subtraction $I(t_2) - I(t_1)$ and $I(t_3) - I(t_2)$, to eliminate the constant component of the absorption current and then, under the condition that the charge time of the geometric capacitance $C_g(R_0+R_d) \approx 1$ s, and the charge time constant of the absorption capacitance C_aR_a >3 s, the constant b in the second interval can be calculated with sufficient accuracy by the formula

$$b = \frac{\ln\left(\frac{I_4 - I_5}{I_5 - I_6}\right)}{t_5 - t_4}. \quad (2)$$

In the first time interval from 0 to 10 s, three points t_1, t_2 and t_3 should be selected, also observing the requirement that $t_2 - t_1 = t_3 - t_2$. Then the charging constant a at the first time interval is calculated as follows

$$a = \frac{\ln\left(\frac{I_1 - I_2}{I_2 - I_3}\right)}{t_2 - t_1}. \quad (3)$$

Coefficients A, B and C are determined from a system of 3 equations taken for three values of the model absorption current curve, preferably at small time values, when the system of equations will be better defined and more accurate coefficient values can be obtained. The system of equations for determining the coefficients of (1) will have the form

$$\begin{cases} a_1 A + b_1 B + C = I_1; \\ a_2 A + b_2 B + C = I_2, \end{cases} \quad (4)$$

where $a_i = \exp(-at_i)$, $b_i = \exp(-bt_i)$, $I_i = I(t_i)$.

The coefficients of the equation A, B and C according to the solution of system (4) are generally equal to the values given in (5):

$$A = \frac{(I_1 - I_2)\cdot(b_2 - b_3) - (I_2 - I_3)\cdot(b_1 - b_2)}{(a_1 - a_2)\cdot(b_2 - b_3) - (b_1 - b_2)\cdot(a_2 - a_3)};$$
$$B = \frac{I_1 - I_2 - A\cdot(a_1 - a_2)}{(b_1 - b_2)}; \quad (5)$$
$$C = I_1 - a_1 A - b_1 B.$$

To write down the formulas for determining the values of the parameters of the generalized equivalent insulation replacement circuit, we write down its conductivity (6) in operator form. This conductivity corresponds to the following time dependence of the current through the insulation (8)

$$Y_1 = \frac{R_d}{R_0 + R_d} \cdot \frac{p^2 + p\left(\alpha_{aa} + \alpha_{ga} + \alpha_{gl}\right) + \alpha_{aa}\alpha_{gl}}{p^2 + p\left(\alpha_{aa} + \alpha_{ga} + \alpha_{gl} + \alpha_{god}\right) + \alpha_{aa}\left(\alpha_{gl} + \alpha_{god}\right)}; \quad (6)$$

$$\alpha_{aa} = \frac{1}{R_a C_a}; \alpha_{ga} = \frac{1}{R_a C_g}; \alpha_{gl} = \frac{1}{R_l C_g}; \alpha_{god} = \frac{1}{C_g\left(R_0 + R_{god}\right)}; \quad (7)$$

$$I_1 = \frac{U_0}{R_0 + R_d} \cdot \left(\frac{\beta}{ab} + \frac{a^2 - \alpha a + \beta}{a(a-b)} \exp(-at) - \frac{b^2 - \alpha b + \beta}{b(a-b)} \exp(-bt) \right), \quad (8)$$

where α and β are the coefficients of the numerator, a and b are the absolute values of the roots of the denominator of the conductivity of the generalized insulation replacement circuit in operator form, which are equal to the inverse values of the time constants of the leakage current.

The equalities hold for the roots of the denominator according to Vieta theorem

$$\begin{aligned} a_1 &= a + b = \left(\alpha_{ga} + \alpha_{aa} + \alpha_{gl} + \alpha_{god}\right); \\ b_1 &= ab = \alpha_{aa} \cdot \left(\alpha_{gl} + \alpha_{god}\right) \end{aligned} \quad (9)$$

The coefficients of the numerator α and β can be determined through the coefficients of the absorption current A and C, taking into account the expressions for a_1 and b_1 according to formula (9)

$$\beta = \frac{b_1 C\left(R_0 + R_d\right)}{U_0}; \quad (10)$$

$$\alpha = a + \frac{\beta}{a} - \frac{A a_1 \left(R_0 + R_d\right)}{U_0}. \quad (11)$$

Now we can move on to determining the values of the parameters of the generalized substitution circuit. Taken into account that R_0 and R_d are known, and $\alpha_{god} = \alpha_1 - \alpha$, it is possible to determine the geometric capacitance

$$C_g = \frac{1}{\left(a_1 - \alpha\right)\left(R_0 + R_d\right)}. \quad (12)$$

Next, using equalities

$$\beta = \alpha_{aa} \cdot \alpha_{gl} \quad \text{and} \quad \alpha_{gl} = \frac{\alpha_{god} \cdot \beta}{b - \beta},$$

we have

$$R_l = \left(\frac{b}{\beta} - 1 \right) \cdot \left(R_0 + R_d\right), \quad (13)$$

and taking into account that

$$\alpha_{gl} = \frac{\left(a - \alpha\right) \cdot \beta}{b - \beta}, \ \alpha_{aa} = \frac{\beta}{\alpha_{gl}} = \frac{b - \beta}{a - \alpha} \ \text{and}$$

$$\alpha_{ga} = \alpha - \alpha_{aa} - \alpha_{gl},$$

we find

$$R_a = \frac{\left(a - \alpha\right) \cdot \left(R_0 + R_d\right)}{\alpha - \frac{b - \beta}{a - \alpha} - \frac{a - \alpha}{b - \beta} \cdot \beta}, \quad (14)$$

$$C_a = \frac{1}{\left(R_0 + R_d\right) \cdot \left(b - \beta\right)} \left(\alpha - \frac{a - \alpha}{b - \beta} \beta - \frac{b - \beta}{a - \alpha} \right). \quad (15)$$

It should be noted that, as shown by more detailed model calculations, the correct determination of the parameters of the insulation replacement circuit by the proposed method for the model example is possible only with a certain ratio. The charge time constant of the geometric capacitance $C_g(R_0+R_d)$ must be within $0.2 < C_g(R_0+R_d) < 1$ s, and therefore it is necessary to know or determine the capacitance of the measurement object with the appropriate accuracy in advance. Considering that for the calculation of the absorption coefficient, the absorption current is determined at 15 s and 60 s after applying the voltage, the time constant C_aR_a should be greater than 3 s. In addition, it is necessary that the product C_gR_l is greater than 0.5 s, and the leakage resistance R_l is less than the absorption resistance R_a.

To illustrate the procedure for using the three-point method, consider an example of calculating the parameter values of a model generalized insulation replacement circuit using the calculated absorption current for a circuit with known parameter values. Let's assume that $5 \cdot 10^3$ Ω, $R_0 = 2 \cdot 10^7$ Ω, $C_g = 7 \cdot 10^{-8}$ F, $R_l = 8 \cdot 10^{11}$ Ω, $C_a = 3 \cdot 10^{-8}$ F, $R_a = 6 \cdot 10^9$ Ω.Then, using (7) – (9) for the absorption current flowing through the model circuit of the replacement of the insulation, we have an expression by which it is necessary to determine the individual values of the parameters of the elements of the model replacement circuit

$$I = 1{,}69 \cdot 10^8 e^{(-0{,}0055t)} + 4{,}98 \cdot 10^6 e^{(-0{,}716t)} + 1{,}25 \cdot 10^{-10}. \quad (16)$$

To determine the values of the time constants of the exponent of the model absorption curve in the first interval, we choose the time values of 1, 2, and 3 s, and in the second – 15, 37.5, and 60 s. Using (2), (3), we find that $a = 5.5 \cdot 10^{-3}$, $b = 0.7164$, which practically coincides with the values of the time constants in (16). Now we can find the calculated coefficients of the equation, which are equal to $A = 1.686 \cdot 10^{-8}$, $B = 4.982 \cdot 10^{-6}$ and $C = 1.25 \cdot 10^{-10}$, respectively, and exactly match the actual values of the coefficients. After calculating a_1 and b_1, we find by (10), (11) $\alpha = 8 \cdot 10^{-3}$, which exactly corresponds to the original value, and a slightly underestimated $\beta = 9.9196 \cdot 10^{-8}$ at an exact value $9.9206 \cdot 10^{-8}$. Having all the necessary values, we calculate the values of the parameters of the insulation replacement circuit using (12) – (15): $C_g = 7 \cdot 10^{-8}$ F, $R_l = 8 \cdot 10^{11}$ Ω, $C_a = 3 \cdot 10^{-8}$ F, $R_a = 8 \cdot 10^{11}$ Ω, which coincide with the original values to the fourth decimal place.

The given calculation example can also be used to theoretically illustrate the advantage of knowing the individual values of the individual parameters of the insulation replacement circuit before the formal use of the absorption coefficient. The absorption coefficient for the model calculation circuit is equal to 1.18, which in practice would give formal grounds for decommissioning the insulation due to unsatisfactory characteristics. However, if we take into account that the through-flow resistance has a value of $8 \cdot 10^{11}$ Ω, and the calculated tgδ for electrical conductivity has a value of $5.7 \cdot 10^{-8}$, then we can come to the opposite conclusion – the insulation has satisfactory characteristics and is not at risk of breakdown.

Thus, the theoretical verification of the proposed model methodology shows that only in the case when the necessary relationships between the values of the insulation parameters and, accordingly, the circuit of its replacement, take place, the calculations of individual values give good accuracy. But it is necessary to keep in mind that when going beyond the above limits of parameter values, the accuracy deteriorates quite sharply.

Theoretically, it is possible to increase the accuracy of determining the values of the parameters of the substitution circuit by performing two calculations. The first calculation should be carried out under the condition that R_0 and $R_d << R_a$ and R_l, and the influence of external resistances on the absorption current can be neglected. Here

$$I = U_0\left(\frac{1}{R_l}+\frac{1}{R_a}\exp\left(-\frac{t}{\tau_a}\right)\right),$$

where $\tau_a = C_aR_a$ is the absorption time constant.

Having chosen three time values in the region of the decline of the absorption curve as before so that $t_2 - t_1 = t_3 - t_2 = \Delta t$, using the current values I_1, I_2 and I_3, we find their differences $dI_{12} = I_1 - I_2$, $dI_{23} = I_2 - I_3$ and the value of absorption time constant

$$\tau_a = \frac{\Delta t}{\ln\left(dI_{12}/dI_{23}\right)}. \qquad (17)$$

Now we can calculate the absorption resistance

$$R_a = \frac{U_0}{\Delta I_{12}}\left(\exp\left(-\frac{t_1}{\tau_a}\right)-\exp\left(-\frac{t_2}{\tau_a}\right)\right), \qquad (18)$$

absorption capacitance

$$C_a = \tau_a/R_a\,, \qquad (19)$$

and through resistance

$$R_l = \frac{U_0}{I(t_1)-\dfrac{U_0}{R_a}\exp\left(-\dfrac{t_1}{\tau_a}\right)}. \qquad (20)$$

At the second stage, we need to make a calculation, choosing R_0 approximately 10^6 Ω to form the charging exponent, using (2), (3) to find the time constants a and b, and then, taking into account that the other parameters are already known almost exactly, calculate the approximate value C_g according to the formula

$$C_n = \left(abC_aR_a\left(R_0+R_d\right)\right)^{-1}. \qquad (21)$$

If the charging time constant $C_g(R_0+R_d)$ is in the range from 0.2 s to 1 s, then C_g will be determined with an accuracy no worse than a few percent, if not, then a new value of R_0 that satisfies the given condition is chosen and the calculation is repeated . Thus, in this case, despite the greater amount of work, it is possible to obtain the exact values of the three parameters that determine the absorption coefficient, and the approximate value of the fourth one.

Theoretically, it is possible to determine all values of the parameters of the insulation replacement circuit by the three-point method even with a single calculation by using, in addition to the absorption curve, also the recovery voltage. To do this, first the first stage of the preliminary calculation is repeated and the absorption current values necessary for the accurate determination of R_l, R_a and C_a are fixed, and then when simulating the method of recovery voltage (short-term insulation shorting for the discharge of the geometric capacitance to a low resistance and measurement with an electrostatic voltmeter or a voltmeter with a resistance, which significantly exceeds the resistance of the insulation, the recovery voltage on the insulation, which arises as a result of the charge of the geometric capacitance from the absorption capacity) the capacitive absorption coefficient is determined

$$k_c = \frac{U_{v\max}}{U_0} = \frac{C_a}{C_g+C_a},$$

where $U_{v\max}$ is the maximum value of the recovery voltage, and the geometric capacity

$$C_g = C_a\left(\frac{1}{k_c}-1\right). \qquad (22)$$

Note that with this model determination of the recovery voltage, the capacitive coefficient of absorption and the geometric capacitance, the possible discharge of the insulation capacitances due to its through resistance in the process of charging the geometric capacitance from the absorption one is neglected, which may lead to some overestimation of the value of the found geometric capacitance.

A more detailed theoretical study of the recovery voltage can be carried out knowing the values of the parameters of the insulation replacement circuit. Consider the case with the inclusion of R_d and R_0 in the discharge circuit, when after charging the insulation and disconnecting the voltage source, a short-term short circuit occurs. Assuming that R_d is so small (less than or equal to 10^4 Ω) that it can be neglected, consider the redistribution of charge between the capacitances C_a and C_g, as well as the discharge of C_a through R_a, R_0 and R_l and C_g through R_l and R_0 under the condition that C_a is charged to U_{ca}, and the charge on C_g is zero. Marking

$$\frac{R_lR_0}{R_l+R_0} = R_{de}\,,$$

from the system of equations for currents I_1 and I_2 in the operator form, taking into account that $U_{rg} = I_2/(pC_g)$, we write down the expression for I_2:

$$I_2\left(R_{de}+R_a\right)\left[\frac{\left(p+\alpha_{gde}\right)}{p}\frac{\left(p+\alpha_{aade}\right)}{p}-\frac{R_{de}}{\left(R_{de}+R_a\right)}\right] = -U_{ca}\,,$$

where $\alpha_{gde} = C_gR_{de}$, $\alpha_{aade} = C_a(R_a+R_{de})$, and for the recovery voltage in the operator form we have

$$U_{rg} = \frac{I_2}{pC_g} = -\frac{U_{ca}}{C_gR_{de}}\frac{p}{\left(p+\alpha_{aa}\right)\cdot\left(p+\alpha_{gdee}\right)},$$

or as the function of time

$$U_{rg} = \frac{U_{ca}}{C_gR_{de}}\frac{\exp\left(-\alpha_{aa}t\right)-\exp\left(-\alpha_{gdee}t\right)}{\alpha_{aa}-\alpha_{gdee}}.$$

Now we can calculate the time at which the recovery voltage has an extremum

$$t_{\max} = \frac{\ln\left(\alpha_{aa}\right)-\ln\left(\alpha_{gdee}\right)}{\alpha_{aa}-\alpha_{gdee}},$$

the maximum value of the recovery voltage

$$U_{r\max} = -\frac{U_{ca}}{\alpha_{gdee}C_gR_a}\left(\frac{\alpha_{gdee}}{\alpha_{aa}}\right)^{\frac{\alpha_{gdee}}{\alpha_{aa}-\alpha_{gdee}}}$$

and the rate of recovery of the voltage on the geometric capacitance, which at $t = 0$ is

$$\frac{\mathrm{d}U_r}{\mathrm{d}t}\Big|_{t=0} = \frac{U_{ca}}{C_g R_a}$$

and depends not only on the parameters of the insulation replacement circuit, but also on the value of the voltage U_{ca}, to which the capacitance C_a is charged. For the classic variant of determining the recovery voltage, when initially the geometric and absorption capacitances are charged to the maximum value of the voltage U_0, the obtained formulas will be valid if $U_{ca}=U_0$ is accepted. We note that the characteristics of the recovery voltage used for diagnosis in [4] and in other works can also be calculated based on the determined individual values of the parameters of the elements of the substitution circuit, without conducting additional measurements.

To make sure of this, we consider that the voltage U_{ca} on the absorption capacitance can be obtained with an incomplete charge of the insulation. If a geometric capacitance is charged through a small resistance $(10^6 – 10^7)$ Ω, so that its charge constant is less than 0.1 s, then with such an absorption constant time, the voltage equal to the applied U_0 will actually occur on the insulation after a second, and the absorption capacitance will be charged with an absorption time constant and the voltage on it will be

$$U_a = U_0\left(1 - \exp\left(-\alpha_{aa} t\right)\right).$$

If we limit the process of applying the constant voltage to the insulation due to a small limiting resistance by time

$$\Delta t = -\frac{1}{\alpha_{aa}} \ln\left(1 - \frac{U_{ca}}{U_0}\right),$$

the absorption capacitance will charge up to the voltage U_{ca}. Then it is necessary to discharge the geometric capacitance to low resistance to zero voltage in a short time and record the increase in voltage on the geometric capacitance due to its charge from the absorption capacitance, which is described above.

Recalculation of the parameters of the generalized equivalent circuit to other insulation replacement circuits. Using the parameter values found above for the generalized equivalent insulation replacement circuit, it is possible to find individual parameter values for other four-element circuits reflecting the possibility of through-current flow (see Fig. 1). Theoretically, the conditions of identity of the response to the action of an external constant electric field can be obtained, for example, by equating their transient characteristics in operator form.

Having chosen as the main one the generalized substitution circuit considered above, shown in Fig. 1,*a*, we will find the relationship between the parameters of different equivalent circuits corresponding to the same time dependence of the current through the dielectric by solving the systems of equations obtained by equating the corresponding coefficients of transient conductances in the operator form at different powers of the operator p. In parallel we will also consider the transition from the parameter values of equivalent insulation replacement circuits to the parameter values of the generalized replacement circuit and present formulas for calculating the absorption coefficient for different insulation replacement circuits. For the equivalent circuit of a two-layer dielectric (Fig. 1,*b*), the conductivity in the operator form is equal to

$$Y_2 = \frac{C_1 C_2}{C_1 + C_2} \frac{p^2 + p\left(\alpha_{11} + \alpha_{22}\right) + \alpha_{11}\alpha_{22}}{p + \alpha_{2e}}, \qquad (23)$$

where

$$\alpha_{11} = \frac{1}{R_1 C_1}; \quad \alpha_{22} = \frac{1}{R_2 C_2}; \quad \alpha_{2e} = \frac{R_1 + R_2}{R_1 R_2 \left(C_1 + C_2\right)}.$$

From a comparison of formulas (6) for Y_1 and (23) for Y_2, we write down a system of equations for the transition from the substitution circuit in Fig. 1,*b* to the substitution circuit in Fig. 1,*a* and vice versa, using the parameters of the elements of the equivalent circuits:

$$C_g = \frac{C_1 C_2}{C_1 + C_2}; \qquad (24)$$

$$\frac{1}{C_a R_a}\frac{1}{C_g R_l} = \frac{1}{C_1 R_1}\frac{1}{C_2 R_2}; \qquad (25)$$

$$\frac{1}{C_g R_a} + \frac{1}{C_a R_a} + \frac{1}{C_g R_l} = \frac{1}{C_1 R_1} + \frac{1}{C_2 R_2}; \qquad (26)$$

$$\frac{1}{C_a R_a} = \frac{R_1 + R_2}{R_1 R_2 \left(C_1 + C_2\right)}. \qquad (27)$$

Equation (24) immediately gives the expression for C_g in terms of C_1 and C_2. From (25), taking into account (24), (27), we have

$$R_l = R_1 + R_2. \qquad (28)$$

Substituting the appropriate values into (26) and performing the necessary transformations, as well as taking into account (7) for α_{aa}, we obtain

$$R_a = \frac{R_1 R_2 \left(R_1 + R_2\right) \cdot \left(C_1 + C_2\right)}{\left(C_1 R_1 - C_2 R_2\right)^2}; \qquad (29)$$

$$C_a = \frac{\left(C_1 R_1 - C_2 R_2\right)^2}{\left(C_1 + C_2\right)\left(R_1 + R_2\right)^2}. \qquad (30)$$

The reverse determination of the coefficients for the transition from the circuit in Fig. 1,*a* to the circuit in Fig. 1,*b* is better carried out by first determining α_{11} and α_{22}. To find α_{11} and α_{22}, we use the system of two equations (25), (26), written in the form

$$\begin{cases} \alpha_{11}\alpha_{22} = \alpha_{aa}\alpha_{gl} = A; \\ \alpha_{11} + \alpha_{22} = \alpha_{aa} + \alpha_{ga} + \alpha_{gl} = B. \end{cases} \qquad (31)$$

Having found α_{11} and α_{22}, as well as taking into account equations (27), (28), it is possible to write the parameters of the elements of the insulation replacement circuit in Fig. 1,*b* through the parameters of the elements of the replacement circuit in Fig. 1,*a*, as well as the expression for the absorption coefficient:

$$C_1 = \frac{\alpha_{aa}\left(\alpha_{11} - \alpha_{22}\right)}{R_l \alpha_{11}\alpha_{22}\left(\alpha_{11} - \alpha_{aa}\right)}; \quad C_2 = \frac{\alpha_{aa}\left(\alpha_{22} - \alpha_{11}\right)}{R_l \alpha_{11}\alpha_{22}\left(\alpha_{22} - \alpha_{aa}\right)}.$$

The absorption coefficient for the circuit in Fig. 1,*b* is equal to

$$k_a = \frac{1 + d_{1b}\exp\left(-60\alpha_{1b}\right)}{1 + d_{1b}\exp\left(-15\alpha_{1b}\right)},$$

where $d_{1b} = \dfrac{\left(R_1 C_1 - R_2 C_2\right)^2}{R_1 R_2 \left(C_1 + C_2\right)^2}$, $\quad a_{1b} = \dfrac{R_1 + R_2}{R_1 R_2 \left(C_1 + C_2\right)}$.

For the substitution circuit in Fig. 1,*c*, we have the transient characteristic in the form

$$Y_3 = C_g \frac{p^2 + p\left(\alpha_{gs} + \alpha_{3s} + \alpha_{33}\right) + \alpha_{gs}\alpha_{33}}{p + \alpha_{3e}}, \quad (32)$$

where $\alpha_{gs} = \frac{1}{R_s C_g}$; $\alpha_{3s} = \frac{1}{R_3 C_s}$; $\alpha_{3e} = \frac{R_s + R_3}{R_s R_3 C_1}$.

After comparing the coefficients at different degrees of the operator p in the numerator and denominator for (32) and (6), we obtain formulas for recalculating the coefficients of the generalized insulation replacement circuit (Fig. 1,*a*) to the coefficients of the circuit (Fig. 1,*c*) and vice versa. Taking into account that C_g remains unchanged, we have:

$$C_g = C_g,\ R_l = R_3 + R_s,\ R_a = \frac{R_s}{R_3}\left(R_3 + R_s\right),\ C_a = C_3\left(\frac{R_3}{R_3 + R_s}\right)^2.$$

The reverse transition from the circuit in Fig. 1,*a* to the circuit in Fig. 1,*c* corresponds to the formulas:

$$C_g = C_g,\ R_3 = \frac{R_l^2}{R_a + R_l},\ R_s = \frac{R_a R_l}{R_a + R_l},\ C_3 = C_a\left(1 + \frac{R_a}{R_l}\right)^2,$$

and the absorption coefficient, expressed in terms of the parameter values of the circuit elements (Fig. 1,*c*), is equal to

$$k_a = \frac{R_s + R_3 \exp\left(-60\alpha_{1v}\right)}{R_s + R_3 \exp\left(-15\alpha_{1v}\right)},\ \alpha_{1v} = \frac{R_s + R_3}{R_s R_3 C_3}.$$

For the circuit (Fig. 1,*d*), the transient conductivity in operator form is equal to

$$Y_4 = \frac{C_4 C_s}{C_4 + C_s} \cdot \frac{p^2 + p\left(\alpha_{sl} + \alpha_{4l} + \alpha_{44}\right) + \alpha_{sl}\alpha_{44}}{p + \alpha_{4e}}, \quad (33)$$

where $\alpha_{sl} = \frac{1}{R_l C_s}$; $\alpha_{4s} = \frac{1}{R_l C_4}$; $\alpha_{4e} = \frac{1}{R_4\left(C_4 + C_s\right)}$.

The transition from the circuit in Fig. 1,*d* to the circuit in Fig. 1,*a*, taking into account (33) and the obvious equality of R_l, is possible according to the formulas obtained as a result of solving the corresponding system of equations:

$$R_l = R_l,\ C_g = \frac{C_s C_4}{C_s + C_4},\ R_a = R_4\left(1 + \frac{C_4}{C_s}\right)^2,\ C_a = \frac{C_s^2}{\left(C_s + C_4\right)}.$$

The transition from the circuit in Fig. 1,*a* to the circuit in Fig. 1,*d* and the absorption coefficient is described by the formulas

$$R_l = R_l,\ C_s = C_g + C_a,\ C_4 = C_g\left(1 + \frac{C_g}{C_a}\right),\ R_4 = R_a\left(\frac{C_a}{C_a + C_g}\right)^2.$$

Absorption coefficient for the circuit in Fig. 1,*d*

$$k_a = \frac{R_4 + d_{1g}\exp\left(-60\alpha_{1g}\right)}{R_4 + d_{1g}\exp\left(-15\alpha_{1g}\right)},$$

where $d_{1g} = \frac{C_b^2 R_b}{\left(C_b + C_4\right)^2}$; $\alpha_{1g} = \frac{1}{\left(C_b + C_4\right)R_4}$.

To illustrate the equivalence of insulation replacement circuits, consider, as an example, the case when the determined values of the parameters of the elements of the generalized equivalent insulation circuit are equal to $C_g = 10^{-9}$ F, $C_a = 10^{-10}$ F, $R_l = 10^{12}$ Ω, $R_a = 2 \cdot 10^{11}$ Ω. Then the calculated values of the parameters of the elements of other equivalent circuits will be: for the circuit in Fig. 1,*b* – $C_1 = 1.098 \cdot 10^{-9}$ F, $C_2 = 1.114 \cdot 10^{-8}$ F, $R_1 = 9.968 \cdot 10^{11}$ Ω, $R_2 = 1.557 \cdot 10^{9}$ Ω; for the circuit in Fig. 1,*c* – $C_g = 9.997 \cdot 10^{-9}$ F, $C_3 = 1.353 \cdot 10^{-10}$ F, $R_p = 1.69 \cdot 10^{11}$ Ω, $R_3 = 8.31 \cdot 10^{11}$ Ω; for the circuit in Fig. 1,*d* – $C_b = 1.093 \cdot 10^{-9}$ F, $C_2 = 1.169 \cdot 10^{-8}$ F, $R_b = 9.999 \cdot 10^{11}$ Ω, $R_2 = 1.486 \cdot 10^{9}$ Ω.

As the calculation based on the listed values of the parameters shows, different substitution circuits give practically the same absorption curves and the same absorption coefficient, which for this case is equal to 2.156. At the same time, the interpretation of the results depending on the insulation replacement circuit will be different due to, as already noted, the different structure of the circuits.

The authors would like to make a few remarks regarding the practical application of the methodology for determining the individual values of the parameters of the elements of the insulation replacement circuits proposed in this article.

In practice, even knowing the values of the parameters of the substitution circuit does not lead to an unambiguous interpretation of the results obtained in the process of diagnosis. When assessing the technical condition of the electrical insulation, it should be taken into account that the change in R_l will correspond to both reversible and irreversible changes in the insulation. Of the reversible changes, it is necessary to distinguish, first of all, heating and moistening of the insulation. Irreversible changes in the insulation can occur as a result of diffusion, chemical, electrochemical processes or as a result of mechanical destruction by the thermal fluctuation mechanism. First of all, the leakage resistance should be affected by the carbonization of organic components during significant overheating, the formation of conductive channels (tracking or treeing) as a result of the action of partial discharges on organic materials or the reduction of metal oxides due to electrolysis, especially at constant voltage, in the case of inorganic materials.

An increase in C_a will indicate an increase in the degree of macroinhomogeneity (the formation of macroscopic defects in the insulation, such as cracks, cavities, delamination, etc., as well as a local change in electrophysical characteristics due to aging in an inhomogeneous field), and a decrease in R_a will indicate an increase in the defectivity of the insulation on microscopic level.

With the practical use of our proposed method, knowledge of the individual values of the parameters of the a priori selected insulation replacement circuits in the presence of information about the composition, properties and operation mode of the insulation will also allow to determine the contribution of different phases to the properties of heterogeneous or composite insulation and to orientate in the physical essence of the processes occurring at its aging in operation. However, due to the wide variety of structures and combinations of properties of insulation components, the question of interpretation of measurement results requires a separate consideration in each specific case.

Conclusions. The article describes the scientific basis of the method of determining the individual values of the parameters of the four-element insulation replacement circuits using the example of the generalized replacement

circuit. To calculate these values, a three-point method was used, when readings of absorption current values are selected so that $t_2 - t_1 = t_3 - t_2$, while the constant component of the current is eliminated, and the parameters of the exponential components used in the calculation of the parameter values are consistently determined without error. The formulas for the mutual recalculation of the individual values of the parameters of the elements of the four-element insulation replacement circuits with through conductivity are given and it is shown that the accuracy of the calculation is satisfactory. The possibility of constructing known diagnostic parameters using individual parameter values of the elements of the generalized insulation replacement circuit is shown.

It is noted that within the framework of absorption diagnostic methods, the problem of determining the technical condition of insulation based on the results of the step voltage response study does not have an unambiguous solution. The choice of the substitution circuit and the interpretation of the measurement results should be based on a priori information about the processes taking place in the insulation, or a hypothesis about its structure and properties.

Conflict of interest. The authors of the article declare that there is no conflict of interest.

REFERENCES

1. Protsenko O.R. *Diagnostics of the electrical equipment condition. Course of lectures*. Kyiv, Igor Sikorsky Kyiv Polytechnic Institute Publ., 2022. 162 p. (Ukr).

2. Németh B., Csépes G., Vörös C. Applicability of the dielectric response methods of diagnostics of power transformers: Hungarian experiences. *2011 Electrical Insulation Conference (EIC)*, 2011, pp. 49-53. doi: https://doi.org/10.1109/EIC.2011.5996114.

3. Saha T.K., Purkait P., Muller F. Deriving an Equivalent Circuit of Transformers Insulation for Understanding the Dielectric Response Measurements. *IEEE Transactions on Power Delivery*, 2005, vol. 20, no. 1, pp. 149-157. doi: https://doi.org/10.1109/TPWRD.2004.835436.

4. Soni G., Dutta S., Baral A. Condition Monitoring of Power Transformer Insulation by Return Voltage Measurement. *2021 IEEE 5th International Conference on Condition Assessment Techniques in Electrical Systems (CATCON)*, 2021, pp. 108-112. doi: https://doi.org/10.1109/CATCON52335.2021.9670485.

5. Sarkar S., Sharma T., Baral A., Chatterjee B., Dey D., Chakravorti S. A new approach for determination of moisture in paper insulation of in-situ power transformers by combining polarization-depolarization current and return voltage measurement results. *IEEE Transactions on Dielectrics and Electrical Insulation*, 2013, vol. 20, no. 6, pp. 2325-2334. doi: https://doi.org/10.1109/TDEI.2013.6678886.

6. Gavrilă D.E., Ciprian I., Gavrilă H.C. Applying the Recovery Voltage Method (RVM) to Study the Degradation of High Power Transformer Insulation. *Advanced Materials Research*, 2014, vol. 911, pp. 260-265. doi: https://doi.org/10.4028/www.scientific.net/amr.911.260.

7. Martinez M., Pleite J. Improvement of RVM Test Interpretation Using a Debye Equivalent Circuit. *2019 6th International Advanced Research Workshop on Transformers (ARWtr)*, 2019, pp. 105-110. doi: https://doi.org/10.23919/ARWtr.2019.8930187.

8. Hubarevych O.V. *Reliability and diagnostics of electrical equipment*. Syevyerodonetsk, V. Dahl EUNU Publ., 2016. 248 p. (Ukr).

9. Khamevko O.N., Sushko D.L. Analysis of methods control and diagnostic parameters isolation the traction engine of direct current. *Collected scientific works of Ukrainian State University of Railway Transport*, 2014, no. 147, pp. 152-155. (Ukr). doi: https://doi.org/10.18664/1994-7852.147.2014.75121.

10. *IEEE Std 43-2000. Recommended Practice for Testing Insulation Resistance of Rotating Machinery*, 2000, 28 p. doi: https://doi.org/10.1109/IEEESTD.2000.91301.

11. Stone G.C., Sasic M. Experience with DC polarization-depolarization measurements on stator winding insulation. *2013 IEEE Electrical Insulation Conference (EIC)*, 2013, pp. 7-10. doi: https://doi.org/10.1109/EIC.2013.6554191.

12. Tamus Z.A., Berta I. Application of voltage response measurement on low voltage cables. *2009 IEEE Electrical Insulation Conference*, 2009, pp. 444-447. doi: https://doi.org/10.1109/EIC.2009.5166387.

13. Filipović-Grčić B., Filipović-Grčić D., Uglešić I. Modeling of polarization in oil-paper insulation using recovery voltage measurements. *International Review of Electrical Engineering*, 2011, vol. 6, no. 1, pp. 430-437.

14. Bezprozvannych G.V., Kostukov I.O., Moskvitin E.S. Differentiation of absorption processes in inhomogeneous insulation by curve of recovering voltage of power high voltage cables. *Technical Electrodynamics*, 2021, no. 6, pp. 13-19. doi: https://doi.org/10.15407/techned2021.06.013.

15. Bezprozvannych, G. V., Moskvitin, E. S., & Kyessayev, A. G. The absorption characteristics of the phase and zone paper-impregnated insulation of power cable at direct voltage. *Electrical Engineering & Electromechanics*, 2015, no. 5, pp. 63-68. doi: https://doi.org/10.20998/2074-272X.2015.5.09.

16. *SOU-N-EE-20.302:2007. Testing norms for electrical equipment*. Kyiv, DP MOU «Voienne vydavnytstvo Ukrainy «Varta», 2007. 262 p. (Ukr).

17. Bezprozvannych G.V. Physical interpretation of the recovery voltage curves based on the equivalent circuits of an inhomogeneous dielectric. *Technical Electrodynamics*, 2009, no. 6, pp. 23-27. (Rus).

18. Bezprozvannych G.V., Kostiukov I.A. Error of control of electrical insulation structures by dielectric absorption parameters according to the concept of uncertainty of measurements. *Electrical Engineering & Electromechanics*, 2020, no. 1, pp. 47-51. doi: https://doi.org/10.20998/2074-272X.2020.1.07.

19. Bezprozvannych G.V., Kostiukov I.A. A method of wavelet analysis of time series of parameters of dielectric absorption of electrical insulating structures. *Electrical Engineering & Electromechanics*, 2020, no. 2, pp. 52-58. doi: https://doi.org/10.20998/2074-272X.2020.2.08.

20. Kyrylenko V.M., Kyrylenko K.V., Budko M.O., Denysiuk P.L. Reasoning of additional diagnostic parameters for electric insulation diagnostics by absorption methods. *Electrical Engineering & Electromechanics*, 2021, no. 6, pp. 39-45. doi: https://doi.org/10.20998/2074-272X.2021.6.06.

Received 09.07.2022
Accepted 04.10.2022
Published 01.07.2023

V.M. Kyrylenko[1], *PhD, Assistant Professor,*
K.V. Kyrylenko[1], *PhD,*
[1] National Technical University of Ukraine
«Igor Sikorsky Kyiv Polytechnic Institute»,
37, Prospect Peremohy, Kyiv-56, 03056, Ukraine,
e-mail: vsemychkirg@gmail.com (Corresponding Author)

How to cite this article:
Kyrylenko V.M., Kyrylenko K.V. Theoretical determination of individual values of insulation four-element equivalent circuits elements parameters at technical diagnostics of insulation by absorption methods. *Electrical Engineering & Electromechanics*, 2023, no. 4, pp. 65-74. doi: https://doi.org/10.20998/2074-272X.2023.4.10

UDC 621.313.322 https://doi.org/10.20998/2074-272X.2023.4.11

K.A. Kuchynskyi, O.H. Kensytskyi

Thermomechanical loads of powerful turbogenerator stator winding insulation in the presence of water cooling defects

Introduction. *An analysis of incidents linked to power units' emergency disconnecting from network as a result of turbogenerators' malfunction on the NPP of Ukraine is conducted. It is identified, that the reason of the majority of incidents is an insufficient reliability of the stator winding's direct cooling system.* ***Problem.*** *The most problematic point in winding for today is the frontal parts, where, while cooling is reduced, there are not only thermal, but also thermomechanical loadings on an insulation appearing. The level of these loading depends on structural design of frontal parts and a character of violation of coolant agent circulation in a bar. In some cases they can exceed limit values. The spread and the quality of research on this issue for today are insufficient.* ***Goal.*** *The aim of the completed research is to determine the thermomechanical loading of insulation of stator winding bar in a powerful turbogenerator with a direct liquid cooling under condition when coolant circulation is malfunctioned.* ***Methodology****. A complex mathematical model of thermomechanical processes in an insulation of stator winding bar of a powerful turbogenerator is developed. It takes into account the real geometry of the winding bar, variable thermal loading of core elements in radial and axial directions, as well as ways of fixation of slot and frontal winding parts. Studies of thermomechanical processes in an insulation of stator winding bar of turbogenerator are conducted.* ***Results****. Values of mechanical displacement and stress for the different modes of malfunction are obtained. Areas of bar, where mechanical loading may exceed the boundaries of mechanical durability of material of insulation of stator winding are identified. With decline of coolant liquid consumption the radial displacement and stress in the winding insulation bar in the area, where the bar exits from the slot are increasing along with that the values of radial stress of insulation of the winding bar in places of frontal parts' fixation exceed limit values.* ***Practical significance.*** *The offered mathematical models allow to realize calculation experiments and can be used in practice for development and validation of diagnostic systems, analysis, design and investigation of emergency situations during exploitation of turbogenerators on power stations of Ukraine.* References 20, table 1, figures 8.

Key words: **turbogenerator, stator winding, water cooling, violation of circulation, thermomechanical loading.**

Проведено аналіз інцидентів на АЕС України, пов'язаних із аварійним відключенням енергоблоків від мережі внаслідок відмов турбогенераторів. Встановлено, що причиною більшості із них є недостатня надійність системи безпосереднього охолодження обмотки статора. Найбільш проблемним вузлом обмотки на сьогодні є лобові частини, де при порушеннях охолодження окрім теплового виникають термомеханічні навантаження ізоляції. Рівень цих навантажень залежить від конструктивного виконання лобової частини і характеру порушення циркуляції холодоагенту в стержні. В деяких випадках вони можуть перевищувати граничні значення. Кількість і якість досліджень з цієї проблеми на сьогодні є недостатніми. Метою виконаного дослідження є визначення термомеханічних навантажень ізоляції стержня обмотки статора потужного турбогенератора з безпосереднім рідинним охолодженням при порушеннях циркуляції холодоагенту. Розроблена комплексна математична модель термомеханічних процесів в ізоляції стержнів обмотки статора потужного турбогенератора, що враховує реальну геометрію стержня обмотки, змінні теплові навантаження елементів осердя в радіальному та аксіальному напрямках, а також умови закріплення пазової та лобової частин обмотки. Проведені дослідження термомеханічних процесів в ізоляції стержня обмотки статора потужного турбогенератора. Отримані значення механічних переміщень і напружень для різних видів порушень. Встановлені ділянки стержня, на яких значення механічних навантажень при певних умовах можуть перевищувати межі механічної міцності матеріалу ізоляції обмотки статора. Зі зниженням витрати дистиляту збільшуються радіальні переміщення і напруження в ізоляції стержня обмотки в зоні виходу стержня із паза. При цьому значення радіальних напружень в ізоляції в місцях закріплення лобових частин перевищують припустимі значення. Запропоновані математичні моделі дозволяють реалізувати обчислювальні експерименти і можуть бути використані на практиці для створення та відпрацювання систем діагностики, аналізу, моделювання і розслідування аварійних ситуацій при експлуатації турбогенераторів на електростанціях України. Бібл. 20, табл. 1, рис. 8.

Ключові слова: **турбогенератор, обмотка статора, водяне охолодження, порушення циркуляції, термомеханічні навантаження.**

Introduction. The analysis of incidents related to unplanned emergency disconnections of power units of NPPs of Ukraine from the network and load reduction shows that a significant share of them (from 30 to 70 %) is the result of insufficient reliability of electrical equipment.

The largest share in underproduction of electricity due to failure of electrical equipment is accounted for by turbogenerators (TGs) (up to 70-80 %), relay protection and automation devices (up to 15 %), measuring transformers (up to 7.5 %), electric drive (5.8 %) and power transformers (up to 2.5 %) [1]. That is, TGs are currently the most problematic (unreliable) from the point of view of underproduction of electricity, since each TG damage leads to long and expensive repairs.

The creation of high-power TGs would be impossible without the use of modern cooling systems for the most electromagnetically loaded nodes. First of all, it concerns the stator winding. The introduction of direct liquid (water) cooling of the stator winding rods made it possible to increase the linear load up to 3000 A/cm and, as a result, to increase the unit power of power units, in particular nuclear power plants. Today, the unit power of most power units of nuclear power plants of 1000-1300 MW is a common phenomenon.

TGs with water-cooled windings have an increased risk of clogging the cooling channels (fouling process). Analysis of information on the occurrence and

development of thermal defects of the TG stator windings shows that all of them are related to cooling disorders. The most dangerous violation is partial or complete blockage of the cooling channels. The main causes of this phenomenon are deposits in the water channels and the ingress of hydrogen into the distillate. When hollow conductors are blocked, their temperature can significantly exceed the permissible level [2].

A statistical analysis of data from the experience of operating powerful TGs with direct cooling of the stator winding shows that the share of failures associated with a violation of the circulation of the distillate in it is 10-20 % of the total number. And the idle time of the power unit for this reason takes about 12 % of the total [3]. In specific value, such failures are inferior only to failures caused by the loosening of the extreme packages of the stator core [4].

According to a large-scale study [5], more than half of all generator failures are related to insulation damage. The effect of high temperatures reduces the electrical and mechanical strength of the insulation due to accelerated thermal aging processes.

According to the results of inspections at power plants [6], 10 rods with reduced distillate consumption were found at 6 out of 15 TGs with direct cooling of the stator winding with power of 320 MW. That is, almost every third generator in operation has rods with clogged cooling channels and distillate consumption below technical standards. This is especially dangerous for TGs of maximum power (800 MW and above), since the current density in them is 2-2.5 times higher. In seven stator winding rods of the TVV-1000-4 type generator, a decrease in distillate consumption below the minimum permissible level was found. One rod of TVV-800-2 had a distillate flow significantly below the minimum acceptable level (about 72 % of the nominal), in two rods the reduction of the distillate flow reached 81 % and 51 % of the nominal.

There are known cases of TG damage caused, among other things, by a violation of the refrigerant circulation due to partial and complete blockage of empty conductors. A final event common to these cases, which requires significant financial and time costs for repair and elimination of the consequences, is a breakdown of the main insulation (in particular, the accident of the TVV-1000-4 type generator of power unit No. 1 of the Kalinin NPP, 1988; the breakdown of the insulation of the stator winding rod of the TVV-500-2U3 generator of the Chernobyl NPP, 1994; the accident of the generator type TVV-1000-2Y3 at Khmelnytska NPP, 1997; emergency disconnection from the network of unit No. 3 of the South Ukrainian NPP due to damage to the upper rod of the stator winding of the generator type TVV-1000-2Y3, 2003; emergency disconnection of the generator of power unit No. 1 of Khmelnytska NPP due to an unacceptable increase in the temperature of the stator winding rod during the execution of the program of start-up operations, 2019, etc.). Cases of clogging of the hollow conductors of the stator winding of four-pole generators of the NPP with power of 1000 MW were also recorded.

Problem definition. Since 2011, 10 out of 13 power units of the NPP of Ukraine have been inspected for the condition of the equipment and a set of works has been carried out to extend the terms of their operation. Among them, the mentioned measures also applied to electrotechnical equipment, including TGs and their support systems. The result of the performed works was the extension of the life of power units by another 20 years beyond the standard (30 years).

However, starting in 2016, the number of TG failures began to increase [1]. Moreover, this applies to machines with power of 1000 MW both in two-pole and four-pole versions. In particular, the damage rate of four-pole TGs with power of 1000 MW in the period 2015-2019 compared to 2006-2010 [7] increased threefold. The analysis of the available data allows us to conclude that the reliability indicators of three two-pole TGs out of five and three four-pole ones out of eight do not meet the requirements of GOST 533-2000.

Today, one of the main problems identified during the operation and repair work of generators of the TVV-1000-4Y3 type is depressurization of the winding rods (zone I in Fig. 1). Most of the cases of depressurization of the winding are detected during the period of planned and preventive repairs, and only in six cases the loss of hermeticity of the winding led to emergency shutdowns of power units. The ingress of distillate into the body insulation during the flow of elementary conductors causes its gradual moistening and leads to its electrical breakdown. The rod fails. Whereupon – long-term repairs with significant economic costs. Table 1 shows the damage indicators of TGs type TVV-1000-4Y3 of power units of NPPs of Ukraine in 2015-2019. The specific damage rate of TGs in the four-pole design of type TVV-1000-4Y3 was 0.24 damages per generator year of operation [1].

Since TGs are one of the most responsible objects that ensure the functioning of the electric power system, the main efforts of specialists are directed to research of electromagnetic and thermal processes, force interactions, and the level of magnetic losses in the cores of stators of various designs [8-11]. However, the analysis of the thermomechanical loads of the stator winding elements under different operating conditions of the TG is also essential and important.

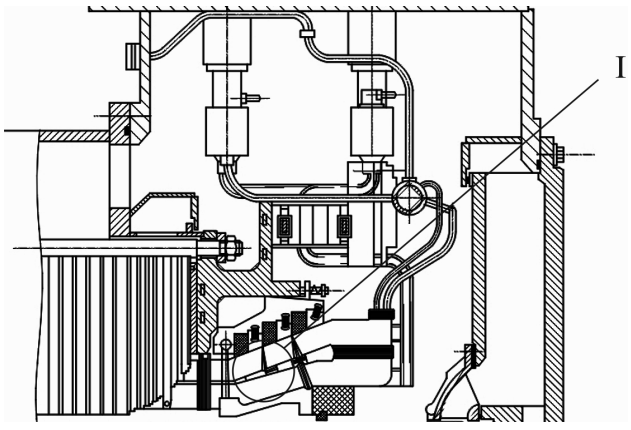

Fig. 1. The end zone of the TG stator of the TVV-1000-4Y3 type

Table 1

Indicators of damage of TGs type TVV-1000-4Y3

Number at the NPPs of Ukraine	8
Number of damage	6
Underproduction of electricity, million kW·h	2230

One of the nodes of the TG with increased damage is the end zone of the stator (Fig. 1), on the elements of which a complex of significant nonuniformly distributed electromagnetic, thermal and thermomechanical loads is concentrated. In connection with this, the actual task of the performed research is to determine the influence of these loads on the reliability of the elements of the end part of the stator winding at the exit from the core slot and in the area of its fastenings when the circulation of the refrigerant in the core is disturbed (zone I, Fig. 1).

The occurrence and development of most thermal defects of the stator winding are associated with cooling disorders. Here, overheating is dangerous not only due to an increase in the probability of a thermal breakdown of the body insulation, but also due to the thermomechanical effect on the elements of the conductors and insulation of the winding, due to the limitations of the thermal expansion of the rod [12].

Significant temperature gradients lead to the emergence of thermoelastic forces, and thermomechanical stresses may exceed the allowable rupture values for the corresponding structural materials. In a number of cases, a defect in the circulation of cooling water in the winding is detected when the process of intensive destruction of the body insulation is already taking place, which leads to its breakdown and a serious accident. Therefore, thermal and thermomechanical aspects of the survivability of high-power generators are among the most important issues subject to experimental research in the coming years [13].

In practice, thermomechanical processes in powerful TGs are modeled mainly by approximate analytical expressions or based on 1D rod calculation schemes.

In [14], the impact of the features of fixing the stator winding in the slot and frontal parts, the reduction of the level of frictional interaction between the winding and the teeth in the end zone at a certain length L_c on the nature of the core pressing pressure distribution was analyzed based on the results of calculations based on the eight-bar 1D model. The considered design with some equivalent thermal and mechanical parameters is considered symmetrical with respect to the middle of the stator. Here, it is assumed that all model's rods are heated uniformly along the length and bore of the stator; the body insulation and the electrically conductive part of the rod do not have mutual axial movements (displacements); the teeth and the back of the core are one whole. Thermomechanical processes are described by a system of 1D differential equations in the axial coordinate x. According to the results, it was concluded that the displacements of the stator winding in the slots lead to mechanical loading of the frontal parts and their fastening elements. These loads are all the greater, the higher the rigidity of the fastening of the frontal parts and the lower the density of fastening the rods in the slots.

The analysis of the results of thermomechanical studies in powerful TGs allows us to conclude that the choice of their parameters is crucial for the theoretical justification of 1D rod calculation schemes. A number of their combinations can usually be obtained only on the basis of the results of experimental studies, which, in turn, are extremely difficult to conduct on real objects in real operating conditions. A number of problems remain unsolved, associated with a relatively high deviation of the calculated results from the field test data, which may be unacceptable for assessing the mechanical condition of the responsible elements of the stator. Therefore, further improvement of approaches to modeling the strength characteristics of the latter is an urgent scientific and technical task.

Assessing the direct mechanical condition of the insulation system is difficult without building correct models of the connected elements of the stator, primarily the core and winding rods, which is due to the high level of model discretization.

In [15], using combined (numerical-analytical) thermomechanical models, mechanical stresses of thermal origin are investigated in a sectioned two-layer bulk winding made of 0.9 mm copper wire, impregnated with epoxy resin, on a segment of a 6-pole stator of a compact reactive machine. The dependencies of stress changes on the coefficient of linear temperature expansion and the coefficient of filling the slot with copper are given. It is noted that at high temperature of copper, stresses can significantly exceed the yield and strength limits of polymer coatings and lead to their destruction.

The paper [16] examines the process of pressing the coils of the stator winding of electric machines under high pressure in order to increase the filling factor of the slots and its effect on the insulation of the conductor of a thermoset polymer film with thickness of 0.05 to 0.1 mm (deformation and thermal conductivity). To predict the effective thermal conductivity of the windings, analytical and numerical (by the Finite Element Method) modeling of the thermal state in steady state and analysis of the mechanical stresses of the compressed electric coils were carried out.

In [17], it is noted that in the insulation of the stators of wind power plants during transient modes, increased levels of thermomechanical stresses occur. To determine their actual level, information on temperatures throughout the year was collected, and their distribution was analyzed using statistical methods.

In [18], a finite element model of the vibration characteristics of the end zone of the TG stator with power of 600 MW is described. The main physical and mechanical properties of the stator elements used in the model are determined by the results of field experiments. Windings cores with direct water cooling, taking into account the complexity of the internal structure, are modeled with a homogeneous isotropic material with properties determined by bending tests.

Approximate methods of solving problems of thermoelasticity are based on the generalized principle of minimum potential energy of deformation together with expressions approximating possible stresses [3]. Here, it is assumed that the body is under the action of surface and volume forces with a known distribution of the temperature field.

Obtaining the most complete results for the values of displacements, deformations and stresses when the temperature changes in the generator elements can be achieved by mathematical modeling of thermomechanical processes in the rods using the Finite Element Method (FEM) in both stationary and transient modes of operation.

The goal of the paper is to develop a mathematical model and analyze thermomechanical processes in the stator elements of the turbogenerator, taking into account the presence of thermal defects and determining the areas of the rod where the thermomechanical stresses are the greatest.

The paper presents the results of theoretical studies of the thermomechanical load parameters of the elements of the stator winding of the generator (rod insulation) in different temperature modes of its operation, in particular, at different distillate consumption (thermal defects of cooling).

Modeling of thermomechanical processes in the insulation of the rods of the stator winding of a water-cooled turbogenerator. Solution of the formulated problem is carried out by using FEM.

The input parameters for studying the thermomechanical displacements and stresses of the nodes of the finite element model under different cooling conditions of the stator winding rod are the temperature distributions of the main nodes of the stator core in a 2D formulation from the central section of the machine to the end zones on the turbine side, as well as the thermomechanical properties of the construction materials (steel, copper, insulation) – their modulus of elasticity E, coefficient of thermal expansion α and Poisson coefficient μ [3].

To solve the problem of thermoelasticity, we use a triangular finite element according to six components of nodal displacements. The coordinates of vertices (nodes) i, j, m in the Cartesian coordinate system can be chosen arbitrarily, which is a significant advantage of FEM. Each element is also characterized by the thickness t and the deviation of its temperature from some equilibrium value ΔT.

It is assumed that the temperature along the length of the rod varies according to a linear law, while the maximum temperature value is reached at the exit of the winding on the side of the turbine, where the heating of the cooling water in the hollow conductors of the rods is the greatest.

The complete system of equations of the element for the calculation of unknown displacements U in nodes [19] is written as

$$[k]\begin{Bmatrix} U_{2i-1} \\ U_{2i} \\ U_{2j-1} \\ U_{2j} \\ U_{2m-1} \\ U_{2m} \end{Bmatrix} = \{f\}, \tag{1}$$

where $[k]$ is the stiffness matrix of the element; variables U with indices «2» (i.e., in the 2D formulation of the problem) correspond to the values of displacement along the y axis, and with indices «2-1» – along the x axis; $\{f\}$ is the load vector of the element due to thermal effects.

The solution for displacement fields using FEM is carried out by minimizing the potential energy of an elastic body [3]. The left-hand side of the system of equations for the elements of the area:

$$[K] = \int_V [B]^T [D][B] dV, \tag{2}$$

where $[B]$ is the matrix of gradients connecting deformations and displacements; $[[B]^T$ is the transposed matrix; $[D]$ is the matrix of elastic constants describing the mechanical properties of connected elements; V is the volume of the finite element.

The right-hand side of the system of equations:

$$\{f\} = -\int_V [N]^T \begin{Bmatrix} X \\ Y \\ Z \end{Bmatrix} dV - \int_V [B]^T [D]\{\varepsilon_0\} dV - \\ -\int_S [N]^T \begin{Bmatrix} P_x \\ P_y \\ P_z \end{Bmatrix} dS - \{P\}, \tag{3}$$

where $[N]^T$ is the transposed matrix of shape functions; X, Y, Z are the volumetric forces; $\{\varepsilon_0\}$ is the initial deformation of the element due to thermal expansion; S is the area of the finite element; P_x, P_y, P_z are the surface loads; $\{P\}$ is the column vector of nodal forces.

Matrix of gradients:

$$[B] = \frac{1}{2S}\begin{bmatrix} b_i & 0 & b_j & 0 & b_m & 0 \\ 0 & c_i & 0 & c_j & 0 & c_m \\ c_i & b_i & c_j & b_j & c_m & b_m \end{bmatrix}, \tag{4}$$

where the coefficients are related to the coordinates of the vertices of the element:

$$\begin{aligned} b_i &= y_j - y_m, & c_i &= x_m - x_j, \\ b_j &= y_m - y_i, & c_j &= x_i - x_m, \\ b_m &= y_i - y_j, & c_m &= x_j - x_i, \end{aligned} \tag{5}$$

matrix of elastic constants:

$$[D] = \frac{E}{1-\mu^2}\begin{bmatrix} 1 & \mu & 0 \\ \mu & 1 & 0 \\ 0 & 0 & \dfrac{1-\mu}{2} \end{bmatrix}. \tag{6}$$

Then

$$[k] = [B]^T [D][B] tS, \tag{7}$$

$$\{\varepsilon_0\} = \alpha\Delta T \begin{Bmatrix} 1 \\ 1 \\ 0 \end{Bmatrix}, \quad (8)$$

$$\{f\} = [B]^T [D]\{\varepsilon_0\} tS = \frac{\alpha E t \Delta T}{2(1-\mu)} \begin{Bmatrix} b_i \\ c_i \\ b_j \\ c_j \\ b_m \\ c_m \end{Bmatrix}. \quad (9)$$

The resulting system of algebraic equations of high order (equal to twice the number of nodes) is solved by the Gaussian elimination method.

After determining the nodal values of the displacement vector based on the heating data of each element and the thermomechanical coefficients of its material, the components of the deformations in the elements are calculated taking into account the corresponding initial and boundary conditions using the solution of the system:

$$\begin{Bmatrix} \varepsilon_x \\ \varepsilon_y \\ \varepsilon_{xy} \end{Bmatrix} = [B] \cdot \begin{Bmatrix} U_{2i-1} \\ U_{2i} \\ U_{2j-1} \\ U_{2j} \\ U_{2m-1} \\ U_{2m} \end{Bmatrix}. \quad (10)$$

Stress components in the material inside the finite element are determined by the difference between the existing and initial deformations of the body due to temperature effects. Thus, the non-zero stress components $\{\sigma\}^T = [\sigma_x, \sigma_y, \tau_{xy}]$ in the elements are calculated according to Hooke law

$$\{\sigma\} = [D]\{\varepsilon\} - [D]\{\varepsilon_0\}. \quad (11)$$

Analysis of the results of numerical investigations. The study was carried out for a four-pole generator type TVV-1000-4Y3 with power of 1000 MW.

The calculation area is the most heated half of the rod (slot and frontal parts) of the stator winding on the turbine side (Fig. 2).

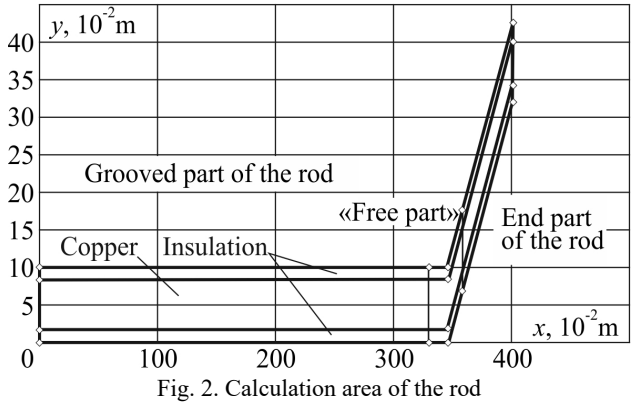

Fig. 2. Calculation area of the rod

For clarity, the upper and lower layers of the model, corresponding to the insulation, are highlighted with a violation of scale. The «free» (from fasteners) zone of the rod is highlighted by vertical lines at the point where the winding exits the slot. Here, it was assumed that the displacements along the *x* axis in the middle of the rod in the active zone of the stator (in the central cross-section of the machine) are equal to zero. The displacements of all nodes of the model along the *y* axis at the bottom of the slot and at the border of the upper and lower rods of the stator winding (slot part of the winding) are also absent. In this area under research, the components free to move – only along the *x* axis.

Thermomechanical characteristics (displacements and stresses in the insulation of the stator winding rod of the generator) were analyzed in nominal load modes under normal conditions of its cooling, as well as in the presence of thermal defects – at 1/2 and 1/3 distillate consumption through the rod.

The fastening should not prevent the displacements of the frontal parts in the axial direction (along the *x* axis) during thermal elongation of the rectilinear slot part of the stator winding. Here, according to the results of the thermomechanical calculation of the half of the stator (from the middle to the end zone on the side of the turbine), the obtained values of the displacements components of the core nodes in the axial section were the boundary conditions of the first kind for the nodes of the rod model, in which the fastening of the frontal parts was «carried out».

Insulation temperatures in the element of each cross-section in the slot part were calculated as the arithmetic mean between the values in the copper of the winding and the iron of the stator of the core model. The change in the temperature of the rod nodes during the transition from element to element along the length of the model was set according to a linear law. As a result, we get rows of values of nodal displacements and stresses in finite elements.

Figures 3, 4 show graphs of changes in thermomechanical displacements and stresses along the insulation layer along the *x* and *y* coordinates (hereinafter curves 1 and 2) in the slot and frontal parts of the winding under the nominal cooling conditions of the stator winding rods.

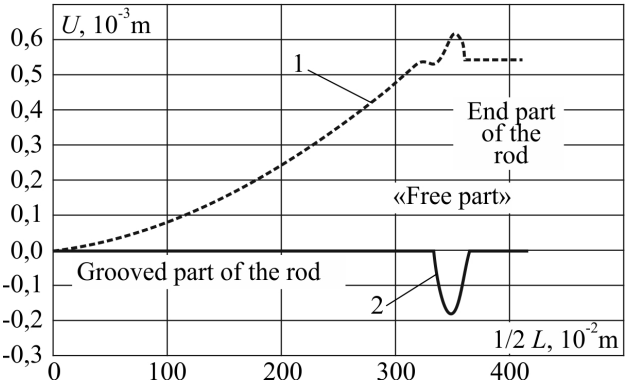

Fig. 3. Distribution of displacements in the insulation along the rod

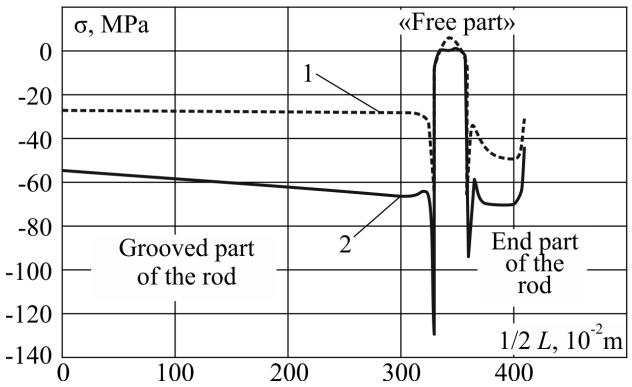

Fig. 4. Distribution of stresses in the insulation along the rod

As can be seen, when the winding is heated, there is an axial displacement of the rods relative to the stator core (Fig. 3, curve 1), which corresponds to the condition of structurally ensuring the freedom of movement of the rod along the *x* axis.

In the area where the winding exits the slot, radial «deformation» of the rod occurs in the area «free» from fasteners (Fig. 3, curve 2). Here, fixing the winding in the frontal zone prevents «unlimited free» displacement, as a result of which compressive forces arise in the rods and in the details of the frontal parts fastening (Fig. 4, curves 1, 2).

In the slot part, the compressive stresses are explained by the boundary conditions in the middle of the model and the impossibility of radial displacements of the rod nodes. There are practically no stresses in the «free» zone of the rod (on its «knee»). «Peaks» at the exit from the slot and at the place of the beginning of fasteners in the frontal part are caused by a sharp change in the boundary conditions at these so-called «special points» and methodical properties of the approximate finite element approach (by the degree of discretization of the computational domain) to solving the problem.

Thus, at the nominal temperature of the winding and its cooling conditions, the values of radial and axial stresses in the insulation along the length of the rod generally do not exceed the permissible values (80-90 MPa).

Figures 5, 6 reflect, respectively, the value and nature of changes in thermomechanical displacements and stresses in the insulation at 1/2 of the flow rate of the coolant through the rod. The flow reduction was assumed to be uniform across all cooling channels.

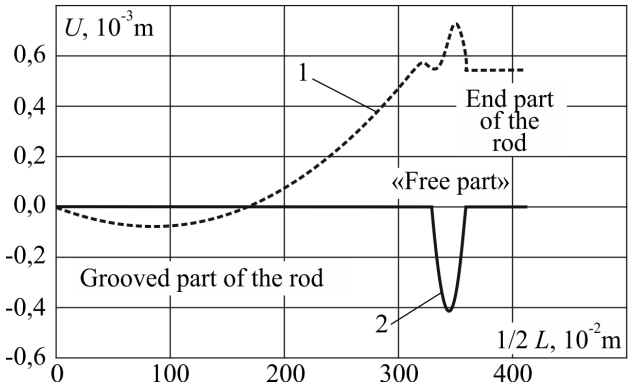

Fig. 5. Distribution of displacements in the insulation along the rod

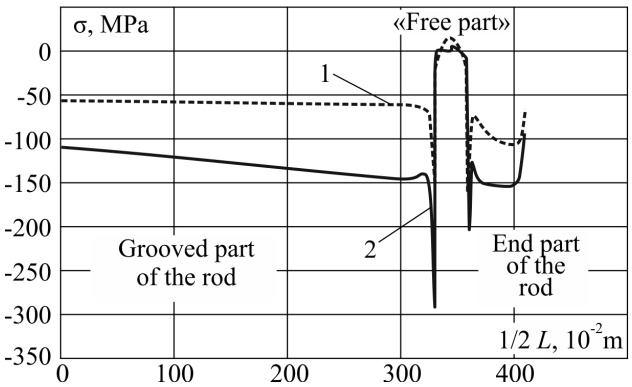

Fig. 6. Distribution of stresses in the insulation along the rod

With a decrease in water flow by 50 %, the axial displacements increase slightly and radial displacements increase significantly (more than two times) at the point where the rod exits the slot. Here, the values of the radial stresses in the insulation elements of the slot zone and in the places where the frontal parts are fastened exceed the permissible values. In the latter, the same applies to axial stresses, too.

As the cooling conditions worsen (when there is only 1/3 of the distillate flow through the winding – Fig. 7, 8), the thermomechanical characteristics of the insulation deteriorate significantly along the entire length of the rod, the stress values exceed the permissible values beyond the mechanical tensile strength of the material, which is unacceptable.

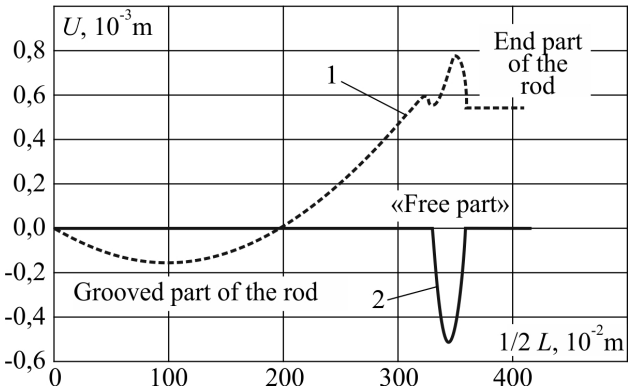

Fig. 7. Distribution of displacements in the insulation along the rod

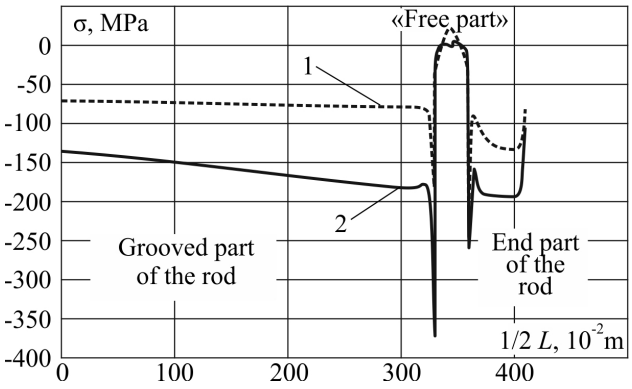

Fig. 8. Distribution of stresses in the insulation along the rod

Thus, in order to avoid emergency situations, it is necessary to constantly monitor the temperature of the stator winding rods. The work [20] emphasizes the importance of thorough regular leak testing of water-cooled rods, contains information on the causes and development of water leaks, describes recommended methods of inspection, pressure drop testing, maintenance, and also offers possible options for timely repair.

Conclusions.

1. A mathematical model and technique of numerical calculation of thermomechanical characteristics in the rod elements of the stator winding of a powerful turbogenerator in the presence of cooling defects have been developed. The technique is based on the Finite Element Method implemented as a package of applied software for a personal computer.

2. The paper presents the results of numerical calculations of the thermomechanical stresses of the elements of the stator winding (rod insulation) of a four-pole generator of the TVV-1000-4Y3 type with power of 1000 MW, depending on the temperature mode, taking into account the change in the distillate flow rate. It is shown that under the nominal cooling conditions of the stator winding rods, displacements reach 600 μm (axial) and 200 μm (radial), thermomechanical stresses are on average 60 MPa and 70 MPa at temperatures of 69.8 °C and 85.3 °C in the slot and front parts of the winding in accordance. In case of violations: 705 μm and 401 μm; stresses – 125 MPa and 150 MPa at temperatures of 100.8 °C and 147.3 °C (1/2 of distillate consumption); 790 μm and 500 μm, 160 MPa and 190 MPa at temperatures of 116.3 °C and 178.3 °C (1/3 of distillate consumption).

3. A comparative analysis of thermomechanical stresses in the insulation of the rod in case of violations of the circulation of the distillate in the stator winding showed that their greatest values are observed near the exit of the rod from the slot and the places where the frontal parts are attached. As the cooling conditions deteriorate, even in the nominal load mode, their values in individual insulation nodes exceed the limit of the material's mechanical tensile strength. At lower than nominal water consumption, the thermal and thermomechanical characteristics of the elements of the winding rod are significantly enhanced in terms of the violation of the physical properties of the insulation material and the reliability of the machine as a whole.

4. The developed models and techniques can be used for the study of thermal and thermomechanical processes, taking into account cooling defects different from those considered in the paper, as well as the presence of external mechanical influences, in maneuvering modes of starting and resetting the electrical load of the TG, for studying the effectiveness of various methods of cooling regulation, etc.

Conflict of interest. The authors of the article declare that there is no conflict of interest.

REFERENCES

1. Kensytskyi O.H. Operating reliability of generating equipment of power units of nuclear power plants of Ukraine. *Proceedings of the Institute of Electrodynamics of the National Academy of Sciences of Ukraine*, 2021, no. 58, pp. 100-106. (Ukr). doi: https://doi.org/10.15407/publishing2021.58.100.

2. Svoboda R., Blecken W.-D. Corrosion and deposits in water-cooled generator stator windings: overview of water cooling of generators. *PowerPlant Chemistry* 2018, vol. 20, no. 5, pp. 290-294.

3. Kuchynskyi K.A. *Thermal and thermomechanical processes in turbogenerators*. Kyiv, TOV Pro Format Publ., 2020. 239 p. (Rus).

4. Khutoretsky G.M., Fedorenko G.M., Vartanyan A.G., Krushinsky A.G. Heating of the stator winding rod of a powerful turbogenerator with direct cooling. *Technical Electrodynamics*, 1990, no. 4, pp. 55-62. (Rus).

5. Brutsch R., Tari M., Frohlich K., Weiers T., Vogelsang R. Insulation Failure Mechanisms of Power Generators [Feature Article]. *IEEE Electrical Insulation Magazine*, 2008, vol. 24, no. 4, pp. 17-25. doi: https://doi.org/10.1109/MEI.2008.4581636.

6. Poliakov V.I. Diagnostics of the technical condition of a water cooling channels and fastenings of the winding rods of powerful turbogenerators for extension of their service. *Elektricheskie stantsii*, 2001, no. 10, pp. 34-39. (Rus).

7. Klyuchnikov O.O., Fedorenko H.M., Vyhovskyi O.V. Prediction thermal defects in the winding and stator core powerful turbogenerators NPP units and their localization with intelligent methods and means. *Problems of nuclear power plants' safety and of Chornobyl*, 2011, no. 17 pp. 17-26. (Ukr).

8. Li S., Gallandat N.A., Mayor J.R., Habetler T.G., Harley R.G. Calculating the Electromagnetic Field and Losses in the End Region of a Large Synchronous Generator Under Different Operating Conditions With 3-D Transient Finite-Element Analysis. *IEEE Transactions on Industry Applications*, 2018, vol. 54, no. 4, pp. 3281-3293. doi: https://doi.org/10.1109/TIA.2018.2823262.

9. Ide K., Hattori K., Takahashi K., Kobashi K., Watanabe T. A Sophisticated Maximum Capacity Analysis for Large Turbine Generators Considering Limitation of Temperature. *IEEE Transactions on Energy Conversion*, 2005, vol. 20, no. 1, pp. 166-172. doi: https://doi.org/10.1109/TEC.2004.842389.

10. Albanese R., Calvano F., Dal Mut G., Ferraioli F., Formisano A., Marignetti F., Martone R., Romano A., Rubinacci G., Tamburrino A., Ventre S. Coupled Three Dimensional Numerical Calculation of Forces and Stresses on the End Windings of Large Turbo Generators via Integral Formulation. *IEEE Transactions on Magnetics*, 2012, vol. 48, no. 2, pp. 875-878. doi: https://doi.org/10.1109/TMAG.2011.2173307.

11. Milykh V.I., Revuzhenko S.A. Comparative analysis of the magnetic losses power in the stator core of a turbogenerator with axial ventilation channels in its yoke and teeth. *Bulletin of NTU «Kharkiv Polytechnic Institute» Series: Electrical Machines and Electromechanical Energy Conversion*, 2019, no. 20(1345), pp. 167-171. (Rus). doi: https://doi.org/10.20998/2409-9295.2019.20.24.

12. Vyhovsky O.V. Analysis, prediction and control of thermomechanical defects in the water cooling system of the stator windings of powerful turbogenerators NPP. *Problems of nuclear power plants' safety and of Chornobyl*, 2015, no. 24, pp. 20-26. (Ukr).

13. Stone G.C., Sedding H.G., Wheeler R., Wilson A. Results of Destructive Analysis of Service-Aged Hydrogenerator Stator Winding Insulation. *CIGRE SCA1 Colloquium*, 26 Sep. 2019, 8 p.

14. Zozulin Yu.V., Antonov O.E., Bychik V.M., Borychevskyi A.M. *Creation of new types and modernization of existing turbogenerators for thermal power stations* Kharkiv, Kolegium Publ., 2011. 228 p. (Ukr).

15. Silwal B., Sergeant P. Thermally Induced Mechanical Stress in the Stator Windings of Electrical Machines. *Energies*, 2018, vol. 11, no. 8, art. no. 2113. doi: https://doi.org/10.3390/en11082113.

16. Kulan M.C., Baker N.J., Widmer J.D., Lambert S.M. Modelling the Mechanical and Thermal Properties of Compressed Stator Windings. *8th IET International Conference on Power Electronics, Machines and Drives (PEMD 2016)*, p. 6. doi: https://doi.org/10.1049/cp.2016.0132.

17. Rui Liang, Xuezhong Liu, Tianlong Zhang, Rui Zhang, Guanfang Liu, Jing Wang, Yonghong Ji, Jian Yang. Determination of thermal and thermo-mechanical stresses in stator insulation of wind turbine generator based on online monitoring temperatures. *2016 IEEE International Conference on Dielectrics (ICD)*, 2016, pp. 1183-1186. doi: https://doi.org/10.1109/ICD.2016.7547829.

18. Zhao Y., Yan B., Chen C., Deng J., Zhou Q. Parametric Study on Dynamic Characteristics of Turbogenerator Stator End Winding. *IEEE Transactions on Energy Conversion*, 2014, vol. 29, no. 1, pp. 129-137. doi: https://doi.org/10.1109/TEC.2013.2294334.

19. Kuchynskyi K.A. Influence of the degree of fixing the winding at the end of the slot of the turbogenerator stator on thermomechanical characteristics of its core isolation. *Proceedings of the Institute of Electrodynamics of the National Academy of Sciences of Ukraine*, 2022, no 61, pp. 31-36. (Ukr). doi: https://doi.org/10.15407/publishing2022.61.031.

20. Worden J.A., Mundulas J.M. *Understanding, Diagnosing, and Repairing Leaks in Water-Cooled Generator Stator Windings*. GE Power Systems, GER-3751A, 2008, no. 1, 28 p.

Received 20.09.2022
Accepted 08.11.2022
Published 01.07.2023

K.A. Kuchynskyi[1], *Doctor of Technical Science, Senior Research Scientist,*
O.H. Kensytskyi[1], *Doctor of Technical Science,*
[1] Institute of Electrodynamics of NAS Ukraine,
56, Peremogy Avenue, Kyiv, 03057, Ukraine,
e-mail: kuchynskyy1962@gmail.com (Corresponding Author),
kensitsky@ukr.net

How to cite this article:
Kuchynskyi K.A., Kensytskyi O.H. Thermomechanical loads of powerful turbogenerator stator winding insulation in the presence of water cooling defects. *Electrical Engineering & Electromechanics*, 2023, no. 4, pp. 75-82. doi: https://doi.org/10.20998/2074-272X.2023.4.11

UDC 621.3 https://doi.org/10.20998/2074-272X.2023.4.12

K. Manikandan, S. Sasikumar, R. Arulraj

A novelty approach to solve an economic dispatch problem for a renewable integrated micro-grid using optimization techniques

Introduction. *The renewable integrated microgrid has considered several distributed energy sources namely photovoltaic power plant, thermal generators, wind power plant and combined heat and power source. Economic dispatch problem is a complex operation due to large dimension of power systems. The objective function becomes non linear due to the inclusion of many constraints. Hourly demand of a commercial area is taken into consideration for performing economic dispatch and five combinations are considered to find the best optimal solution to meet the demand.* ***The novelty*** *of the proposed work consists of a Sparrow Search Algorithm is used to solve economic load dispatch problem to get the better convergence and accuracy in power generation with minimum cost.* ***Purpose.*** *Economic dispatch is performed for the renewable integrated microgrid, in order to determine the optimal output of all the distributed energy sources present in the microgrid to meet the load demand at minimum possible cost.* ***Methods.*** *Sparrow Search Algorithm is compared with other algorithms like Particle Swarm Optimization, Genetic Algorithm and has been proved to be more efficient than Particle Swarm Optimization, Genetic Algorithm and Conventional Lagrange method.* ***Results****. The five combinations are generation without solar power supply system and Combined Heat and Power source, generation without solar and wind power supply systems, generation including all the distributed energy sources, generation without wind power supply system and Combined Heat and Power source, generation without thermal generators.* ***Practical value.*** *The proposed optimization algorithm has been very supportive to determine the optimal power generation with minimal fuel to meet the large demand in commercial area.* References 20, table 4, figures 11.

Key words: **economic dispatch, combined heat and power source, solar power, thermal generators, wind power, optimization techniques.**

Вступ*. Відновлювана інтегрована мікромережа розглядає кілька розподілених джерел енергії, а саме фотоелектричну електростанцію, теплові генератори, вітряну електростанцію та комбіноване джерело тепла та електроенергії. Завдання економічної диспетчеризації є складною операцією через велику розмірність енергосистем. Цільова функція стає нелінійною через включення безлічі обмежень. На виконання економічної диспетчеризації враховується погодинна потреба торгової площі, і розглядаються п'ять комбінацій, щоб знайти найкраще оптимальне рішення задоволення попиту.* ***Новизна*** *запропонованої роботи полягає в тому, що алгоритм пошуку горобця використовується для вирішення економічного завдання диспетчеризації навантаження, щоб отримати кращу збіжність та точність при виробленні електроенергії з мінімальними витратами.* ***Мета****. Економічна диспетчеризація виконується для відновлюваної інтегрованої мікромережі, щоб визначити оптимальну потужність всіх розподілених джерел енергії, присутніх у мікромережі, для задоволення потреби навантаження з мінімально можливими витратами.* ***Методи****. Алгоритм пошуку горобця порівнюється з іншими алгоритмами, такими як оптимізація рою частинок, генетичний алгоритм, і було доведено, що він ефективніший, ніж оптимізація рою частинок, генетичний алгоритм і традиційний метод Лагранжа.* ***Результати****. П'ять комбінацій: генерація без сонячної системи енергопостачання та комбінованого джерела тепла та електроенергії, генерація без систем сонячного та вітрового енергопостачання, генерація, що включає всі розподілені джерела енергії, генерація без системи вітрової енергії та комбінованого джерела тепла та електроенергії, генерація без теплової енергії. генератори.* ***Практична цінність****. Запропонований алгоритм оптимізації дуже допоміг визначити оптимальне виробництво електроенергії з мінімальною витратою палива для задоволення великого попиту в комерційній сфері.* Бібл. 20, табл. 4, рис. 11.

Ключові слова: **економічна диспетчеризація, теплоелектроцентраль, сонячна енергетика, теплові генератори, вітроенергетика, методи оптимізації.**

1. Introduction. Due to rapid increase in load demand of residential and commercial consumers, the cost of electric power generation plays major role in the power system planning and operation. In order to reduce the cost of energy consumption, the most suitable way is the integration renewable energy sources among distributed network. The complexity of interconnections and the size of the distributed energy sources of electric power systems that are controlled in a coordinated way. It leads to the optimal allocation of generators which are present in power system to meet the entire load demand with minimum possible cost. Whether a generator ought to participate in sharing the load at a given interval of your time could leads to a problem of unit commitment. Once the unit commitment problem has been resolved, it becomes a haul of optimum allocation of the obtainable generations to satisfy the forecasted load demand for this interval. Optimal load dispatch, a sub-problem of the unit commitment problem, is considered a particularly important problem that deals with the minimization of operational cost and power generation facilities and by in power systems economics point of view. In optimization problems, the most desirable objectives are minimization of fuel cost, total real and reactive power losses in the system, improvement of voltage profile by minimizing the voltage deviation. Among these objectives, in economic dispatch (ED) problem the minimization of fuel cost is considered by taking real power outputs of thermal generators and renewable energy sources like solar, wind, combined heat and power source (CHP) source, fuel cell and micro turbine etc.

2. Literature Review. In [1] the modified version of tradition Lagrange algorithm for solving the dynamic combined economic and emission dispatch problem has been proposed. The effective operation of diesel generator in large power network was analysed using whale optimization algorithm. In [2] the authors stated that there are two species of captive house sparrows, and they typically use both producer and scrounger behaviors to get their food.

Authors of work [3] stated that the producers energetically look for food, while the scroungers acquire food by producers and the birds use behavioral strategies flexibly, and toggle between producing and scrounging.

In [4] the authors proposed the concept to use particle swarm technology to optimize nonlinear functions. The connections between Particle Swarm Optimization (PSO), artificial life, and Genetic Algorithm (GA) are explored. They developed a social-science context for PSO. They illustrated that the evidence from computer simulations create an powerful technique called information processing technique which is sufficient to control the vast amount of information comprising human familiarity.

In [5] an enhanced energy management operation by managing distributed energy resources to achieve better energy efficiency at the lowest possible cost by operating a system over a time horizon and assure several key constraints has been proposed.

In [6] the authors illustrated a design layout methodology for a grid-connected PV-Battery-Diesel microgrid in that applied power management strategy in various system's components was considered.

In [7] the authors explained a detailed connection between the investment cost, lifetime, cost function, and the fluctuant energy forecasting of solar and wind resources. In [8] the authors illustrated the onshore wind power generation cost through a geographical distribution method which gives the data of technical potential and an estimation of the local unit cost structure. In [9] a bird's eye view of PSO applications by analyzing more that 700 PSO application papers has been presented. In [10] the formulation and solution approach for the ED problem by considering various micro grid operational constraints has been given. The suggested method allows the microgrid to function cost-effectively in grid-connected mode and also maintaining stability in islanded mode.

In [11] the authors proposed Attractive and Repulsive Particle Swarm Optimization (ARPSO) algorithm for economic load dispatch, which relieves the assumptions imposed on the optimized objective function. The common problem in all evolutionary computation techniques is premature convergence and overcome in ARPSO algorithm. In [12] microgrid energy management as an optimal power flow problem has formulated, and a distributed Energy Management Strategy has been proposed, where the Microgrid Central Controller and the local controllers jointly compute an optimal schedule has been formulated. In [13] the authors proposed a new swarm intelligence optimization technique called Sparrow Search Algorithm (SSA) to solve optimization problems in various engineering applications.

In [14] the method to determine low carbon optimal dispatch problem by considering carbon tax mechanism and verified the performance of emission on IEEE test system has been proposed. In [15] the analytical based hierarchy process algorithm to ensure the weight coefficients for each objective function has been developed. For a standalone microgrid system, the multiobjective based optimal dispatch problem was developed by incorporating the various renewable energy sources. To get optimal power dispatch quantum PSO was developed and validated.

In [16] the authors illustrated the new strategy to determine the optimal solution for the Combined Economic and Emission Dispatch problem. In this case study the location of East Coast of USA generating units were considered. In this proposed method the cost functions for solar and wind energy was considered and determined the solution using modified Harmony Search Algorithm. In [17] the dynamic nature of the load for various buildings has been considered. In this fuel cost and operational cost of the generating units were incorporated during the sizing of the various components. In [18] the mixed integer programming method to fetch the optimal allocation of renewable energy sources based on 24 hours time horizon has been developed. The test cases were considered for two different mode of operation like standalone mode and grid connected mode.

In [19, 20] the comprehensive optimization method to solve the multi objective ED problem has developed. The nonlinear and non-convex constrained optimal power problem was solved using Gray Wolf Optimization techniques.

The novelty of this paper has developed the new optimization algorithm – Sparrow Search Algorithm (SSA) to determine the optimal generator scheduling by incorporating the renewable energy sources. In this paper the obtained results from the developed algorithms was compared with the conventional method and other optimization techniques like GA and PSO techniques. The main advantages of proposed algorithm will provide the improved search space and better convergence.

3. Formulation of ED problem with renewable energy sources. For solving ED problem, a microgrid consists of two traditional generators (synchronous generators), one CHP, wind generator and solar generator is considered. The optimal dispatch of renewable energy sources is shown in Fig. 1.

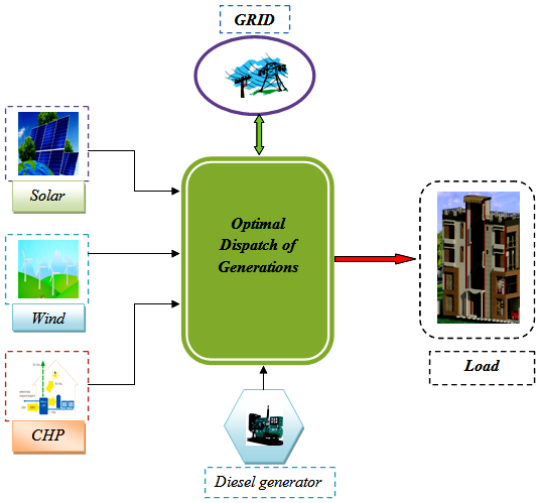

Fig. 1 Operation of optimal dispatch problem

The 24 hours load demand profile is shown in Fig. 2.

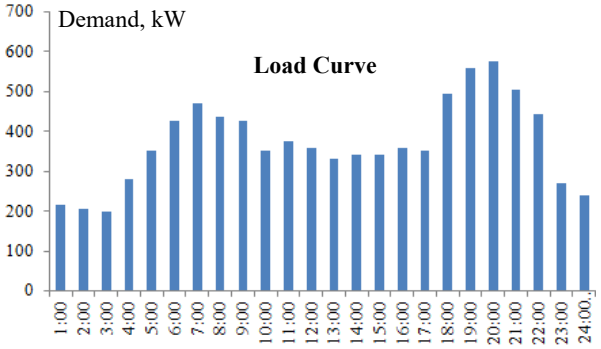

Fig. 2. 24 hours load profile

A. Modeling of diesel generators (DG's) and CHP. The second order polynomial function is considered as the cost function for the CHP and two conventional generators and given the assumed cost coefficients in Table 1.

Table 1

Cost coefficients

Cost coefficients	CHP	Generator 1	Generator 2
a	0.024	0.029	0.021
b	21	20.16	20.4
c	1530	992	600

The lower and upper generation limits of DG's are:

$$0 \text{ kW} \le P_{gi} \le 650 \text{ kW}. \quad (1)$$

The lower and upper generation limits of CHP are:

$$0 \text{ kW} \le P_{gc} \le 600 \text{ kW}. \quad (2)$$

Calculations for the generation of generators and CHP:

$$\lambda = \frac{P_{load} + \sum_{i=1}^{n}\left(\frac{b_i}{2a_i}\right)}{\sum_{i=1}^{n}\left(\frac{1}{2a_i}\right)}. \quad (3)$$

To find the generation of each generator individually using the following formula:

$$P_{gi} = \frac{\lambda - b_i}{2a_i}. \quad (4)$$

where λ is the incremental cost.

The non linear quadratic cost function (F_i) of diesel generator is given in (5) [2, 3], where P_{gi} is the output power:

$$F_i = c_i + b_i \cdot P_{gi} + a_i \cdot P_{gi}^2. \quad (5)$$

The total cost F_T is calculated by summing up the costs of individual generator:

$$F_T = F_1 + F_2 + F_c. \quad (6)$$

B. Modeling of solar. HOMER software – the Micropower Optimization Model provided the critical photovoltaic (PV) data needed to complete the case study. The formula used to determine solar power generation is as follows:

$$P_{PV} = P_{STC} \cdot \frac{G_{ac}}{G_{STC}} \cdot \left(1 + k \cdot \left(T_c - T_i\right)\right), \quad (7)$$

where P_{PV} is the output power, kW; P_{STC} is the maximum power of PV under standard test conditions (STC), 330 kW; G_{ac} is the incident solar radiation, W/m^2; G_{STC} is the solar irradiance at STC, 1000 W/m^2; k is the temperature coefficient, –0.0047; T_i is the reference temperature, 25 °C; T_c is the cell temperature, °C.

The solar power generation cost function is as in [4] and it considers the operation and maintenance (O&M) costs of the generated energy and also investment cost of the equipments.

1) Cost of generation without including investment cost is the:

$$G^E \cdot P_{PV}, \quad (8)$$

where G^E is the O&M cost per unit generated energy (0.016 \$/kW); P_{PV} is the solar power output.

When compared to wind energy the solar is very costly, but can be included in a system with the support of solar renewable energy credits.

2) Cost of generation including investment cost is the:

$$a \cdot I^P \cdot P_g + G^E \cdot P_{PV}, \quad (9)$$

where

$$a = \frac{r}{\left(1 - (1+r)^{-N_j}\right)}, \quad (10)$$

r is the rate of interest (0.09); N is the investment lifetime (20 years); I^P is the investment costs per unit installed power (5000 \$/kW) or 1630 \$/kW by considering the renewable energy credits.

The above equation is used to compute the entire generating cost of solar energy, which includes the depreciation of all generation equipment.

C Modeling of wind. HOMER software – the Micropower Optimization Model was used to acquire the wind data needed for the investigation. The formula used to determine wind power generation (P) is as follows:

$$P = \frac{1}{2} \cdot \left(\rho \cdot A \cdot V^3\right), \quad (11)$$

where ρ is the air density, kg/m^3; A is the wind swept area, $\pi \cdot r^2 = \pi \cdot (22/2)^2 = 380.1327$ m^2; V is the velocity of wind, m/s.

The cost function for wind generation is as shown in [4], and it takes into account both the equipment investment and the generated energy's O&M costs:

1) Cost of generation without including investment cost:

$$G^E \cdot P_W, \quad (12)$$

where G^E is the O&M cost per unit generated energy (0.016 \$/kW); P_W is the wind power output.

2) Cost of generation including investment cost

$$a \cdot I^P \cdot P_W + G^E \cdot P_W, \quad (13)$$

where

$$a = \frac{r}{\left(1 - (1+r)^{-N_j}\right)} = 0.1095, \quad (14)$$

r is the interest rate (0.09); N is the investment lifetime (20 years); I^P is the investment costs per unit installed power (1400 \$/kW).

The above equation can be used to compute the entire generating cost of wind energy, taking into account all of the generation equipment's depreciation.

4. Proposed methodologies. Sparrows are social birds that come in a variety of colours and sizes. They can be found in almost every section of the globe and like to live in human-populated areas. They eat mostly grain and weed seeds. The sparrow, unlike some of the other little birds, is highly intelligent and has an excellent memory. The producer and the scrounger [2] are two varieties of captive house sparrows. Producers actively seek out food sources, whereas scroungers rely on producers to provide them with food. Furthermore, research suggests that birds switch between generating and scrounging behavioural methods frequently [3]. In order to locate food, sparrows frequently employ both the producer and scrounger strategies [2]. Individuals in the group keep an eye on each other's actions. Temporarily, the attackers in the bird herd battle for food resources with the partners with large intakes in order to increase their own predation rate [4] [3]. Individual energy reserves are crucial when sparrows employ varied foraging techniques, the sparrows with low energy reserves more scrounging. Birds on the outside of the colony are more likely to be attacked by predators and

are continuously trying to improve their position [5]. The birds in the center come closer to their neighbors in order to reduce the size of their danger zone [7, 14]. It is commonly known that sparrows have a natural interest about everything while also remaining attentive. When a bird detects a predator, for example, one or more individuals chirp, and the entire flock flies away [14].

Application of SSA to solve ED problem:

1. Initialize the SSA parameters i.e., the maximum iteration count (G), the amount of producers (PD), the sparrows count who recognize the danger (SD), the alarm value (A_2), the number of sparrows (n).

2. Initialization of fitness function i.e., sum of individual cost function of various generators in various power stations.

3. The cost coefficients and generation limits of various generators, total demand is given as input.

4. After executing the first step of the program a large number (equal to the population size) of vectors of real power fulfilling the total demand and generation limits are randomly allocated.

5. The fitness function's value is calculated for each vector of active power. To obtain f_g, the values obtained in one iteration are compared to the values obtained in the preceding iteration. If the f_g obtained in one iteration is better than the f_g obtained in previous iteration then the value of f_g is updated, otherwise it is left unchanged.

6. The active power vector (L_{best}) reflects the economic load dispatch solution, and the ultimate value of f_g is the minimal cost.

The flow chart for solving ED problem using SSA is shown in Fig. 3.

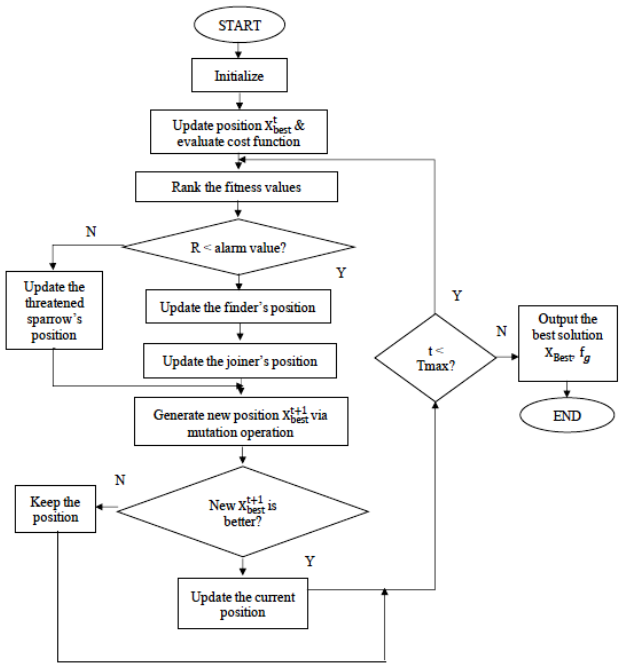

Fig. 3. Flowchart for solving ED problem using SSA

5. Results and discussion. The ED problem is performed using the MATLAB platform and the total power generation costs for the five scenarios mentioned below for the microgrid are compared. Five scenarios considered are:

Case 1: 2 Diesel Generators + CHP;
Case 2: 2 Diesel Generators + Solar;
Case 3: 2 Diesel Generators + Wind;
Case 4: CHP + Solar + Wind;
Case 5: 2 Diesel Generators + CHP + Solar + Wind.

This is to identify the optimal arrangement of generations that can be incorporated into a micro grid for the least or moderate cost.

After conducting the ED operation among the three dispatchable generations, the generation cost is determined from the cost functions corresponding to its generated power. The cost of wind and solar power generation is also calculated depending on generation using their respective cost functions. As a result, the overall cost of production may be estimated.

Genetic algorithm. The total cost of generation for each hour, obtained using GA for Case 1 is shown in Fig. 4.

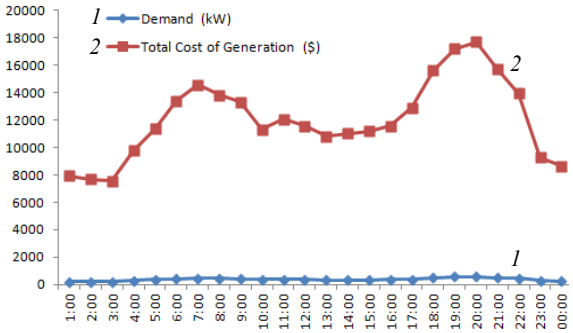

Fig. 4. Variation of demand and cost analysis for Case 1

The total cost of generation excluding investment cost, total cost of generation including investment cost, total cost of generation including investment cost with renewable energy credits for solar for each hour, obtained using GA for Case 2 are shown in Fig. 5.

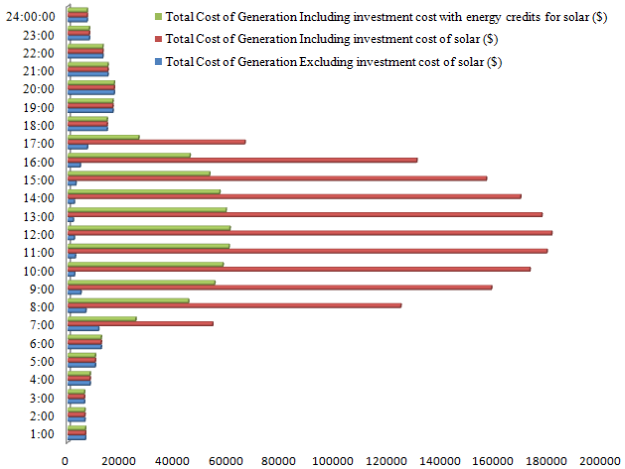

Fig. 5. Variation of demand and cost analysis for Case 2

The total cost of generation excluding investment cost, total cost of generation including investment cost for each hour, obtained using GA for Case 3 are shown in Table 2.

The total cost of generation excluding investment cost, total cost of generation including investment cost, total cost of generation including investment cost with renewable energy credits for solar for each hour, obtained using GA for Case 4 are shown in Fig. 6.

Table 2

Power generation and cost analysis for Case 3 using GA

Time, hrs	Demand, kW	Total generation cost excluding investment cost of wind, $	Total generation cost including investment cost of wind, $
1:00	215	6520.8	6520.8
2:00	205	6060.93	7310.17
3:00	200	5310.763	10706.61
4:00	280	7214.224	13198.28
5:00	350	8374.143	18368.07
6:00	425	11614.43	15711.21
7:00	470	13180.34	16402.54
8:00	435	10852	20423.74
9:00	425	9463.016	24947.54
10:00	350	7886.234	20676.66
11:00	375	8928.383	20263.07
12:00	360	8946.674	17323.44
13:00	330	7909.188	18337.57
14:00	340	8173.499	17745.24
15:00	343	8832.256	15125.83
16:00	360	9491.263	14887.11
17:00	350	8668.774	17045.54
18:00	495	14218.21	16226.28
19:00	560	16510.13	17759.37
20:00	575	17182.05	17694.08
21:00	503	14908.02	15077.87
22:00	444	13079.02	13248.87
23:00	270	7927.52	8127.26
24:00	240	7060.974	7771.51

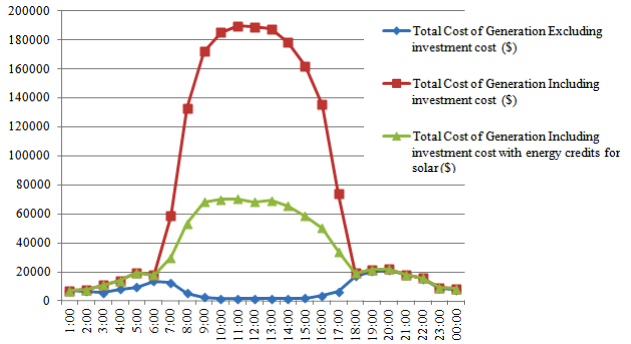

Fig. 6. Variation of cost analysis for Case 4 using GA

The total cost of generation excluding investment cost, total cost of generation including investment cost, total cost of generation including investment cost with renewable energy credits for solar for each hour, obtained using GA for Case 5 are shown in Fig. 7.

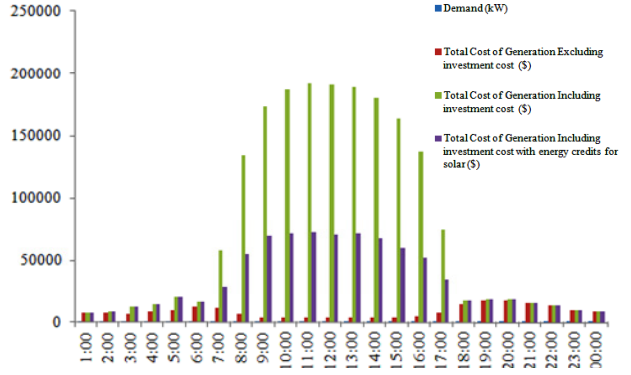

Fig. 7. Variation of cost analysis for Case 5 using GA

Sparrow Search Algorithm (SSA). The total cost of generation for each hour, obtained using SSA for Case 1 is shown Fig. 8.

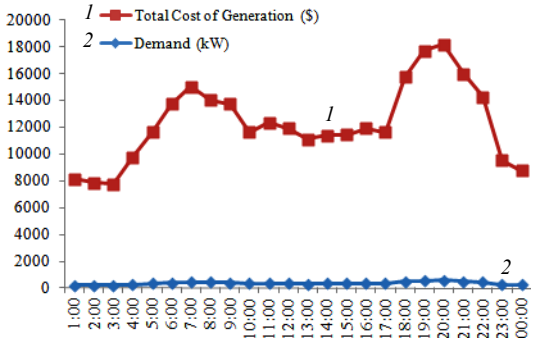

Fig. 8. Variation of cost analysis for Case 1 using SSA

The total cost of generation excluding investment cost, total cost of generation including investment cost, total cost of generation including investment cost with renewable energy credits for solar for each hour, obtained using SSA for Case 2 are shown in Fig. 9.

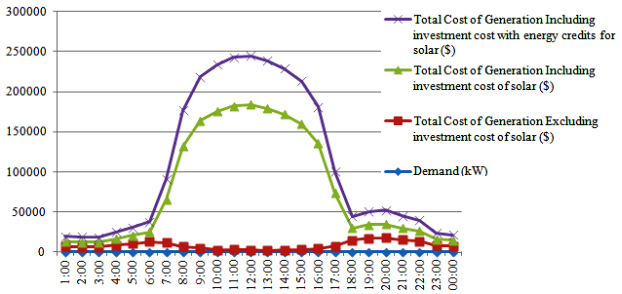

Fig. 9. Variation of cost analysis for Case 2 using SSA

The total cost of generation excluding investment cost, total cost of generation including investment cost for each hour, obtained using SSA for Case 3 are shown in Fig. 10.

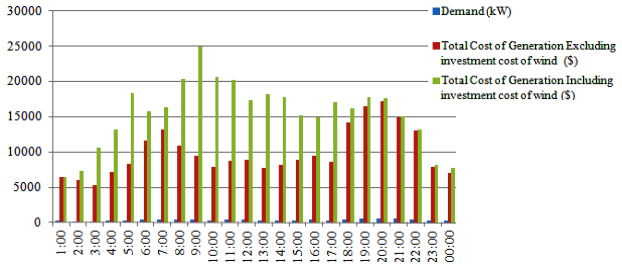

Fig. 10. Variation of cost analysis for Case 3 using SSA

The total cost of generation excluding investment cost, total cost of generation including investment cost, total cost of generation including investment cost with renewable energy credits for solar for each hour, obtained using SSA for Case 4 are shown in Fig. 11.

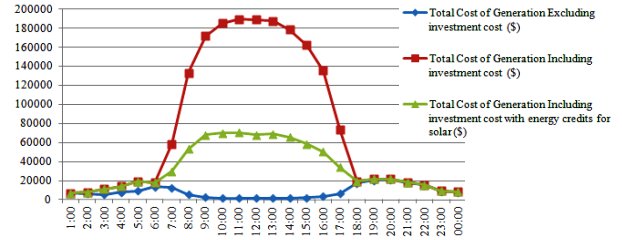

Fig. 11. Variation of cost analysis for Case 4 using SSA

The total cost of generation excluding investment cost, total cost of generation including investment cost, total cost of generation including investment cost with

renewable energy credits for solar for each hour, obtained using SSA for Case 5 are shown in Table 3. The total cost of generation per day for all the five cases obtained using Lagrange's method, GA, PSO, SSA are shown in Table 4.

Table 3

Cost analysis for Case 5 using SSA

Time, hrs	Total cost of generation excluding investment cost, $	Total cost of generation including investment cost, $	Total cost of generation including investment cost with energy credits for solar, $	Time, hrs	Total cost of generation excluding investment cost, $	Total cost of generation including investment cost, $	Total cost of generation including investment cost with energy credits for solar, $
1:00	7909.8	7909.8	7909.8	13:00	3128.217	189074	70775.26
2:00	7474.43	8723.67	8723.67	14:00	3127.884	179871.9	67197.82
3:00	6722.963	12118.81	12118.81	15:00	3561.15	163635.3	59987.18
4:00	8536.324	14520.38	14520.38	16:00	5136.048	136613.6	51634.52
5:00	9623.343	19617.27	19617.27	17:00	7257.599	74653.77	34874.69
6:00	12580.43	16677.21	16677.21	18:00	14891.21	16899.28	16899.28
7:00	11853.58	57801.14	29004.26	19:00	16912.13	18161.37	18161.37
8:00	6547.547	134121.6	54588.05	20:00	17498.05	18010.08	18010.08
9:00	4022.912	173348.3	69659.57	21:00	15461.02	15630.87	15630.87
10:00	3128.32	186525.1	71536.42	22:00	13798.02	13967.87	13967.87
11:00	3128.346	191129.8	72056.39	23:00	9219.72	9419.46	9419.46
12:00	3128.102	190386.2	69820.2	24:00	8403.574	9114.11	9114.11

Table 4

Cost comparison between Lagrange's method, PSO, GA, SSA

Cases considered	Total cost of generation per day obtained using various optimization techniques, $			
	Lagrange's method	GA	PSO	SSA
2 DG's and 1 CHP	286244.76	289970.9	286435.4	286357.8
2 DG's and solar excluding investment cost	190337.6	190662.1	190370.7	190341.68
2 DG's and solar including investment cost	1712631.41	1712956	1712665	1712636.2
2 DG's and solar including investment cost with renewable energy credits	686605.61	686930.1	686638.7	686609.7
2 DG's and wind excluding investment cost	237607.55	238312.8	237665.5	237610.7
2 DG's and wind including investment cost	370193.42	370898.7	370251.4	370196.6
1 CHP, solar and wind excluding investment cost	200178.2	200178.2	200178.2	200178
1 CHP, solar and wind including investment cost	1855051.97	1855051.97	1855051.97	1855051.97
1 CHP, solar and wind including investment cost with renewable energy credits for solar	829204.37	829204.37	829204.37	829204.37
2 DG's, 1 CHP, solar and wind excluding investment cost	202994.67	205910	203139.688	203050.7
2 DG's, 1 CHP, solar and wind including investment cost	1857959.21	1860790.4	1858019.842	1857931
2 DG's, 1 CHP, solar and wind including investment cost with renewable energy credits for solar	831931.21	834763.69	831993.502	831904.6

6. Conclusions. Economic dispatch aims to schedule the outputs of all available generation units in the power system to keep fuel costs as low as possible while meeting system restrictions. Many traditional algorithms and optimization techniques can be used to solve economic dispatch problem among which Sparrow Search Algorithm (SSA) is used. Traditional method i.e., Lambda iteration method and optimization methodology i.e., Genetic Algorithm (GA) and Particle Swarm Optimization (PSO) are solved to prove that SSA gives better results than those.

A renewable integrated microgrid with two synchronous generators, one combined heat and power source, a wind power plant, and a solar power plant is already being proposed. The MATLAB code for traditional method i.e., Lambda iteration method, PSO, GA, SSA has been executed successfully for all the considered cases and a comparison table was made to compare the total cost of generation obtained in PSO, GA, SSA, Lambda iteration method. It can be concluded that SSA produce better and accurate results than all other algorithms used. SSA gives better convergence speed than PSO and GA.

Conflict of interest. The authors declare that they have no conflicts of interest.

REFERENCES

1. Mehdi M.F., Ahmad A., Ul Haq S.S., Saqib M., Ullah M.F. Dynamic economic emission dispatch using whale optimization algorithm for multi-objective function. *Electrical Engineering & Electromechanics*, 2021, no. 2, pp. 64-69. doi: https://doi.org/10.20998/2074-272X.2021.2.09.

2. Barnard C.J., Sibly R.M. Producers and scroungers: A general model and its application to captive flocks of house sparrows. *Animal Behaviour*, 1981, vol. 29, no. 2, pp. 543-550. doi: https://doi.org/10.1016/S0003-3472(81)80117-0.

3. Barta Z., Liker A., Mónus F. The effects of predation risk on the use of social foraging tactics. *Animal Behaviour*, 2004, vol. 67, no. 2, pp. 301-308. doi: https://doi.org/10.1016/j.anbehav.2003.06.012.

4. Kennedy J., Eberhart R. Particle swarm optimization. *Proceedings of ICNN'95 - International Conference on Neural Networks*, 1995, vol. 4, pp. 1942-1948. doi: https://doi.org/10.1109/ICNN.1995.488968.

5. Abou Houran M., Chen W., Zhu M., Dai L. Economic Dispatch of Grid-Connected Microgrid for Smart Building Considering the Impact of Air Temperature. *IEEE Access*, 2019, vol. 7, pp. 70332-70342. doi: https://doi.org/10.1109/ACCESS.2019.2915528.

6. Hijjo M., Felgner F., Frey G. PV-battery-diesel microgrid design for buildings subject to severe power outages. *2017 IEEE PES PowerAfrica*, 2017, pp. 280-285. doi: https://doi.org/10.1109/PowerAfrica.2017.7991237.
7. Augustine N., Suresh S., Moghe P., Sheikh K. Economic dispatch for a microgrid considering renewable energy cost functions. *2012 IEEE PES Innovative Smart Grid Technologies (ISGT)*, 2012, pp. 1-7. doi: https://doi.org/10.1109/ISGT.2012.6175747.
8. Fueyo N., Sanz Y., Rodrigues M., Montañés C., Dopazo C. The use of cost-generation curves for the analysis of wind electricity costs in Spain. *Applied Energy*, 2011, vol. 88, no. 3, pp. 733-740. doi: https://doi.org/10.1016/j.apenergy.2010.09.008.
9. Poli R. Analysis of the Publications on the Applications of Particle Swarm Optimisation. *Journal of Artificial Evolution and Applications*, 2008, pp. 1-10. doi: https://doi.org/10.1155/2008/685175.
10. Ahn S.-J., Moon S.-I. Economic scheduling of distributed generators in a microgrid considering various constraints. *2009 IEEE Power & Energy Society General Meeting*, 2009, pp. 1-6. doi: https://doi.org/10.1109/PES.2009.5275938.
11. Swarup K.S., Kumar P.R. A new evolutionary computation technique for economic dispatch with security constraints. *International Journal of Electrical Power & Energy Systems*, 2006, vol. 28, no. 4, pp. 273-283. doi: https://doi.org/10.1016/j.ijepes.2006.01.001.
12. Shi W., Xie X., Chu C.-C., Gadh R. Distributed Optimal Energy Management in Microgrids. *IEEE Transactions on Smart Grid*, 2015, vol. 6, no. 3, pp. 1137-1146. doi: https://doi.org/10.1109/TSG.2014.2373150.
13. Xue J., Shen B. A novel swarm intelligence optimization approach: sparrow search algorithm. *Systems Science & Control Engineering*, 2020, vol. 8, no. 1, pp. 22-34. doi: https://doi.org/10.1080/21642583.2019.1708830.
14. Yu F., Chu X., Sun D., Liu X. Low-carbon economic dispatch strategy for renewable integrated power system incorporating carbon capture and storage technology. *Energy Reports*, 2022, vol. 8, pp. 251-258. doi: https://doi.org/10.1016/j.egyr.2022.05.196.
15. Zhao Y., Song X., Wang F., Cui D. Multiobjective optimal dispatch of microgrid based on analytic hierarchy process and quantum particle swarm optimization. *Global Energy Interconnection*, 2020, vol. 3, no. 6, pp. 562-570. doi: https://doi.org/10.1016/j.gloei.2021.01.008.
16. Parimalasundar E., Senthil Kumar R., Chandrika V.S., Suresh K. Fault diagnosis in a five-level multilevel inverter using an artificial neural network approach. *Electrical Engineering & Electromechanics*, 2023, no. 1, pp. 31-39. doi: https://doi.org/10.20998/2074-272X.2023.1.05.
17. Parimalasundar E., Kumar N.M.G., Geetha P., Suresh K. Performance investigation of modular multilevel inverter topologies for photovoltaic applications with minimal switches. *Electrical Engineering & Electromechanics*, 2022, no. 6, pp. 28-34. doi: https://doi.org/10.20998/2074-272X.2022.6.05.
18. Nazari-Heris F., Mohammadi-Ivatloo B., Nazarpour D. Economic Dispatch of Renewable Energy and CHP-Based Multi-zone Microgrids Under Limitations of Electrical Network. *Iranian Journal of Science and Technology, Transactions of Electrical Engineering*, 2020, vol. 44, no. 1, pp. 155-168. doi: https://doi.org/10.1007/s40998-019-00208-4.
19. Ayachi B., Boukra T., Mezhoud N. Multi-objective optimal power flow considering the multi-terminal direct current. *Electrical Engineering & Electromechanics*, 2021, no. 1, pp. 60-66. doi: https://doi.org/10.20998/2074-272X.2021.1.09.
20. Mezhoud N., Ayachi B., Amarouayache M. Multi-objective optimal power flow based gray wolf optimization method. *Electrical Engineering & Electromechanics*, 2022, no. 4, pp. 57-62. doi: https://doi.org/10.20998/2074-272X.2022.4.08.

Received 05.09.2022
Accepted 03.11.2022
Published 01.07.2023

Krishnan Manikandan[1], *Research Scholar*,
Sivakumar Sasikumar[1], *PhD*, *Associate Professor*,
Rajendran Arulraj[2], *PhD*, *Assistant Professor*,
[1] Department of Electrical Engineering,
Annamalai University, Chidambaram, Tamilnadu – 608002, India,
e-mail: mani.ksmv@gmail.com (Corresponding Author);
ssasikumar77@yahoo.in
[2] Department of Electrical and Electronics Engineering,
K. Ramakrishnan College of Engineering,
Samayapuram, Tiruchirappalli, Tamilnadu – 621112, India,
e-mail: arulrajcdm88@gmail.com

How to cite this article:
Manikandan K., Sasikumar S., Arulraj R. A novelty approach to solve an economic dispatch problem for a renewable integrated micro-grid using optimization techniques. *Electrical Engineering & Electromechanics*, 2023, no. 4, pp. 83-89. doi: https://doi.org/10.20998/2074-272X.2023.4.12

UDC 621.3 https://doi.org/10.20998/2074-272X.2023.4.13

P. Venkatesh, N. Visali

Enhancing power system security using soft computing and machine learning

Purpose. *To guarantee proper operation of the system, the suggested method infers the loss of a single transmission line in order to calculate a contingency rating.* ***Methods****. The proposed mathematical model with the machine learning with particle swarm optimization algorithm has been used to observe the stability analysis with and without the unified power flow controller and interline power flow controller, as well as the associated costs. This allows for rapid prediction of the most affected transmission line and the location for compensation.* ***Results****. Many contingency conditions, such as the failure of a single transmission line and change in the load, are built into the power system. The single transmission line outage and load fluctuation used to determine the contingency ranking are the primary emphasis of this work.* ***Practical value****. In order to set up a safe transmission power system, the suggested stability analysis has been quite helpful.* References 16, figures 9.
Key words: **machine learning, particle swarm optimization, power system security, interline power flow controller, unified power flow controller.**

Мета*. Щоб гарантувати правильну роботу системи, запропонований метод передбачає втрату однієї лінії передачі розрахунку рейтингу непередбачених обставин.* ***Методи****. Запропонована математична модель з алгоритмом машинного навчання з оптимізацією рою частинок використовувалася для спостереження за аналізом стійкості з уніфікованим регулятором потоку потужності та міжлінійним регулятором потоку потужності та без нього, а також з відповідними витратами. Це дозволяє швидко передбачити найбільш постраждалу лінію передачі та місце для компенсації.* ***Результати****. Багато позаштатних ситуацій, таких як відмова однієї лінії електропередачі та зміна навантаження, вбудовані в енергосистему. Основна увага у цій роботі приділяється відключенню однієї лінії електропередачі та коливанням навантаження, які використовуються для визначення рейтингу непередбачених обставин.* ***Практична цінність****. Пропонований аналіз стійкості виявився дуже корисним до створення безпечної системи передачі електроенергії.* Бібл. 16, рис. 9.
Ключові слова: **машинне навчання, оптимізація рою частинок, безпека енергосистеми, вбудований контролер потоку потужності, уніфікований контролер потоку потужності.**

Introduction. Multiple renewable and non-renewable power sources have been added to the grid in recent years in an effort to keep up with rising demand. Generators, transmission lines, and distribution networks already have it rough, and transient load changes make matters worse. Investigating the most appropriate load modeling is necessary for predicting the system's features. When paired with contingency criteria and constant-impedance, constant-current, and constant-power loads, the ZIP load model creates accurate and durable representations of loads over extended time periods (ZIP is a common acronym for the polynomial load model – constant impedance Z, constant current I, constant active power P).

Even the most basic contemporary lives require complex electrical systems. Therefore, it is crucial to keep the electrical system reliable. A power system's users, infrastructure, and bottom line must all be safeguarded if the system is to be considered secure. The failure of a transmission line or generator, an unexpected increase in load demand, the destruction of a transformer, etc. are just a few examples of the kinds of occurrences that might make such a power system useless. Maintaining the safety of the power system is an intriguing problem. Power outages have increased as a consequence of system instability. Many companies go bankrupt, and the lives of regular people are disrupted. Because this is the source of the blackout, taking decisive action to stop it from spreading to other lines is crucial. The reliability of a system after an outage or other disruption may be swiftly evaluated with the use of a contingency analysis. The device's normal operation may be affected once a faulty part is removed; thus, the backup strategy must account for this possibility. Any significant disruption to line traffic has the potential to overload neighboring lines and set off a chain reaction. There needs to be swift action from the regulator when a line failure leads to a spike in demand. The electricity grid's operators and planners should always have the system's future in mind. The process of contingency screening utilizes a wide variety of static and time-dependent techniques [1, 2].

Load models allow for the prediction of how loads will react to a change in voltage or frequency. Finding a load model that is user-friendly and accurate across a variety of load response scenarios is crucial. Implementing strategies is essential. The impacts of the polynomial load model and the steady-state load model are compared in this study. The model's imprecision stems from its over-reliance on a single load to characterize three distinct types of attributes. In terms of constant impedance, constant current, and constant power, polynomial load models can characterize resistive loads, induction motor loads, and variable-frequency loads. As a result, the accuracy of the polynomial load model is maximized. Devices in the flexible AC transmission system (FACTS) may reduce the impact of many disturbances in the power grid. The line overload index and the voltage stability index must be used together to estimate system stress in an emergency. Faulty bus hotspots may be found more quickly and precisely using the line stability index because it takes less time and effort to calculate [3-7].

The most flexible FACTS device is the unified power flow controller (UPFC), which uses a combination of series and parallel inverters connected over a DC bus. In practice, devices are positioned along the weakest line to mitigate its effects. A proposed severity index is a grading system for outcomes. It is hypothesized that the UPFC will be in the most perilous position. Paycheck distribution is a top priority in UPFC's layout. The suggested technique is tested in a pilot program using the IEEE 30 bus system. In this post, we will describe the techniques used to analyze the reliability of electrical grids. The criteria for determining vital lines and the procedures to follow in the event of an interruption are detailed. There is no hiding from the book's significance and effectiveness. We compare the outcomes from before and after compensation were provided.

Examination of contingency method. Unpredictability and instability characterize the occurrence of a contingency phenomenon within a control framework. In the field of control systems, numerous substantial investigations of

probable outcomes have been done. The particle swarm optimization (PSO) technique is used to determine the best possible FACTS installation site and configuration settings.

Load modeling is the most common causes of contingencies are unexpected shifts in load. When analyzing various loads, load modeling is crucial. Modeling the relationship between power and voltage on a load bus mathematically is known as load modeling. It has far-reaching implications for research into electrical grids [8, 9]. In this research, we consider two distinct load models to conduct our risk assessment. Models of constant and variable loads as below.

Steady state load model. The continuous load paradigm is also known as steady state load. The model's active and reactive power equations are:

$$P_i = \sum_{j=1}^{n} V_i Y_{ij} V_j \cos\left(\theta_{ij} + \delta_j - \delta_i\right); \quad (1)$$

$$Q_i = -\sum_{j=1}^{n} V_i Y_{ij} V_j \sin\left(\theta_{ij} + \delta_j - \delta_i\right). \quad (2)$$

Elements of active power and reactive power, both on and off the diagonal, are derived using P_i and Q_i as the active and reactive powers, respectively.

Polynomial load model. A common acronym for the polynomial load model is ZIP (constant impedance *Z*, constant current *I*, constant active power *P*). Power equations for the model are :

- at bus *i*:

$$P_i = \left[\sum_{j=1}^{n} V_i Y_{ij} V_j \cos\left(\delta_{ij} + \theta_j - \theta_i\right)\right]\left[P_1 V_i^2 + P_2 V_i + P_3\right]; \quad (3)$$

$$Q_i = \left[-\sum_{j=1}^{n} V_i Y_{ij} V_j \sin\left(\delta_{ij} + \theta_j - \theta_i\right)\right]\left[P_1 V_i^2 + P_2 V_i + P_3\right]; \quad (4)$$

- at bus *j*:

$$P_j = \left[\sum_{i=1}^{n} V_j Y_{ji} V_i \cos\left(\delta_{ji} + \theta_i - \theta_j\right)\right]\left[P_1 V_j^2 + P_2 V_j + P_3\right]; \quad (5)$$

$$Q_j = \left[-\sum_{i=1}^{n} V_j Y_{ji} V_i \sin\left(\delta_{ji} + \theta_i - \theta_j\right)\right]\left[P_1 V_j^2 + P_2 V_j + P_3\right], \quad (6)$$

where bus *i* has an active power of P_i, whereas bus *j* has a reactive power of Q_i and so on. Values of nodal voltage at buses *i* and *j* are denoted by V_i and V_j; δ_{ij} is the angular voltage of the i^{th} and j^{th} units; the line's admissions denoted by Y_{ji}; the parameters for the ZIP load are denoted by P_1, P_2, and P_3.

Machine learning (ML). Waikato University in New Zealand is responsible for developing WEKA (short for Waikato Environment for Knowledge Analysis). The program includes data-processing tools, machine-learning algorithm implementation, and visualization resources. It's open-source and free, so you may use it to analyze as much data as you like. Prediction techniques in ML are known as supervised learning. The case distribution in a dataset may be seen with unsupervised learning. Input-outcome associations are uncovered using supervised learning techniques. The relationships between them are a model. Common supervised approaches include classification and regression models. Different kinds of data analysis are available in ML. In this study, the J48 algorithm is employed to group information based on the suggested indices. The j48 tree represents C4.5. It's used to make data sets. Decision trees are useful for sorting data into groups. A tree is structured using this way. Assuming the tree already exists, we append the structure of data. Predicted missing values are disregarded by j48 during tree building.

Proposed index to find the severity of the line is named as hybrid lines stability ranking index (HLSRI) is employed to forecast and categorize, in descending order, a set of important lines' numerical values. After that, compensation is employed to guarantee the system's continued security:

$$HLSRI = \frac{4XQ_n}{[V_m]^2}\left[\frac{|Z|^2}{X_{Line}}\beta - \frac{XQ_n}{[\sin(\theta-\delta)]^2}(\beta-1)\right] \le 1; \quad (7)$$

where $\beta = \begin{Bmatrix} 1 & \delta < \delta_C \\ 0 & \delta \ge \delta_C \end{Bmatrix}$,

where δ is used as a modifier and β is utilized as a toggle. In a stable system, HLSRI is less than 1, whereas in an unstable system, HLSRI is close to 1 [10]. The generated values of HLSRI is upload to train the ML tool (Fig. 1). The j48 category also is shown in Fig. 1.

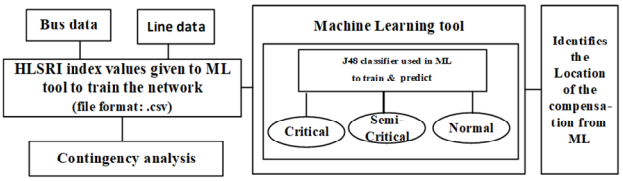

Fig. 1. Transmission line data analysis, categorization, and prediction

The configuration described is seen in Fig. 2. The 5-foot tree has 3 leaves and 1 branch. It demonstrates that the range of the HLSRI fluctuates [11, 12], while the size and number of leaves in the decision tree remain constant. Here, we classify rankings according to 3 criteria for the testing system [13]:

Classifier model, J48 tree Structure, IEEE 30

1) most stress/critical (7.0): HLSRI > 0.0461;
2) moderate stress/semi-critical (10.0): 0.0296 > HLSRI ≤ 0.0461;
3) healthy line/non-critical (24.0): HLSRI < 0.0296.

Weka Classifier Tree Visualizer

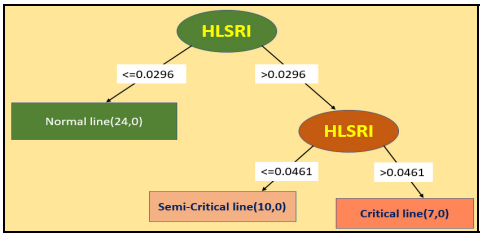

Fig. 2. HLSRI using ML-J48 algorithm tree structure for IEEE 30 bus

Modeling of custom power devices is also included are works from the UPFC and interline power flow controller (IPFC). An injection model may be used to estimate the ranking index for actual and reactive power flow, which is relevant for FACTS appliance control restrictions. Here is a basic summary of the mathematical modelling process used by FACTS.

Shunt and series controller (UPFC). There are really 2 controllers at work in a unified power flow system which is linked to the transmission line through DC link capacitors shared by the shunt and series voltage source converters. The arrangement converter's yield voltage is added to the nodal voltage at bus *i* to get the final nodal voltage at bus *j*. How the power's intensity is controlled is

shown by the δ_{CR} phase angle, and the voltage's direction is provided by the yield voltage V_{CR}. A three-stage UPFC is supported by 2 voltage sources and power restrictions.

$$E_{VR} = V_{CR}(\cos\delta_{CR} + j\sin\delta_{CR}); \quad (8)$$

$$R_e = \{-E_{VR}I_{VR} + E_{VR}I_m\}. \quad (9)$$

Active and reactive power equations at bus i are:

$$P_i = \{V_i^2 G_{ii} + V_i V_j [G_{ij}\cos(\theta_i - \delta_j) + B_{ij}\sin(\theta_i - \delta_j)] + V_i V_{CR}[G_{ij}\cos(\theta_i - \delta_{CR}) + B_{ij}\sin(\theta_i - \delta_{CR})] + V_i V_{CR}[G_{VR}\cos(\theta_i - \delta_{CR}) + B_{ij}\sin(\theta_i - \delta_{CR})]\}[P_1 V_i^2 + P_2 V_i + P_3]; \quad (10)$$

$$Q_i = \{-V_i^2 B_{ii} + V_i V_j [G_{ij}\sin(\theta_i - \delta_j) - B_{ij}\cos(\theta_i - \delta_j)] + V_i V_{CR}[G_{ij}\sin(\theta_i - \delta_{CR}) - B_{ij}\sin(\theta_i - \delta_{CR})] + V_i V_{CR}[G_{VR}\sin(\theta_i - \delta_{CR}) - B_{ij}\cos(\theta_i - \delta_{CR})]\}[P_1 V_i^2 + P_2 V_i + P_3], \quad (11)$$

where G_{ij} and B_{ij} are the conductance and susceptance between bus i and bus j, respectively. Equations (10), (11) modified mathematical expressions of UPFC with ZIP load model [13].

Series and series controller (IPFC) typically makes use of many DC-to-AC converters, all of which provides series compensation for a different line. The IPFC really includes a number of the static synchronous series compensators. All of the converters have high reactive power transmission and storage capacities. In addition, the converters can produce or soak up reactive power at will. A series converter connected between bus i and bus j can provide complicated power, as described by below equations in that order:

$$P_{ij} = \{V_i^2 G_{ii} - \sum_{\substack{j=1 \\ j\neq i}}^{n} V_i V_{ij}(G_{ij}\cos\theta_{ij} - B_{ij}\sin\theta_{ij}) + \sum_{\substack{j=1 \\ j\neq i}}^{n} V_i V_{seij}(G_{ij}\cos(\theta_{ij} - \theta_{seij}) - B_{ij}\sin(\theta_{ij} - \theta_{seij}))\}[P_1 V_i^2 + P_2 V_i + P_3]; \quad (12)$$

$$Q_{ij} = \{V_i^2 B_{ii} - \sum_{\substack{j=1 \\ j\neq i}}^{n} V_i V_{ij}(G_{ij}\sin\theta_{ij} - B_{ij}\cos\theta_{ij}) - \sum_{\substack{j=1 \\ j\neq i}}^{n} V_i V_{seij}(G_{ij}\sin(\theta_{ij} - \theta_{seij}) - B_{ij}\cos(\theta_{ij} - \theta_{seij}))\}[P_1 V_i^2 + P_2 V_i + P_3]; \quad (13)$$

$$P_{ji} = \{V_i^2 G_{ii} - \sum_{\substack{j=1 \\ j\neq i}}^{n} V_i V_{ji}(G_{ij}\cos\theta_{ji} - B_{ij}\sin\theta_{ji}) - \sum_{\substack{j=1 \\ j\neq i}}^{n} V_i V_{seij}(G_{ij}\cos(\theta_{ij} - \theta_{seij}) - B_{ij}\sin(\theta_{ij} - \theta_{seij}))\}[P_1 V_i^2 + P_2 V_i + P_3]; \quad (14)$$

$$Q_{ji} = \{V_i^2 B_{ii} - \sum_{\substack{j=1 \\ j\neq i}}^{n} V_i V_{ji}(G_{ij}\cos\theta_{ji} - B_{ij}\sin\theta_{ji}) - \sum_{\substack{j=1 \\ j\neq i}}^{n} V_i V_{seij}(G_{ij}\sin(\theta_{ij} - \theta_{seij}) - B_{ij}\cos(\theta_{ij} - \theta_{seij}))\}[P_1 V_i^2 + P_2 V_i + P_3]; \quad (15)$$

where V_i and V_j are the maximum allowed bus i and j voltages, p.u.; V_{seij} and the conjugate of I_{ij} are the maximum allowed bus i and j series voltage and reference current. Mathematical expressions of IPFC incorporated in ZIP load model to assess its behavior and the above (12)–(15) modified IPFC mathematical expression with ZIP load model.

Results and discussion with compensation devices. To analysis the contingency of IEEE test system to asses the status of the power security:

Case 1: IEEE 30 bus with ML algorithm.

Case 2: Soft computing techniques are applied for modified IEEE test system.

Case 1: IEEE 30 bus with ML algorithm. IEEE 30 bus is considered from the historical data for ML algorithm to predict severity and status of the system in power system security point of view. Figure 3 represents voltage profile vs bus no. in ZIP load model under various load conditions.

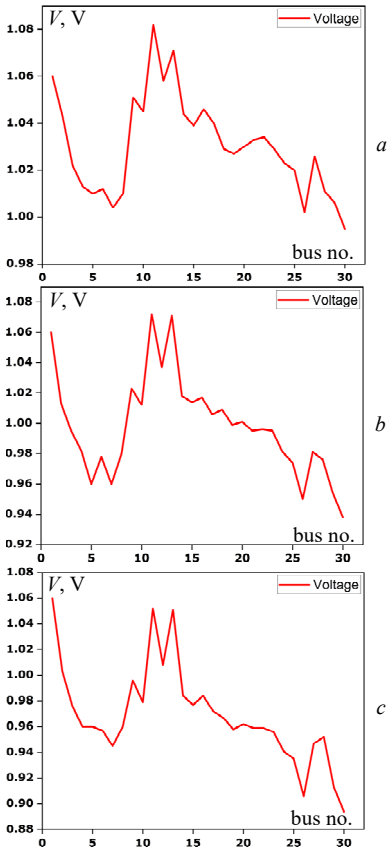

Fig. 3. Voltage profile vs bus no. with various loaded condition: *a* – base case; *b* – 130 % loading; *c* – 150 % loading

Figure 4 shows the demand, active generator capacity and corresponding fuel cost during various loading conditions.

Figure 5 shows the total active generator capacity and corresponding fuel cost before and after FACTS devices using ML. From Fig. 4, 5 it is clear that, IEEE 30 bus system consists of 6 generators, but only 2 generators are utilized (one slack bus another generator bus) due to this, generator is burden to meet the demand and fuel cost gets increases. Hence IEEE modified bus system is consider with 6 generators units.

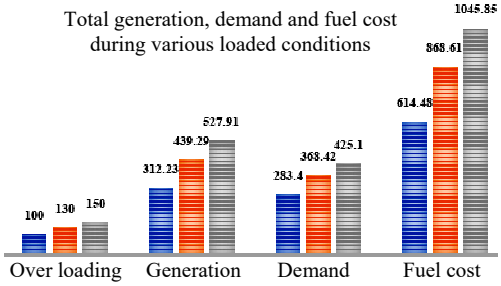

Fig. 4. Generation and fuel cost for various load conditions

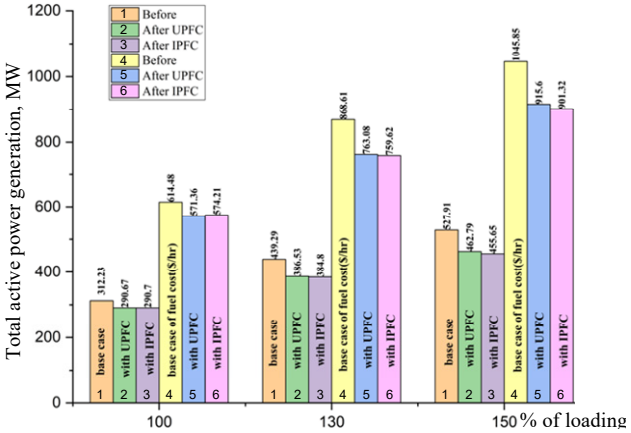

Fig. 5. Generation and fuel cost for various load conditions with compensation

Case 2: Soft computing techniques are applied for modified IEEE test system. In this case 1 IEEE 30 system having 6 generators, but only 2 are utilized due to this generator under stress and it leads to increase loss and fuel cost. So IEEE 30 bus system is modified and to reduce the stress on generators, generator reschedule is required and it is achieved by the objective function.

In order to get the optimal generation values for the generators to meet the required demand. An objective function is developed. In the below analysis ML tool is used to find severity of line leads to the location of compensation and for optimal generator values PSO is utilized.

Particle swarm optimization (PSO). Many fields benefit from PSO's unique properties. PSO optimizes complex problems using collective intelligence. PSO finds optimal or near-optimal solutions using swarm particle communication and exploration. High-dimensional PSO outperforms traditional optimization methods. It solves complex problems efficiently. Also, PSO's iterative nature lets it adapt to changing environments. By adapting, PSO exploits search space. Finally, PSO is simple, its efficacy and simplicity make it popular across disciplines. So, PSO inspired efficient optimization algorithms and hybrid methods for complex problems [14, 15]. Figure 6 shows the block diagram shows the utilization of ML tool in combination with PSO to get minimum fuel cost with optimum generators values.

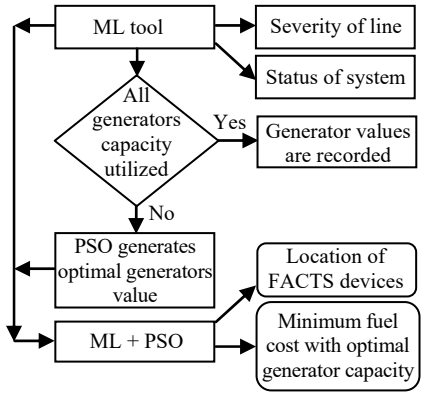

Fig. 6. Block diagram of ML+PSO

Objective function. The novel method mitigates the IEEE 30 bus severity index, power outages, capital costs, fuel use, and voltage changes. The PSO method is used to determine optimal generator values for the minimum fuel cost and dimensions of FACTS hardware. Here, we can see the objective function:

$$F = \min(F_1 + F_2 + F_3), \quad (16)$$

where F is the objective function; F_1, F_2, F_3 are the corresponding iterations. This objective function is implemented using PSO algorithm along with ML algorithms.

Optimization of real power loss. At this point, we've reached a point where our active power loss is as small as it can get. Effectively depicting the preliminary objective function, (17) shows how to significantly reduce the actual power loss in transmission lines:

$$F_1 = P_{Loss} = \sum_{k=1, j\neq i}^{n} G_{kj}[V_k^2 + V_j^2 - 2V_k V_j \cos(\delta_k - \delta_j)], \quad (17)$$

where P_{Loss} is the actual power loss; n is the number of transmission lines; G_{kj} is bus k and j's conductance; V_k and V_j are their voltages; δ_k and δ_j are their angles.

Capital expenditures for FACTS devices. Here, the capital expenditure ($/h) for UPFC and IPFC are analyzed as:

$$F_3 = Cost_{UPFC} + Cost_{IPFC}, \quad (18)$$

where: $Cost_{UPFC} = 0.0003 \cdot s^2 - 0.26911 \cdot s + 188.22$;
$Cost_{IPFC} = Cost_{IPFCA} + Cost_{IPFCB}$;
$Cost_{IPFCA} = 0.00015 \cdot s_i^2 - 0.0134 \cdot s_i + 94.11$;
$Cost_{IPFCB} = 0.00015 \cdot s_j^2 - 0.0134 \cdot s_j + 94.11$;
$s = |Q_2| - |Q_1|$; $s_i = |Q_{i2}| - |Q_{i1}|$; $s_j = |Q_{i2}| - |Q_{i1}|$.

After the FACTS have been configured in MVAR, the reactive power flow in the line is represented by Q_2, whereas it was represented by Q_1 beforehand. The reactive power flow down the line is represented by Q_{i1} and Q_{i2}, and the cost function S_{ij} of the converters linked to buses i and j is shown in [10, 13, 16].

Cost reduction of fuel. Reduced fuel costs in the generator have finally been realized. The cost of fuel for the generator can be thought of as the quadratic of the sum of the costs involved in using fuel functions that are themselves convex. Equation (19) depicts the generators' quadratic fuel cost function:

$$F_4 = \min \text{Cost} \sum_{i=1}^{N_g} [a_i p_{gi}^2 + b_i p_{gi} + c_i p_{gi}], \quad (19)$$

where N_g is the total number of generators; i is the index of the bus; a_i, b_i and c_i are the i^{th} generator's fuel cost coefficients; p_{gi} is its maximum active power output.

Results and discussion. This study demonstrates the modified IEEE 30 bus system under varying loads and failure scenarios. Figure 7 shows the voltages profiles with soft computing techniques.

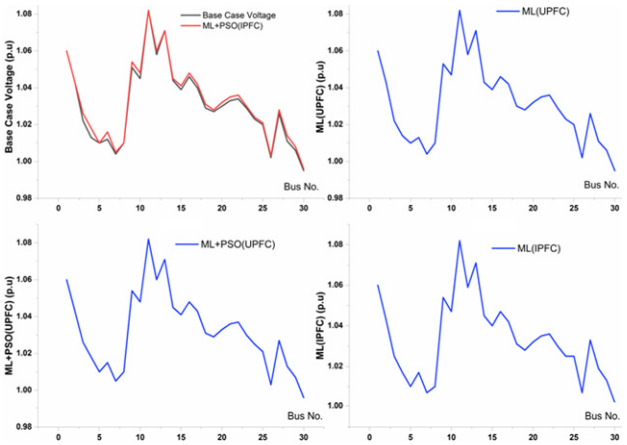

Fig. 7. Voltage profiles of modified IEEE 30 system

Figure 8 shows the active power transfer enhancement along with total system losses for ML and ML combined with PSO.

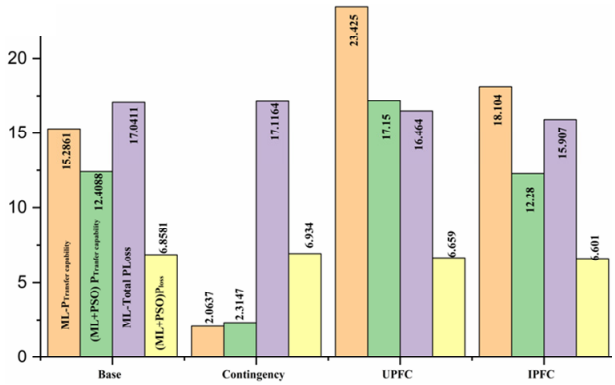

Fig. 8. Enhancement of active power and total system losses with soft computing techniques of modified IEEE 30 system

Figure 9 shows the total generator capacity based on demand along with fuel cost using ML and ML+PSO with 100% loading.

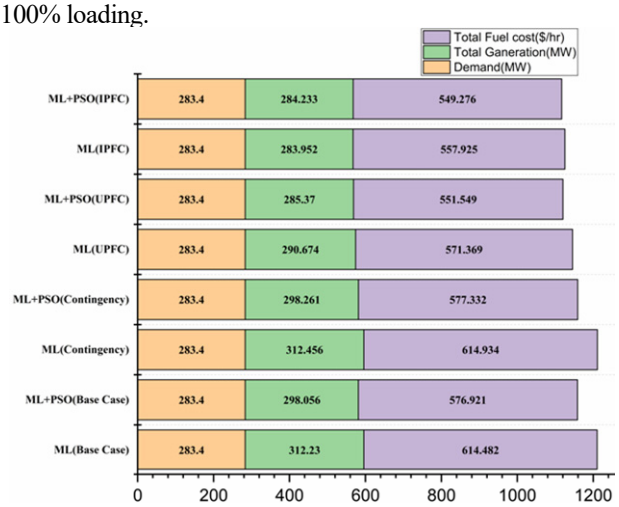

Fig. 9. Demand, generation and fuel cost with soft computing techniques

Conclusion. Hence mathematical analysis of ZIP load modeling and contingency analysis along with economic analysis is carried out for IEEE 30 and modified IEEE 30 test system in the view of the single line outage and overloading. The effective way of finding the critical lines during the faulted condition using hybrid lines stability ranking index. An objective function is developed to find the cost of devices with minimum fuel cost by optimal location of flexible AC transmission system devices (unified and interline power flow controllers) using particle swarm optimization algorithms. Here compensation devices (unified and interline power flow controllers) are used to maintain the stable and secure.

Conflict of interest. The authors declare that they have no conflicts of interest.

REFERENCES

1. Gamboa R.A., Aravind C.V., Chin C.A. Power System Network Contingency Studies. *2018 IEEE Student Conference on Research and Development (SCOReD)*, 2018, pp. 1-6. doi: https://doi.org/10.1109/SCORED.2018.8711362.

2. Venkatesh P., Visali N. Assessment of Power System Security Using Contingency Analysis. *International Journal of Control and Automation*, 2019, vol. 12, no. 5, pp. 25-32. doi: https://doi.org/10.33832/ijca.2019.12.5.03.

3. Venkateswaran J., Manohar P., Vinothini K., Shree B.T.M., Jayabarathi R. Contingency analysis of an IEEE 30 bus system. *2018 3rd IEEE International Conference on Recent Trends in Electronics, Information & Communication Technology (RTEICT)*, 2018, pp. 328-333. doi: https://doi.org/10.1109/RTEICT42901.2018.9012509.

4. Biswas P.P., Arora P., Mallipeddi R., Suganthan P.N., Panigrahi B.K. Optimal placement and sizing of FACTS devices for optimal power flow in a wind power integrated electrical network. *Neural Computing and Applications*, 2021, vol. 33, no. 12, pp. 6753-6774. doi: https://doi.org/10.1007/s00521-020-05453-x.

5. Srinivasan G., Mahesh Kumar Reddy V., Venkatesh P., Parimalasundar E. Reactive power optimization in distribution systems considering load levels for economic benefit maximization. *Electrical Engineering & Electromechanics*, 2023, no. 3, pp. 83-89. doi: https://doi.org/10.20998/2074-272X.2023.3.12.

6. Nasser A., Adnan H. A Literature Review on the Unified Power Flow Controller UPFC. *International Journal of Computer Applications*, 2018, vol. 182, no. 12, pp. 23-29. doi: https://doi.org/10.5120/ijca2018917775.

7. Asawa S., Al-Attiyah S. Impact of FACTS device in electrical power system. *2016 International Conference on Electrical, Electronics, and Optimization Techniques (ICEEOT)*, 2016, pp. 2488-2495. doi: https://doi.org/10.1109/ICEEOT.2016.7755141.

8. Alhejji A., Ebeed Hussein M., Kamel S., Alyami S. Optimal Power Flow Solution With an Embedded Center-Node Unified Power Flow Controller Using an Adaptive Grasshopper Optimization Algorithm. *IEEE Access*, 2020, vol. 8, pp. 119020-119037. doi: https://doi.org/10.1109/ACCESS.2020.2993762.

9. Mishra A., Kumar G.V.N. A risk of severity based scheme for optimal placement of interline power flow controller using composite index. *International Journal of Power and Energy Conversion*, 2017, vol. 8, no. 3, art. no. 257. doi: https://doi.org/10.1504/IJPEC.2017.10003636.

10. Venkatesh P., Visali N. Machine Learning for Hybrid Line Stability Ranking Index in Polynomial Load Modeling under Contingency Conditions. *Intelligent Automation & Soft Computing*, 2023, vol. 37, no. 1, pp. 1001-1012. doi: https://doi.org/10.32604/iasc.2023.036268.

11. Yari S., Khoshkhoo H. Assessment of line stability indices in detection of voltage stability status. *2017 IEEE International Conference on Environment and Electrical Engineering and 2017 IEEE Industrial and Commercial Power Systems Europe (EEEIC / I&CPS Europe)*, 2017, pp. 1-5. doi: https://doi.org/10.1109/EEEIC.2017.7977454.

12. Eladl A.A., Basha M.I., ElDesouky A.A. Multi-objective-based reactive power planning and voltage stability enhancement using FACTS and capacitor banks. *Electrical Engineering*, 2022, vol. 104, no. 5, pp. 3173-3196. doi: https://doi.org/10.1007/s00202-022-01542-3.

13. Bhattacharyya B., Raj S. Swarm intelligence based algorithms for reactive power planning with Flexible AC transmission system devices. *International Journal of Electrical Power & Energy Systems*, 2016, vol. 78, pp. 158-164. doi: https://doi.org/10.1016/j.ijepes.2015.11.086.

14. Chorghade A., Kulkarni Deodhar V.A. FACTS Devices for Reactive Power Compensation and Power Flow Control – Recent Trends. *2020 International Conference on Industry 4.0 Technology (I4Tech)*, 2020, pp. 217-221. doi: https://doi.org/10.1109/I4Tech48345.2020.9102640.

15. Goutham N.S., Mohd. Z.A. Ansari. Determination of Optimal Location of FACTS Devices for Power System Restoration Including Load Flow and Contingency Analysis. *International Journal of Engineering Research & Technology (IJERT)*, 2017, vol. 5, no. 18.

16. Venkatesh P., Visali N. Investigations on hybrid line stability ranking index with polynomial load modeling for power system security. *Electrical Engineering & Electromechanics*, 2023, no. 1, pp. 71-76. doi: https://doi.org/10.20998/2074-272X.2023.1.10.

Received 22.08.2022
Accepted 13.12.2022
Published 01.07.2023

Peruthambi Venkatesh[1], *Research Scholar*,
Nagalamadaka Visali[1], *Professor*,
[1] Department of Electrical & Electronics Engineering,
JNTUA College of Engineering (Autonomous) Ananthapuramu,
Ananthapuramu-515002, Andhra Pradesh, India,
e-mail: venkateshp.engg@gmail.com (Corresponding Author);
nvisali.eee@jntua.ac.in

How to cite this article:
Venkatesh P., Visali N. Enhancing power system security using soft computing and machine learning. *Electrical Engineering & Electromechanics*, 2023, no. 4, pp. 90-94. doi: https://doi.org/10.20998/2074-272X.2023.4.13

Матеріали приймаються за адресою:
Кафедра "Електричні апарати", НТУ "ХПІ", вул. Кирпичева, 2, м. Харків, 61002, Україна
Електронні варіанти матеріалів по e-mail: a.m.grechko@gmail.com

Довідки за телефонами: +38 067 359 46 96 Гречко Олександр Михайлович

Передплатний індекс: 01216